Universitat de les Illes Balears
CSIC
IFISC
Instituto de Física Interdisciplinar y Sistemas Complejos

Synchronization and application of delay-coupled semiconductor lasers

TESIS DOCTORAL

Konstantin Hicke

Director: Prof. Ingo Fischer

Ponente: Prof. Maxi San Miguel

Universitat de les Illes Balears
2014

SYNCHRONIZATION AND APPLICATION OF DELAY-COUPLED SEMICONDUCTOR LASERS

Konstantin Hicke
Tesis realizada en el Instituto de Física Interdisciplinar y Sistemas Complejos, IFISC (CSIC-UIB).
Presentada en el Departamento de Física de la Universitat de les Illes Balears.

PhD Thesis

Supervisor: Prof. Ingo Fischer
Ponente: Prof. Maxi San Miguel

For an updated version of this thesis please contact:
konstantin@ifisc.uib-csic.es

Palma de Mallorca, 21 de Mayo de 2014.

Tesis doctoral presentada por Konstantin Hicke para optar al título de Doctor, en el Programa de Física del Departamento de Física de la Universitat de les Illes Balears, realizada en el IFISC bajo la dirección de Prof. Ingo Fischer (IFISC-CSIC).

Visto bueno
Director de la tesis
Prof. Ingo Fischer

Visto bueno
Ponente
Prof. Maxi San Miguel

Doctorando
Konstantin Hicke

Palma de Mallorca, 21 de Mayo de 2014.

Konstantin Hicke reconoce con gratitud la ayuda financiera concedida por el Govern de les Illes Balears (Conselleria d'Educació, Cultura i Universitats) para la formación de personal investigador.

La ayuda ha sido seleccionada en el marco de un programa operativo cofinanciado por el Fondo Social Europeo.

Invertim en el seu futur

Unió Europea
Fons Social Europeu

Govern de les Illes Balears
Conselleria d'Educació, Cultura i Universitats
Direcció General d'Universitats,
Recerca i Transferència del Coneixement

To Anka

Resumen

El trabajo presentado en esta tesis se centra en la dinámica compleja de láseres de semiconductor (SL) cuando reciben retroalimentación óptica con retraso de una cavidad externa o bien, se encuentran acoplados con retraso a un segundo láser de semiconductor. Investigamos las propiedades fundamentales y la dinámica inducida por la retroalimentación con retraso y por el acoplamiento con retraso. Además, se estudia el uso de la dinámica compleja transitoria de un único SL, surgida de la retroalimentación con retraso y de la inyección de señal externa, para esquemas neuro-inspirados de procesamiento de datos. Basándonos en experimentos y en simulaciones numéricas, investigamos sistemas de dos SLs acoplados, comprendiendo el papel del láser y de los parámetros de acoplamiento en las propiedades de sincronización de dichos sistemas. Relacionamos ciertos aspectos de la dinámica de sincronización, como eventos intermitentes de desincronización, con la dinámica no lineal subyacente en el sistema láser acoplado.

Por consiguiente, nuestro trabajo combina tanto conocimientos fundamentales sobre láseres acoplados con retraso como perspectivas para nuevas aplicaciones.

Con el objetivo de explorar el potencial de un único SL con retroalimentación con retraso, seguimos el concepto de "reservoir computing" (RC) basado en sistemas con retraso. En particular, estudiamos dos tareas computacionalmente exigentes para los sistemas de cálculo tradicionales. Exploramos diferentes configuraciones de retroalimentación, métodos de inyección de datos y regímenes de funcionamiento del láser e identificamos las condiciones óptimas en función de la tarea. Nuestro trabajo demuestra el potencial de montajes fotónicos sencillos y del concepto de RC para futuros paradigmas computacionales.

Asimismo, estudiamos las propiedades de sincronización en sistemas de dos SLs acoplados con retraso por medio de un relé. Se exploran las consecuencias de las asimetrías en este montaje en las propiedades dinámicas y de sincronización. Un aspecto relevante es cómo decrece o se pierde la sincronización, siendo de especial importancia para aplicaciones en esquemas de comunicaciones caóticas y protocolos de intercambio de llaves (key-exchange protocols). Llevamos a cabo una aproximación basada en eventos, y relacionamos cambios en los niveles de sincronización al variar diferentes parámetros o desajustes con el inicio de los eventos de desincronización y sus características. Nuestros resultados con respecto a los niveles y capacidad de sincronización enfatizan la importancia de la simetría y del ajuste entre parámetros para alcanzar sincronización idéntica de osciladores acoplados con retraso.
Aplicamos nuestros descubrimientos sobre la posibilidad de desarrollar e implementar un método experimental basado en sincronización idéntica para identificar determinismo en la dinámica caótica de un SL con retroalimentación retrasada. Nuestro método se basa en la sincronización a retraso cero (zero-lag) del láser con un sistema gemelo. Centramos nuestra investigación en las caídas de potencia (power dropouts) que tienen lugar en el régimen de Fluctuaciones de Baja Frecuencia (Low Frequency Fluctuations) del SL, puesto que representan características dinámicas cuyo origen ha sido fuente de controversia en el pasado. Nuestro trabajo es de gran relevancia en la investigación de la dinámica no lineal, pues la mayoría de nuestros resultados y procedimientos pueden adaptarse a otros sistemas con retraso y proporcionar conocimientos generales a las propiedades de los sistemas acoplados con retraso.

Abstract

The work in this thesis is focused on the complex dynamics of semiconductor laser (SL) devices which receive time-delayed feedback from an external cavity or are delay-coupled with a second semiconductor laser. We investigate fundamental properties of the dynamics and study the utilization of transient complex dynamics of a single SL arising from delayed feedback and external signal injection for a neuro-inspired photonic data processing scheme. Based on experiments and numerical modelling, we investigate systems of two coupled SLs, gaining insights into the role of laser and coupling parameters for the synchronization characteristics of these systems. We link certain features of the synchronization dynamics, like intermittent desynchronization events, to the underlying nonlinear dynamics in the coupled laser system.

Our research thus combines both fundamental insights into delay-coupled lasers as well as novel application perspectives.

In order to explore the capabilities of a single SL with delayed feedback, we follow the concept of reservoir computing (RC) based on delay systems. In particular, we study two different tasks, which are computationally hard for traditional computing concepts. We explore several feedback configurations, data injection methods and operating regimes of the laser and identify the task-dependent optimal operating conditions. Our work demonstrates the potential of simple photonic setups and the RC concept for future computational paradigms.

Furthermore, we study the synchronization properties in systems of two delay-coupled SLs with relay. We explore the consequences of asymmetries in this basic setup for the dynamics and synchronization properties. One key question is, how synchronization decays or is lost, which is of significant importance for applications in chaotic communications schemes and key-exchange protocols. We follow an event-based approach and connect

changes in the synchronization levels for varying operating parameters or varying mismatches to the onset and characteristics of desynchronization events. Our results regarding synchronization levels and synchronizability underline the significance of symmetry and matching parameters for the identical synchronization of delay-coupled oscillators.

We apply our findings regarding the possibility for identical synchronization to develop and implement an experimental method to identify determinism in the chaotic dynamics of a SL with delayed feedback. Our method is based on zero-lag synchronization of the laser with a twin system. We focus our investigation on power dropouts in the Low Frequency Fluctuations regime of a SL since they represent distinct dynamical features whose origin had been controversially discussed in the past. Our method can be adapted in principle to other nonlinear delay systems which exhibit intrinsic noise to test for traces of determinism.

Our work is of general relevance for research in nonlinear dynamics, as many of our results and methods can be adapted for other delay systems and provide general insights into the characteristics of delay-coupled systems.

Acknowledgements

First of all, I would like to thank Prof. Ingo Fischer for his great guidance during all the studies at IFISC that led to this thesis. Ingo gave me much freedom to explore different topics and approaches while always being willing to give me helpful advice and support. The discussions with him immensely improved my understanding of the subject matter we were working on. He always has had the ability to motivate me and to rekindle my enthusiasm when I needed it, and his friendly, uncomplicated attitude created a really pleasant and supportive working environment. I am very grateful to have had an advisor as committed as him.

I would also like to thank all of my collaborators who contributed to our joint publications. I especially thank Valentin Flunkert, Otti d'Huys, Jordi Tiana-Alsina, Xavier Porte and Miguel Angel Escalona-Morán with all of whom working was not only interesting and productive but a pleasure. I would also like to thank Prof. Jordi Garcia-Ojalvo for his great hospitality when he invited me for a research stay in Barcelona. Also, I thank the members of the PHOCUS project consortium for the interesting collaboration, fascinating discussions, enjoyable project meetings, and for giving me the opportunity to participate in truly interdisciplinary work.

I am grateful for the help and advice that Dr. Daniel Brunner provided me. He was always willing to answer or help me with my many questions and was a neverending source of advice and good ideas. Dr. Miguel Cornelles Soriano and Dr. Thomas Jüngling also deserve my deepest gratitude for their support. I thank Prof. Claudio Mirasso for his great help to me when I moved to Palma and his advice on many scientific topics, as well as on administrative matters.

There are several people I want to thank for helping me with the corrections when I was finishing this thesis. I am especially grateful to Valérie Molière for her immense help with the copyediting. I am also very lucky to have had the help of Miguel Soriano, Thomas Jüngling, Marina Diakonova, Neus Oliver and Xavier Porte with the final corrections and the polishing of this work.

The years at IFISC and on Mallorca were a wonderful and very enjoyable experience for me for which the people of IFISC deserve the credit. I am very glad I had the chance to meet and interact with so many nice and interesting people who also helped me see things from many different perspectives. I was lucky to gain many new friends here who made me feel at home on Mallorca. I especially want to thank Daniel, Xavi, Neus, Marina, Adrian, Juan, Luis and Maria for all the great times and experiences we shared over the years.

Finally, I want to thank my family and my friends at home for believing in me, supporting me and simply being there for me. Above all, I thank my partner Anka for her endless love, patience, support and understanding. Without her, I could not have finished this thesis.

Contents

Titlepage **i**

Resumen **vii**

Abstract **ix**

Acknowledgements **xi**

Contents **xiii**

1 Introduction **1**

2 Single laser with feedback: Modeling and characteristics **7**
- 2.1 Introduction . . . 7
- 2.2 Characteristic features . . . 9
  - 2.2.1 Susceptibility to perturbations . . . 9
  - 2.2.2 Amplitude-phase coupling . . . 10
  - 2.2.3 Relaxation oscillations and characteristic timescales . 11
  - 2.2.4 Feedback-affected power-current characteristics . . . 15
  - 2.2.5 Effect of feedback on spectral characteristics . . . 17
- 2.3 Single mode rate equations . . . 17
  - 2.3.1 Lang-Kobayashi model . . . 17
  - 2.3.2 External cavity modes . . . 19
  - 2.3.3 Model limitations and suitability . . . 22
- 2.4 Polarization modes - extended model . . . 24
  - 2.4.1 Polarization-rotated optical feedback . . . 24
  - 2.4.2 Model . . . 27

2.4.3 Nondimensionalization 28
2.5 Characteristic dynamical regimes 30
2.5.1 The Low Frequency Fluctuations regime 30
2.5.2 Full Coherence Collapse 38
2.5.3 Dynamics induced by Polarization-rotated feedback . 41
2.5.4 Concluding remarks 43

3 Coupled semiconductor lasers:Influence of asymmetries on dynamics and synchronization 45
3.1 Introduction 45
3.1.1 Synchronization of chaotic lasers in different coupling schemes 45
3.1.2 Chapter Outline 48
3.1.3 Collaborative work related with this chapter 48
3.2 Relay configuration with coupling mismatch 49
3.3 Drive-response configuration with coupling mismatch 55
3.4 Relay configuration with delay mismatch 56
3.4.1 Synchronization properties 57
3.4.2 Dynamical regimes under delay mismatch 60
3.5 Nonlinear gain saturation 68
3.6 Frequency detuning 71
3.6.1 Modeling and synchronization properties 71
3.6.2 Spectral and dynamical features with detuning 74
3.7 Summary 81

4 Identical synchronization and intermittent desynchronization events in delay-coupled lasers 83
4.1 Introduction 83
4.1.1 Bubbling and on-off intermittency 83
4.1.2 Chapter Outline 85
4.1.3 Contributions to the work in this chapter 86
4.2 Experimental setup 86
4.3 Identical synchronization 87
4.4 Noise-induced bubbling 91
4.4.1 Synchronization degradation due to bubbling 91
4.4.2 Bubbling event statistics for different pump currents . 95
4.5 Detuning-induced desynchronization 97
4.5.1 Experimental work 97
4.5.2 Numerical modeling of the noiseless system 103
4.6 Bubbling due to mismatch 109
4.7 Summary 116

5 Characterizing the deterministic nature of individual events in chaotic laser dynamics 119
5.1 Introduction 119
5.2 Method 121
5.3 Experiments 121
5.4 Limitations of method 125
5.5 Numerical corroboration 127
5.6 Discussion, Adaptability and Outlook 133

6 Data processing using transient laser dynamics 137
6.1 Reservoir computing 137
6.2 Single dynamical node 140
6.3 Computational tasks 142
  6.3.1 Isolated spoken digit recognition 143
  6.3.2 Santa Fé timeseries prediction 144
6.4 Modeling 145
  6.4.1 Model characteristics 145
  6.4.2 Relation of modes 147
  6.4.3 Feedback configurations 148
  6.4.4 Signal injection methods 148
  6.4.5 Applied simplifications and parameters 151
6.5 Numerical results 151
  6.5.1 Spoken digit recognition 152
  6.5.2 Time series prediction 155
  6.5.3 Influence of system-intrinsic noise 158
6.6 Comparison with experiments 160
6.7 Possible improvements 163
  6.7.1 Polarization-resolved intensity readout 163
  6.7.2 Virtual node separation optimization 166
6.8 Summary and Outlook 167

Summary and Conclusions 171

Appendices 175

A Nondimensionalization of Lang-Kobayashi rate equations 177

B Transverse stability of External Cavity Modes 183

List of Figures 185

Bibliography 201

1

Introduction

Synchronization is one of the most important phenomena of interacting dynamical systems. The principle was discovered by Christiaan Huygens in the 17th century while studying pendulum clocks attached to the same wall. He noticed how the pendulums would adjust their rhythm to each other, even after being intentionally perturbed.

Synchronization is ubiquitous in nature [1–4] and it is essential to certain biological processes [5]. It is observed in physiology [5–7], in neuronal systems [8, 9], in chemical systems [10] and even in human behavior [11, 12].

The strongest form of synchronization is complete or identical synchronization, describing the situation where the dynamics of the interacting systems coincide completely. A subset of identical synchronization is zero-lag or isochronous synchronization, where the dynamics are instantaneously synchronized. Identical synchronization may involve a finite timeshift between the synchronized dynamics of the respective subsystems. In principle, it can only be achieved for identical systems. A weaker form of synchronization is generalized synchronization (GS) [13–16]. GS does not require identical or even similar oscillators. It implies that the dynamics of the interacting systems are not identical but that there is a well-defined relationship between them. The dynamics of two systems exhibiting GS may be significantly correlated with or without a certain time shift. However, generalized synchronization can also exhibit no significant correlation among the involved dynamical systems [17, 18].

In the early 1990s, Pecora and Carroll found that it is even possible to synchronize chaotic dynamics [19, 20]. Since then, chaos synchronization has been shown in many different systems, like electrical circuits, optoelectronic systems, lasers, generic oscillators, and neuron populations [2, 21–29]
Synchronization requires an interaction between the involved oscillators. In real-world systems, time-delayed interactions are ubiquitous due to the finite speed of information propagation. Synchronization of systems with

delay turned out to be relevant in many fields of research and have been investigated in many contexts, including neural networks, laser dynamics [30], traffic dynamics [31], chaos control [32, 33], and gene regulatory networks, among others. From a mathematical standpoint, delayed self-feedback renders a system infinite dimensional. It has been shown that delayed feedback can induce chaotic behavior in nonlinear dynamical systems, including semiconductor lasers, which are the central topic of this thesis.

Semiconductor lasers are omnipresent in our lives. Since their first developement in the 1960s [34–36], they have been extensively researched and developed into technologies for applications in communications, as sensors, as scientific tools, in consumer products, and for medical and industrial applications. When feedback-induced instabilities in SLs, e.g., from a distant reflector, were discovered [37], they were, and sometimes still are, viewed as a nuisance, since they can act as noise-like perturbations and deteriorate performance in applications like communications. Nevertheless, SLs with delayed feedback have since then received widespread attention from the nonlinear dynamics community. It has been recognized that they serve as excellent testbed systems to study delay-dynamics, chaos-synchronization and applications based thereon (see e.g. [30]). They are well-controllable systems and their structure plus the feedback lead to the emergence of several dynamical timescales, which make them especially versatile. SLs with delayed feedback or coupling were shown to exhibit rich dynamical behavior, including chaos [38–52]. Moreover, the study of SLs has contributed to the understanding of the classical routes to chaos, i.e., via intermittency [53], bifurcation cascades [54], period-doubling [44, 46] and quasi-periodicity [41].

Semiconductor lasers are intrinsically noisy systems because of spontaneous emission. The complex dynamics arising in a semiconductor laser with time-delayed feedback can be interpreted as an interplay between deterministic mechanisms and noise perturbations. There has been a long discussion about the origin or the dominant drive underlying the complex dynamics of a chaotic semiconductor laser, focusing on whether stochastic processes due to noise or deterministic behavior dominate certain dynamical behaviors [39, 42, 55–62]. In this work, we will introduce a method based on identical synchronization to test for traces of determinism in certain features of the dynamics of an SL subject to time-delayed self-feedback pumped with a low pump current.

It was shown that for large coupling delays, bidirectionally coupled lasers can not synchronize isochronously, even if the coupling is completely symmetrical and the lasers are identical. The laser dynamics then show significant lag correlation with the coupling delay [23, 63–70]. This behavior has been identified with generalized synchronization of leader-laggard type, even though, in the symmetric case, the roles of leader and laggard are not fixed and may switch irregularly [23]. The zero-lag synchronized solution exists but is unstable to perturbations [63, 65].

In order to achieve stable identical synchronization between mutually delay-coupled nonlinear systems, a relay element can be introduced in between the coupled oscillators. With a relay, very distant coupled oscillators can synchronize identically, due to the increased symmetry. Employing a relay results in the coupled oscillators receiving the same delayed signal (comprising self-feedback and coupling) at any time and irrespective of their current dynamical state. If the relay is placed in the exact middle between the coupled oscillators, they can exhibit zero-lag synchronization. This was demonstrated for optically-coupled lasers [71, 72], optoelectronically-coupled lasers [73–75], fiber ring lasers [66, 67], neurons [76, 77], optoelectronic oscillators [78] and electronic circuits [79]. The relay can be active, e.g., a relay laser or relay neuron, or passive, like a semitransparent mirror or a relay fiber loop for the coupled laser case. In the case of an active relay, the outer elements do not synchronize identically with the relay element, but rather with each other

Klein et al. [80] showed, that if one introduces delayed feedback to two mutually coupled subsystems identical synchronization can be established. If the feedback delays equal the coupling delay, zero-lag synchronization is possible. Adding self-feedback with appropriate delay times to coupled nonlinear oscillators has the same effect for the stability of identical synchronization as introducing a relay element between them.

The possibility of chaos synchronization led to the development of the idea to use it in chaos-based applications, such as chaos-encrypted communication schemes or chaos-based key-exchange [24–27, 81–91]. Commonly, this involves hiding messages in chaotic carrier dynamics that are synchronized between the coupled dynamical systems. The above-described relay configurations might be attractive for chaos-based communication systems.

Using SLs for chaos communication schemes has several advantages compared to other oscillators: SLs exhibit broadband dynamics on fast timescales, enabling rapid and efficient exchange of data. Furthermore, since modern fiberoptic communication is based on SLs, existing infrastructure can be used to employ chaos communication over medium to long distances, as was done by Argyris et al. during a field experiment in Athens [86].

Even in coupled systems in which identical synchronization is stable, there exists, an effect that can lead to the loss of synchronization, if noise or parameter mismatches are present. This phenomenon was named attractor bubbling or riddling [45, 92, 93], and is associated with transversely unstable invariant sets in the chaotic attractor. Bubbling has been observed in e.g., coupled electronic oscillators [94]. It has also been observed [95, 96] and theoretically shown to exist [97, 98] in systems of delay-coupled lasers. The bubbling phenomenon is characterized by intermittent desynchronization events, interrupting time intervals of complete synchronization.

Attractor bubbling thus has adverse effects on synchronization-based communication schemes like chaotic key-exchange protocols. In this thesis, we will investigate noise- and mismatch- induced bubbling events in bidirectional relay-configurations of two coupled semiconductor lasers. We

characterize their occurrence in dependence on the operating regimes and on the magnitude of certain mismatches.
The richness in complex dynamics that SLs with delayed feedback or injection exhibit, has also garnered interest to use them as reservoir elements in the framework of Reservoir Computing (RC). Reservoir computing [99] is based on Recurrent Neural Networks (RNN), which are inspired by and emulate some functionalities of the brain. RC utilizes the transient response of a complex network of nonlinear nodes to injected input signals for data processing purposes. These may include pattern recognition (classification) [100], time series prediction [101] and even mathematical operations [102]. Traditionally, RC requires complex networks with many elements, forming high-dimensional dynamical systems [103]. It was demonstrated, however, that a single nonlinear node with time-delayed feedback can perform classic RC tasks as well, due to the high-dimensional dynamics induced by the feedback [104]. RC has been demonstrated in electronic systems [104], in optoelectronic systems [105, 106] and with semiconductor optical amplifiers [107, 108]. Recently, all-optical RC using a single semiconductor laser with feedback was experimentally demonstrated [109].

We implement an extensive numerical study analyzing the computational potential of such a basic setup of a single SL with delayed feedback, and investigate the influence of different feedback and injection configurations, respectively, on the performance in two benchmark RC tasks. We furthermore study and analyze the system's performance in different operating regimes resulting from the variation of key parameters which are accessible experimentally.
The work in this thesis covers the study of the dynamics of semiconductor lasers receiving time-delayed optical feedback and the application of the dynamics, as well as the extension from a single SL system to a system of two mutually coupled semiconductor lasers receiving self-feedback. In the coupled system, we focus on the investigation of the synchronization properties of the complex dynamics.

The thesis is organized as follows: first, in Chapter 2, we introduce the particularities of a single SL subject to time-delayed feedback, and describe typical dynamical regimes. We introduce models, based on rate equations, for the description of such a laser. We will adapt these models in the following chapters for systems of two mutually-coupled lasers with feedback.

In Chapter 3, we investigate the synchronization properties of a system of two lasers with feedback that are mutually coupled via a passive relay. In particular, we investigate analytically the transverse stability of the synchronized solution when different asymmetries come into play. We consider an asymmetrically-placed relay leading to a feedback delay mismatch and a mismatch of the coupling and the feedback strength, respectively. We analyze numerically the dynamics in the system resulting from these asymmetries. We also study qualitatively the dynamics and synchronization properties in the case of frequency detuning of the two SLs in a numerical simulations.

Chapter 4 covers the exploration of intermittent desynchronization in the relay configuration due to noise or mismatch. We follow an event-based approach and characterize individual desynchronization events stemming from noise-induced bubbling for different operating conditions in an experimental system. Furthermore, we analyze detuning-induced episodic desynchronization observed in experiments and numerics. Moreover, we numerically study bubbling events that are induced by a small mismatch of the pump currents of the coupled SLs and compare them with noise-induced bubbling.

In Chapter 5, we apply our previously-obtained results regarding the influence of asymmetries, mismatches and noise on synchronization of coupled SLs. We develop a method to test whether specific dynamical events in the chaotic dynamics of a single SL subject to delayed feedback are dominantly driven by the underlying deterministic drive or by stochastic processes due to intrinsic noise. The method is based on isochronous synchronization with a twin laser.

Finally, Chapter 6 is devoted to extensive numerical studies of the data processing capabilities of a single SL with time-delayed feedback in the context of reservoir computing. We explore different feedback configurations, input injection methods, as well as operating regimes and their effect on the system's performance in two different computational tasks. We corroborate previous experimental results and identify optimized operating conditions for efficient low-error data processing in different kinds of tasks.

2

Single laser with feedback: Modeling and characteristics

2.1 Introduction

Semiconductor lasers (SLs) are ubiquitous in our world. Since their invention in the 1960s [34–36], they have been researched and developed to great extent. Nowadays, technology based on SLs is prevalent in our daily lives. SLs are used in optical data storage, in communications, in material processing, in medical applications, as pump sources and in consumer products. Because of the large diversity of SLs, referring to different SL materials, different cavity geometries (e.g. edge-emitting lasers [EELs], semiconductor ring lasers, vertical-cavity surface-emitting lasers [VCSELs], distributed feedback lasers [DFB], etc.) and different gain concepts (e.g. bulk semiconductor, quantum well [QW], quantum dash, quantum dots [QD], and quantum cascade), a variety of characteristics can be accessed as needed for tailored research conditions or applications. Moreover, semiconductor lasers are cheap, mass-produced devices with low power consumption and high wall-plug efficiency. Since most of the world's communication networks are based on fiber-linked semiconductor lasers, one can also use existing infrastructure for application and large-scale experiments.

Although SLs can be considered a mature technology, one has to be aware of certain particularities they have. One particularity of SLs is their strong sensitivity to external perturbations by optical feedback or optical coupling, around which the work in this thesis is centered. In Fig. 2.1, we show a schematic of a semiconductor laser with feedback from an external cavity.

The very strong susceptibility of SLs to external optical feedback was first observed decades ago by Risch and Voumard [37]. On the one hand, this sensitivity was (and sometimes still is) considered a nuisance and detrimental to applications. This is especially the case if the feedback-induced instabilities fall within the signal bandwidth they can deteriorate the usefulness of the laser in e.g. communications.

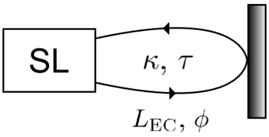

Figure 2.1: Schematic of a semiconductor laser (SL) in an external cavity. The external cavity is characterized by the cavity length L_{EC}, the corresponding round trip delay τ, the feedback strength κ, and the feedback phase ϕ.

On the other hand, the sensitivity of SLs to optical feedback also provides many opportunities in research and applications, as it was recognized that SLs are excellent devices to study Nonlinear Dynamics (NLD), especially when it comes to delayed feedback-induced dynamics. They are versatile devices offering a large range of different nonlinear behaviors, including chaos [38–52] and, as test-bed systems, are well-controllable in a set of system parameters that influence the dynamics. Most critical parameters are usually known or can be measured, which provides ideal circumstances for defined and controllable experimental conditions.

The intrinsic nonlinearity of SLs manifests itself in their strong amplitude-phase-coupling and is usually expressed by the so-called linewidth enhancement factor α. SLs also provide a number of time scales that can span several orders of magnitude. This provides a basis for complex nonlinear dynamics and phenomena. The slowest relevant timescale in SLs is related to the carrier decay and corresponds to an order of nanoseconds. It is roughly the timescale of the complex laser dynamics due to external perturbations. Since the dynamics is still very fast, it enables experimentalists to measure long dynamics timeseries for analysis while the system parameters' variation can be considered constant during acquisition.

The susceptibility of SLs to external perturbations is not only beneficial for the use of SLs as testbed systems in the study of NLD. Especially the possibility to generate chaotic intensity dynamics via optical feedback also led to the developement of several application concepts, such as chaos-based encrypted communication schemes or chaos-based key-exchange protocols [24–27, 81–91, 110]. Several approaches of chaos communications and key exchange using SLs have already been demonstrated (see e.g. [86]). Furthermore, due to their various dynamical characteristics, SLs have also been investigated regarding their capabilities in photonic computing and all-optical data processing [109]. We will pursue this concept in Chapter 6.

In this chapter we introduce some of the fundamental properties of semiconductor lasers with delayed optical feedback in Section 2.2. We introduce the most-used model for the dynamics of such SLs, which is based on rate equations, in Section 2.3, where we also calculate and analyze their basic solutions, called External Cavity Modes. In Section 2.4, we present an extension of the model from Section 2.3 that considers two different othogonal modes, which are related to polarization orientation. Finally, we show characteristic dynamical regimes of SLs when subject to delayed optical feedback in Section 2.5, such as Low Frequency Fluctuations (LFF), Coherence Collapse (CC) and square-wave switching (SW).

This chapter can be considered introductory to the following ones, though the features shown here were obtained by original experimental and numerical investigations. Since we study coupled laser systems, their synchronization and their application in later chapters, we consider it essential to start with the characteristics of the core element of all the configurations and schemes that are discussed later on: a single semiconductor laser device subject to delayed optical feedback.

2.2 Characteristic features

2.2.1 Susceptibility to perturbations

Compared to other laser types, SLs exhibit very fast timescales stemming from light-matter interaction in the semiconductor material. The photon lifetime is typically of the order of picoseconds, while the carrier decay takes place on a timescale of the order of nanoseconds or sub-nanoseconds. The interaction between the electric field and the carrier inversion determines the timescale of the laser dynamics.

Semiconductor laser materials as gain media exhibit high optical gain values. This results in the strong sensitivity to external perturbations. This sensitivity is additionally supported in SL devices in which the facet reflectivity is defined only via the refractive index of the SL material [110]. A low or moderate reflectivity leads to a low Q-factor which in turn results in the enhanced susceptibility to external perturbations [110]. However, a low Q-factor is not necessary for an SL device to exhibit a strong sensitivity to perturbations. VCSELs, for example, often exhibit strong sensitivity to perturbations and a high Q-factor. The perturbations can be delayed optical feedback signals, injected light, or noise. Feedback from external cavities can induce instabilities in the emitted intensity [37, 39]. With increasing strength of the feedback, the dynamics undergoes several bifurcations that can ultimately lead to chaos [46, 49, 111]. Depending on the system parameters, many different dynamical regimes are attainable like period-2-periodicity, period-4-periodicity, bistability, intermittency and different chaotic regimes.

2.2.2 Amplitude-phase coupling

SLs exhibit a particularly strong amplitude-phase coupling of the electric field in the laser medium. Small changes in intensity (e.g. by spontaneous emission, current transients or feedback) lead to excess perturbations in the phase of the lasing modes. This is due to the particular nature of the lasers' semiconductor material. In contrast to other types of lasers, e.g. gas lasers, which exhibit lasing transitions between discrete energy levels during stimulated emission, semiconductor lasers have partially filled (quasi-)continuous energy bands. This property of SLs lead to an asymmetric gain curve [112] and thus to a dispersion relation for the refractive index with a zero crossing at higher frequencies than the maximum of the gain curve [110, 113]. A small change in the gain g due to a change in carrier density (by intensity variation) in the laser material is accompanied by a variation of the refractive index μ of the semiconductor material. This then leads to a phase change of the lasing modes.

The gain g and refractive index μ are directly related to the imaginary and real parts of the semiconductor material's susceptibility $\chi = \chi_r + i\chi_i(n)$, respectively. The amplitude-phase coupling is caused by simultaneous variation of the imaginary part χ_i and the real part χ_r by carrier variation, both of which are linked by the Kramers-Kronig-relations [114, 115]. The amplitude-phase coupling is described by the so-called linewidth-enhancement factor or simply α-factor [116, 117]:

$$\alpha = -\frac{d(\chi_r(n))/dn}{d(\chi i(n))/dn} \tag{2.1}$$

where n is the carrier density. Any change in χ_i (i.e., the gain) leads to a change in χ_r (i.e., the frequency). For laser types with discrete energy levels involved in the lasing transitions the gain curve is symmetric [118]. The refractive index crosses zero at the maximum gain frequency and the symmetry is independent of the inversion n. Therefore, two-level lasers have a negligible α-factor. In contrast, for many types of SLs α usually takes nonzero values due to the asymmetry of their gain curves.

Several methods have been developed to experimentally determine the α parameter [119]. The most popular methods are based on net gain measurements of the SL material [120, 121], on the investigation of injection locking effects [122], or self-mixing phenomena [123] but many others exist (see e.g. [124]).

Because of the great diversity of semiconductor lasers, one has to be specific about the type of lasers under investigation. Lasing transitions in quantum-dot (QD) lasers and quantum cascade lasers, for example, are fundamentally different from common quantum well (QW) lasers, even though they are semiconductor lasers too. The lasing transitions in QD- and in quantum cascade lasers, like in many non-semiconductor lasers, take place between discrete energy levels. Consequently, these types of lasers are, in theory, expected to exhibit zero α in ideal cases because of their symmetric gain profiles. However, different physical reasons, like inhomogeneous broadening due to a broad QD size distribution, result in α-values significantly different from theoretical predictions.

In this thesis we focus our studies on common edge-emitting lasers (EELs) of the quantum-well (QW) type. These lasers usually exhibit an α between $\alpha = 1$ and $\alpha = 7$ [110]. In the future, we will refer to QW edge-emitters as SL.

The α parameter is one of the fundamental SL parameters and is important for a number of dynamical processes, especially optical feedback-related effects [41]. It was called linewidth-enhancement factor because it results in an excess linewidth broadening by a factor of $1 + \alpha^2$ [117, 125] as compared to the prediction of Schawlow and Townes [126]. The α parameters depends on the detuning of the emission wavelength from the gain maximum [119, 125]. This spectral dependence can be linearized around the solitary lasing threshold:

$$\alpha = -k \frac{d\mu/dn}{dg/dn} \tag{2.2}$$

Here, $d\mu/dn$ and g/dn are the derivatives of the refractive index and the gain per unit length, respectively, with respect to the carrier density. k denotes the free-space wave vector. The spectral dependence is dominated by the pronounced spectral dependence of the gain.

However, because the spectral dynamics occurring in the studies presented in this thesis are confined to a small range where the frequency variation is small, we assume constant α in all cases.

2.2.3 Relaxation oscillations and characteristic timescales

Relaxation oscillations (ROs) are a characteristic feature of Class B lasers, as which semiconductor lasers are often described, though the Class B laser model includes many approximations. Class B lasers have at least two degrees of dynamical freedom which is necessary for periodic solutions. In SLs, periodic solutions can occur as energy oscillations between the optical field and the carrier inversion. In solitary SLs, these oscillations are damped. If the laser is operated in the continuous wave (CW) regime, the gain and losses balance each other and the output power stays constant is over time. Spontaneous emission can lead to a deviation from the stable output power after which the power returns to the solitary CW power via the damped relaxation oscillations. These oscillations have a natural frequency ω_{RO} which originates from the light-matter interactions in the laser cavity [91, 118, 127, 128]:

$$\omega_{\mathrm{RO}} = \sqrt{\gamma\gamma_e \left(\frac{I}{I_{\mathrm{thr,sol}}} - 1 \right) - \lambda_{\mathrm{RO}}} \tag{2.3}$$

where

$$\lambda_{\mathrm{RO}} = \frac{1}{2}\gamma_e \frac{I}{I_{\mathrm{thr,sol}}} \tag{2.4}$$

is the damping rate of the ROs. In (2.3) and (2.4), γ describes the photon decay rate, γ_e is the carrier decay rate, and I and $I_{\mathrm{thr,sol}}$ are the pump current and the solitary threshold pump current, respectively. Conventional SLs can exhibit relaxation oscillations of the order of GHz, depending on the specific laser type and especially on the pump current.

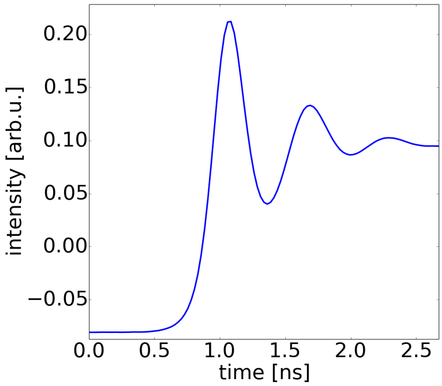

Figure 2.2: Experimentally obtained relaxation oscillations in a solitary laser's intensity output due to a pump current modulation pulse. The laser is pumped at $I = 1.05 I_{\mathrm{thr,sol}}$, the current modulation amplitude corresponds to $\delta I = 0.09 I_{\mathrm{thr,sol}}$. The plot was obtained after averaging 200 oscillations induced by modulation pulses of the same amplitude. Figure courtesy of Xavier Porte.

Fig. 2.2 shows an exemplary experimentally obtained intensity timeseries depicting ROs with a frequency of roughly $\omega_{\mathrm{RO}} \approx 1.67$ GHz as reaction to a current modulation pulse. The plot was obtained after averaging 200 different relaxation oscillations induced by modulation pulses of the same amplitude. The solitary laser is pumped at $I = 1.05 I_{\mathrm{thr,sol}}$, the current modulation amplitude corresponds to $\delta I = 0.09 I_{\mathrm{thr,sol}}$.
ω_{RO} is proportional to the square root of the pump current in excess of the threshold. Fig. 2.3 shows experimentally determined relaxation oscillation frequencies in dependence of the laser's excess pump current (black squares) in a log-log plot as well as a linear fit (red line). The linear fit has a slope of 0.49, reflecting the square root dependence. The accuracy of the fit is underlined by the resulting $R^2 = 0.994$.

The damping of the relaxation oscillations can vanish when the laser is subject to external perturbations. Especially delayed optical feedback,

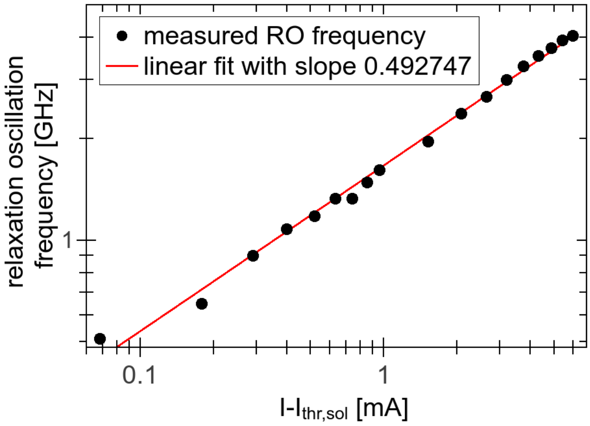

Figure 2.3: Measured relaxation oscillation frequencies of a SL in dependence of its normalized pump current. The black squares are the measured frequencies, the red line depicts a square-root fit.

even with very small amplitude, can undamp the relaxation oscillations. Undamped ROs are of crucial importance for the dynamics of SLs with delayed optical feedback. Their frequency defines one of the fundamental dynamical timescales in such a system. Because of the strong sensitivity of semiconductor lasers to perturbations and the fact that optical feedback undamps the ROs, feedback-induced instabilities in the intensity domain emerge on the timescale of the relaxation oscillations which corresponds to a sub-nanosecond timescale. This way, the ROs impose an upper limit to the modulation speed of SLs. High relaxation oscillation frequencies thus also allow for sub-nanosecond modulation of the laser's output intensity, a requirement for modern high-transmission-rate optical communication systems.

The undamped relaxation oscillations enable broadband dynamics in the laser, a fact that is also reflected in the comparison of radio frequency (rf) spectra between the solitary case and the case with feedback. The optical feedback undamps a broad range of frequencies, and the peak frequency is shifted toward higher frequencies. In the solitary laser case, the RO frequency is visible as a resonance in the rf-spectrum. In Fig. 2.4 we show experimentally obtained spectra of an SL in both situations.

Characteristic timescales

In a system of a single semiconductor laser that receives time delayed optical feedback from a distant reflector or via a feedback fiber loop (each forming an external cavity), several important timescales are prevalent: As

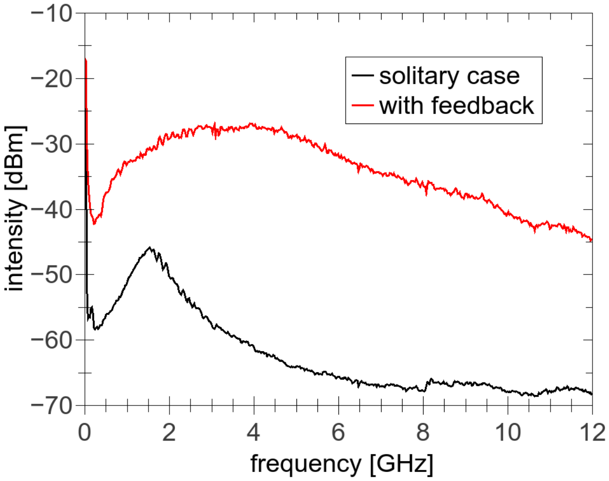

Figure 2.4: Experimentally obtained rf-spectra of a single semiconductor laser for the cases of solitary operation and with feedback, respectively. The peak in the solitary laser spectrum corresponds to the relaxation oscillation frequency. The feedback leads to an undampening of a broad range frequencies. Figure courtesy of Xavier Porte.

we learned above, the RO frequency plays a very important role for the dynamics timescale since it usually defines the dynamical bandwidth of the semiconductor laser.

The feedback delay time τ which is the roundtrip time through the external cavity is another crucial timescale intrinsic to this system. Among effects on spectral dynamics (see below), the signature of the feedback delay can be found in the output dynamics as well as in the rf-spectra.

In Fig. 2.5 we show the low frequency part of an rf-spectrum of a laser subject to feedback from a fiber loop resulting in a round-trip time of $\tau \approx 70$ ns. The spectrum exhibits peaks that are evenly spaced and come from the roundtrip in the external cavity. The corresponding round-trip frequency defines the spacing between neighboring peaks. In general, higher-order delay-peaks are also prevalent throughout the spectrum. However, for increasing order, the peaks are more and more suppressed.

Another important timescale is the intra-cavity round-trip time through the laser cavity. Commonly sized cavities of edge-emitters have a corresponding round-trip time of 2-20 ps. This time defines the spacing of the longitudinal modes in a conventional SL which thus have mode spacing of the order of 50-500 GHz.

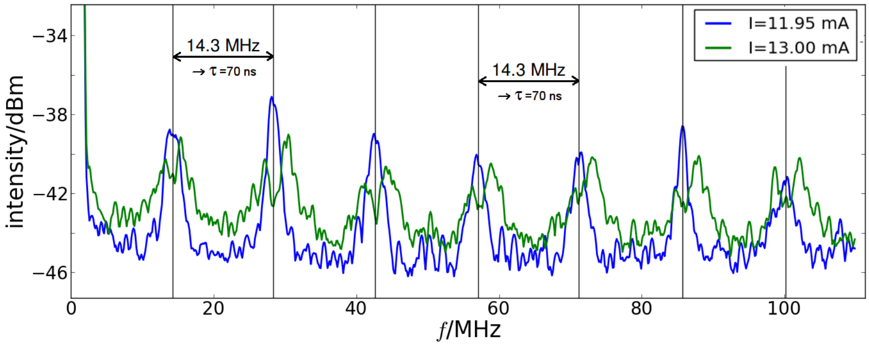

Figure 2.5: Delay time signature in the low frequency part of the rf-spectrum of a single laser subject to moderate feedback for two different pump currents. The peak spacing corresponds to the inverse of the round-trip time through the external cavity (i.e., the delay time) τ.

2.2.4 Feedback-affected power-current characteristics

Solitary semiconductor lasers exhibit an (almost) linear relation between output power and bias current starting at the threshold current $I_{\mathrm{thr,sol}}$. The threshold is defined as the point where the internal and external losses of the laser are compensated by the gain. Coherent optical feedback reduces the effective lasing threshold because the photons that are reinjected into the laser cavity reduce the losses and thus lasing starts for a lower pump current.

The pump-power (P-I-)characteristics of a semiconductor laser with feedback exhibits another distinct feature. In contrast to the solitary case, the P-I curve shows a kink for pump currents around the solitary lasing threshold [39, 42, 53]. This divergence from the otherwise linear relation of power and pump current above threshold can be attributed to the onset of irregular intensity fluctuations with a significant low-frequency component, which are induced by the feedback (see Section 2.5).

Two experimentally obtained P-I-curves, one for the solitary case and one for the situation with feedback, respectively, are depicted in Fig. 2.6. In this example, the feedback reduces the threshold by $\approx 15\%$. Furthermore, the slope efficiency is reduced. This is a common feature for edge-emitters due to asymmetric reflection coating in the laser cavity [129, 130].
The reduction of the lasing threshold in dependence of the feedback strength follows a complicated logarithmic relation depending on the different reflectivities in the laser cavity and in the external cavity [129, 131, 132]. Fig. 2.7 depicts experimentally obtained lasing thresholds normalized by the solitary threshold $I_{\mathrm{thr}}/I_{\mathrm{thr,sol}}$ in dependence of the feedback attenuation in dB where

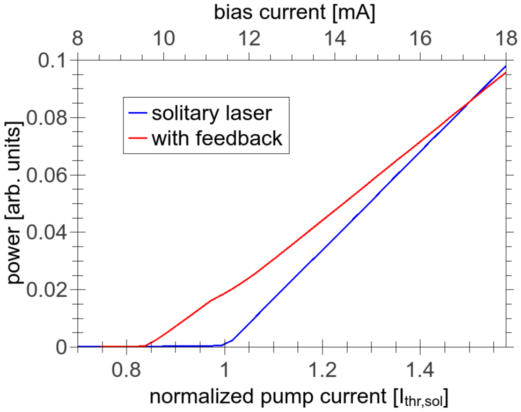

Figure 2.6: Experimentally obtained power-bias current characteristics for a single mode QW edge-emitting laser. Shown are the P-I-curves of the solitary laser (blue) and of the laser receiving optical feedback (red).

zero attenutation corresponds to full feedback strength.

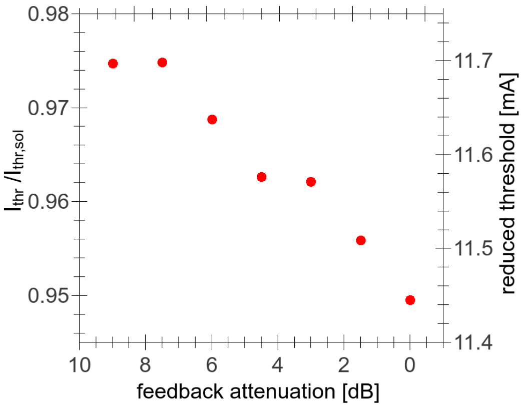

Figure 2.7: Measured threshold pump currents (normalized with the solitary threshold) for different feedback strengths/feedback attenuations. The feedback strength increases exponentially with decreasing feedback attenuation (in dB). Zero attenuation means full strength feedback. In the experiments that corresponded to a few percent of emitted light coupled back into the cavity.

2.2.5 Effect of feedback on spectral characteristics

As noted earlier, optical feedback can result in complex dynamical behavior of the laser's output. In conjunction the spectrum of the laser broadens significantly. The corresponding dynamical regime has been accordingly coined Coherence Collapse by Lenstra [38]. Additionally, the emission frequencies are redshifted by the feedback in comparison to the solitary case. Both effects are related to the SL-intrinsic nonlinearity represented by the α parameter. In Fig. 2.8 we show exemplary optical spectra obtained from experiments for the solitary laser case and for the feedback case. The relevant spectral part broadens significantly to several GHz due to moderate optical feedback.

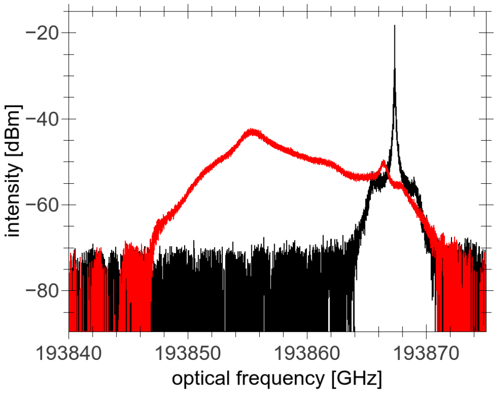

Figure 2.8: Optical spectra of a solitary edge-emitting SL (black) and of the same laser subject to optical feedback (red). The spectrum broadens to several GHz, the feedback accounted for $\approx 6-7\%$ of the emitted light.

As we will see later (see Section 2.3), we can roughly estimate the α-factor from the linewidth broadening in highly resolved optical spectra if the feedback rate is known.

2.3 Single mode rate equations

2.3.1 Lang-Kobayashi model

The dynamics of a semiconductor laser subject to time-delayed optical feedback from an external cavity (e.g. from a mirror placed at a distance) can often be decribed by a rate equation model for the slowly varying electric field amplitude $\mathcal{E}(t)$ and the carrier inversion $N(t)$ and by adding feedback terms to the field equation as introduced by Lang and Kobayashi in 1980 [133]:

$$\begin{aligned}\dot{\mathcal{E}}(t) &= \frac{1}{2}(1+i\alpha)\left(\mathcal{G}(\mathcal{E},N)-\gamma\right)\mathcal{E}(t)+\kappa e^{i\psi}\mathcal{E}(t-\tau_{ec})+F_{\mathcal{E}} \qquad (2.5)\\ \dot{N}(t) &= \frac{I}{e}-\gamma_e N(t)-\mathcal{G}(\mathcal{E},N)\left|\mathcal{E}(t)\right|^2 \qquad (2.6)\end{aligned}$$

with the gain function

$$\mathcal{G}(\mathcal{E},N)=g\frac{N(t)-N_T}{1+\epsilon\left|\mathcal{E}(t)\right|^2}. \qquad (2.7)$$

Here, α is the linewidth enhancement factor describing the amplitude-phase coupling (note the imaginary i), γ is the photon decay rate describing the losses in the laser cavity, κ represents the strength of the optical feedback in terms of a feedback rate, ψ corresponds to the feedback phase, τ_{ec} is the feedback delay time from round-trip through the external cavity, I is the laser's pump current, e is the elementary charge, and γ_e is the carrier decay rate.

The gain is modeled as nonlinear with the differential gain g, the carrier number at transparency N_T and the gain saturation coefficient ϵ. Without considering gain saturation $\epsilon = 0$, the gain is linear with the carriers N. The nonlinear gain saturation is a phenomenologically introduced term that is motivated by nonlinear effects in the semiconductor gain medium like spectral hole burning and carrier heating. A linear gain theory cannot account for those phenomena. With increasing pump current (and thus increasing output intensity $|\mathcal{E}|^2$), the nonlinear gain saturation becomes more relevant and has an increasing effect on the dynamics of the lasers. The gain only significantly saturates for large intensities.

Spontaneous emission effects are included in the model by adding a Langevin noise term $F_{\mathcal{E}}$ to the field equation. Its characteristics are described in the following. In general, an additional noise term for carrier noise can be added to Eq. (2.6) to accout for shot noise. Some works have investigated the effect of carrier noise on the dynamics [134, 135]. However, carrier noise is most often omitted in the literature considering the numerical treatment of semiconductor laser using rate equations, as it was found that it can be disregarded in many instances. In this thesis, we also choose to omit carrier noise terms and thus neglect carrier noise.

Noise implementation

The noise from spontaneous emission is implemented as a complex Gaussian white noise term $F_{\mathcal{E}}$ in the field equations:

$$F_{\mathcal{E}}=F_1+iF_2. \qquad (2.8)$$

where the real and imaginary parts are independent random processes. The term has zero mean

$$\langle F_{\mathcal{E}}(t)\rangle = 0 \qquad (2.9)$$

and the following holds

$$\left\langle F_{\mathcal{E}}(t)\overline{F_{\mathcal{E}}(t')}\right\rangle = \beta\gamma_e N(t)\delta(t-t') \tag{2.10}$$

Here, β is the spontaneous emission factor, describing the fraction of spontaneously photons emitted into the respective lasing mode.

Nondimensionalization

In order to be able to numerically study the system's equations in a convenient way, they are often transformed into a dimensionless form by nondimensionalization [98]. This has two main advantages: very large and very small numerical values are avoided and the number of parameters is reduced in the dimensionless form by combining several parameters into one. The detailed nondimensionalization is not shown here but is provided in Appendix A.

After nondimensionalization, Eqs. (2.5)-(2.7) reduce to

$$\begin{aligned}
\dot{E}(s) &= \frac{1}{2}(1+i\alpha)\left(G(E,n)-1\right)E(s) \\
&\quad +Ke^{i\psi}E(s-\tau)+F_E && (2.11)\\
\dot{n}(s) &= \frac{1}{T}\left(p-n(s)-G(E,n)\left|E(s)\right|^2\right) && (2.12)\\
G(E,n) &= \frac{n(s)+1}{1+\mu\left|E(s)\right|^2}. && (2.13)
\end{aligned}$$

The times are scaled to the photon lifetime (i.e., the inverse of photon decay γ) $s=t/\gamma$. Furthermore, τ is the dimensionless feedback delay time, K is the dimensionless feedback strength and ψ is the feedback phase. α remains since it is already dimensionless, T is the so-called timescale parameter, describing the relation of the photon and carrier decay rates $T=\gamma/\gamma_e$, p describes the dimensionless pump parameter in excess of the threshold ($p=0$ corresponds to $I=I_{\text{thr,sol}}$, where $I_{\text{thr,sol}}$ is the solitary lasing threshold current), and μ is the dimensionless gain saturation coefficient.
The noise is converted in the same way. The correlation corresponding to Eq. (2.10) then comes out to

$$\left\langle F_E(s)\overline{F_E(s')}\right\rangle = \beta\left(n+n_0\right)\delta(s-s').$$

$n_0 = 1+\frac{g}{\gamma}N_T$ takes the role of the carriers at threshold in dimensionless units.

2.3.2 External cavity modes

External Cavity Modes (ECMs) are the basic solutions to the the rate Eqs. (2.11), (2.12) with constant amplitude, frequency and carrier number, respectively:

$$\begin{aligned} E(t) &= Ae^{i\omega t} && (2.14)\\ n(t) &= n && (2.15)\\ A, \omega, n &= \text{const} && (2.16) \end{aligned}$$

They are often referred to as continuous wave (CW) solutions or CW-states, while mathematically they are periodic orbits in (E, n)-phase [136]. ECMs are divided in two groups - modes and antimodes, respectively. They stem from constructive (modes) and destructive (antimodes) interference in the external cavity and thus strongly depend on the length of the cavity, which corresponds to the feedback delay τ, and the strength of the feedback, but also on other parameters.

They organize the phase space and provide a skeleton for the output dynamics of the laser with feedback from an external cavity [50, 55, 98, 136].

To calculate these solutions, we first convert the dimensionless model (Eqs. (2.11),(2.12)) to equations for amplitude, phase and inversion by substituting $E(t) = A(t)e^{i\phi(t)}$:

$$\begin{aligned} \dot{A}(t) &= \frac{1}{2}\left(G(A,n) - 1\right)A(t) \\ &\quad + KA(t-\tau)\cos\left(\phi(t-\tau) - \phi(t) + \psi\right) && (2.17)\\ \dot{\phi}(t) &= \frac{\alpha}{2}\left(G(A,n) - 1\right) + K\frac{A(t-\tau)}{A(t)}\sin\left(\phi(t-\tau) - \phi(t) + \psi\right) && (2.18)\\ \dot{n}(t) &= \frac{1}{T}\left(p - n(t) - G(A,n)A^2\right), && (2.19) \end{aligned}$$

with the gain

$$G(A,n) = \frac{1 + n(t)}{1 + \mu A(t)^2}. \qquad (2.20)$$

We now insert the ECM-ansatz (2.14)-(2.16) into (2.17)-(2.19) and gain after some algebra

$$\begin{aligned} \omega &= -K\sqrt{\alpha^2 + 1}\sin(\omega\tau + \arctan\alpha + \psi) && (2.21)\\ n &= \frac{p\mu - 2K\cos(\omega\tau + \psi)}{1 + \mu} && (2.22)\\ A &= \sqrt{\frac{p - n}{n + 1}} = \sqrt{\frac{p + 2K\cos(\omega\tau + \psi)}{(1 + \mu)(1 - 2K\cos(\omega\tau + \psi))}}. && (2.23) \end{aligned}$$

We numerically solve the transcendental equation (2.21) and gain a full set of solutions (ω, n, A). These fixed point solutions lie on an ellipse in the phase space of (angular) frequency shift and excess carriers (ω, n) around the solitary laser mode ($\omega_{\text{sol}}, n_{\text{sol}}$). We set $\omega_{\text{sol}} = 0$ and $n_{\text{sol}} = 0$, so the phase space coordinates are relative to the solitary laser. The fixed points with lower inversion and therefore higher gain have lower frequencies as compared to the solitary laser mode. The extent of the ellipse in the frequency domain is $\pm\omega_{\max} = \pm K\sqrt{\alpha^2+1}$. This extent is measurable in experiments with high-resolution optical spectrum analyzers. If the feedback rate is known, one can estimate the α-factor.

The solutions are created in pairs via a saddle-node bifurcation [48]. The fixed points on the stable branch are called modes, the ones on the unstable branch are called antimodes. If the feedback strength is increased, new mode-antimode pairs are created at the low-frequency end of the ellipse. The modes may be destabilized by the feedback via a Hopf bifurcation and remain as attractor ruins. At least one mode is stable: the mode with maximum gain, i.e., with the minimum inversion. This mode is consequently called Maximum Gain Mode (MGM) [57, 137]. Other modes close to the MGM can remain stable as well, depending on the α-parameter. The condition for mode stability was found to be [137, 138]

$$-\arctan(\alpha^{-1}) < \omega\tau \bmod 2\pi < 0 \tag{2.24}$$

The modes that remain stable besides the MGM are called Stable High Gain Modes (HGM). We will later see the significance of these modes for the laser's dynamics. The stronger the laser's nonlinearity, meaning the larger the α-factor, the fewer modes are stable.

The number of modes Z_{modes} with negative frequency shift relative to the solitary laser mode can be calculated by dividing the frequency extent of the ellipse $K\sqrt{\alpha^2+1}$ by the frequency separation between neighboring modes i and j, $|\omega_i - \omega_j| = \frac{2\pi}{\tau}$:

$$Z_{\text{modes}} = K\tau\sqrt{\alpha^2+1}/(2\pi). \tag{2.25}$$

In Fig. 2.9 we show exemplary cases for the positions of the ECMs in phasesapce for different values of α. As is obvious from Eq. (2.21), the α parameter not only influences the extent of the mode ellipse but also its eccentricity because of the addtional phase term $\arctan\alpha$. This and the decreasing number of stable modes with increasing α is reflected in Fig. 2.9 for $\alpha = 1.0$ (a), $\alpha = 2.0$ (b), $\alpha = 3.0$ (c) and $\alpha = 3.5$ (d). There, the blue diamonds represent stable modes with the MGM shown in yellow. The unstable modes are shown as green circles and the antimodes are represented by red squares. With α increasing from $\alpha = 1.0$ to $\alpha = 3.5$, the number of stable modes decreases from 6 to 2 (including the MGM).

We will describe how the laser's dynamics is organized by the ECMs and affected by their relative position in detail in Section 2.5.

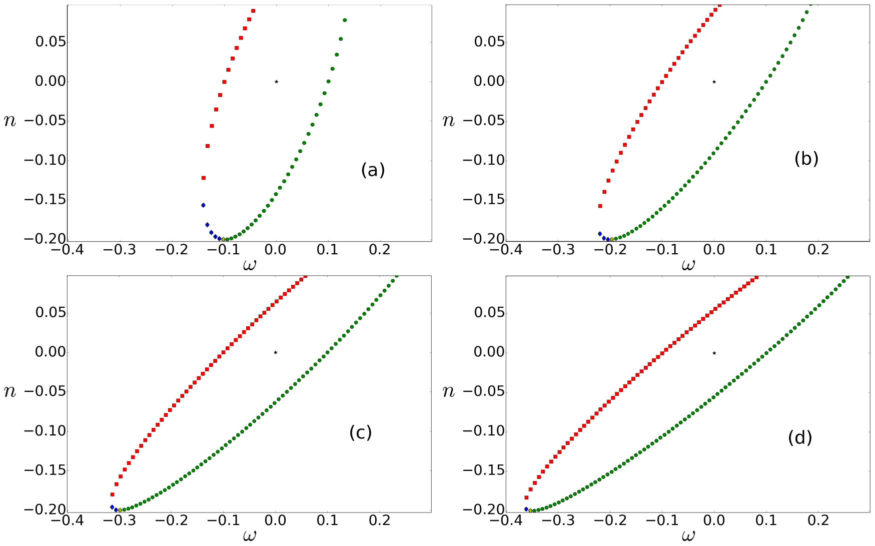

Figure 2.9: ECM structure in (ω, n) phase space for different values of α. (a) $\alpha = 1.0$, (b) $\alpha = 2.0$, (c) $\alpha = 3.0$ and (d) $\alpha = 3.5$. The green circles are the modes, the red squares are the antimodes, the blue diamonds denote the stable modes, the yellow diamonds represent the maximum gain mode (MGM) and the black star is the solitary laser mode. For this calculation, the following parameters were chosen: $K = 0.1$, $\tau = 1000$, $p = 0.1$, $\mu = 0$, and $\psi = 0$.

2.3.3 Model limitations and suitability

The Lang-Kobayashi (LK) model is a phenomenological model that includes a number of simplifications and approximations. First and foremost is the fact, that only single mode operation is accounted for, multimode behavior can not be reproduced with this model.

The model accomodates low to moderate feedback levels. Strong feedback scenarios are not accounted for because multiple reflections from (or multiple roundtrips through) the external cavity are disregarded.

Fundamental characteristics of the feedback scheme, like the linewidth broadening and the lasing threshold reduction, are reproduced by this model. Fig. 2.10 shows numerically obtained optical spectra of a solitary laser ($K = 0$) and of a laser with low feedback levels ($K = 0.1$), respectively, with an obvious visible broadening. The spectra are produced by a Fast-Fourier-transform of the complex field variable $E(t)$.

Numerically obtained P-I-curves for solitary and PMOF operation are presented in Fig. 2.11. The increasing reduction of the lasing threshold with increasing feedback strength is accounted for. The small kink in the curves

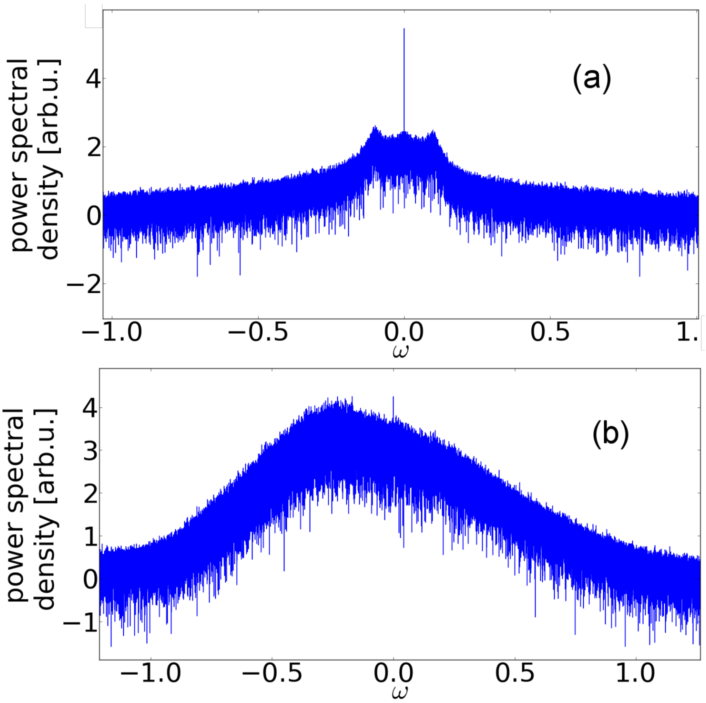

Figure 2.10: Optical spectra numerically obtained from the model in Eqs. (2.5)-(2.7) for the solitary case with $K = 0$ (a) and the case with feedback (b). For (b) the feedback has strength $K = 0.1$. The other simulation parameters for both situations are $p = 2.0$, $\tau = 2000$, $\alpha = 3.0$, $\mu = 0.02$, $T = 200$ and $\beta = 10^{-6}$.

around the solitary threshold, which one usually finds in experimental data for significant feedback strengths, is replaced in our numerics by the onset of fluctuations in the P-I-curve. A reduced slope efficiency which is commonly occurring in experiments (compare Fig. 2.6), is not reproduced since we did not take asymmetric coating of the laser facets into account [129, 130].

The mechanisms of light-matter-interactions are strongly simplified in the LK-model and employs a mean-field approach. For example, the spatial extent of the laser is neglegted. This can lead to inconsistencies with experiments, if one investigates broad SL structures. Also spatial inhomogeneities, carrier diffusion, and thermal effects can alter the laser dynamics but are not included in this model. Traveling wave models can capture some of the effects that originate from the spatial extent of the device under investigation.

Many experimentally observed complex dyamical behaviors, however,

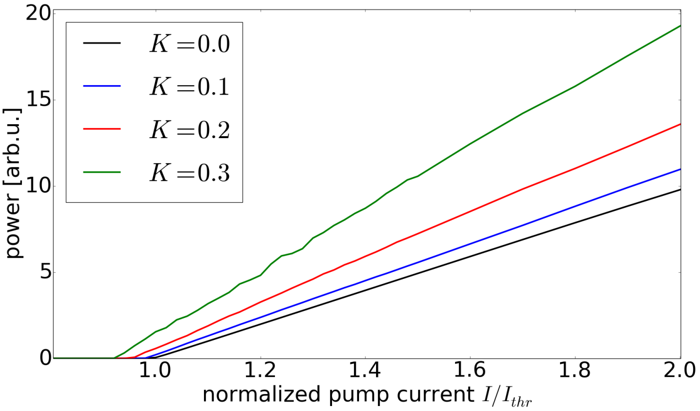

Figure 2.11: Numerically produced P-I-characteristics of a single SL subject to delayed optical with different strengths K. The growing reduction of the lasing threshold with increasing feedback level is reproduced. The simulation parameters correspond to those given for Fig. 2.10.

were found to be reproduced by the LK-model in spite of its simplicity [23, 42, 44, 48, 50, 58, 138–140]. For a review see e.g. [30]. Some of the most prominent dynamics of SLs with feedback like Low Frequency Fluctuations [42, 48, 50] and Coherence Collapse [38] are well-reproduced by the model and discussed in Section 2.5.

Several modifications of the Lang-Kobayashi-based model exist to account for other behaviors like multimode emission, spatial inhomogeneities and other spatial effects. In this work we consider the basic one-mode model (Eqs. (2.5)-(2.7)) which captures the effects of polarization-maintained feedback, which we are most interested in, as well as an extended two-mode model considering dynamics in two orthogonal modes linked to the polarization alignment of the feedback. The latter model is introduced in the following section.

2.4 Polarization modes - extended model

2.4.1 Polarization-rotated optical feedback

In this section, we introduce an extension to the common Lang-Kobayashi-based rate equation model (Eqs. (2.5)-(2.7)). This extension describes the laser's dynamics via two equations for the electric fields that we equate with polarization modes. This extended model allows us to simulate polarization-rotated optical feedback (PROF) in an edge-emitting SL, i.e., feedback whose polarization direction is rotated by 90°relative to the emission. PROF results in interesting dynamical regimes different from those induced by polarization-maintained optical feedback (PMOF) as modeled by Eqs. (2.5)-(2.7).

In most edge-emitting lasers (EELs), one of the orthogonal modes is usually dominant while the other is strongly suppressed [141, 142]. We will call the modes the parallel polarization mode ($\|$) and the perpendicular polarization mode ($\perp$), and will assume in the following, that the parallel mode dominates over the perpendicular one. This is, however, not a generality. The two modes are also often referred to as TE- (transverse electric) and TM- (transverse magnetic) mode, respectively. The perpendicular mode can be excited by rotating the polarization axis of the feedback signal by 90 degrees, in fiber-based experiments this is often accomplished via a Faraday-mirror or by adjusting the polarization axis with a polarization controller (PC). However, much stronger feedback levels are necessary to stimulate the perpendicular mode as compared to the dominant parallel mode. Then the perpendicular polarization mode can overcome the losses and compete for the gain with the parallel polarization mode.
Already the P-I-characteristics of an SL subject to PROF differs significantly from that of a laser with polarization-maintained feedback: the lasing threshold is usually not or only minutely reduced by PROF, in contrast to PMOF [139]. This is illustrated in Fig. 2.12 in comparison with Fig. 2.6 which depict experimenal pump current-power characteristics of SLs subject to PROF and PMOF, respectively.

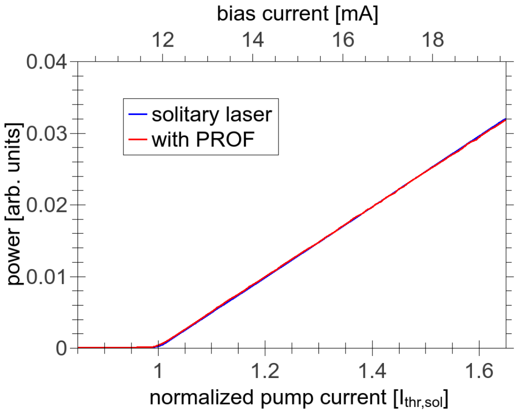

Figure 2.12: Experimentally obtained pump current-output power characteristics of an SL subject to polarization-rotated feedback (red) compared with the solitary case (blue). As can be seen, the lasing threshold and the slope of the P-I curve remain similar.

The PROF-induced dynamics have been described as only weakly chaotic and sometimes quasiperiodic [139] for small to intermediate feedback strengths. However, dynamics induced by larger PROF rates are seen as to exhibit a high complexity which is reflected by vanishing autocorrelation peaks of the intensity outputs [143]. Radio-frequency (rf) spectra of a laser with PMOF or PROF, respectively, exhibit significant differences underlining the dynamical differences in both feedback regimes. Fig. 2.13 depicts two rf-spectra for a PMOF and a PROF scheme, respectively, with comparable feedback attenuation along the optical path. The curve for PROF exhibits enhanced, relatively narrow peaks at the relaxation oscillation (RO) frequency and its first resonance, while the spectrum of a laser with PMOF exhibits a broad continuum, indicating more complex dynamics. We note, however, that during the corresponding experiment the feedback strengths were low, corresponding to only a few percent of emitted light coupled back into the laser cavity after the external cavity round-trip. For strong polarization-rotated feedback, broad bandwidth rf-spectra can be obtained as well.

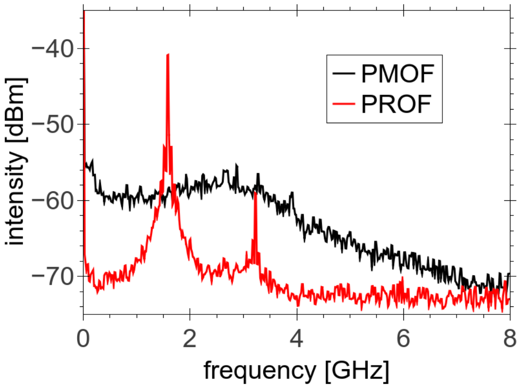

Figure 2.13: Experimentally obtained rf-spectra of a single SL with polarization-maintained feedback (PMOF, black) and with polarization-rotated feedback (PROF, red). The feedback attenuation along the optical path in the experimental setup is of comparable magnitude and in results in a low feedback level of a few percent of emitted light coupled back into the laser cavity after the external cavity round-trip.

PROF has been investigated experimentally and numerically and decicive differences between PROF-induced and PMOF-induced dynamics and spectral characteristics, respectively, have been found [139, 141, 142, 144].

It was shown experimentally that PROF can induce square-wave switching behavior in both modes with a period corresponding to approximately twice the feedback delay [145–149]. Additionally, it can result in synchronization of the parallel polarization mode and the orthogonal polarization mode [147, 150, 151]. Square wave switching resulting from PROF has potential applications in communications, data processing etc.

PROF-induced dynamics has been investigated with respect to its application in random number generation [143, 152]. These schemes benefit from the fact that due to the additional indirect interaction between the perpendicular polarization mode and the dominant parallel polarization mode via the carrier reservoir, the delay signature in the dynamical time series and the autocorrelation can be suppressed. This is thought to enhance the randomness of the generated number in these schemes.

It is important to note the difference between two different schemes to produce PROF: first, a rotation by 90°of the polarization direction of the feedback signal which leads to the light from one of the modes being coupled into the respective other and vice versa. Second, a coupling scheme where only light from the dominant mode is coupled into the suppressed one, which is often called selective orthogonal feedback [147, 153–155]. Both schemes lead to different characteristics. Nevertheless, square-wave switching and synchronization between both orthogonal modes can be accomplished in both schemes.

2.4.2 Model

The question how to model polarization-rotated feedback has been investigated and discussed for quite some time now [139, 141, 151, 156–160]. Often, a model with a single mode (the dominant one) was employed with the feedback term going only into the equation of the carriers. The rotated feedback was called "incoherent feedback" because this simple model did not allow for coherent interaction between the delayed feedback signal and the main mode [141, 142, 156, 157]. Features like square wave switching [147, 149, 151, 160], which have been observed experimentally, can not be reproduced with such a simple model.

To date, PROF is mostly modeled by extending the LK-equations (2.5)-(2.7) to two field equations, one for the parallel polarization mode ($\mathcal{E}_{\|}$) and one for the perpendicular polarization mode ($\mathcal{E}_{\perp}$), with both modes sharing one carrier reservoir:

$$\begin{aligned}
\dot{\mathcal{E}}_{\|}(t) &= \frac{1}{2}(1+i\alpha)\left(\mathcal{G}_{\|}(\mathcal{E}_{\|},N)-\gamma_{\|}\right)\mathcal{E}_{\|}(t) \\
&\quad +\kappa_{\|}\mathcal{E}_{\|}(t-\tau_{ec})+F_{\mathcal{E}_{\|}} && (2.26) \\
\dot{\mathcal{E}}_{\perp}(t) &= -i\Delta\Omega\mathcal{E}_{\perp}(t)+\frac{1}{2}(1+i\alpha)\left(\mathcal{G}_{\perp}(\mathcal{E}_{\|},N)-\gamma_{\perp}\right)\mathcal{E}_{\perp}(t) \\
&\quad +\kappa_{\perp}\mathcal{E}_{\|}(t-\tau_{ec})+F_{\mathcal{E}_{\perp}} && (2.27) \\
\dot{N}(t) &= \frac{I}{e}-\gamma_e N(t)-\mathcal{G}_{\|}(\mathcal{E}_{\|},N)\left|\mathcal{E}_{\|}(t)\right|^2-\mathcal{G}_{\perp}(\mathcal{E}_{\perp},N)\left|\mathcal{E}_{\perp}(t)\right|^2 && (2.28)
\end{aligned}$$

with the correspondingly defined gain functions

$$\mathcal{G}_{\|}(\mathcal{E}_{\|}, N) = g_{\|}\frac{N(t) - N_T}{1 + \epsilon\left|\mathcal{E}_{\|}(t)\right|^2} \tag{2.29}$$

$$\mathcal{G}_{\perp}(\mathcal{E}_{\perp}, N) = g_{\perp}\frac{N(t) - N_T}{1 + \epsilon\left|\mathcal{E}_{\perp}(t)\right|^2}. \tag{2.30}$$

Here, $\Delta\Omega$ describes the frequency detuning between both modes. The other parameters are defined like for the one-mode-model in Section 2.3. Because the parallel polarization mode is dominant, the detuning is given relative to its frequency. It is important to note, that both modes may have significantly different parameters, especially the differential gains $g_{\|}$, $g_{\perp}$ should reflect the dominance of mode $\mathcal{E}_{\|}$ over mode $\mathcal{E}_{\perp}$. The photon lifetimes in both modes might be different as well.

There are only two feedback terms in our model: the feedback $\kappa_{\|}\mathcal{E}_{\|}(t - \tau_{ec})$ from the parallel mode to itself with feedback strength $\kappa_{\|}$ and the polarization-rotated feedback term $\kappa_{\perp}\mathcal{E}_{\|}(t - \tau_{ec})$ that is coupled from the dominant mode into the suppressed perpendicular polarization mode with strength $\kappa_{\perp}$. Since in experiments often the whole polarization state of a feedback signal with *both* orthogonal components is rotated to obtain PROF, one might expect bidirectional coupling between both modes in terms of feedback, i.e., a feedback term going from the perpendicular to the parallel mode and addtionally a self-feedback term for the perpendicular mode. However, due to the natural suppression of the perpendicular mode, we choose to neglect feedback from the perpendicular to the parallel mode and thus model the coupling between the modes as unidirectional in this thesis (i.e. 'selective orthogonal feedback').

We will only consider two different "pure" feedback cases: polarization-maintained optical feedback (PMOF), meaning $\kappa_{\perp} = 0$, or polarization-rotated optical feedback (PROF) with $\kappa_{\|} = 0$. We will use this polarization-resolved two-mode model in Chapter 6, when investigating the transient complex dynamics of a single laser subject to delayed feedback with different polarization orientations: PMOF and PROF.

2.4.3 Nondimensionalization

In correspondence to Section 2.3, we employ the same nondimensionalization to reduce our model to dimensionless units and fewer parameters. The procedure is described in Appendix A. Eqs. (2.26)-(2.30) then become

$$\begin{aligned}
\dot{E}_{\|}(s) &= \frac{1}{2}(1+i\alpha)\left(\frac{n(s)+1}{1+\mu\left|E_{\|}(s)\right|^2}-1\right)E_{\|}(s) \qquad (2.31)\\
&+K_{\|}E_{\|}(s-\tau)+F_{E_{\|}}\\
\dot{E}_{\perp}(s) &= \frac{1}{2}(1+i\alpha)\left(\sigma\frac{n(s)+1}{1+\frac{\mu}{\sigma}\left|E_{\perp}(s)\right|^2}-\rho\right)E_{\perp}(s) \qquad (2.32)\\
&+K_{\perp}\sqrt{\sigma}E_{\|}(s-\tau)-i\Delta E_{\perp}(s)+F_{E_{\perp}}\\
\dot{n}(s) &= \frac{1}{T}(p-n(s)-\frac{n(s)+1}{1+\mu\left|E_{\|}(s)\right|^2}\left|E_{\|}(s)\right|^2 \qquad (2.33)\\
&-\frac{n(s)+1}{1+\frac{\mu}{\sigma}\left|E_{\perp}(s)\right|^2}\left|E_{\perp}(s)\right|^2).
\end{aligned}$$

The extra parameters compared to the dimensionless model (2.11)-(2.13) here are the ratio of photon lifetimes $\rho = \frac{\gamma_\perp}{\gamma_\|}$, the ratio of the modal gains $\sigma = \frac{g_\perp}{g_\|}$, and the spectral detuning between the modes $\Delta = \frac{\Delta\Omega}{\gamma_\|}$. These define the relation of the two modes in terms of excitability (gain ratio), timescale (photon lifetime ratio) and emission spectrum (frequency detuning).
Because we focus on edge-emitting lasers (EELs) in this work, we set the frequency detuning between the two modes to $\Delta\Omega = 0$, in agreement with previous work. However, zero detuning between polarization modes is not generally observed in EELs. Oliver from our lab measured the frequency detuning between the polarization modes of several edge-emitters to be ≈ 200 GHz. Nevertheless, in numerical simulations, a detuning of that magnitude has negligible effects on the dynamics. Vertical-cavity-emitting lasers (VCSLs) for example often exhibit a detuning between both orthogonal modes of the order of several to tens of GHz. Furthermore, for simplicity we assume equal photon lifetimes $\rho = 1.0$. As for the gain ratio we typically set $\sigma = 0.84$, a value we adapt from [139].

With this model we can reproduce the P-I-characteristics of a single SL with PROF like shown in Fig. 2.12. This is shown in Fig. 2.14. Like in our experiments, simulated PROF does not reduce the lasing threshold and does not significantly change the slope efficiency.

We qualify the difference of the two modes with respect to their sensitivity to feedback by calculating bifurcation diagrams of local overall intensity extrema $|E_\||^2 + |E_\perp|^2$ for varying feedback strengths corresponding to the respective feedback scheme: $K_\|$ for PMOF and $K_\perp$ for PROF. This is depicted in Fig. 2.15. We see that in order to induce instabilities, PROF strengths $K_\perp$ of an order of magnitude higher than for the PMOF scheme are required for the given parameter set. These parameters are given in the caption of Fig. 2.15.

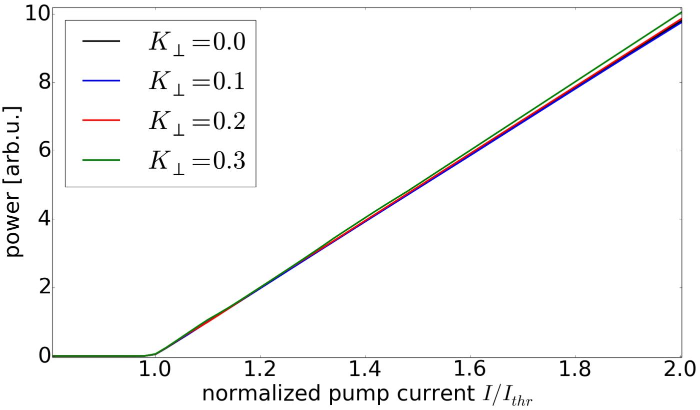

Figure 2.14: Numerical P-I-curves for the solitary case ($K_{||} = K_\perp = 0$) and for different PROF strengths $K_\perp$. The simulation parameters are $T = 200$, $\tau = 2000$, $\alpha = 3.0$, $\mu = 0.02$, $\sigma = 0.84$, $\rho = 1.0$, $\beta_{||} = \beta_\perp = 10^{-6}$ and $\Delta = 0$.

2.5 Characteristic dynamical regimes

In this section we describe typical dynamical regimes and dynamical features of a single laser subject to time-delayed feedback. We will use the insight gained in the previous sections to explain the occurrence of several well-known dynamics which are reproduced by the modeling in Sections 2.3 and 2.4. The dynamical regimes we detail like Low Frequency Fluctuations (LFF) and full Coherence Collapse (CC) result from polarization-maintained feedback or are induced by polarization-rotated feedback (PROF) like square-wave dynamics.

We focus here on the so-called "Long Cavity Regime". Whether an external cavity is considered "long" or "short" is defined considering the ratio of the external cavity round-trip frequency $1/\tau$, where τ is the feedback delay from the external cavity, and the relaxation oscillation frequency ω_{RO}. A cavity is considered "long", if $1/\tau \ll \omega_{\text{RO}}$.

The dynamics shown in this section are obtained from the numerical model (2.32)-(2.34) but reproduce experimentally observed dynamics in the corresponding operating regimes.

2.5.1 The Low Frequency Fluctuations regime

Low Frequency Fluctuations is a prominent dynamical regime within the coherence collapse of a single semiconductor laser subject to delayed polarization-maintained feedback, when the laser is pumped with a bias current close to its solitary lasing threshold. It has been investigated for a long time from many

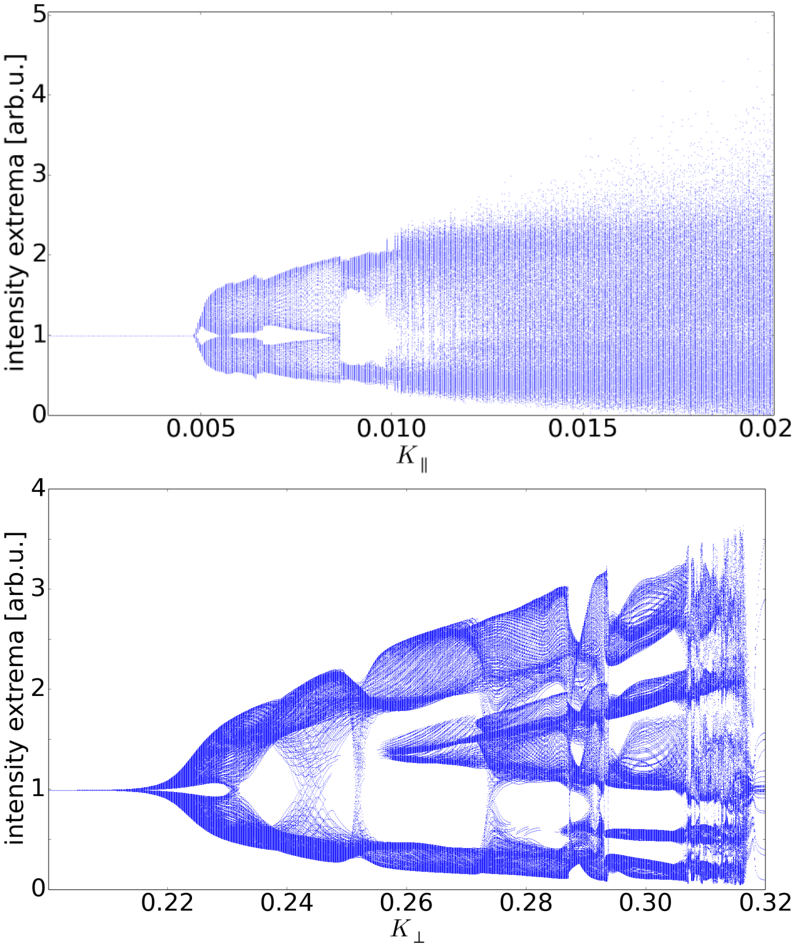

Figure 2.15: Bifurcation diagram of single laser subject to polarization-maintained (a) and polarization-rotated (b) optical feedback, respectively. Depicted are (local) intensity extrema versus the nondimensional feedback strengths $K_{\|}$ and $K_{\perp}$, respectively. The perpendicular polarization mode requires much stronger feedback than the parallel polarization mode to induce instabilities. The defining parameter for this is the gain ratio $\sigma = 0.84$. The other system parameters are $T = 200$, $p = 1.0$, $\mu = 0.02$, $\tau = 2000$, $\alpha = 3.0$, $\rho = 1.0$, $\Delta = 0$. Noise due to spontaneous emission is neglected for these simulations $\beta_{\|} = \beta_{\perp} = 0$.

different points of view [42, 44, 48, 50, 55–57, 62, 161–165]. It is characterized by irregular sudden power dropouts followed by a power-buildup phase until the next dropout, all the while exhibiting fast chaotic intensity fluctuations.

The dropouts occur on a much slower timescale than the chaotic fluctuations - the regime has thus been named appropriately. We show exemplary numerically obtained LFF-intensity dynamics in Fig. 2.16(a).

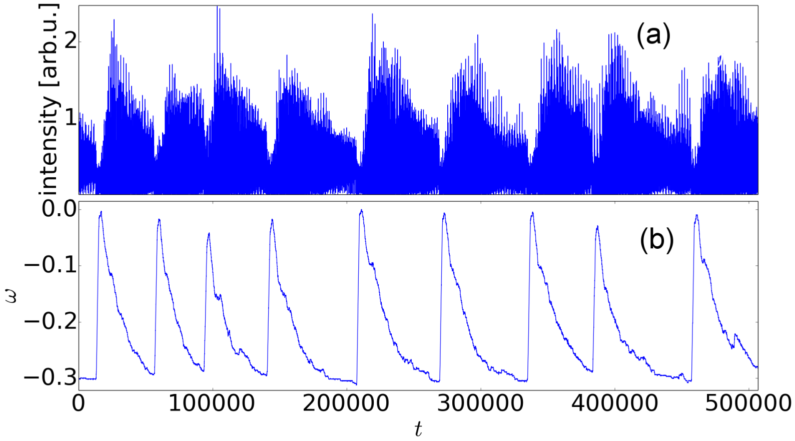

Figure 2.16: Numerically obtained LFF-dynamics in intensity (a) and frequency (b). The power buildup coincides with a drift toward lower frequencies. The simulation parameters are $p = 0.1$, $\tau = 2000$, $K_{\|} = 0.1$, $\alpha = 3.0$, $\mu = 0.02$, $T = 200$, $\beta_{\|} = \beta_{\perp} = 10^{-6}$.

To investigate the system from a spectral point of view we calculate the instantaneous frequency $\omega(t)$ via the delay-phase difference averaged over the previous delay time interval of length τ:

$$\omega(t) = \left(\phi(t) - \phi(t-\tau)\right)/\tau. \tag{2.34}$$

while the momentary continuous phase $\phi(t)$ is gained by connecting non-continuous jumps in the phase computed from the complex field $E(t)$:

$$\phi(t) = \arctan\left(\Im\left[E(t)\right]/\Re\left[E(t)\right]\right). \tag{2.35}$$

From the spectral perspective, the LFF regime has been described as chaotic itinerancy with a drift [48, 50]. This is, because the dynamics' trajectory in frequency-carrier phase space itinerates between different External Cavity Mode (ECM) solutions with a drift toward lower frequencies, i.e., toward the High Gain Modes (HGM) region, until the subsequent power dropout. We illustrate this for an exemplary set of parameters in Fig. 2.17(b) where the trajectory in the (ω, n)- phase space corresponds to the intensity and frequency dynamics, respectively, that are shown in Fig. 2.17(a). The spectral drift slows down while the dynamics approach the high gain region - the dwell time of the phase space trajectory around modes at the lower end of the ECM ellipse (see Section 2.3) is longer than for modes closer to the solitary laser frequency. This is illustrated by the decreasing slope in the corresponding frequency dynamics' time series (see Fig. 2.17(a) lower panel). In Fig. 2.16(b) we show the frequency dynamics over a longer interval including several corresponding power dropouts which are reflected in frequency jumps to the vicinity of the solitary laser frequency.

The origin of the power dropouts was long debated, especially whether it is a intrinsic deterministic property of the system or mainly driven by noise from spontaneous emission. Sano explained the occurrence of the power dropouts as "crisis" events when the trajectory gets too close to the saddle node of an unstable antimode [55]. This brings the system back to the "off state" (the solitary laser state) - the power drops and the trajectory is ejected toward the solitary laser frequency and the power buildup and spectral drift starts anew. This repeating process has been appropriately coined the "Sisyphos effect" [48]. It was shown, that purely deterministically obtained dynamics without noise reproduce the LFF structure with dropouts but that noise can influence the frequency of the power dropouts. We investigate the question of the dominant drive underlying the dropouts on an individual event basis in Chapter 6.

Fig. 2.17(c) depicts an optical spectrum generated by Fast Fourier Transform (FFT) of the complex field variable for parameters corresponding to the dynamics shown in (a) and (b). The spectrum illustrates the feedback-induced spectral broadening, time-resolved by the trajectory in (b) and the red-shifting of the emission frequencies relative to the solitary laser frequency, which corresponds to the spectral drift to lower frequencies over time. The inset depicts a magnification for a narrow frequency band showing peaks corresponding to emission around different ECMs involved in the chaotic intineracy.

Influence of α and stable High Gain Mode emission

We have seen in the previous Sections that the α-factor is a crucial parameter of our system in terms of nonlinearity as well as in terms of position and frequency extent of the ECMs. Because LFF-dynamics are mediated by the modes, a changed position in phase space results in altered characteristics of the LFFs. The dynamics' dependence on the α-parameter will be significant especially in Chapter 5 where we investigate the deterministic nature of LFF power dropouts. An increased α increases the eccentricity of the mode ellipse. Increasing the eccentricity means that the distance between modes and unstable antimodes is reduced, the intensity (or carrier) fluctuations are thus more likely approach the stable manifold of a saddle earlier in the itinerancy process. An increased α also results in a faster intineracy and thus a shorter dwell time of the trajectory around an individual ECM.

We illustrate this in Fig. 2.18 for $\alpha = 3.5$ (a) and $\alpha = 4.0$ (b). The length of the depicted dynamics correspond to that shown in Fig. 2.17(a,b),

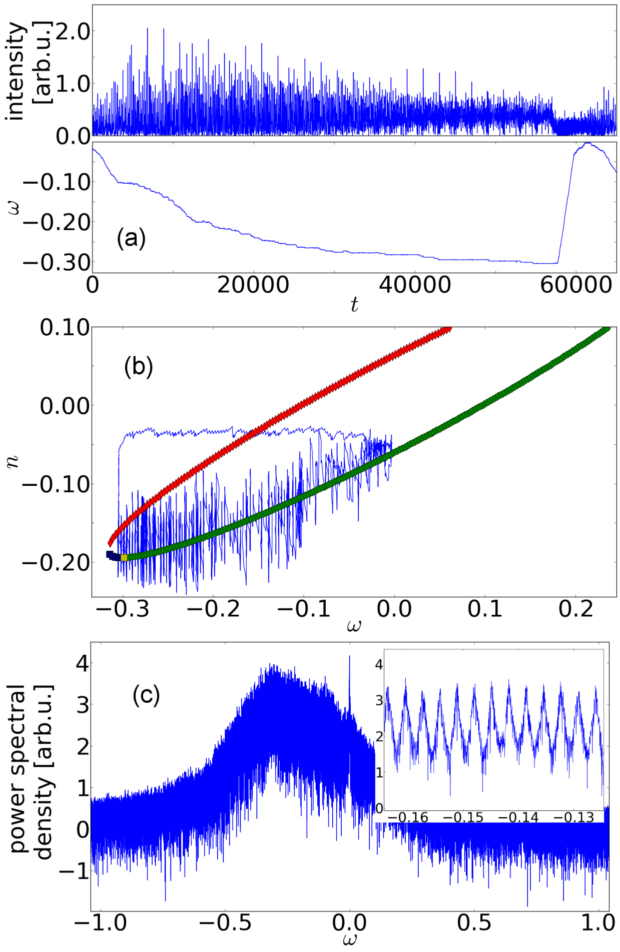

Figure 2.17: Dynamical and spectral characteristics in the LFF regime: (a) depicts intensity (upper panel) and frequency (lower panel) dynamics within the interval between two subsequent power dropouts. (b) shows the corresponding phase space trajectory in (ω, n) space, where the green dots represent modes, red dots are antimodes, blue squares represent stable High Gain Modes and the yellow square depicts the Maximum Gain Mode (MGM). (c) shows a numerically computed optical spectrum for the corresponding parameters, the inset is a magnification depicting peaks corresponding to individual ECMs. The simulation parameters for all plots are $p = 0.1$, $\tau = 2000$, $K_{\parallel} = 0.1$, $\alpha = 3.0$, $\mu = 0.02$, $T = 200$, $\beta_{\parallel} = \beta_{\perp} = 10^{-6}$.

as do the remaining simulation parameters. We emphasize that the reverse of the above described is also true: a smaller α slows down the itinerancy, the dynamics are enabled to reach lower frequencies relative to the spectral bandwidth for the corresponding α. We present a similar phase space trajectory for $\alpha = 2.5$ in Fig. 2.18(c).

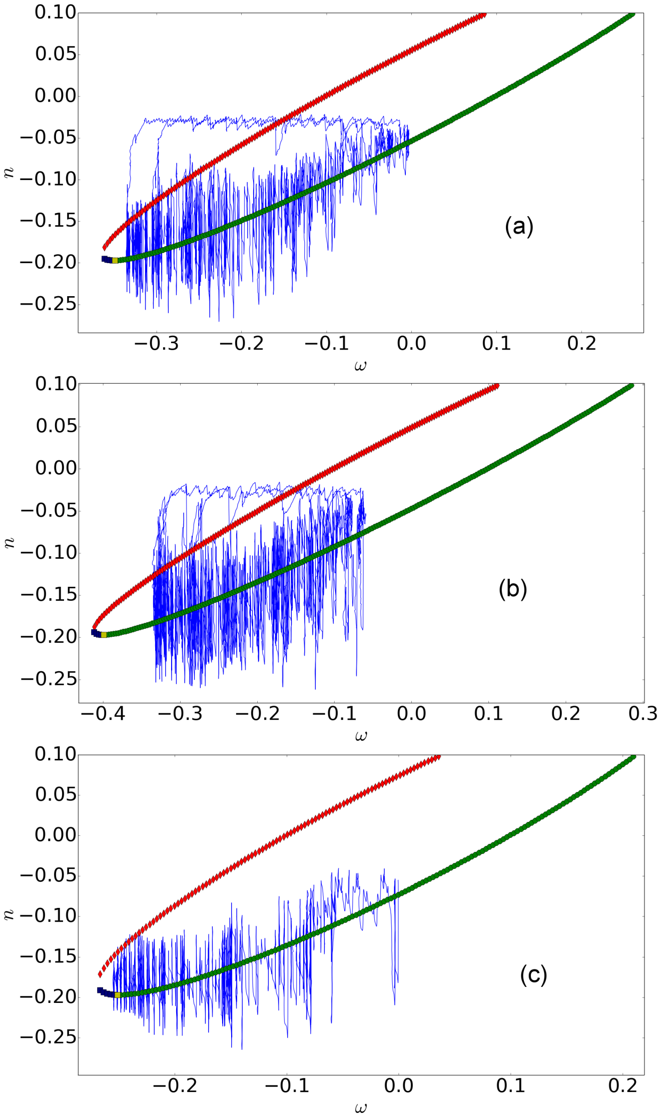

Figure 2.18: Dynamics trajectory in (ω, n)-phase space for $\alpha = 3.5$ (a), $\alpha = 4.0$ (b), and $\alpha = 2.5$ (c). The lengths of the dynamics match as do their other simulation parameters. These correspond to the ones given in the caption of Fig. 2.17. Note the different scales in the frequency (x-) axis. Green symbols represent modes, red symbols are antimodes, the yellow squares corresponds to the Maximum Gain Mode (MGM) and the blue symbols are Stable High Gain Modes.

As we have seen in Section 2.3, a decreased α increases the number of stable modes in the vicinity of the maximum gain mode (MGM) called the High Gain Modes (HGM). The probability of the dynamical trajectory for a given pump current and a given feedback strength to be (at least temporarily) captured by one of these stable modes increases with decreasing α. If the dynamics remain in the vicinity of a single HGM, the laser emits a stable output. This coexistence between LFF dynamics and stable emission that can occur for certain values of the pump current and the feedback strength, respectively, has been shown experimentally before [57, 138]. Increasing the pump current leads to larger fluctuations around each ECM and therefore again increases the probability of a critical event with an antimode and a subsequent power dropout.

In Fig.2.19 we present an experimentally obtained dynamics timeseries showing the coexistence of LFF and stable emission. The narrow band corresponds to emission at a HGM, while the bursts are Low Frequency Fluctuations.

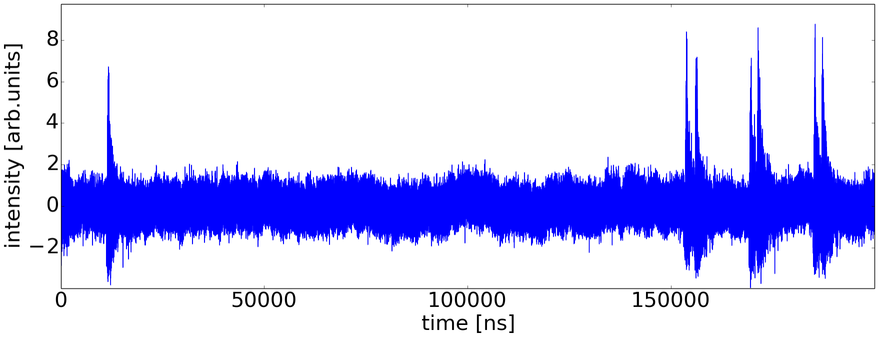

Figure 2.19: Coexistence between stable output and LFF in the dynamics of a single laser with feedback. The laser was pumped with $p = 1.1$, the feedback delay corresponded to $\tau = 75.2$ ns, and the feedback rate was $\kappa \approx 45$ ns^{-1}. Figure courtesy of Xavier Porte.

In Fig. 2.20(a) and (b) we present numerically obtained timetraces of intensity and frequency, respectively, showing the capture of the laser dynamics by a stable HGM for a value of $\alpha = 2.1$. The dynamics approach a stable HGM, is captured by its attractor and remains within its direct vicinity. The frequency reaches a fixed value while the intensity exhibits very low amplitude oscillations around the ECM value. Due to hardware restrictions we can not simulate very long timeseries. We therefore note, that the shown behavior could be either in the coexistence regime or transient behavior. We note that Zamora-Munt et al. interpreted LFF as predominantly transient behavior [166].

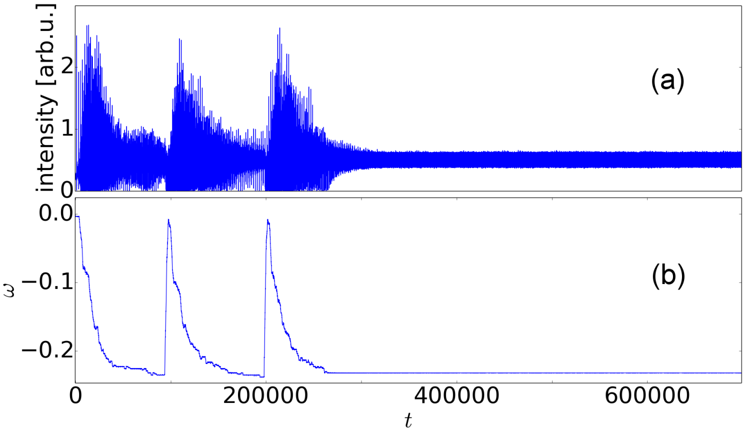

Figure 2.20: Numerically obtained dynamics showing the transition between LFF and stable emission. (a) depicts intensity dynamics and (b) shows the time evolution of the frequency ω. After three LFF cycles, the dynamics gets stuck within the basin of attraction of one high gain mode (HGM). The parameters are $p = 0.2$, $\tau = 2000$, $K_{||} = 0.1$, $\alpha = 2.1$, $\mu = 0.02$, $T = 200$, $\beta_{||} = \beta_{\perp} = 10^{-6}$

2.5.2 Full Coherence Collapse

The LFF regime is usually associated with lasers that are pumped close to their solitary lasing threshold current. If one increases the pump current further, the defining features of the LFF regime will gradually disappear until the full Coherence Collapse (CC) regime is attained. In CC, the low-frequency components are lost as the clearly defined power dropouts vahish, the dynamics exhibit large intensity fluctuations on only fast timescales.

The transition from LFF to CC was found to be smooth. This can be understood if one again considers spectral dynamics in conjunction with intensity dynamics: The mechanism underlying spectral dynamics are the same as for the LFF regime. The trajectory in phase space tends toward frequencies smaller than the solitary frequency. When the trajectory comes too close to an antimode, the trajectory jumps to a higher frequency. In the CC regime the dynamics comprises a chaotic itinerancy among the modes and global antimode dynamics [97, 167]. Between clear LFFs and fully developed CC, there exist intermediate dynamical regimes where the chaotic dynamics still exhibit remnants of the low-frequency structure of LFF, though these become increasingly overshadowed by fast timescale fluctuations when increasing the pump current.

In the fully developed CC, the frequency jumps to higher frequencies occur more often and the itinerancy is more erratic as compared with the

LFF case. Consequently, there is no power buildup like in the LFF regime. Thus, ejections of the phase space trajectory to the vicinity of the solitary laser mode do not occur, instead, the frequency dynamics jump to modes with higher frequencies within an extended neighborhood. Concurrently, the spectral range is often restricted to a narrower band. This is illustrated in Fig. 2.21(a) and (b), where we show exemplary CC dynamics in the time-domain (a) for intensity and frequency (upper and lower panel, respectively) and in (ω, n)-phase space (b). Fig. 2.21(c) depicts the corresponding optical spectrum obtained from the FFT of the simulated complex field variable.

For very large pump current values, the output intensity saturates, if the laser has a saturable gain medium or if gain saturation is included in the model ($\mu \neq 0$). Otherwise, the averaged output intensity increases further. Since the dynamics timescale is limited by the relaxation oscillation frequency which depends on the square root of the bias current, dynamics in the CC regime can be much faster than the fast fluctuations in the LFF regime.

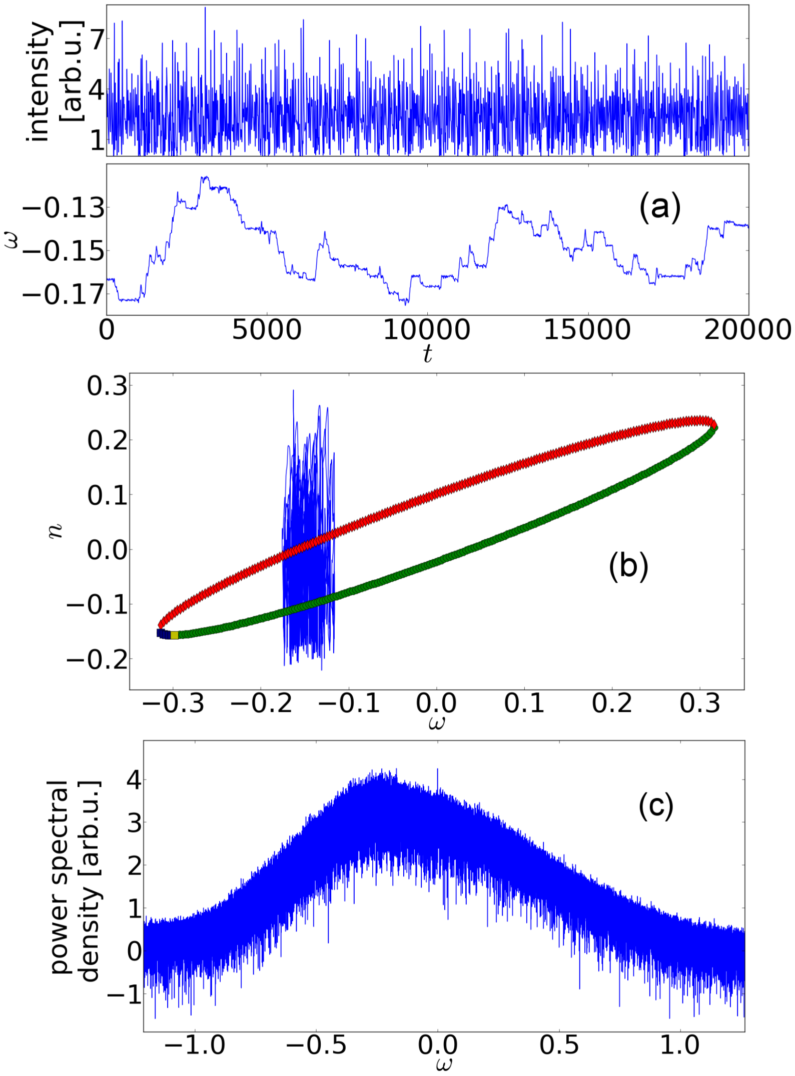

Figure 2.21: Dynamical and spectral characteristics in the CC regime: (a) depicts intensity (upper panel) and frequency (lower panel) dynamics within a comparably short time interval. (b) shows the corresponding phase space trajectory in (ω, n) space, where the green dots represent modes, red dots are antimodes, blue squares represent stable High Gain Modes and the yellow square depicts the Maximum Gain Mode (MGM). (c) shows a numerically computed optical spectrum for the corresponding parameters. The simulation parameters for all plots are $p = 2.0$, $\tau = 2000$, $K_{\|} = 0.1$, $\alpha = 3.0$, $\mu = 0.02$, $T = 200$, $\beta_{\|} = \beta_{\perp} = 10^{-6}$. These parameters correspond to those of Fig. 2.17, except for the pump parameter.

2.5.3 Dynamics induced by Polarization-rotated feedback

Dynamics induced by PROF have significantly different characteristics than dynamics which are incited by PMOF [139, 141, 142, 150]. The two orthogonal polarization modes $E_{||}$ and $E_{\perp}$ can exhibit in-phase as well as antiphase correlations. Depending on the operating conditions, periodic or quasiperiodic oscillations can be easily obtained. We show exemplary intensity dynamics incited by PROF in Fig. 2.22.

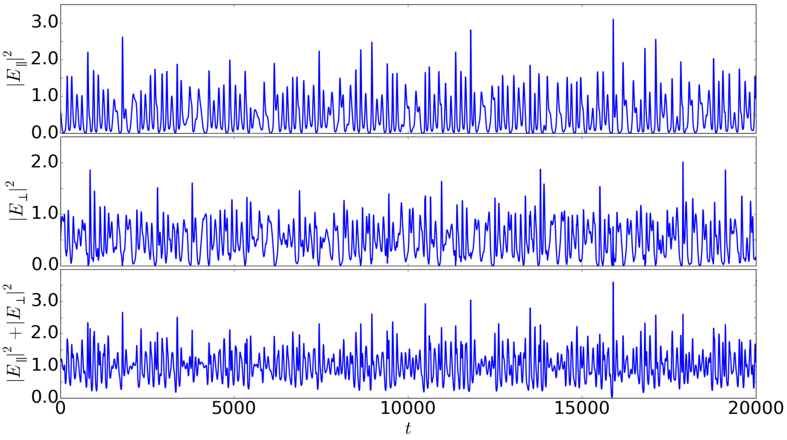

Figure 2.22: PROF-induced intensity dynamics in the parallel polarization mode $|E_{||}|^2$ (a), in the perpendicular polarization mode $|E_{\perp}|^2$(b) and in the overall intensity output $|E_{||}|^2 + |E_{\perp}|^2$ (c). The parameters to obtain these dynamics are $\sigma = 0.84$, $\rho = 1.0$, $\Delta = 0$, $p = 1.0$, $\tau = 2000$, $K_{\perp} = 0.3$, $\alpha = 3.0$, $\mu = 0.02$, $T = 200$, $\beta_{||} = \beta_{\perp} = 10^{-7}$.

Oliver et al. from our lab experimentally found, that very strong PROF in conjunction with a large bias current can lead to highly complex dynamical behavior in the overall dynamics resulting in vanishing second order autocorrelation peaks ac(2τ) of the output dynamics of the laser [143]. They utilized this highly complex PROF-induced dynamics in a random number generation scheme [143, 152].

We showed earlier in Section 2.4, that if the parallel polarization mode strongly dominates over the perpendicular polarization mode, a quite large feedback strength is necessary to induce intensity fluctuations (compare with Fig. 2.15). However, this was the case for zero detuning between both polarization modes. It can be shown that the required feedback levels to excite instabilities in the laser's dynamics can be reduced, if the detuning between the two modes is negative.

We illustrate this in Fig. 2.23. The Figure shows intensity outputs for $K_{\perp} = 0.1$, $p = 0.1$ and $\sigma = 0.84$. Noise was disregarded in this simulation.

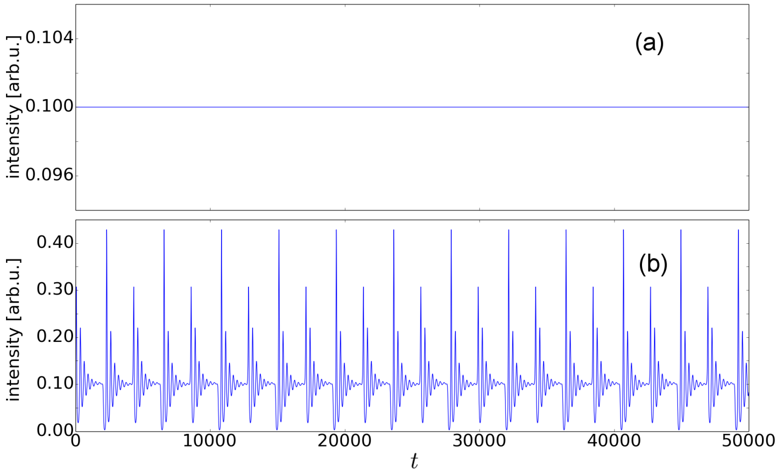

Figure 2.23: PROF-induced instabilities in the overall intensity dynamics $|E_{||}|^2 + |E_\perp|^2$ for low feedback strength $K_\perp = 0.1$ and for two different frequency detunings between the polarization modes. (a) shows stable emission for zero detuning $\Delta = 0$, (b) shows periodic relaxation oscillations for $\Delta = -0.2$. The other parameters to obtain these dynamics are $\sigma = 0.84$, $\rho = 1.0$, $p = 0.1$, $\tau = 2000$, $K_\perp = 0.1$, $\alpha = 3.0$, $\mu = 0.02$, $T = 200$, $\beta_{||} = \beta_\perp = 0$.

Fig. 2.23(a) shows the overall overall intensity dynamics $|E_{||}|^2 + |E_\perp|^2$ for zero detuning $\Delta = 0$ between the modes, and (b) depicts the situation for a negative detuning of $\Delta = -0.2$. We see, that while the feedback strength is not sufficient to excite sustained instabilities in the dynamics for zero detuning, if a negative frequency detuning is implemented, the feedback results in periodic relaxation oscillations. The 2τ-periodicity in Fig. 2.23(b) stem from RO-modulated square wave oscillations in both modes that have a relative τ shift (not shown here). The following Subsection will cover square wave switching.

Square waves in the Polarization-rotated feedback regime

Experiments and numerical studies by different groups over the last years [147, 149, 151] identified an interesting dynamical regime which can be incited in semiconductor lasers (edge-emitters) if subject to polarization-rotated feedback with a medium to large feedback rate: square wave switching in the dynamics of both polarization modes. Different symmetric and antisymmetric square wave regimes were identified, depending on system parameters that characterize the relation between the polarization modes like the detuning Δ and the gain ratio σ. Most often, a square wave periodicity of roughly twice the feedback delay was found.

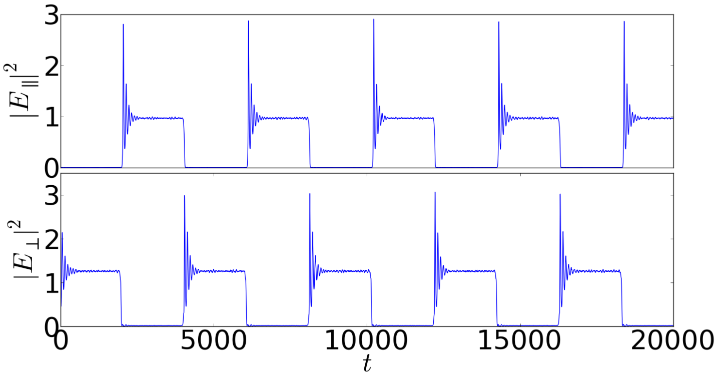

Figure 2.24: Square wave switching in the intensity outputs of both modes $|E_{||}|^2$ and $|E_{\perp}|^2$. The square waves exhibit antiphasic switching between both modes with a period of $\approx 2\tau = 4000$. The parameters to obtain these dynamics are $\sigma = 0.84$, $\rho = 1.0$, $\Delta = 0$, $p = 1.0$, $\tau = 2000$, $K_{\perp} = 0.3$, $\alpha = 3.0$, $\mu = 0.02$, $T = 200$, $\beta_{||} = \beta_{\perp} = 10^{-7}$.

We note that, during our numerical investigations, the square waves were sensitive to noise when assuming a zero detuning $\Delta = 0$. Simulating the PROF scheme with the usual spontaneous emission factor $\beta_{||} = \beta_{\perp} = 10^{-6}$ results in vanishing square wave switching. To compute the square wave dynamics shown in Fig.2.24 we reduced the spontaneous emission factors by one order of magnitude to $\beta_{||} = \beta_{\perp} = 10^{-7}$.

Friart et al. investigated analytically the occurrence of square wave switching (SW) in an SL subject to PROF, supplemented by numerical simulations [160]. They found, that the frequency detuning Δ and the gain ratio σ between both modes heavily influence the appearance of SW in the intensity outputs. They showed that a certain negative detuning between the parallel polarization mode and the perpendicular polarization mode leads to a transition from stable output to sustained ROs and subsequent SW for a considerably smaller feedback strength $K_{\perp}$ than for the case $\Delta = 0$ (see Fig. 2.23(b)).

2.5.4 Concluding remarks

Many dynamical regimes and features that have been observed in experiments with semiconductor lasers subject to time-delayed optical feedback can be reproduced by the rate equation model based on the Lang-Kobayashi equations. If the feedback is implemented as polarization-maintained feedback (PMOF), the simplified one-mode model (2.11)- (2.13), which is an approximation of the extended two-polarization-modes-model (2.32)-(2.34) for vanishing PROF strength $K_\perp = 0$, is sufficient to reproduce a multitude of dynamical behaviors with good correspondence to experimental observations.

PROF-induced dynamics can be qualitatively reproduced with the extended model, however, some specific investigations may require modifications in terms of the way both modes are coupled. For our investigations presented in this thesis, we assume an adequate agreement of experiments and numerics using this model.

3

Coupled semiconductor lasers: Influence of asymmetries on dynamics and synchronization

3.1 Introduction

3.1.1 Synchronization of chaotic lasers in different coupling schemes

Synchronization of coupled nonlinear systems has been investigated for the last decades and in many different fields of research. These include, e.g., neuroscience, biology, chemistry and social sciences [1, 2, 168].

For many technological applications and biological processes, synchronization is essential. In the brain, for example, synchronization of neuron populations is believed to play an important role for instance in the binding problem [169, 170].

An especially interesting phenomenon from a nonlinear dynamics perspective is synchronization of chaos, the possibility of which was only discovered about 20 years ago by Pecora and Carroll [19–21]. Chaos synchronization is also of interest for secure communication technology [24]. In this framework, semiconductor laser systems have been proposed [25, 83, 87, 90] as a physical realization of chaos-based crypto systems. Semiconductor laser systems have a number of advantages for physical implementations, a major one being that their use in communication schemes would allow the use of existing fiber-based communication infrastructure [86].

Coupling lasers over significant distances introduces a coupling delay, due to the finite signal propagation speed. From a mathematical perspective, such delays render the system infinite dimensional and also lead to a richness in different dynamical bahaviors including hyperchaos [161, 171]. Coupling delays also influence the synchronization properties of coupled systems [68–70, 172].

For instance, it was shown that in a setup of bidirectionally-coupled lasers, which exhibit complex dynamics on their own, identical zero-lag synchronization of chaotic dynamics is impossible if the coupling delay is longer than the intrinsic dynamical time scale [173]. In this case of mutually-coupled lasers, the zero-lag synchronized solution exists but is unstable [63]. These findings were later generalized [68, 69] to evaluate the ability of any network with large coupling delay and arbitrary type of nodes to synchronize.

Of particular interest is that it was shown that chaos synchronization is generally unstable in the network motif of two bidirectionally-coupled systems. What occurs instead is a generalized synchronization dynamics of leader-laggard type [23, 63]. The lasers then do not synchronize identically, but exhibit a constant time-lag equal to the coupling delay in the cross-correlation functions [23, 68]. Under fully symmetric conditions, i.e., with identical coupled subsystems and equal coupling strengths, which subsystem is leading the dynamics and which is following is defined by initial conditions and may switch irregularly [65–67]. The above applies for a single coupling delay. Englert et al. found that introducing multiple couplings with certain integer delay time ratios enables zero-lag synchronization [174].

Soriano et al. showed that the dynamics in this scheme can be identified with the dynamics of a single laser subject to delayed feedback by a simple construction method [175]. The dynamics of the single laser with feedback delay 2τ is subdivided into two sequences of timeseries of length τ with relative timeshift τ. This means that the sequences describe the dynamics in intervals starting at an odd number τ-shift $[(2m+1)\tau,(2m+2)\tau]$ and intervals beginning at an even number τ-shift $[2m\tau,(2m+1)\tau]$, respecively, with integer m. The concatenated τ-length intervals then form the new constructed timeseries. In a similar manner, for the bidirectionally-coupled system with coupling delay τ, two sequences of timeseries are constructed by concatenating odd- and even-numbered delay intervals. Each of the newly-constructed timeseries for the coupled system and the single system, respectively, then gives rise to the chaotic attractor as its corresponding counterpart [175].

An important step forward for bidirectional chaos synchronization was made when it was discovered that a relay component, be it passive, such as a semitransparent mirror for coupled lasers [80, 176], or active, like a third laser [75, 78, 177], between the two coupled lasers, can stabilize zero-lag synchronization. This stabilization occurs due to the fact that both lasers always receive the same input from the relay, no matter if they are showing synchronized dynamics or not. Some similar processes might even take place in the brain, where neuron populations serving as relay can help synchronize two other neuron populations that are spatially separated [76, 77, 178].

Other coupling schemes, apart from bidirectionally-coupled lasers, have been considered for chaos synchronization and communication purposes. The most common configuration is the transmitter-receiver scheme, where a transmitter laser is unidirectionally coupled to a receiver laser [64, 161, 179, 180].

From a nonlinear dynamics perspective, in the above-described coupling schemes, chaos synchronization is stable if the chaotic attractor in the synchronization manifold (SM) is transversely stable, i.e., the maximum transverse Lyapunov exponent is negative. It has also been recognized that the transverse stability of individual periodic orbits that are embedded in the attractor is crucial for the transverse stability properties of the attractor [181]. This is especially the case if the considered system has intrinsic noise, such as spontaneous emission noise in lasers. In that case, and even if the usual global transverse stability requirements for synchronization are given, noise may induce desynchronization of the dynamics close to transversely unstable periodic orbits in the attractor of the coupled system. This phenomenon of desynchronization due to local loss of transverse stability has been named bubbling [92] and has also been found for delay-coupled lasers [95–97]. For systems consisting of a single laser with self-feedback or that are made up of coupled lasers, the fundamental periodic orbits, which structure the phase space, are the external cavity modes (ECMs) [136, 182]. They organize the dynamics of the system and, in case of a coupled system, their own transverse stability affect the synchronization properties and synchronization dynamics of the whole system.

Here, we investigate chaos synchronization properties of different coupling schemes of two lasers under the influence of different asymmetries between them or within the coupling topology. In particular, we analytically and numerically investigate the effect of mismatched feedback delays and mismatched feedback and coupling strengths.

Another relevant possible asymmetry in systems of two coupled lasers is a detuning of their emission frequencies. We numerically study its effect on the lasers' synchronizability and their synchronized dynamics in an otherwise symmetric relay-configuration. We link the spectral overlap and frequency locking properties of the lasers with the synchronization properties of the coupled system, and describe the occurrences of desynchronized dynamics in terms of episodic synchronization, as introduced by Búldu et al. [183] who investigated a unidirectional coupling scheme with similar synchronization properties.

We investigate the coupling- and feedback-related asymmetries by analytically and numerically investigating the modes arising from the particular setup and the stability properties of these modes. For the case of frequency detuning, detailed analyses of mode stability and dynamical bifurcations and locking behavior in systems of bidirectionally-coupled lasers have been performed before [182, 184]. However, those studies were limited to setups with bidirectional coupling of autonomous lasers, excluding the possibility of zero-lag chaos synchronization. Here, we investigate the relay configuration allowing for zero-lag identical synchronization of chaotic dynamics, and concentrate on the connection between synchronization and frequency dynamics. We relate the mechanism underlying desynchronization with frequency locking properties, and consequently explain the synchronization behavior in terms of episodic synchronization.

The study of the effect of asymmetries on synchronization is of general importance, and especially so for real-world systems where unavoidable mismatches always result in asymmetries.

3.1.2 Chapter Outline

This chapter is organized as follows. In Section 3.2, we study a model of two lasers bidirectionally coupled via a semitransparent mirror, and we investigate the effect of a mismatch in reflection and transmission of the relay-mirror. We show that desynchronization episodes are enhanced as the mismatch is increased.

In Section 3.3, we make a comparison between the synchronization dynamics of a bidirectional relay-configuration and a drive-response setup. We find that the stability of synchronization for the open- and closed-loop configuration corresponds to the synchronization stability for a bidirectional setup with symmetrical and asymmetrical coupling, respectively.

In Section 3.4, we consider a configuration where the semitransparent mirror relay is not positioned centrally between the lasers leading to a mismatch of the feedback delays of the two lasers. We show that, in this case, the lasers nevertheless synchronize identically, but with a time-lag corresponding to the delay mismatch. Moreover, we study the changes in the ECM spectrum and, thus, the dynamics which result from the introduction of a delay mismatch.

In Section 3.5, we analyze the influence of nonlinear gain saturation in our rate equation model on the dynamics and stability of synchronization in the bidirectional relay setup.

Section 3.6 is concerned with optical frequency detuning between both coupled lasers and its effect on their synchronization properties and dynamics in the LFF regime. We connect the spectral properties and spectral dynamics of the coupled system with synchronization levels and the occurrence of desynchronzation in regimes with small to intermediate detuning.

Finally, in Section 3.7, we summarize our results.

3.1.3 Collaborative work related with this chapter

The results presented in Sections 3.2-3.5 of this chapter have been published as "K. Hicke, O. D'Huys, V. Flunkert, E. Schöll, J. Danckaert, and I. Fischer: *Mismatch and synchronization: Influence of asymmetries in systems of two delay-coupled lasers*, Physical Review E **83**, 056211 (2011)".

The analytical investigations of Sections 3.3 and 3.4 were done in collaboration with Otti D'Duys and Valentin Flunkert. The analytics presented in Section 3.2 were carried out by Otti D'Huys, some of the numerical results shown in that Section were also computed by her.

3.2 Relay configuration with coupling mismatch

The first configuration we consider comprises two identical semiconductor lasers that are bidirectionally coupled with a coupling strength K and that are each also subject to their own feedback with strength L. Both, feedback and coupling are delayed by time τ for both lasers. This scheme can be realized physically by placing a semitransparent mirror with transmittivity K and reflectivity L in the middle between the lasers or with a fiber loop that accounts for coupling and for feedback distribution.

We can describe this system with the following equations:

$$\dot{X}_1 = f(X_1) + LCX_1(t-\tau) + KCX_2(t-\tau)\,, \tag{3.1}$$

$$\dot{X}_2 = f(X_2) + KCX_1(t-\tau) + LCX_2(t-\tau). \tag{3.2}$$

Here, $X_j = (E_j, n_j)$, where the dimensionless variables E_j and n_j represent the complex electric field amplitude and the excess carriers of the j-th laser, respectively, $f(X_j)$ represents the nonlinear laser dynamics according to the Lang-Kobayashi-equations ([133], see also Chapter 2), and

$$C = \begin{pmatrix} 1 & 0 \\ 0 & 0 \end{pmatrix} \tag{3.3}$$

is a coupling matrix describing the optical feedback and the optical coupling between the lasers (i.e, only the optical fields are coupled). The coupling strengths $K = \kappa e^{i\phi_K}$ and $L = \lambda e^{i\phi_L}$ are the complex self-feedback and coupling amplitudes, respectively. For simplicity, we choose identical feedback and coupling delays τ (see section 3.4 for the case of mismatched delays), and identical feedback and coupling phases $\phi_L = \phi_K = 0$. A sketch of this configuration is shown in Fig. 3.1.

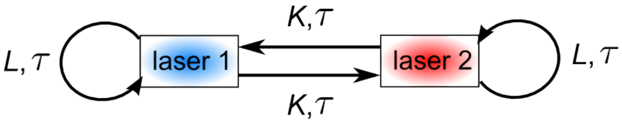

Figure 3.1: Symmetric setup of bidirectionally-coupled lasers with feedback. The distances are given in time for a one-way trip. L and K are the strength of the feedback and the coupling, respectively.

The nonlinear laser dynamics can be described via the dimensionless equations

$$f\begin{pmatrix} E_j \\ n_j \end{pmatrix} = \begin{pmatrix} \frac{1}{2}(1+i\alpha)(G(n_j,E_j)-1)E_j + F_E \\ \frac{1}{T}(p - n_j - G(n_j,E_j)\,|E_j|^2) \end{pmatrix} \tag{3.4}$$

with the gain function

$$G(n_j,E_j) = \frac{n_j+1}{1+\mu|E_j|^2} \tag{3.5}$$

and the field noise F_E originating from spontaneous emission which is modelled as Gaussian white noise with correlation $\langle F_E(s)\overline{F_E(s')}\rangle = \beta(n+n_0)\delta(s-s')$ and zero mean $\langle F_E(s)\rangle = 0$. The model characteristics and parameters are described in Chapter 2. Since we describe general dynamical features and synchronization properties of the Lang-Kobayashi model, we use the one-mode dimensionless model as described in Section 2.3.1 for simplicity.
Without self-feedback ($L = 0$) the two lasers are coupled face to face. As discussed in section 3.1, it is known that the identically synchronized solution $X_1(t) = X_2(t)$ is unstable in such a configuration, the lasers are in generalized synchronization of leader-laggard type [23, 65]. With self-feedback but vanishing coupling strength $K = 0$, we have two separate identical chaotic systems. If the coupling is symmetric in strength ($L = K$) and in-phase (here: $\phi_L = \phi_K = 0$), the zero-lag synchronized solution can be stable [80]. However, intermittent desychronization due to bubbling [97] is present in the system for nonzero noise. The bubbling phenomenon is described and investigated for such a system in detail in Chapter 4.
To analyze the stability of the zero-lag synchronization, we define a symmetric variable

$$S(t) = \tfrac{1}{2}(X_1(t) + X_2(t)) \tag{3.6}$$

and an antisymmetric variable

$$A(t) = \tfrac{1}{2}(X_1(t) - X_2(t)) \tag{3.7}$$

The dynamics in these variables is then described by

$$\dot{S} = \tfrac{1}{2}(f(S+A) + f(S-A)) + (L+K)CS(t-\tau) \tag{3.8}$$

$$\dot{A} = \tfrac{1}{2}(f(S+A) - f(S-A)) + (L-K)CA(t-\tau)\,. \tag{3.9}$$

The identically synchronized state $A(t) = 0$ always exists, independent of L and K due to the symmetry of the system. When the system is synchronized, it behaves like a single laser subject to feedback, with a strength equal to the sum of feedback strength and coupling strength $K + L$. Its synchronized dynamics does, in particular, not depend on the coupling mismatch $L - K$.

The linear stability of the isochronously-synchronized state is derived from the time-dependent variational equation for a small perturbation $\delta A(t)$ transverse to the synchronization manifold

$$\delta \dot{A}(t) = Df(S(t))\delta A(t) + (L-K)C\delta A(t-\tau) \tag{3.10}$$

and depends on the mismatch $L-K$ between self- and crosscoupling. Here, $Df(S(t))$ denotes the Jacobian of f evaluated along the trajectory $S(t)$. We note that for symmetric strengths of coupling and feedback ($L = K$), the explicit delay dependence vanishes.
We calculate numerically the crosscorrelation, defined as

$$C(\Delta t) = \sum_{s=-\infty}^{\infty} I_1(s) I_2(\Delta t + s), \tag{3.11}$$

at zero lag $\Delta t = 0$ for varying feedback and coupling strengths. $I_j = |E_j|^2$ is the optical intensity of laser j. We obtain a correlation plot (Fig. 3.2) exhibiting axial symmetry regarding the axis $L = K$. A large value $C(0)$ corresponds to a high overall level of synchronization. The synchronization level depends only on the absolute value $|L-K|$ of the coupling mismatch and not on its sign. Our system exhibits this symmetry for large delays τ (as is the case here). This symmetry can be explained with the rotational symmetry in the complex plane of the Master-Stability-Function (MSF) [185] for large delays that was found by Flunkert et al. [69]. The MSF describes the transverse stability of a coupled system via the maximal Lyapunov exponent, which is calculated for the eigenvalues of the coupling matrix. In our case, these are $\lambda_{1,2} = L \pm K$. With the rotational symmetry around the complex origin of the MSF, the transverse stability depends only on the absolute difference $|L-K|$, thus the symmetry in Fig. 3.2.

The chaotic dynamics of a laser with delayed feedback is, to some extent, organized by the external cavity modes (ECMs) [44, 49, 50, 55, 136, 182, 186]. The ECMs are rotating wave solutions of the form $E(t) = A_\star e^{i\omega_\star t}$ and $n(t) = n_\star$ with constant amplitude $A_\star$, frequency $\omega_\star$ and carrier number $n_\star$ of the lasers. These modes are arranged along an ellipse in the (ω, n)-plane. On the lower half of the ellipse, the solutions result from constructive interference in the external cavity. These solutions are periodic orbits and are called modes. The solutions on the upper half of the ellipse, on the other hand, originate from destructive interference. They are called antimodes. The ECMs are not only the steady-state solutions of the single laser system with feedback but are also steady state solutions in the case of synchronization of the corresponding coupled system. They then structure the dynamics of the coupled system within the synchronization manifold (SM). The ECMs are discussed in detail in Chapter 2.
A well studied dynamical regime of a semiconductor laser with feedback is the low frequency fluctuation (LFF) regime. In the LFF regime [42, 55], the laser switches chaotically between the modes, with a drift over time toward

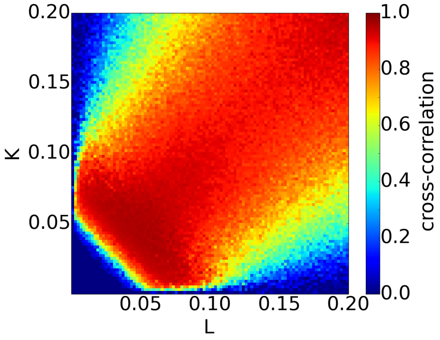

Figure 3.2: Zero-lag crosscorrelation $C(0)$ of the two coupled lasers' intensities in dependence of coupling strength K and feedback strength L. Coupling and feedback have the same delay τ. The parameters used for this simulation are $\mu = 0.26$, $p = 1.0$, $\alpha = 4.0$, $T = 200$, $\tau = 1000$ and $\beta = 10^{-5}$.

the maximum gain mode located at the bottom of the ellipse. During this process, intensity builds up, until the trajectory is ejected along the unstable manifold of a saddle point (antimode), causing a power dropout (see also Chapter 2).

Also for two coupled lasers, it has been shown that the occurrence of desynchronization (bubbling) can be related to the ECMs in the synchronization manifold [97, 187]. Starting from Eq. (3.10), it is possible to calculate the transverse stability of the ECMs. This is discussed in more detail in Appendix B. Close to transversely stable modes, the two lasers' outputs synchronize well, while bubbling typically occurs in the neighbourhood of transversely unstable ECMs [97].

Without mismatch between self- and crosscoupling ($L = K$), the modes involved in the coupled lasers' dynamics are transversely stable, and the antimodes are transversely unstable. Consequently, the lasers only desynchronize during a power dropout, as shown in Fig. 3.3(a). The system has this characteristic because only during power dropouts, which result in an excursion of the dynamics toward the solitary laser mode, does the trajectory approach an unstable antimode, and desychronization can occur.

However, since noise-induced, desynchronization does not occur during all power dropouts as both lasers can exhibit a dropout simultaneously, i.e., stay synchronized during the dropout. This is investigated in detail in Chapter 5.

With an increasing mismatch $L - K$, and while keeping $K + L$ constant, an increasing number of modes involved in the buildup process become transversely unstable. We thus observe desynchronized dynamics not only during power dropouts, but also during the power buildup process (Fig. 3.3(b)). The synchronized dynamics itself only depends on the sum $K + L$ (see Eq. (3.8)) and remains qualitatively the same if $K+L$ is kept constant (Fig. 3.3).

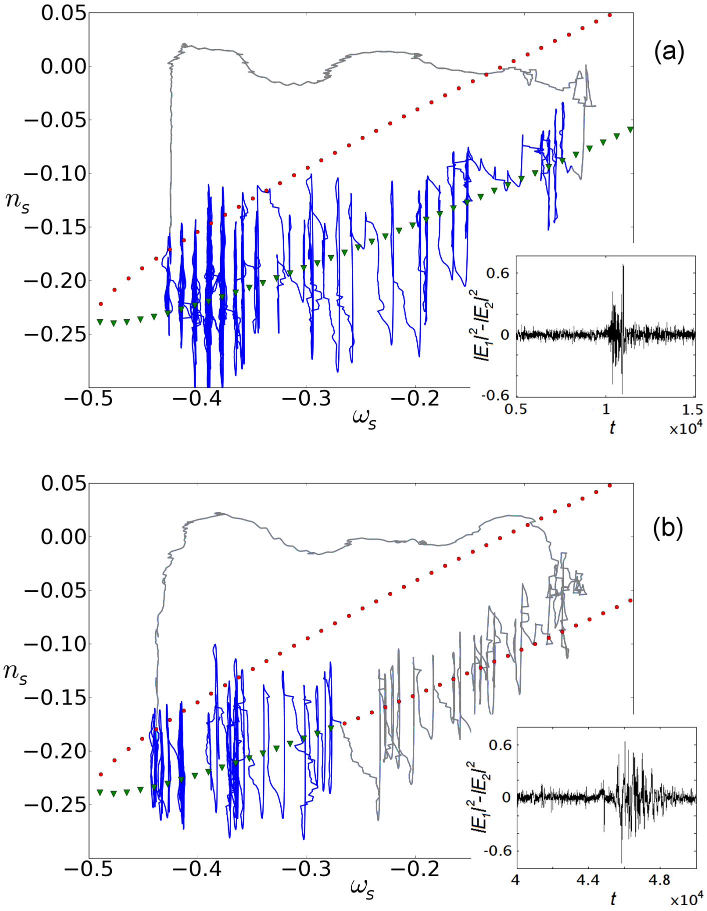

Figure 3.3: Dynamics of the symmetrized solution $S(t)$ (see Eq. (3.6)) of two lasers coupled according to Fig. 3.1 for different coupling mismatches. The dynamics are plotted in the (ω_S, n_S)-phase space. The frequency is calculated by $\omega_S = (\phi_S(t) - \phi_S(t-\tau))/\tau$, with $\phi_S = \frac{1}{2}(\phi_1 + \phi_2)$ describing the phase in the synchronization manifold. $n_S = \frac{1}{2}(n_1 + n_2)$ is the corresponding carrier number. The blue part of the trajectory is well synchronized, the grey part is not. Transversely stable modes are depicted as green triangles, unstable modes are shown as red circles. The insets depict the intensity difference corresponding to the shown phase space trajectory. The simulation parameters are $\tau = 500$, $T = 200$, $\alpha = 4$, $p = 0.1$, $\beta = 10^{-5}$. (a) shows the case without mismatch $K = L = 0.06$; for (b) the feedback-coupling mismatch corresponds to $K = 0.03$, $L = 0.09$. The computation was performed by O. D'Huys.

For vanishing feedback, $L = 0$, the transversal and longitudinal (within the synchronization manifold) stability properties of the modes are equal. Since all modes, except for the maximum gain mode, are longitudinally unstable, zero-lag synchronization is unstable, too [63]. For $K = 0$, the two systems are uncoupled and therefore uncorrelated. If $L = 0$, only achronal generalized synchronization is possible [23, 63]. The correlation of both lasers' outputs is then reduced (see Fig. 3.2).

Dynamics in the coherence collapse regime (see Chapter 2) can be described as a chaotic itinerancy between modes and antimodes, due to the large amplitude fluctuations. Like for the LFF regime, the number of transversely stable modes decreases with increasing mismatch $L - K$, leading to more desynchronization events (see Section 4.4). Also noteworthy is the fact that the number of stable modes decreases for increasing pump current if gain saturation is neglected, i.e., $\mu = 0$. The transverse stability of the modes is higher, when taking into account gain saturation, which explains the large region of high correlation in Fig. 3.2. The influence of a nonlinear gain saturation on the synchronization properties and on the dynamics are discussed in more detail in section 3.5.
As mentioned above, the zero-lag correlation between the two lasers at zero lag depends on the difference of feedback- and coupling strength, but not on the sign of the mismatch, i.e., whether $K > L$ or $L > K$. Again, this can be understood by taking a look at the ECMs' transverse stability, which depends on the magnitude of $L - K$, but not on its sign.

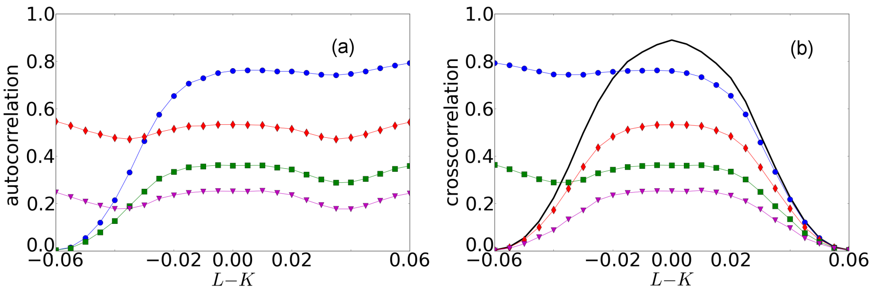

Figure 3.4: Peaks of the autocorrelation (a) and crosscorrelation function $C(\Delta t)$ (b), respectively, in dependence of the coupling mismatch $L - K$. Both correlations are calculated for the lasers' intensities. Black thick line: crosscorrelation at zero lag $C(0)$, blue circles): correlation peak at one delay time $C(\tau)$, red diamonds: $C(2\tau)$, green squares: $C(3\tau)$, magenta triangles: $C(4\tau)$. Simulation parameters are: $\tau = 1000$, $\mu = 0$, $p = 1.0$, $T = 200$, $\beta = 10^{-5}$. The computation to produce these plots were done by O. D'Huys.

When we investigate the correlation at nonzero lags and the stability of synchronization of leader-laggard type, we get different results. Considering the peaks of the crosscorrelation function at shifts of multiples of the delay time, $k\tau$, $k \neq 0$, we find that if $L - K$ increases (positive mismatch), all examined non-zero-lag peaks decrease in the same way. This is shown in Fig. 3.4(b). The corresponding peaks of the autocorrelation and hence the dynamical complexity of the lasers do not change much with a positive mismatch $L - K > 0$ (see Fig. 3.4(a)).

For a negative mismatch ($K > L$), the lasers gradually change from identical zero-lag synchronization to generalized synchronization of leader-laggard type: the crosscorrelation peak at one delay time, and higher order odd numbered peaks do not change a lot with the mismatch, but the correlation at zero-lag and at even multiples of the delay vanish (Fig. 3.4(b)). The autocorrelation is affected as well: the even peaks remain, the odd peaks vanish (Fig. 3.4(a)).

3.3 Drive-response configuration with coupling mismatch

We now consider unidirectional coupling schemes, in which the output of one laser drives the other laser. In this section, we point out certain similarities between those schemes and bidirectional ones, in terms of stability of synchronization. We focus on the drive-response configuration, because it is prominently used for chaos communication purposes [26, 27, 83, 86]. The drive laser, or transmitter, receives its own delayed feedback; the responding laser, or receiver, is injected with chaotic input from the transmitter. In what is called closed-loop configuration (shown schematically in Fig. 3.5) the receiver is also a chaotic element on its own, because it, too, is subject to self-feedback. In the so-called open-loop configuration, the receiver has no self-feedback, and, thus, exhibits stable continuous wave output when not coupled to the transmitter. Both configurations can be modeled by

$$\begin{aligned} \dot{X}_1 &= f(X_1) + KCX_1(t-\tau) && (3.12)\\ \dot{X}_2 &= f(X_2) + (1-\epsilon)KCX_1(t-\tau_c) + \epsilon KCX_2(t-\tau)\,. && (3.13) \end{aligned}$$

If $\epsilon = 0$, we have an open loop receiver, for $\epsilon > 0$ the configuration is called a closed loop.

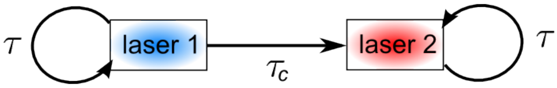

Figure 3.5: Sketch of a closed loop setup as an example for a drive-response configuration. The feedback-delay is τ, the coupling delay is τ_c.

The dynamics in the synchronization manifold is the dynamics of the transmitter laser, $S(t) = X_1(t)$. It is important to note that the coupling delay τ_c has no effect on the dynamics in a drive-response configuration.

We define the antisymmetric direction for the unidirectional coupling scheme as $A(t) = X_1(t) - X_2(t - (\tau - \tau_c))$. The dynamics can then be rewritten as

$$\begin{aligned} \dot{S} &= f(S) + KCS(t-\tau) && (3.14) \\ \dot{A} &= f(S) - f(S-A) + \epsilon KCA(t-\tau)\,. && (3.15) \end{aligned}$$

When we linearize around $A(t) = 0$, we find that the linear stability of the zero-lag synchronized solution in an open loop configuration ($\epsilon = 0$) is the same as for the setup of two bidirectionally-coupled lasers with feedback where feedback and coupling have the same strengths $L = K$. The stability in this case is also derived from Eq. (3.10) (compare Eq. (3.9) with Eq. (3.15)).

A closed-loop receiver contrasts with an open-loop receiver in terms of the stability of the synchronization manifold. The stability is the same as for a bidirectional coupling setup with self-feedback (as shown in Fig. 3.1) with mismatched feedback and coupling strengths $L \neq K$. Consequently, a closed-loop configuration has to be carefully symmetrized with respect to the involved coupling/feedback strengths for high-level synchronized behavior. A closed-loop configuration is thus more complicated to implement in experiments.

On the one hand, the open-loop configuration is usually preferred over the closed-loop scheme in chaotic communication because it is more robust against parameter mismatches and much easier to implement. In addition, the resynchronization time in case of a sudden interruption of the connection is much shorter (see Ref. [90] and references therein). One has to consider, however, that an increased requirement of the receiver to well-match the transmitter increases the security of this communication scheme.

On the other hand, it was shown [64], that if the feedback delays in a closed-loop scheme are identical, the synchronization level is higher than for an open-loop due to increased symmetry of the setup. Vicente et al. showed that the performance of closed-loop receivers is less sensitive to a frequency detuning between emitter and receiver laser [64, 188]. Furthermore, several methods considering chaotic communications have been proposed that take advantage of specific properties of the closed-loop configuration [90, 189].

3.4 Relay configuration with delay mismatch

We return to the case of a bidirectional coupling between two interacting lasers that are subject to their own feedback. As mentioned above, this can be realized experimentally, for example with a semitransparent mirror placed between the lasers. Now, we assume the mirror is not exactly in the center anymore. This leads to changes in the synchronization properties and in the dynamical characteristics when compared to the completely symmetric case. Since a perfect alignment of a mirror in an experimental setup is challenging, the work in this section is useful also from an experimentalist's point of view.

3.4.1 Synchronization properties

A misalignment of the relay mirror from the exact center of the coupling configuration results in the lasers being subject to feedback with different delays $\tau_{1,2} = \tau \pm \Delta\tau$. They do, however, still receive signals from the respective other laser with a coupling delay $\tau = \frac{1}{2}(\tau_1 + \tau_2)$, since the distance between the lasers remains unchanged. Fig. 3.6 depicts a schematic of this configuration.

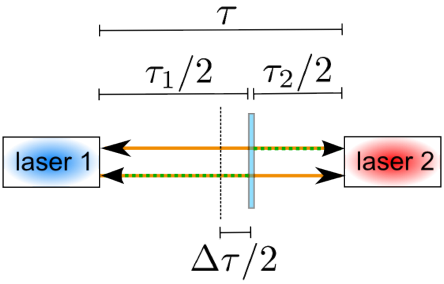

Figure 3.6: Scheme of a bidirectional coupling setup with a mismatch of the feedback delays of both lasers. This can be realized with a semitransparent mirror in the middle between the lasers, when the mirror is shifted from the exact center of the setup. The given delays correspond to the propagation times for a one-way trip. The orange lines represent the coupling signals from one laser to the other, being transmitted trought the mirror, the green lines are the respective feedbacks, reflected by the mirror. Both feedbacks have strength L, both coupling strengths equal K.

We can model this system with the equations

$$\dot{X}_1 = f(X_1) + \tfrac{1}{2}LCX_1(t-(\tau+\Delta\tau)) + \tfrac{1}{2}KCX_2(t-\tau) \tag{3.16}$$

$$\dot{X}_2 = f(X_2) + \tfrac{1}{2}LCX_2(t-(\tau-\Delta\tau)) + \tfrac{1}{2}KCX_1(t-\tau)\,, \tag{3.17}$$

where we set without loss of generality $\Delta\tau \geq 0$.

The first laser then experiences a larger feedback delay ($\tau_1 = \tau + \Delta\tau$) than the second laser ($\tau_2 = \tau - \Delta\tau$). The zero-lag synchronized state $X_1(t) = X_2(t)$ is no longer a solution of this system. Instead a time-shifted synchronized solution $X_1(t) = X_2(t - \Delta\tau)$ is possible[78]. To analyze the stability of this time-shifted identically-synchronized solution, we define the symmetric $S(t)$ and antisymmetric $A(t)$ variables, respectively, as

$$\begin{aligned} S(t) &= \tfrac{1}{2}(X_1(t+\Delta\tau)+X_2(t)), && (3.18)\\ A(t) &= \tfrac{1}{2}(X_1(t+\Delta\tau)-X_2(t)). && (3.19)\end{aligned}$$

The temporal evolution of these two variables is then given by

$$\begin{aligned} \dot{S} &= \frac{1}{2}\left[f(S+A)+f(S-A)\right]\\ &\quad +\tfrac{1}{2}(L+K)C\left[S(t-\tau_1)+S(t-\tau_2)\right]\\ &\quad +\tfrac{1}{2}(L+K)C\left[A(t-\tau_1)-A(t-\tau_2)\right] && (3.20)\\ \dot{A} &= \frac{1}{2}\left[f(S+A)-f(S-A)\right]\\ &\quad +\tfrac{1}{2}(L-K)C\left[S(t-\tau_1)-S(t-\tau_2)\right]\\ &\quad +\tfrac{1}{2}(L-K)C\left[A(t-\tau_1)+A(t-\tau_2)\right]. && (3.21)\end{aligned}$$

The time-shifted identically synchronized solution $A(t)=0$ only exists if self- and cross-coupling are equal $L=K$. Otherwise, the temporal evolution of the antisymmetric variable A would depend on the symmetric one S. This is in contrast to the case without delay mismatch (see Section 3.2), where, for any values of K and L, a synchronized solution exists in general, although it may be unstable. Therefore, for the case with delay mismatch, we expect a strong dependence of the synchronization level on the coupling mismatch $L-K$.

For $K=L$, the synchronized solution corresponds to one laser subject to two different feedbacks with the same strength $\frac{1}{2}(K+L)=K$ and the delays τ_1 and τ_2. We perform a linear stability analysis of Eq. (3.21), describing the dynamics orthogonal to the synchronization manifold. We linearize around the synchronized state $A(t)=0$ and obtain

$$\delta\dot{A}(t)=Df\,(S)\delta A. \qquad (3.22)$$

Comparing this characteristic equation for the stability of the case with delay mismatch with the situation without delay-mismatch (Eq. (3.10)), we notice that the variational equations are identical. Therefore, we conclude that similar ECMs (i.e., solutions $S(t)$ with similar frequency ω_S and similar carrier numbers n_S) will have comparable stability properties.

Provided that the feedbacks and couplings have equal strengths $L=K$, we can thus assume that an asymmetrically-placed semitransparent mirror leading to different feedback delays, that sum up to two times the coupling delay $\tau=\frac{1}{2}(\tau_1+\tau_2)$, does not have large effect on the synchronization properties of the considered system.

When we simulate the system numerically, we indeed find identical synchronization of the two lasers' outputs with a time lag corresponding to the delay mismatch $\Delta\tau$. The corresponding cross-correlation function exhibits

its main correlation peak at a shift $\Delta t = -\Delta\tau$. Fig. 3.7 shows exemplary intensity timetraces of two lasers coupled in that manner (Fig. 3.7(a)). Further shown is the according cross-correlation function (Fig. 3.7(b)).

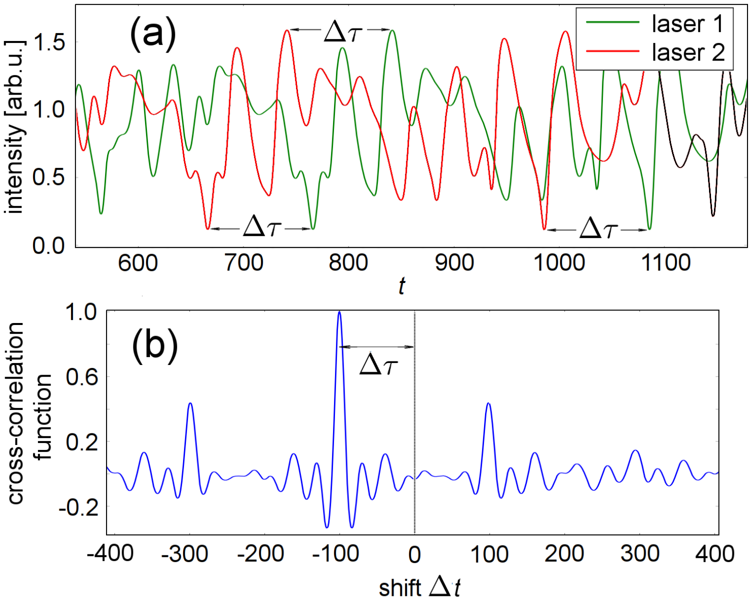

Figure 3.7: Numerically-obtained dynamics (a) and cross-correlation of two delay-coupled lasers with a feedback delay-mismatch of $\Delta\tau = 100$ operated in the coherence collapse regime. The simulation parameters are $\tau = 2000$, $\alpha = 4.0$, $p = 1.0$, $\mu = 0.26$, $T = 200$ and $L = K = 0.05$. For clarity, noise was disregarded for this simulation.

To investigate the dependence of the level of time-shifted synchronization (i.e. the height of the $\Delta\tau$-shifted peak of the correlation function), we plot the correlation peak value as a function of the delay-mismatch. This is depicted by the red curve in Fig. 3.8. For most of the possible range $0 \leq \Delta\tau < \tau$, the correlation peak is large, which implies stable synchronization. The mirror position and the corresponding delay-mismatch therefore do not have a large effect on the synchronization stability.

If we consider both a mismatch of the transmittivity and reflectivity of the laser $L \neq K$ and a delay mismatch at the same time $\Delta\tau \neq 0$, we find that, for almost equal coupling strengths, i.e., $L \approx K$, the system synchronizes well, whereas for significant mismatches $L - K$, the correlation breaks down. This is shown in Fig. 3.9 which depicts the correlation (at $-\Delta\tau$) in dependence on L andf K for a small delay mismatch $\Delta\tau = 20$ (Fig. 3.9(a)) and for a large one $\Delta\tau = 900$ (Fig. 3.9(b)). This increase of sensitivity is in contrast to the results shown in Fig. 3.2, which exhibit high correlation values (good

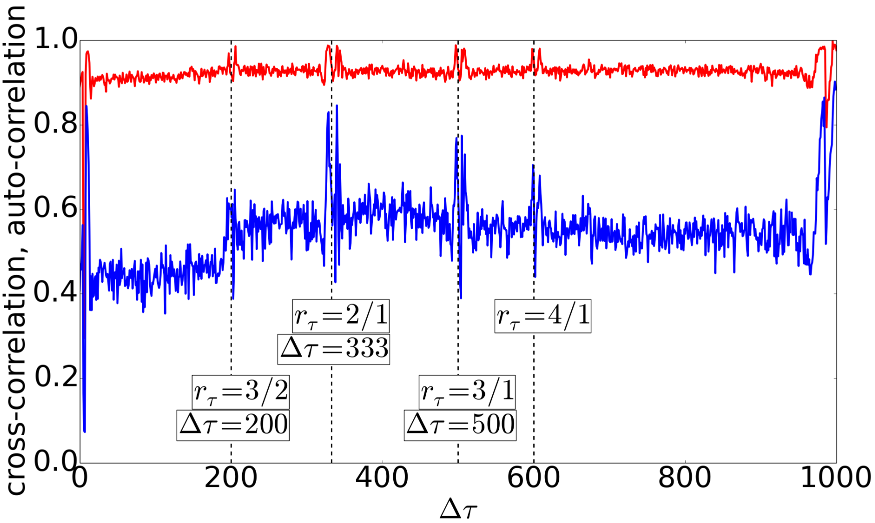

Figure 3.8: Cross-correlation $C(\delta t)$ peak at shift $\Delta t = \Delta\tau$ of the output intensities of two coupled lasers in a relay configuration as depicted in Fig. 3.6 (red line) and the peak at $\Delta t = 2\tau$ of the autocorrelation function of one laser's output (blue line) as a function of the delay mismatch parameter $\Delta\tau$. The peaks coincide: higher regularity of the dynamics (peak in the autocorrelation) implies crosscorrelation. The simulation parameters are $\tau = 1000$, $\alpha = 4.0$, $p = 1.0$, $\mu = 0.26$, $T = 200$ $\beta = 10^{-5}$. Coupling and feedback are equal in strength $L = K = 0.05$.

synchronization) for large ranges of the coupling mismatch $L - K$. If the semitransparent mirror in our setup is placed asymmetrically (not in the exact center), the system's synchronization is much more sensitive to an additionally-applied coupling mismatch, as was implied by Eq. (3.21) and discussed above.

3.4.2 Dynamical regimes under delay mismatch

Even though we find that a delay mismatch does not affect the identical synchronization level of the coupled lasers, it does have a significant effect on the system's dynamics within the synchronization manifold. When the two lasers are (lag-)synchronized, they behave like a single laser receiving two equally strong feedback signals with different delays τ_1 and τ_2. This addition of a second delay alters the position of the external cavity modes (ECM).

The ECM ansatz $E(t) = A_\star e^{i\omega_\star t}$, $n(t) = n_\star$ leads, after eliminating the amplitude $A_\star$ and assuming $L = K$, to a transcendental frequency equation and an equation for the carriers

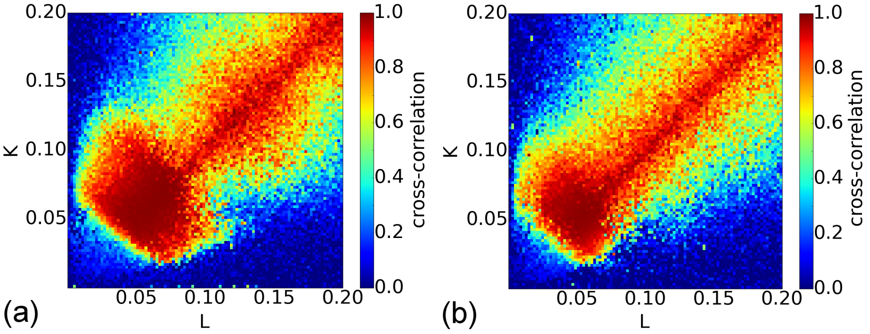

Figure 3.9: Cross-correlation $C(\Delta t)$ peak at shift $\Delta t = \Delta\tau$ of the field intensities of two lasers coupled according to Fig. 3.6 versus the feedback strength L and the coupling strength K, respectively, for an applied delay-mismatch $\Delta\tau = 20$ (a) and for $\Delta\tau = 900$ (b). When compared to Fig. 3.2, one notes that the system's synchronization is more sensitive to a coupling mismatch $L - K$ if it also features a delay-mismatch. The other parameters for the numerics are $\tau = 1000$, $\mu = 0.26$, $p = 1.0$, $\alpha = 4.0$, $T = 200$ and $\beta = 10^{-5}$.

$$\omega_\star = -2K\sqrt{1+\alpha^2}\sin(\omega_\star\tau + \arctan\alpha)\cos(\omega_\star\Delta\tau)\ , \tag{3.23}$$

$$n_\star = \frac{p\mu - 4K\left(\cos(\omega_\star\tau)\cos(\omega_\star\Delta\tau)\right)}{1+\mu}. \tag{3.24}$$

The modes of this system are located inside the area of the ellipse that is the solution space for a laser subject to only one feedback with a strength of $2K$. We note that if the ratio of the two feedback delays are rational $r_\tau = \tau_1/\tau_2 \in \mathbb{Q}$, the modes lie on a closed curve. Irrational ratios r_τ result in a more complicated mode spectrum.

Tronciu et al. [87], who investigated the corresponding case of lasers subject to feedback from an integrated double cavity, found chaotic behavior for lower feedback strengths than is needed for the case of single feedback. The more complex mode structure was postulated as a cause for a more complex dynamics.

The complex structure of the modes for $\Delta\tau \neq 0$ depends only on the ratio of the delay times, not on the absolute delay τ. Since the (synchronized) dynamics is organized by the mode spectrum, it is strongly affected by the changes in the mode structure.

Würtenberger [190] investigated experimentally and numerically a system comprising a single laser subject to feedback from a Michelson interferometer and extensively characterized the arising dynamics depending on the free spectral range (FSR) of the interferometer. Because we can identify the synchronized dynamics in our coupling setup with the dynamics of a single laser subject to two different feedbacks, the FSR of the Michelson-interferometer directly corresponds to the delay mismatch $\Delta\tau$ in our system. Würtenberger furthermore calculated the mode structure of the Michelson system in a corresponding way to Eqs. (3.23) and (3.24), and showed the formation of mode islands for values of the FSR that correspond to small delay mismatches. The extent of the mode island surrounding the solitary laser mode (SLM) corresponds to the free spectral range of the Michelson-interferometer.

Similar to her results, we find mode islands for small $\Delta\tau$ forming within the phase space area of the mode ellipse for matching feedback delays. The double feedback setup (Fig. 3.6) exhibits a similar filtering effect as the Michelson-interferometer. The frequencies for which $\omega\Delta\tau \approx (2m+1)\frac{\pi}{2}$, $m \in \mathbb{Z}$ are filtered out. Close to simple rational ratios of r_τ we observe similar phenomena.

We calculate here the mode structure for a broad range of delay mismatches, and study its effects on the dynamics of the synchronized system. The makeup of our configuration allows for an arbitrary delay mismatch in the interval $\Delta\tau \in [0, \tau[$ for which we calculate the transverse stability of the modes resulting from this double delay configuration.
Fig. 3.10 depicts exemplary portraits of the frequency-carriers (ω_S, n_S)-phase space showing the position of the ECMs and the resulting dynamics in the synchronization manifold for different values of the delay-mismatch $\Delta\tau$ for a mean delay time/ coupling delay of $\tau = 1000$. The phase space areas where transversely stable modes are located are similar for all delay mismatches. Due to the changes in the ECM spectrum, the dynamics are significantly altered compared to the case with equal feedback delays $\Delta\tau = 0$. For some values of the delay mismatch, the system's dynamics becomes regular or stable, respectively, a feature also found for certain values of the FSR in the Michelson-interferometer setup [190].

A semiconductor laser subject to two self-feedbacks with different strength and delay has been studied by Liu and Ohtsubo [191], who showed that one can stabilize the dynamics to fixed points or limit cycles. This effect was found strongest for unequal feedback strengths. Rogister et al. [192] showed that chaotic dynamics and LFF can be suppressed for a single laser subject to two different feedbacks, by suppressing the antimodes that are responsible for the power dropouts [55]. This stabilization of the dynamics occurs mainly for a short second feedback. Increasing the second feedback strength from a low level to the magnitude of the first one results in a bifurcation cascade in the laser leading to several dynamical regimes including stable behavior.

In our coupling configuration here, we observe a richness in dynamical behaviors as well, including stabilization of the dynamics for one long and one very short delay $\tau_1 \gg \tau_2$ (very large delay mismatch).

We calculate the secondary peak of the autocorrelation (at shift $\Delta t = 2\tau$) of each laser to indentify the regularity of the dynamics. The height

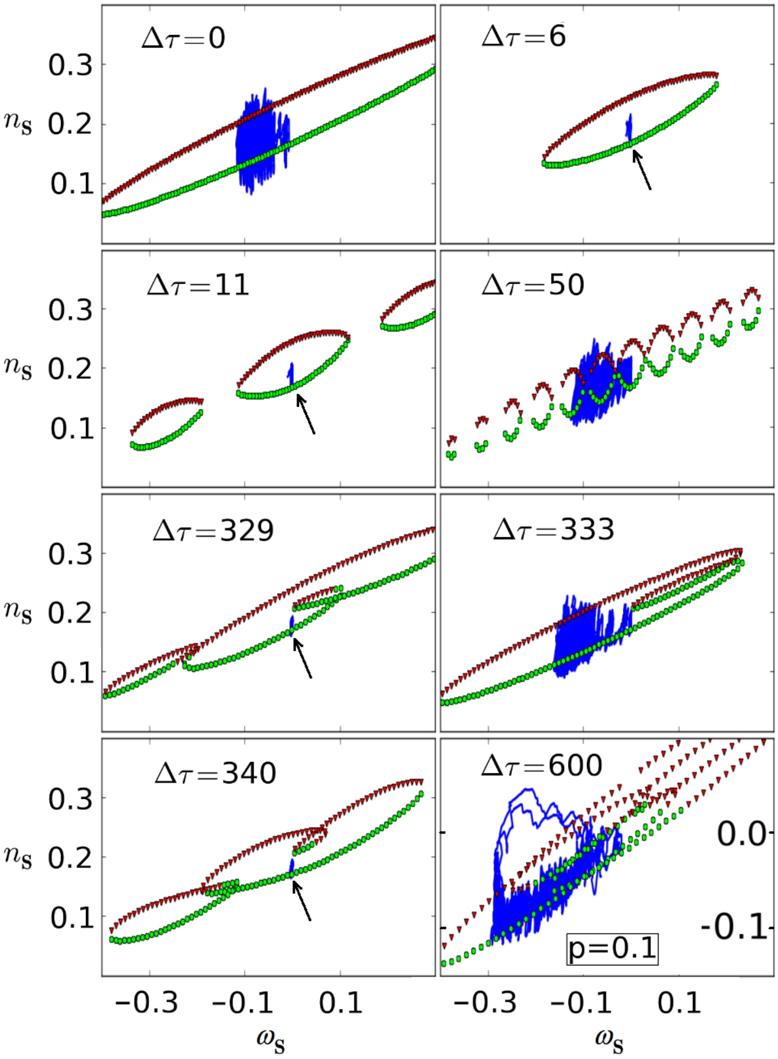

Figure 3.10: Dynamics of the symmetrized solution $S(t)$ (see Eq. (3.6)) in (ω_S, n_S)-phase space for different values of the delay mismatch parameter $\Delta\tau$ after $t = 5 \cdot 10^4$. For definition of ω_S and n_S, see Fig. 3.3. Green circles indicate transversely stable modes, red triangles are transversely unstable modes and antimodes. The dynamics trajectory (in blue) is marked with an arrow if stabilized. The mean delay time τ is fixed at $\tau = 1000$, the other parameters are $\alpha = 4.0$, $p = 1.0$ (except lower right), $\mu = 0.26$ and $L = K = 0.05$. Note that the lower right plot has a different y-scale than the others.

of the autocorrelation peak exhibits significant extrema for certain delay mismatches. The autocorrelation secondary peak value as a function of the delay mismatch is depicted in Fig. 3.8 (blue line). In particular, we find dips and peaks in the vicinity of simple rational values of r_τ, around $r_\tau = 1$, meaning $\Delta\tau \approx 0$, and around $r_\tau \to \infty$, meaning an almost vanishing second delay. Concurrently, the crosscorrelation also exhibits extrema (see Fig.3.8 (red line)) for the same $\Delta\tau$. Magnifications of the cross- and autocorrelations in Fig.3.8 for the ranges encompassing delay mismatches corresponding to these special delay time ratios are shown in Fig. 3.11.

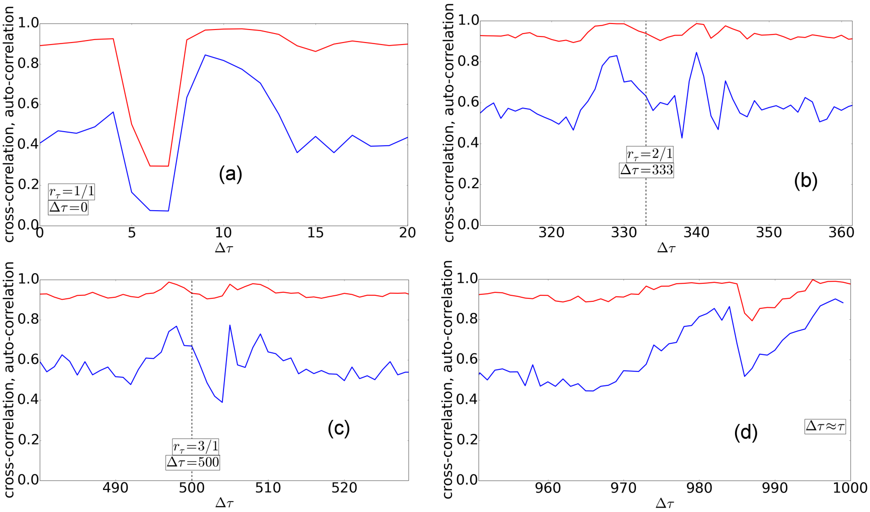

Figure 3.11: Cross-correlation $C(\delta t)$ at lag $\Delta t = \Delta\tau$ (red lines) and autocorrelation at $\Delta t = 2\tau$ (blue lines) vs the delay mismatch parameter $\Delta\tau$ for rational ratios of the feedback delays $r_\tau = \tau_1/\tau_2$. Magnification of Fig. 3.8 around (a) $r_\tau = 1$, (b) $r_\tau = 2/1$, (c) $r_\tau = 3/1$ and for (d) $\Delta\tau \approx \tau$. Simulation parameters are as for Fig. 3.8.

The extrema in the crosscorrelation function are caused by a change in the underlying dynamical state of the system and not primarily by a change of the synchronization. Lowered crosscorrelation values have been found to be caused by small signal-to-noise ratio when the dynamics is stabilized to a fixed point. Delay mismatches that lead to a stabilization of the dynamics to a limit cycle result in a peak in the auto- and the crosscorrelation due to the regular behavior.

To study the dynamical changes caused by varying delay mismatch in the intensity domain, we compute a bifurcation diagram as a function of $\Delta\tau$. Fig. 3.12 shows this bifurcation diagram with resulting intensity minima and maxima plotted against the delay mismatch. From the distribution of the extrema, we notice significant dynamical changes over the entire range of $0 \leq \Delta\tau < \tau$, which is evident, for example, by the changes in the variance of the intensity outputs. When the delay times are close to simple rational ratios, the effect on the dynamics is most pronounced in such a way that the variance of the intensity dynamics strongly narrows, implying (more) regular dynamics. Especially for $\Delta\tau \approx 0$ (almost equal delay times) and $\Delta\tau \lessapprox \tau$ (when one delay is very short), the variance decreases dramatically. Also we notice a significant drop in variance at around $\Delta\tau = 333$. This delay mismatch corresponds to a rational ratio of $r_\tau = 2/1$ of the delay times. At these values of the delay mismatch, the dynamics settles on a stable periodic orbit. The bifurcation corresponding to these three cases are shown in the magnifications in Fig. 3.12.

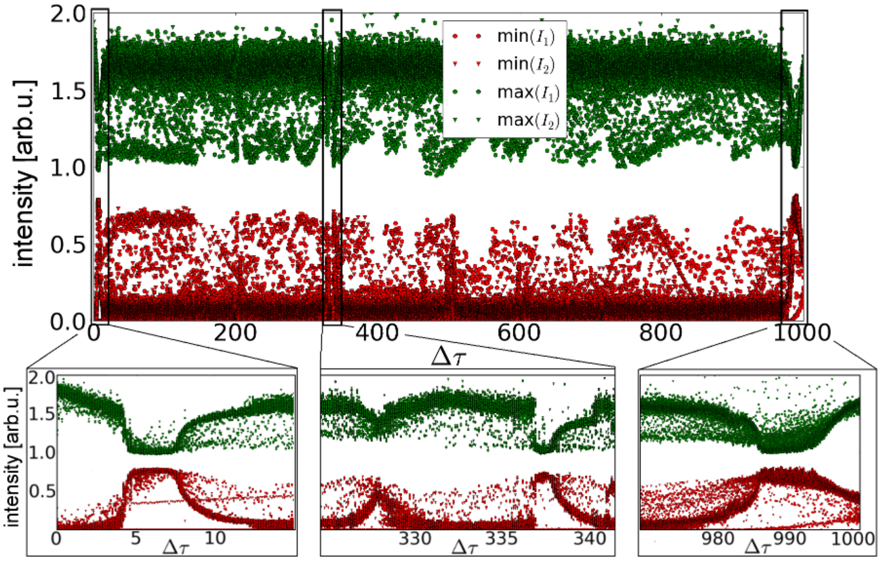

Figure 3.12: Intensity extrema of the two lasers versus the delay mismatch parameter $\Delta\tau$. Green points are maxima, red points are minima. Magnifications are shown for a small delay mismatch $\Delta\tau < 15$ (lower left), for a delay times ratio of $r_\tau \approx 2/1$ (lower center) and for one of the delays being very short $\tau_1 \gg \tau_2$ (lower right). The other simulation parameters are: $\tau = 1000$, $\alpha = 4.0$, $\mu = 0.26$, $p = 1.0$, $T = 200$, $\beta = 10^{-5}$, $K = L = 0.05$.

The smallest differences between maxima and minima indicate stable single mode emission. For these cases, the auto- and crosscorrelation show large peaks; however, this does not correspond to chaos synchronization.

The stabilization of the dynamics for several delay mismatches is illustrated in the phase space plots in Fig. 3.10, which shows the laser dynamics projected onto the (ω_S, n_S)-phase space of the synchronization manifold. Close to the rational ratio $r_\tau = 2/1$ (here $\Delta\tau \approx 333$), we see oscillations of the dynamics around a single mode (Fig. 3.10(e),(g)). The values for the delay mismatch correspond to those of the local peaks in the autocorrelation function in Fig. 3.11(b). For delays corresponding to the exact rational ratio $\Delta\tau = 333$, however, no such stabilization is observed (Fig. 3.10(f)). For small delay mismatches (Fig. 3.10(b),(c)) the dynamics exhibits robust and fast stabilization to a single mode.

This stabilizing property for a slightly misaligned semitransparent mirror tested robust against the variation of several parameters such as the mean delay τ, the coupling strength K and the noise magnitude β. Simulations over a range of these parameters result in stabilization of the dynamics.

With a sufficiently large gain saturation coefficient μ, the dynamics and mode spectrum can exhibit high-level synchronization, as well as stabilization of the dynamics. The effect of nonlinear gain saturation is described in more detail in Section 3.5.

We explain the stabilization at small delay mismatches and at delay mismatches close to simple delay ratios r_τ as follows: We consider a laser subject to a delayed feedback from two feedback loops with delays $\tau + \Delta\tau$ and $\tau - \Delta\tau$, which corresponds to the synchronized dynamics of two coupled lasers subject to their respective feedback with different delays $\tau + \Delta\tau$ and $\tau - \Delta\tau$. Let us assume that at $\Delta\tau = 0$, the laser operates in a chaotic regime, where the chaos is induced by the feedback. Although the laser dynamics is chaotic, there is, on average, a short term phase correlation of the electric field, i.e., the peak at the origin of the autocorrelation function of the field is surrounded by local minima and maxima. The first local minimum and maximum are usually very pronounced, because of a characteristic small oscillation period present in the chaotic signal. If the delay mismatch is adjusted such that it corresponds to the first minimum, then, on average, the incident feedback signals destructively interfere, and, thus, diminish the amplitude and the fluctuations of the feedback signal. This may lead to more regular behavior of the laser dynamics. The above usually also holds for the choice of a small rational ratio of the delay times, i.e. $\frac{\tau_1}{\tau_2} \in \mathbb{Q}$. Modifying $\Delta\tau$ will then evidently lead to a different shape of the autocorrelation function, in particular in case of dynamical stabilization. Nevertheless, it can still be assumed that a mechanism of destructive interference of this kind can result in stabilization of the dynamics.

We demonstrate this mechanism via an exemplary case. We first consider a case with no delay mismatch $\Delta\tau = 0$ for $\tau = 997$. The dynamics of the coupled system is then chaotic (LFF-regime) as shown in Fig. 3.13(a). The autocorrelation function of the dynamics is shown in Fig.3.13(b) and exhibits the first minimum next to the peak at $\Delta t = 34$.

We now construct the case with a delay mismatch of $\Delta\tau = 17$, which corresponds to the case of a single laser with two feedbacks with $\tau_1 = 997$ and $\tau_2 = 1031$. According to our above explanation this should lead to a stabilization/regularization of the coupled system's dynamics because of destructive interference between the feedback of each laser and the delayed

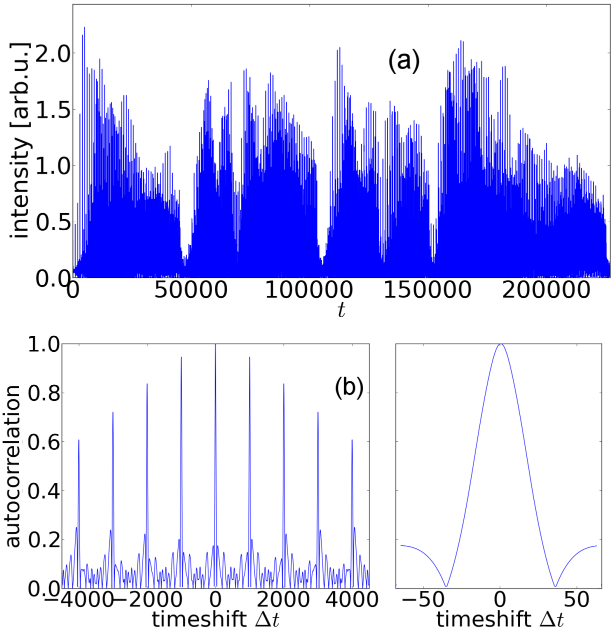

Figure 3.13: Dynamics of the coupled system without delay mismatch $\Delta\tau = 0$ (a) and the corresponding autocorrelation function (b). The other simulation parameters are $L = K = 0.05$, $\alpha = 4.0$, $p = 0.0$, $\mu = 0.0$, $T = 200$, $\beta = 10^{-6}$, $\tau = 997$.

coupling-signal from the respective other laser. We plot the resulting dynamics in the (ω_S, n_S)-phase space in Fig. 3.14(a). It indeed exhibits a stabilization to a single ECM after a transient time.

To check whether this stems from destructive interference, we calculate the phase difference between the feedback signal of one laser and the coupling signal from the respective other laser, which corresponds to the interference condition at the laser facet. The phase of the first laser is delayed by $\tau + \Delta\tau$, the phase of the coupling signal is delayed by the coupling time τ. We now compute a histogram of $\phi_1(t + \tau + \Delta\tau) - \phi_2(t + \tau)$ to see the distribution of the relative phase differences. The histogram is depicted in Fig. 3.14(b) and shows a dominant peak at a phase difference of -9π. Since this is an odd number π-shift, this corresponds to destructive interference in terms of relative phases.

The above serves as indication for our hypothesis that stabilization, for a small delay mismatch or a delay mismatch resulting in a delay ratio close to a simple rational one, stems from destructive interference of the two incident signals to one of the coupled lasers, one being the delayed self-feedback, the other one being the delayed coupling.

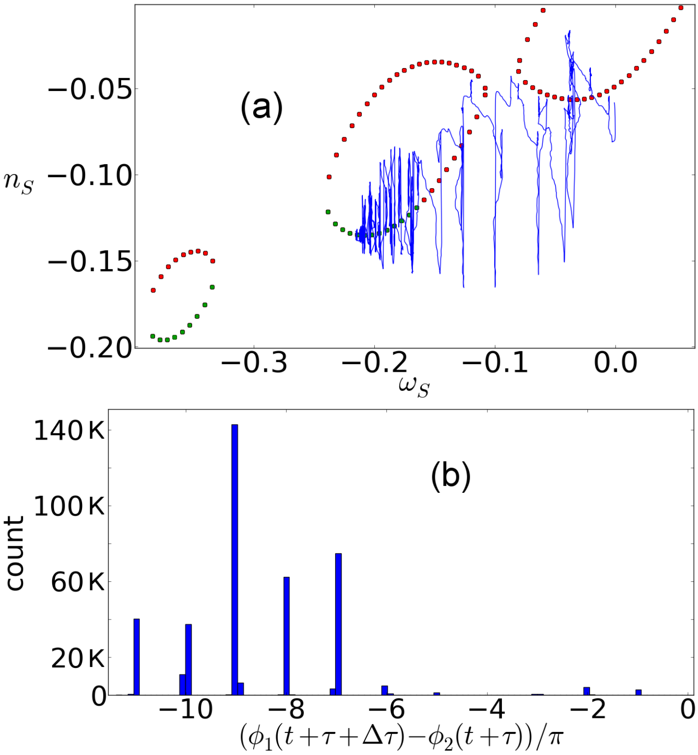

Figure 3.14: Synchronized dynamics of the coupled system in (ω_S, n_S)-phase space (see Fig. 3.3) for the case of a delay mismatch $\Delta\tau = 17$ (a). The coupling delay is $\tau = 1014$, the other simulation parameters are $L = K = 0.05$, $\alpha = 4.0$, $p = 0.0$, $\mu = 0.0$, $T = 200$, $\beta = 10^{-6}$, $\tau = 997$. (b) shows a histogram of the corresponding phase differences of the delayed feedback and the delayed coupling $\phi_1(t + \tau + \Delta\tau) - \phi_2(t + \tau)$.

3.5 Effect of nonlinear gain saturation on synchronization

In this section, we investigate the effect of nonlinear gain saturation on the synchronization and the dynamical properties of our bidirectional coupling scheme with a focus on cases with delay mismatch and coupling mismatch.

We have used a Lang-Kobayashi type model with a nonlinear gain function $G(E_j, n)$ during our numerical studies. A nonlinear gain, that saturates for high intensities, is often used to account for nonlinear deviations of the (otherwise linear, see Chapter 2) characteristic dependence of the optical power on the pump current far above the lasing threshold.

The nonlinear gain saturation is a phenomenologically-introduced term that is motivated by nonlinear effects in the semiconductor gain medium like spectral hole burning and carrier heating. A linear gain theory cannot account for those phenomena. With increasing pump current, the nonlinear gain saturation becomes more relevant and has an increasing effect on the dynamics of the lasers. This is because the laser modes that organize the dynamics change position with varying pump current p if the gain saturation coefficient is nonzero (see Eq. (3.24)). The transverse stability of the external cavity modes is also affected (see Appendix B).

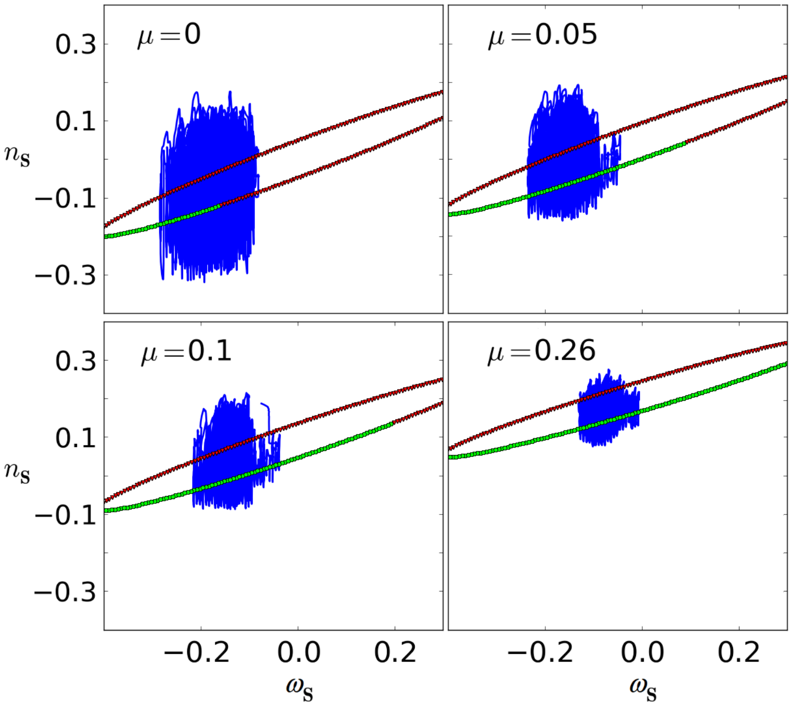

Figure 3.15: Effect of the nonlinear gain saturation on the position and transverse stability of the external cavity modes in (ω_S, n_S)-phase space. The pump current $p = 1.0$ results in coherence collapse dynamics. The larger the pump current value, the more pronounced the effect is. Red circles incicate transversely unstable modes and antimodes, green circles represent transversely stable modes. The dynamics is shown in blue. The other simulation parameters are: $\tau = 1000$, $\Delta\tau = 0$, $\alpha = 4.0$, $T = 200$, $L = K = 0.05$ and $\beta = 10^{-5}$.

When operating in the LFF-regime, the effect of nonlinear gain saturation can often be neglected due to the relatively low powers. In the coherence collapse (CC) regime, on the other hand, the higher power means that gain saturation plays an increasing role. The effect of gain saturation on the position of the ECMs and on transverse mode stability is illustrated in Fig. 3.15.

Increasing the nonlinear gain saturation μ leads to a shift of the ECMs to a region of larger transverse stability. The number of transversely stable modes increases with increasing μ, and the modes are shifted such that critical events with antimodes and subsequent desynchronization (bubbling) are less likely. The synchronized state is thus more stable. However, because of the dampening effect, the dynamics is also less complex.

Additionally, raising the gain saturation coefficient also results in a smaller maximum field intensity and a decreased variance of the intensity and of the carrier number. Fig. 3.16 illustrates this effect via a distribution of intensity maxima and minima for varying μ.

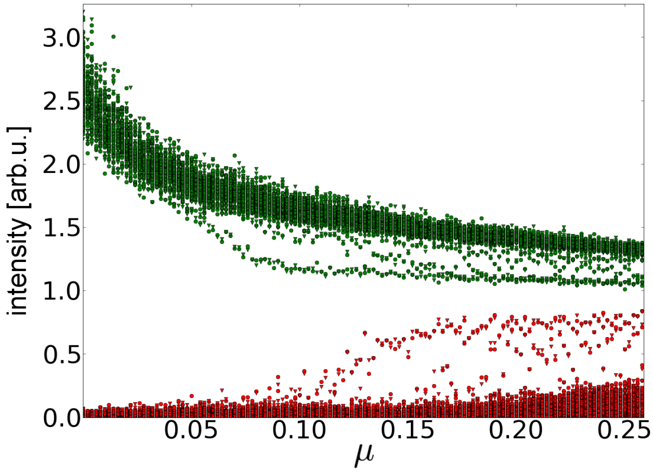

Figure 3.16: Intensity extrema of the coupled system for varying μ. Green points represent intensity maxima, the red points are intensity minima. The numerical parameters are the same as for Fig. 3.15.

If the considered model omits the nonlinear gain ($\mu = 0$), all modes in the vicinity of the minimum gain mode (around $\omega = 0$) are transversely unstable above a critical pump current (see Fig. 3.15). Without gain saturation, the lasers experience many desynchronization events or do not synchronize at all, depending on parameters. The plots in Fig. 3.17 show the dependence of the maximum correlation peak on the feedback and coupling strengths, respectively, for vanishing gain saturation coefficient $\mu = 0$ and symmetric delay times (a) as well as for a delay mismatch of $\Delta\tau = 20$ (b).

When we compare these results with the corresponding ones for nonzero gain saturation, as shown in Figs. 3.2 and 3.9, it is evident that the regions of overall stable synchronization (high cross-correlation) are smaller for the case of linear gain ($\mu = 0$) when compared to nonzero gain saturation.

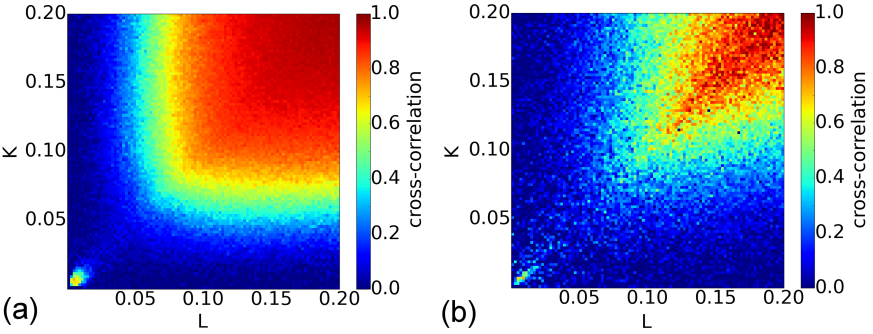

Figure 3.17: Cross-correlation of the field intensities versus the feedback strength L and the coupling strength K, respectively, with and without delay mismatch. (a) Symmetric delays $\Delta\tau = 0$ resulting in zero-lag synchronization; (b) with delay mismatch $\Delta\tau = 20$ - the crosscorrelation is computed for $\Delta t = \Delta\tau$. The nonlinear gain saturation is neglected for these simulations. Corresponding plots with $\mu > 0$ are shown in Figs. 3.2 and 3.9, respectively. The simulation parameters here correspond to $\mu = 0$, $p = 1.0$, $\alpha = 4.0$, $T = 200$, $\tau = 1000$ and $\beta = 10^{-5}$.

3.6 Relay configuration with spectral detuning

We again consider the bidirectional coupling setup with symmetric delays corresponding to Fig. 3.1, now with equal coupling and feedback strengths $L = K$. As another possible asymmetry in such a system, we now investigate the influence of optical frequency detuning of the solitary laser emission frequencies on the synchronization and dynamics of both coupled lasers. Frequency detuning often takes place in experimental systems, as the emission frequencies of two coupled lasers can only be adjusted to some precision. If both lasers have slightly different P-I-characteristics as well, obtaining full symmetry in such a coupled laser system can turn out to be challenging.

For a fundamental understanding, as well as when considering chaos communication schemes, it is therefore sensible to investigate the effect of detuning on the synchronization and synchronizability of two bidirectionally-coupled lasers with feedback.

3.6.1 Modeling and synchronization properties

There are two prominent methods of frequency detuning in a system of two interacting semiconductor lasers: the first case is that the detuning is symmetric, meaning both lasers' main frequencies are at the same time equally shifted to opposing sides of the mean frequency of the system. We then write the nondimensional model (see Section 2.3.1) in the reference frame of the mean frequency. The other possible case is asymmetric detuning where one laser's frequency remains fixed (the undetuned laser) and the main frequency of the other laser is shifted (the detuned laser). The nondimensional model we use then works in the reference frame of the undetuned laser. In experiments related to detuning, the latter option is often chosen since symmetric spectral adjustments are difficult to accomplish in real-world systems.

To introduce the detuning into our model, we have to modify Eq. (3.4) and add the detuning terms [193] corresponding to the case - symmetric or asymmetric detuning, respectively. For symmetric detuning, the field equations are modified to

$$\begin{aligned} \dot{E}_j = \; & \tfrac{1}{2}(1+i\alpha)\left[G(E_j,n_j)-1\right]E_j + (-1)^j \tfrac{i}{2} 2\pi\Delta E_j \\ & +LE_j(t-\tau)+KE_{3-j}(t-\tau)+F_{E_j}, \end{aligned} \tag{3.25}$$

for $j = 1, 2$, where $\Delta = \Omega_1 - \Omega_2$ is the optical frequency detuning in dimensionless units and G is the nonlinear gain function as defined in Eq. (3.5). The term $2\pi\Delta$ describes the anglular frequency detuning. For asymmetric detuning, the term only goes into the field equation of the detuned laser:

$$\begin{aligned} \dot{E}_1 &= \frac{1}{2}(1+i\alpha)\left[G\left(E_1(t),n_1(t)\right)-1\right]E_1(t) \\ & \quad +LE_1(t-\tau)+KE_2(t-\tau)+F_{E_1}, \end{aligned} \tag{3.26}$$

$$\begin{aligned} \dot{E}_2 &= \frac{1}{2}(1+i\alpha)\left[G\left(E_2(t),n_2(t)\right)-1\right]E_2 + i2\pi\Delta E_2 \\ & \quad +LE_2(t-\tau)+KE_1(t-\tau)+F_{E_2}, \end{aligned} \tag{3.27}$$

whereas the carrier equations for both ways of detuning remain unmodified like given by Eq. (3.4):

$$\dot{n}_j(t) = \frac{1}{T}\left(p - n_j(t) - G(E_j,n_j)\left|E_j(t)\right|^2\right) \tag{3.28}$$

for $j = 1, 2$. In the following, we restrict our studies to the case of symmetric detuning.

In order to quantify the synchronization level depending on varying frequency detuning, we calculate the crosscorrelation function between the lasers' output dynamics. It has been shown [23] that a certain frequency detuning between two coupled lasers leads to the predominance of generalized synchronization with a time lag corresponding to the delay. The laser leading the dynamics is the one emitting at a higher frequency. Even though correlation at a time shift of $\Delta t = -\tau$ or $\Delta t = \tau$ might be larger than at zero-lag, the zero-lag correlation remains at a comparably high level within the locking range. Fig. 3.18 shows the crosscorrelation at zero-lag $C(0)$ as well as the correlations $C(\tau)$ and $C(-\tau)$ in dependence of the symmetric detuning coefficient Δ.

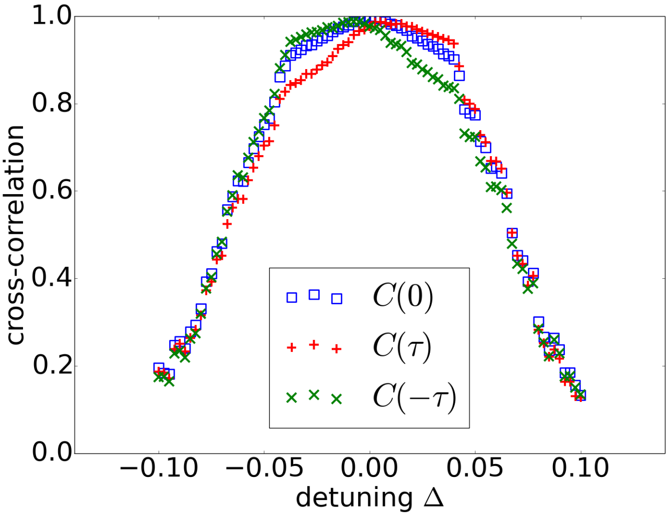

Figure 3.18: Zero-lag crosscorrelation (blue squares), crosscorrelation at $\Delta t = \tau$ (red pluses) and crosscorrelation at $\Delta t = -\tau$ (green crosses) versus the detuning Δ. Already for comparably small detuning lag-synchronization becomes predominant, even though the zero-lag synchronization exhibits high levels as well. The numerical parameters are: $\alpha = 3.0$, $\mu = 0.02$, $p = 0.0$, $T = 200$, $\tau = 2000$, $K = L = 0.15$ and $\beta = 10^{-6}$.

The blue squares depict the zero-lag crosscorrelation which exhibits a range of high-level correlation for $|\Delta| \lessapprox 0.045$ corresponding to the central locking range. With further increasing detuning, the correlation rapidly decreases, a feature we will explain in the following section in terms of spectral overlap and episodic synchronization [183].

The lag correlations at τ (red pluses) and $-\tau$ (green crosses) underline the change of the system to predominant generalized synchronization with a time lag for increasing detuning, and make clear that the role of leading laser switches if the sign of the detuning Δ switches.

If the detuning is asymmetric, the vertical symmetry of the crosscorrelation in respect to the axis $\Delta = 0$ vanishes, but the locking range will have comparable extent for both positive and negative detuning if the coupling strength is not too large. Otherwise, because feedback-induced dynamics usually exhibit a drift to lower frequencies [50], the dynamics will remain synchronized for a larger negative detuning than for a positive detuning.

We will describe the mechanism underlying the correlation decay with increasing detuning in the following section.

3.6.2 Spectral and dynamical features with detuning

Frequency detuning influences the dynamical regimes of the two coupled lasers via their frequency dynamics. Here, we connect the overlap of the optical spectra with the dynamics and synchronization level of both lasers.

Búldu et al. [183] introduced the concept of episodic synchronization for the case unidirectional injection: A semiconductor laser, which exhibits stable emission without input, is being dynamically injected by a drive laser exhibiting chaotic dynamics for different detunings of their solitary emission frequencies. They showed that the dynamics of the response laser, which is induced by the injected signal from the drive laser, is synchronized if and when it is within the injection locking range of the drive laser. In that manner, synchronization is related to the overlap of the spectral ranges of the drive and response lasers, respectively. Here, we investigate a system of two coupled lasers dynamically injecting each other. We adapt the notion of episodic synchronization for the bidirectional coupling case and link the correlation characteristics with varying detuning to the overlap of each laser's spectral range and injection locking range. We attribute the correlation decay with increasing absolute detuning (the detuning is symmetric) to an increasing fraction of the lasers' dynamics occurring outside the overlap of their respective locking ranges.

We evaluate the time-resolved correlation by calculating the sliding-window crosscorrelation (slcc) and analyze the spectral overlap depending on the detuning.

For our numerical investigation, we consider the cases of small, intermediate and large detuning. We simulate the lasers as being operated in the LFF regime so the changes in the dynamics induced by the detuning become easily visible. In addition, LFF dynamics exhibit more extended phase space itinerancies than coherence collapse (CC) dynamics (see Chapter 2), so changes of the frequency range due to detuning are more obvious for LFFs than for CC. The system parameters for our simulations are chosen as in Fig. 3.18.

In Fig. 3.19, we show several averaged frequency extrema $\omega_{1,2}(t)$ of both lasers extracted versus the detuning Δ. We identify the range from the averaged minimum to the averaged maximum frequency (the shaded areas in Fig. 3.19) for each laser with its respective (effective) spectral range.

The frequencies $\omega_{1,2}$ are calculated as follows: First the connected (increasing) phases $\phi_{1,2}$ are calculated from the complex field variables $E_{1,2}$ by

$$\phi_{1,2}(t) = \arctan\left(\frac{\Im\left[E_{1,2}(t)\right]}{\Re\left[E_{1,2}(t)\right]}\right) \tag{3.29}$$

and transformed to connected phases. The (angular) frequencies $\omega_{1,2}$ are then calculated as delay-time averaged phase difference

$$\omega_{1,2} = \left(\phi_{1,2}(t) - \phi_{1,2}(t-\tau)\right)/\tau, \tag{3.30}$$

and are given in the reference frame of the average solitary angular frequency $\omega_{\text{mean}} = (\omega_1 + \omega_2)/2$.

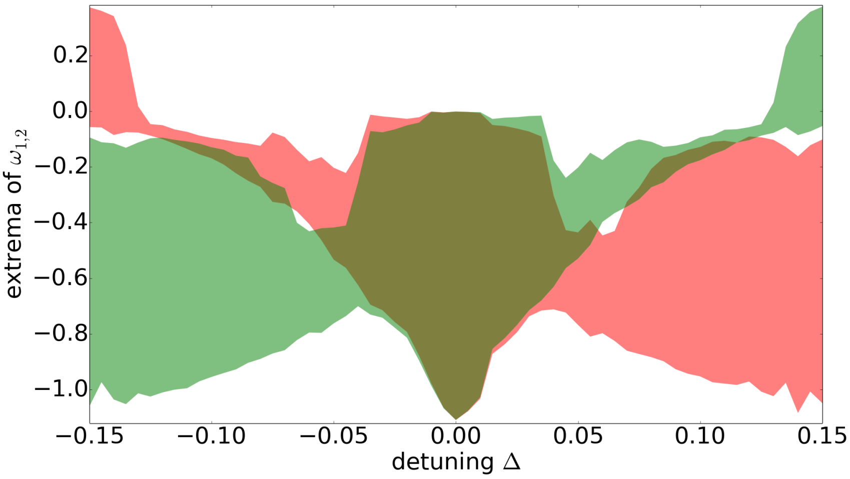

Figure 3.19: Spectral ranges computed from the average of several frequency extrema of two coupled lasers with feedback versus their relative symmetric detuning. The red shaded area describes the spectral range of laser 1, the green area is the spectral range of laser 2 and the brown region illustrates the spectral overlap. The frequencies are given relative to the mean solitary frequency $\omega_{\text{mean}} = (\omega_1 + \omega_2)/2 = 0$. The extrema are averaged from a five-fold sampling of one timetrace per detuning-value with a length of $8 \cdot 10^5$ points each. The frequencies are calculated according to Eqs. (3.29) and (3.30). The simulation parameters correspond to those given in Fig. 3.18.

The red shaded areas in Fig. 3.19 depict the spectral range of laser 1, the green shaded regions are the spectral range of laser 2, and the brown areas are the spectral overlap between the lasers.

This overlap can be connected to frequency locking and synchronization of the lasers in the respective detuning regime. The larger the overlap, the better the locking and the synchronization. For small values of the detuning Δ, we observe almost complete overlap of the spectral ranges; this region corresponds to the range of high correlation values as depicted in Fig. 3.18. For an increasing absolute detuning, the overlap diminishes while the spectral range of the laser that is tuned to higher frequencies decreases significantly (laser 1 (red) for negative symmetric detuning, laser 2 (green) for positive symmetric detuning Δ). For very large absolute detuning $|\Delta| > 0.13$, the lasers' average frequencies unlock completely and their overlap vanishes. However, since the frequencies calculated from the delay phase (Eq. (3.29)) are averaged and collapsed into one value, we emphasize that the actual complete spectra still have a significant overlap (see below).

Because the diagram in Fig. 3.19 describes a stationary perspective and we want to unveil the mechanism underlying the synchronization decline, we study the time-dependent frequency variables. To qualify the current synchronization state, we compute the sliding-window cross-correlation (slcc). It is calculated as cross-correlation of the intensities for a shifting window of length 200 points with a step size of 1.
Time traces of the lasers' emission frequencies (as computed by Eq. (3.30)) and intensity outputs as well as the corresponding slcc are shown in Fig. 3.20 for detuning values $\Delta = 0.01$ (a), $\Delta = 0.025$ (b) and $\Delta = 0.04$ (c). The center panels depicting the time evolution of $\omega_{1,2}$ exhibit the unlocking of both lasers (averaged) frequencies during the power dropouts for small detuning (a). Furthermore, they show unlocked behavior during the increasingly large interval encompassing the power dropouts for larger detuning (b,c). The slcc-time traces (top panels) show corresponding dips, confirming desynchronization which can also be seen in the intensity dynamics as depicted in the lower panels.

Unlocking occurs at low frequencies close to the end of the spectral range of the laser tuned to a higher solitary emission frequency. We interpret this behavior as corresponding to episodic synchronization in [183]: the dynamics of the laser tuned to lower frequencies move out of the locking range of the other laser, and desynchronization sets in. As the lasers are increasingly detuned from each other, the shared spectral range diminishes and less of the dynamics are synchronized. Resynchronization takes place close to the upper edge of the locking range of the laser tuned to lower frequencies. Because an increasing symmetric frequency detuning reduces the spectral overlap of both lasers from both the high and the low frequency end, the desynchronization episodes are centered around the times of occurrence of power dropouts. Their increasing duration leads to the decay of correlation of the lasers' outputs as shown in Fig. 3.18.

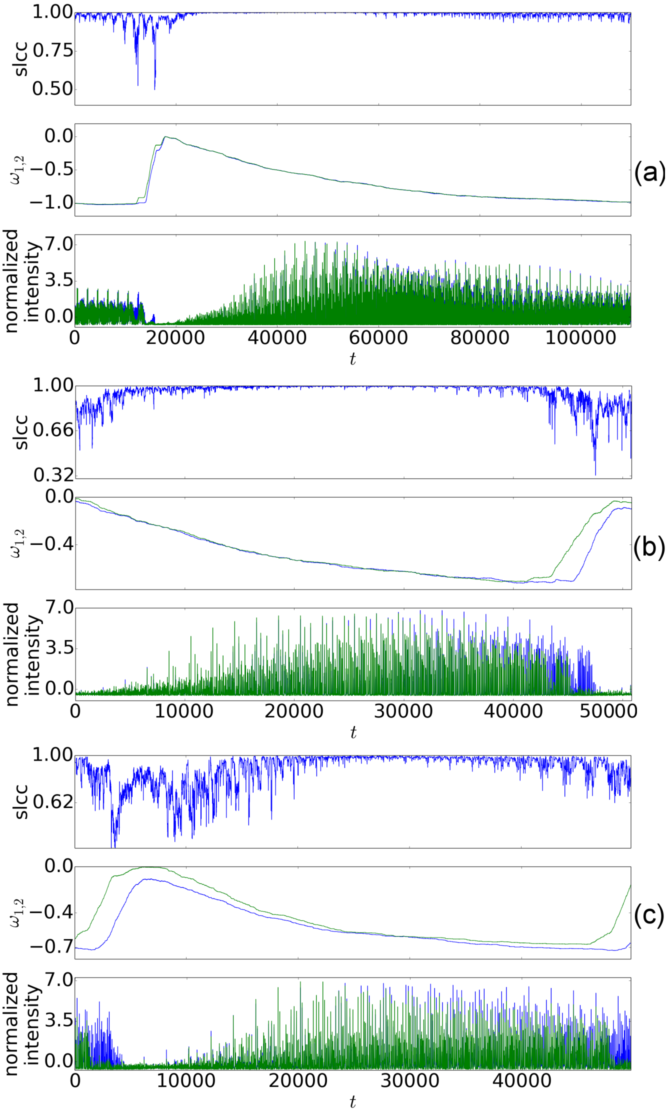

Figure 3.20: Time series of the sliding cross-correlation (top panels), of both frequencies $\omega_{1,2}$ (middle panels) and of the corresponding output intensities $|E_{1,2}(t)|^2$ (lower panels) during one LFF cycle for different values of the detuning. The frequency dynamics and intensity dynamics, respecively, of laser 1 are depicted in blue, the corresponding dynamics of laser 2 are shown as green curves. The detuning values are $\Delta = 0.01$ (a), $\Delta = 0.025$ (b) and $\Delta = 0.04$ (c). The simulation parameters correspond to those given in Fig. 3.18.

By the length of the time interval shown, one can also see that the length of one LFF dynamical cycle is significantly reduced by an intermediate detuning (Fig. 3.20 (b,c)) as compared to the case with small detuning (Fig. 3.20(a)). The characteristics and the occurrence of the unsynchronized intervals in dependence of the detuning is investigated further in Chapter 4.

The unlocking of both lasers' frequencies is accompanied by a power dropout and spectral jump toward the solitary lasing frequency of the laser tuned to higher frequencies. The other laser emits further at the lower end of its frequency range until it experiences a power dropout and spectral jump induced by the coupling signal of the first laser after the coupling delay τ. In that way, a frequency detuning between the two lasers increases the frequency of occurrence of the power dropouts which is a defining timescale in the LFF regime.

Fig. 3.21 shows dynamical trajectories $\omega_{1,2}(t), n_{1,2}(t)$ in the (ω_S, n) phase space for the same detuning $\Delta = 0.01$ (a), $\Delta = 0.025$ (b) and $\Delta = 0.04$ (c). The light green and light red parts describe the dynamics of laser 1, the dark green and dark red parts are the dynamics of laser 2. The red portions of the trajectories describe unsynchronized intensity dynamics according to a correlation threshold $C_{\text{thr}} = 0.95$ of the sliding-window cross-correlation, the fractions that are green describe synchronized dynamics (for the slcc timetraces see Fig. 3.20).

In Fig.3.21(a), we see phase space trajectories of both lasers with extended frequency range, corresponding to the time traces in Fig. 3.20, that mirror the large spectral range shown in Fig. 3.19 for small detuning. This range roughly corresponds to the extent of the ECM mode ellipse of a single laser subject to feedback with strength $L + K$. The dynamics are synchronized almost completely, except during their power dropouts. This desynchronization during dropouts is investigated in more detail in Chapters 4 and 5. For the case of an increased detuning $\Delta = 0.025$, which is depicted in Fig. 3.21(b), the frequency range of both lasers' dynamics is significantly diminished because of temporary unlocking. Also, both dynamics need longer to resynchronize after the preceding power dropouts and subsequent frequency jumps. Fig. 3.21(c) shows the situation for $\Delta = 0.04$; an even longer resynchronization time of the dynamics is illustrated there. However, since most of the dynamics in the LFF regime take place at lower frequencies (corresponding to the lower end of the ECM ellipse, see Chapter 2), most of the dynamics are still well-synchronized. This can be recognized in Fig. 3.18 and in the top panels of Fig. 3.20. During the time intervals in which the frequencies are unlocked, the dynamics exhibit unsynchronized behavior. These unsynchronized episodes become longer with increasing detuning and thus decrease the overall synchronization as depicted for $|\Delta| \lessapprox 0.045$ in Fig. 3.18.

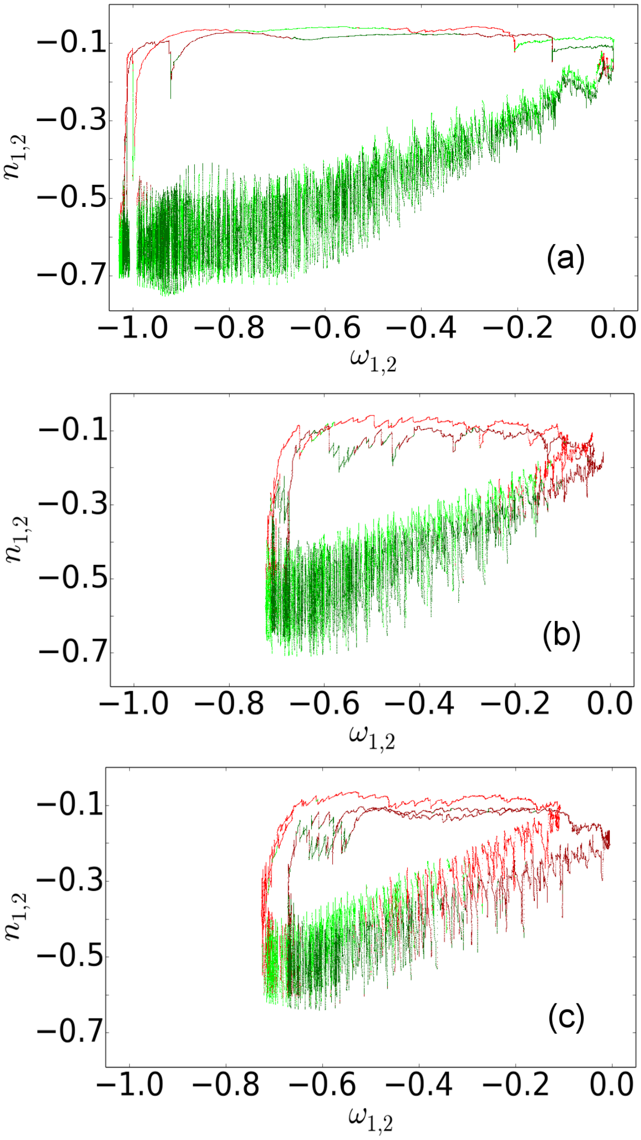

Figure 3.21: Dynamical trajectories in (ω_S, n) phase space for different detuning values $\Delta = 0.01$ (a), $\Delta = 0.025$ (b) and $\Delta = 0.04$ (c). The light green and dark red trajectories are describe the dynamics of laser 1, the dark green and dark red parts describe laser 2. Both red shares of the trajectories describe dynamics which are unsynchronized according to a slcc-threshold value of $C_{\text{thr}} = 0.95$, the green curves are synchronized dynamics. The simulation parameters correspond to those given in Fig. 3.18.

The lasers emit at several frequencies at a time. Therefore, to have an overall spectral picture for the three considered detuning values within the locking range, and to compare with the case of large detuning (and consequently unlocked frequencies), Fig. 3.22 shows optical spectra computed from a Fast Fourier Transform (FFT) of the dynamics shown in Figs. 3.20 and 3.21 for $\Delta = 0.01$, $\Delta = 0.025$ and $\Delta = 0.04$, respectively, as well as of dynamics computed for a large detuning $\Delta = 0.075$ of comparable length. The spectra of laser 1 are shown in light red, those of laser 2 are shown in light blue, and the overlap is presented in purple. The y-axis is in log-scale.

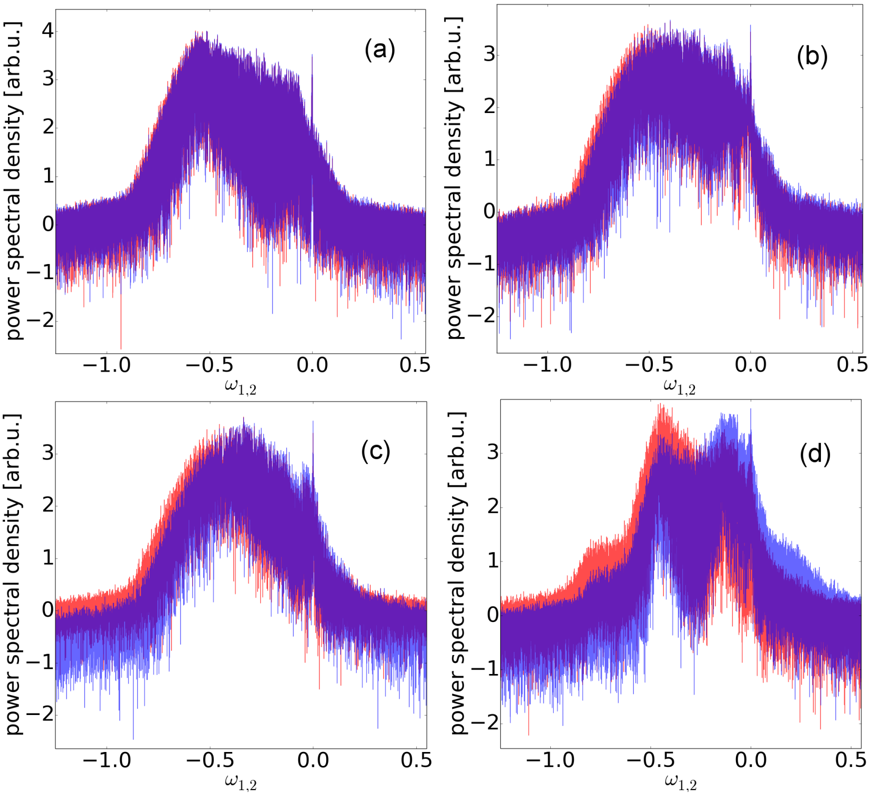

Figure 3.22: Optical spectra generated by FFT from the dynamics shown in Fig. 3.20 and for larger detuning. Laser 1's spectra are shown in light red, the spectra of laser 2 are depicted as light blue and the overlap is the purple area. The detuning values are $\Delta = 0.01$ (a), $\Delta = 0.025$ (b), $\Delta = 0.04$ (c) and $\Delta = 0.075$ (d). Note that the y-axis is in log-scale.

One immediately notices the diminishing overlap with increasing detuning. Especially the lowest exhibited frequencies are only emitted by the laser which is negatively detuned with respect to the average solitary laser frequency ω_S. For $\Delta = 0.075$ the lasers' spectra are significantly more shifted from each other, they unlock for most of their dynamical trajectories and exhibit individual main peak structures that are highly suppressed in the respective other laser.

To sum up, in a phenomenological way, we have linked the frequency dynamics and the spectral overlap of two mutually-coupled lasers with relative detuning to their synchronization properties. The synchronization characteristics are also connected to dynamical changes due to the detuning. Desynchronization events that are related to LFF-power dropouts show increased frequency with increasing detuning. They result in the overall decline of the synchronization within the detuning range of well-synchronized behavior (see Fig. 3.18).

3.7 Summary

We have numerically and analytically investigated the dynamical and synchronization properties of a system of two delay-coupled semiconductor lasers in different coupling schemes. We employed a model for a scheme of two lasers coupled via a semitransparent mirror, which serves as a passive relay, and studied the influence of a mismatch between the transmission and reflection of the mirror, i.e., a mismatch between coupling and feedback strength. Furthermore, we investigated the effect of a delay mismatch corresponding to a misalignment of the mirror from the middle. We have further studied numerically the effect of frequency detuning of the two lasers on their synchronization level and dynamics, respectively, the detuning serving as another important potential mismatch.

We have shown that a mismatch of coupling and feedback strengths deteriorates the stability of the synchronized solution, but does not change the synchronized dynamics. An increasing mismatch leads to longer desynchronization events, since less modes are transversely stable. However, high-level synchronization is still observed if the mismatch $|L-K|$ remains comparably small. The zero-lag crosscorrelation of the lasers' dynamics does not depend on the sign of the mismatch between coupling and feedback $L-K$ but only on the modulus.

Considering a saturable nonlinear gain, a reduction of complexity in the timeseries is observed. At the same time, a broader domain of parameter mismatches exists that leads to high synchronization levels, because the gain saturation increases the transverse stability of the ECMs.

Our analysis has shown that the synchronization properties of a configuration with a semitransparent mirror are the same as those of a drive-response configuration, at least on the level of the ECMs. Comparing open-loop and closed-loop drive-response configurations, it was shown that an open loop configuration synchronizes best; the transverse stability of the modes involved in the dynamics of both lasers equal those in a bidirectional setup without coupling mismatch. Adding self-feedback to the receiver laser has the same effect on stability as introducing a coupling mismatch in the relay configuration.

In the situation of a mismatch of the feedback and coupling delays, we have found that the lasers can synchronize identically with a nonzero lag. The output time series then exhibit a relative time shift proportional to the delay difference. The stability of the time-shifted identical synchronization of the lasers is almost unaffected by the magnitude of the delay mismatch. However, the dynamics are drastically altered by a varying $\Delta\tau$, because the ECM positions are changed compared to the case of symmetric delays.

In particular very small mismatches, mismatches leading to rational ratios of the delay times, and cases where the second delay is very short compared to the first one, respectively, result in the possibility of suppressing the chaotic dynamics and stabilizing them toward either single mode output or periodic dynamics. These qualitative features do not depend on the amount of the delay, but solely on the ratio of the delay times. We found these characteristics to be robust for broad ranges of the coupling strengths (i.e., the transmission and reflection of the relay-mirror) and even for strong spontaneous emission noise levels. We speculate that they are caused by destructive interference phenomena.

We also found that applying a delay mismatch to the system leads to a much increased sensitivity toward an additional coupling mismatch. The synchronization level decreases faster when both a delay and a coupling mismatch, respectively, are present in the configuration, than in the case with only a coupling mismatch but symmetric delays.

Furthermore, we have phenomenologically linked the decreasing spectral overlap occurring for two coupled lasers that are increasingly spectrally detuned with the synchronization level of the lasers' dynamics. In the LFF regime, the alterations of the dynamics due to (small to intermediate) detuning can be connected with changes in synchronization levels. Intervals of desynchronization, related to the power dropouts, occur more often with increasing detuning and longer periods of unlocking lead to longer periods of desynchronization.

The presented results are of great relevance for further investigations into the dynamics and synchronizability of delay-coupled lasers. The possibility to target specific stability regions via intentionally-introduced mismatches can for example be helpful for chaos communication systems or random number generation. Moreover, our results are not only relevant for chaotic communication, but may also be helpful to scientists in other fields, such as computational neuroscience, engineering, and biology. The presented analytical results can be transferred to other delay-coupled systems with corresponding network topology and thus could facilitate the developement of applications, e.g., in electro-optic or neuronal systems.

4

Identical synchronization and intermittent desynchronization events in delay-coupled lasers

4.1 Introduction

4.1.1 Bubbling and on-off intermittency

Chaos synchronization is an interesting phenomenon in coupled nonlinear systems. Besides its fundamental importance in laser systems, applications of the phenomenon add to its appeal. One can take advantage of chaos synchronization in laser systems for chaos-based communication schemes and key-exchange-protocols [25, 83, 84, 86, 90, 176]. Message recovery in these concepts heavily depends on synchronization of the involved lasers because information can not be recovered from unsynchronized output states. It was shown, that coupling two nonlinear subsystems via a relay, which can be active [71, 194] or passive [78, 176], or adding corresponding self-feedbacks to the coupled subsystems [80], can lead to zero-lag synchronization. As we show in Chapter 3, symmetric setups and coupling topologies and identical subsystems (or subsystems with minimal parameter mismatches) favor zero-lag synchronization.

There have been studies that investigated quantitatively the issue of synchronization loss in coupled chaotic systems under the influence of noise or with key system parameters' variation [92, 93, 95, 97, 195–197]. Studies that address the underlying mechanisms behind the synchronization loss, especially from an experimental perpective, are, however, rare. Changes in operating parameters or introduction of mismatches frequently alter the dynamics of such coupled systems, and, therefore, might modify the desynchronization mechanisms as well.

There are two major mechanisms for the loss of synchronization of near-identical coupled nonlinear oscillators: transverse instability of the synchronization manifold (SM) due to a blowout-bifurcation [92, 93] and attractor bubbling [92, 94, 95, 97, 195, 196, 198, 199].

Transverse stability of a manifold is often characterized by the largest transverse Lyapunov exponent. A negative exponent means transverse stability. A blowout-bifurcation is defined as the zero-crossing point of the largest Lyapunov exponent under variation of a key parameter, often the coupling strength. A transition through a blow-out bifurcation results in intermittent desynchronization events. This phenomenon is called on-off intermittency [93, 95, 200, 201] and occurs close to a blowout-bifurcation.

Attractor bubbling arises via a so-called bubbling bifurcation. It describes how invariant sets (such as periodic orbits), that are embedded in a transversely stable attractor within the (invariant) synchronization manifold, lose their transverse stability. Transverse perturbations by noise or by small mismatches between the coupled elements can then induce intermittent desynchronization events, even though the maximum transverse Lyapunov exponent of the chaotic attractor is negative. In this case, the trajectory can be pushed toward the transversely unstable sets by noise or mismatch and leave the SM. If no other attractor is present, the trajectory will then return to the SM and the coupled subsystems resynchronize. The bubbling bifurcation is the point where the very first invariant set becomes transversely unstable. Similar to on-off-intermittency, the bifurcation can be traversed by varying a key system parameter, often the coupling strength between the involved subunits. Dynamically, bubbling is characterized by intermittent desynchronization events, similar to on-off-intermittency. The latter, however, occurs also in systems with coupled identical elements and without noise, since the attractor lacks transverse stability. Furthermore, certain scaling laws have been found to describe the time the dynamics spend close to the synchronized state [95, 201].

Venkataramani et al. showed analytically, that there are two transitions to bubbling: the hard transition and the soft transition [195, 196]. In soft transitions, the desynchronization burst amplitude scales with the square root of a normal parameter μ [96, 195, 202]. This normal parameter describes the distance to the bubbling bifurcation. A normal parameter only changes the transverse stability of solutions in the synchronization manifold, but not the dynamics within the synchronization manifold. In hard transitions, the bursts set in with a finite burst amplitude.

Here, we investigate the time-resolved synchronization properties in a system of bidirectionally coupled semiconductor lasers with feedback. Bubbling has been shown to exist in such a system [97], and the transverse stability of the external cavity modes (see Chapters 2 and 3) play an important role for the stability of the chaos synchronization. If our system is completely symmetric, bubbling is mostly induced by noise and the transversely unstable antimodes, which are saddle nodes. However, small parameter mismatches between the lasers can also destabilize other modes, which then can, too, mediate desychronization events.

In delay-coupled Stuart-Landau oscillators and Kuramoto oscillators similar unstable periodic orbits, as in the chaotic attractor of our system, exist as well [68]. Thus bubbling can be expected to occur in these kinds of system, too. Overall, bubbling has been found for a multitude of dynamical systems: lasers [95, 96], electronic circuits [94, 203], biological cells [204], and various generic oscillators (see e.g. [195]).

Whether the bubbling transition in our coupled laser system is a hard or a soft transition can not be rigorously determined; a normal parameter does not exist in this system [96, 98] as all laser and coupling parameters affect the synchronized dynamics. However, numerical simulations of Lang-Kobayashi rate equations have shown [98] that the desynchronization burst amplitude (synchronization error) is not changed by parameter variations in that model, which we employ also. This suggests, that the bubbling transition is a hard transition in our system.

In this chapter, we connect the general synchronization level of two bidirectionally-coupled laser with feedback, as quantified by crosscorrelation coefficients, with the occurrence of distinct desynchronization events. We follow this approach for three different cases: first, we investigate noise-induced bubbling in an experimental laser system, and second, we study mismatch-induced bubbling in numerical simulations. Studying the effect of mismatches on synchronization dynamics numerically enables us to disregard noise, a feature that is prevalent in real physical systems. In experimental laser systems, intrinsic noise stems from spontaneous emission.

For the third case, we study the characteristics of intermittent desynchronization events due to frequency detuning between the two lasers in experiments and via a numerical study, respectively. We described the mechanism of this desynchronization phenomenon in Chapter 3 from the viewpoint of episodic synchronization as introduced in [183]. In this concept, the desynchronization is linked with diminishing spectral overlap of both lasers with increasing detuning. Here, we characterize the properties of these desynchronization episodes in a quantitative manner.

4.1.2 Chapter Outline

This chapter is organized as follows. First we introduce our experimental setup in Section 4.2. We then present experimental results showing high-level zero-lag synchronization of two bidirectionally-coupled semiconductor lasers, that are coupled in a relay-configuration in Section 4.3. Furthermore, we show the decline of synchronization with increasing pump currents in that system. In Section 4.4, we investigate the synchronization characteristics for different pump currents on a local time scale using a sliding-window cross-correlation (slcc) analysis, and we connect the occurence of the found desynchronization events with the dynamical features of the respective operating regime. We interpret these desynchronized intervals as bubbling events. Our results are supported by a statistical analysis of the characteristics of these desynchronization events. Then, in Section 4.5 we investigate first experimentally in 4.5.1 as well as numerically in 4.5.2 the synchronization characteristics and -dynamics (also using slcc) in the same scheme as described above but introducing a frequency detuning. We describe and characterize the arising desynchronization events due to detuning in terms of episodic synchronization. Finally, we study the effect that a mismatch between the pump currents of the two lasers has on their synchronization in Section 4.6. For this, we simulate the system without noise and analyze the synchronization dynamics. We find that for small mismatches, synchronization is deteriorated only by intermittent desynchronization events. For large mismatches, however, overall correlation is lost and the two subsystems only rarely synchronize intermittently, if at all.

4.1.3 Contributions to the work in this chapter

A part of the results presented in this chapter has been published as "J. Tiana-Alsina, K. Hicke, X. Porte, M. C. Soriano, M. C. Torrent, J. Garcia-Ojalvo, and I. Fischer: *Zero-lag synchronization and bubbling in delay-coupled lasers*, Physical Review E **85**, 026209 (2012)".

The experiments described here were planned and prepared in collaboration with Jordi Tiana-Alsina and Xavier Porte, and executed together with Xavier Porte. The analysis of synchronization dynamics using sliding-window cross-correlation for the zero-detuning case with varying pump currents and for the experimental frequency detuning case, respectively, were done in colloboration with Jordi Tiana-Alsina.

4.2 Experimental setup

Our experimental setup is depicted in Fig. 4.1. It consists of two similar discrete mode semiconductor lasers (Eblana Photonics), operating at a nominal wavelength of $\lambda \approx 1540$ nm. The lasers are coupled symmetrically via a fiber loop. This loop serves as a semitransparent mirror, accounting for symmetric feedback and coupling. It comprises a 50/50 optical coupler, whose output arms on one side are connected, forming the loop. An optical isolator is placed in the loop to ensure a single propagation direction in the fiber loop and thus to avoid interference effects between counter-propagating waves. The two laser outputs are combined in the loop via the ingoing arms of the 50/50 optical coupler and then redistributed evenly via the same coupler upon leaving the loop. Therefore, we assume identical feedback and coupling strengths. The relay loop provides for feedback and coupling with equal delay times, if both arms of the setup (optical path between each respective laser and the main optical coupler) are of equal length. The coupling relay consequently leads to chaotic behavior in both lasers, in addition to identical synchronization of their outputs. The absence of asymmetries in the coupling provides near-optimal synchronization conditions [205] (see also Chapter 3).

We are using single-mode optical fiber (SMF) in our experiments. Since the polarization states are not maintained in these fibers and are affected by birefringence, we use polarization controllers in both arms of the setup to assure appropriate polarization and phase conditions for polarization-maintained feedback (see also model sections in Chapter 2).

By autocorrelation analysis of the intensity dynamics of both lasers in the coupled configuration, the feedback and coupling delay in our setup was determined to be $\tau = 73.125 \pm 0.025$ ns. On the one hand, the autocorrelation method does have an inherent absolute bias, depending on the operating regime [206], which may result in an offset to the determined delay times. On the other hand, determining the relative delay difference is unaffected. Hence, delay symmetry in our setup can be assumed.

The effective coupling strengths can be calculated from the losses in each component in the optical paths, the connector losses and the losses at the fiber-laser cavity coupling. With these, we estimate the coupling and feedback strengths as corresponding to $\approx 6\%$ of emitted light being coupled back into the respective laser. This relatively strong coupling ensures that we avoid the regime of transverse instability due to a blow-out bifurcation [97].

The spectral characteristics of the two lasers, i.e., their emission frequencies, are adjusted by tuning their temperature. The laser temperatures and pump currents are controlled by a Thorlabs PRO8000 laser controller with accuracies of $\Delta T = \pm 0.01$ °C and $\Delta I_p = \pm 0.01$ mA, respectively.

We measure the laser outputs by using fast Miteq DR-125G-A photodetectors with 13 GHz bandwidth, whose outputs are recorded by a LeCroy WaveMaster 816Zi oscilloscope with an analog bandwidth of 16 GHz and a sampling rate of 40 GS/s. The high time resolution enables us to resolve the fast intensity dynamics on a picosecond timescale, and allows us to observe and distinguish very short intervals of synchronization or unsychronized behavior with unprecedented detail.

4.3 Identical synchronization of two delay-coupled semiconductor lasers

In this section, we show experimentally that two semiconductor lasers, coupled with delay via a passive relay, can exhibit high-level identical chaos synchronization. We will show that the lasers synchronize identically with zero lag, i.e., that they exhibit isochronous synchronization, due to the delay symmetry of our experimental setup.

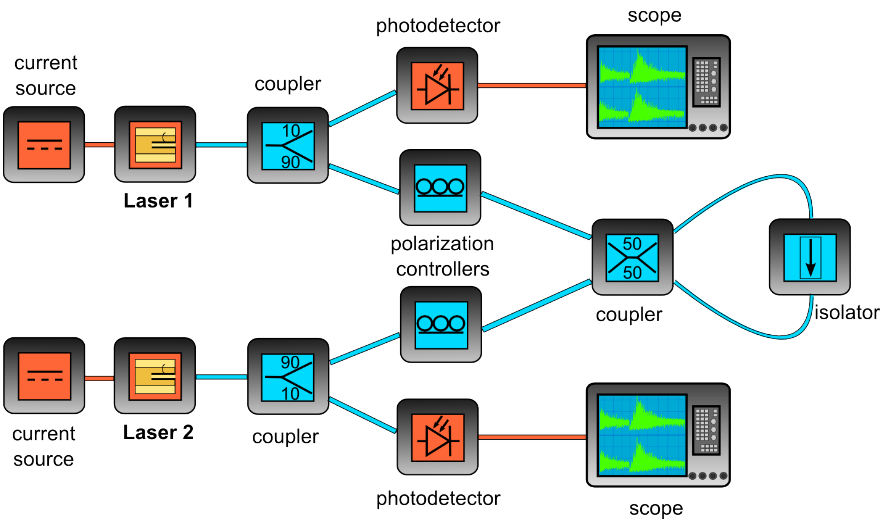

Figure 4.1: Schematic experimental setup. The lasers are symmetrically coupled with a delay via a feedback and coupling fiber loop consisting of a 50/50 optical coupler and an optical isolator. The loop serves as passive relay. The numbers in the symbols for the couplers correspond to their respective coupling ratios (in percent). The orange lines depict electrical connections, the blue ones represent single-mode optical fiber (SMF).

In order to achieve optimal synchronization conditions, we have to assure zero spectral detuning (i.e., maximum overlap of the optical spectra) by adjusting the laser temperatures accordingly. Because both lasers are very well matched in parameters, we can then neglect mismatch or detuning as the principle reason for intermittent desynchronization.
We analyze the synchronization behavior of the coupled lasers in a current range of $I_p = 12 - 17$ mA. This corresponds in our case to a value of the normalized pump current

$$p = I/I_{thr} \tag{4.1}$$

of $p = 1.04 - 1.48$, where I_{thr} is the respective solitary lasing threshold. With our setup as described in the previous section we are able to achieve high-level zero-lag synchronization, as shown in the exemplary high-resolution time traces of Fig. 4.2(a). The plot depicts near-perfect synchronization, with one distinct short desynchronization event clearly visible in the intensity difference (i.e. synchronization error) as shown in Fig. 4.2(b). We attribute this desynchronization event to the bubbling phenomenon.

In the pump current range studied here, the two laser systems may operate in two different dynamical regimes [57]: the Low-Frequency Fluctuations (LFF) regime and the fully-developed coherence collapse regime (CC).

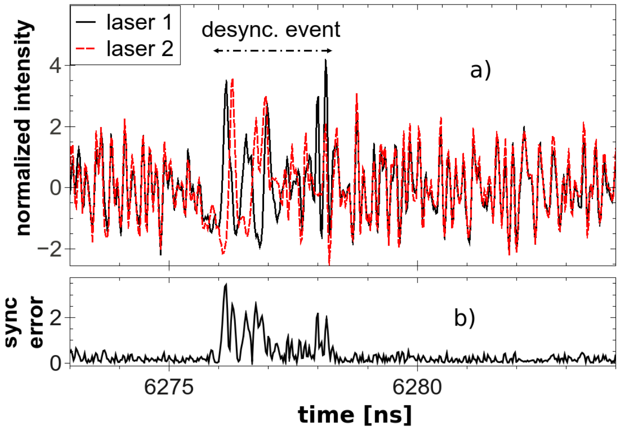

Figure 4.2: (a) Experimental time series of synchronized fast intensity dynamics in the coherence collapse regime. A short desychronization event is highlighted. The lasers are pumped with a pump current corresponding to $p = 1.25$. The intensities have been normalized by shifting the traces by their respective mean values and scaling with their standard deviations. (b) shows the corresponding synchronization error, i.e., the normalized intensity difference.

The LFF regime is characterized by a slow timescale associated with the global dynamics on the mode ellipse (see previous Chapters, especially 2). The regime manifests itself in the intensity dropouts, followed by a subsequent intensity buildup until the next dropout. During the buildup process, the laser dynamics drifts over several optical modes. This chaotic itinerancy almost monotonically tends toward higher average intensities [50]. The dropout occurs when the trajectory approaches the stable manifold of an antimode, which has the characteristics of a saddle point [55]. This antimode also corresponds to a transversely unstable mode of the laser's chaotic attractor. In contrast to the LFF regime, the global dynamics in the CC regime occurs on a faster timescale. The dynamics of the laser in the CC regime exhibits larger intensity fluctuations and more frequent critical events with transversely unstable antimodes. This results in more frequent subsequent bubbling (desynchronization) events. The dynamical characteristics of these two regimes are described in more detail in Chapter 2. Here, we compare the different synchronization dynamics in the two regimes.

We quantify the degree of zero-lag synchronization between the two lasers by using the cross-correlation coefficient at zero lag C_{corr} of two corresponding intensity time series

$$C_{\mathrm{corr}} = \frac{\langle [I_1(t) - \langle I_1 \rangle] [I_2(t) - \langle I_2 \rangle] \rangle}{\sqrt{\left\langle [I_1(t) - \langle I_1 \rangle]^2 \right\rangle \left\langle [I_2(t) - \langle I_2 \rangle]^2 \right\rangle}} \tag{4.2}$$

where $\langle \cdot \rangle$ denotes time averaging. To further account for fast dynamical fluctuations, we integrate and normalize the synchronization error $|I_1 - I_2|$ over shifting windows of one delay time τ, and calculate the mean value over all windows:

$$\chi = \frac{\langle |I_1 - I_2| \rangle}{\langle I_1 + I_2 \rangle}. \tag{4.3}$$

This definition corresponds to the normalized average synchronization error. In our numerical simulations, the denominator is calculated by averaging over the entire time series while the numerator is calculated for shifting windows of length τ and subsequently averaged. The two quantifiers C_{corr} and χ are shown in Fig. 4.3 for equally increasing applied normalized pump currents of the two lasers.

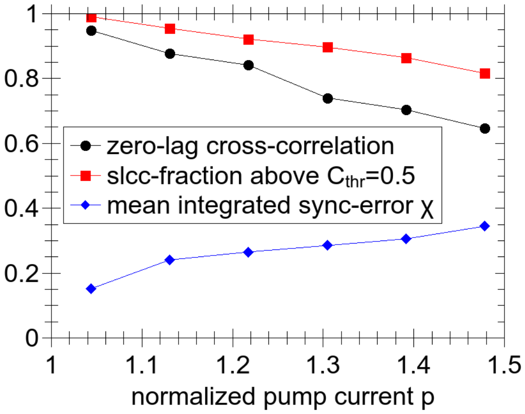

Figure 4.3: Cross-correlation coefficient at zero lag C_{corr} (black circles), fraction of the sliding-window cross-correlation above the correlation threshold of $C_{\mathrm{thr}} = 0.5$ (red squares) and mean averaged synchronization error χ (blue diamonds), respectively, versus the applied normalized pump current of both lasers.

As the currents increase, the zero-lag cross-correlation (black circles) decreases, and correspondingly the mean integrated synchronization error χ (blue diamonds) increases almost linearly.
We want to understand why the correlation (synchronization level) deteriorates with increasing pump current, and how that decrease is related to

changes in the dynamical regime (from LFF for $p \approx 1$ to coherence collapse for $p \approx 1.5$). Figure 4.2(b) shows that the instantaneous synchronization error is subject to short bursts that correspond to desynchronization events. To account for fast-timescale synchronization and desynchronization events of this kind, we additionally introduce and calculate the sliding-window cross-correlation slcc. For this, the standard cross-correlation coefficient at zero lag C_{corr} is calculated over a shifting window of 1 ns width with a step size corresponding to 0.1 ns. That way we obtain a time trace of instantaneous correlation values. A significant drop of the slcc below a correlation threshold C_{thr} implies the occurance of a desychronization event. We can then quantify the fraction of synchronized dynamics with respect to the total length of the dynamics time series. This fraction decreases with pump current, similarly to the zero-lag cross correlation, as shown in Fig. 4.3 for $C_{\text{thr}} = 0.5$.

4.4 Bubbling in different pump regimes

In this section, we investigate how intermittent loss of synchronization leads to a decrease in overall synchronization level for increasing pump current. We identify the experimentally-measured intermittent short-lived desynchronization events as manifestations of bubbling in our system. Here, we investigate the bubbling characteristics in dependence on the pump currents and therefore on the dynamical regime - LFF and CC.

As it is unrealistic to calculate transverse stability in terms of the maximum transverse Lyapunov exponents from experimental data, we can not prove that the intermittent desynchronization events we measure in our experiments are manifestations of bubbling, rather than of on-off-intermittency. There are, however, indications that we indeed observe bubbling and not on-off-intermittency, apart from the fact, that the effective coupling strength in our experiments is quite large, which should provide for a transversely stable synchronization manifold. We will present these indications during the discussion of our experimental results in the following subsection.

4.4.1 Synchronization degradation due to bubbling

In the LFF regime, intensity dropouts that occur simultaneously in both lasers can be interpreted as deterministically-induced events. The issue of deterministic dropout events and noise-driven ones is investigated in detail in Chapter 5. In some cases, noise can lead to a dropout in only one laser, therefore resulting in the loss of synchronization. In these cases, the other laser is usually affected by the dropout after one coupling delay τ, subsequently undergoing a power dropout itself. After this second dropout, the lasers can, and usually will, resynchronize. [23].

Fig. 4.4(a) depicts output intensity time traces of both lasers in the LFF regime that include a few desynchronization events as marked by a large drop in the corresponding sliding-window cross-correlation (slcc) time series shown in Fig. 4.4(c). Fig. 4.4(b) and (d) show a magnified view on one of the bubbling events in the intensity and the slcc time series, respectively.

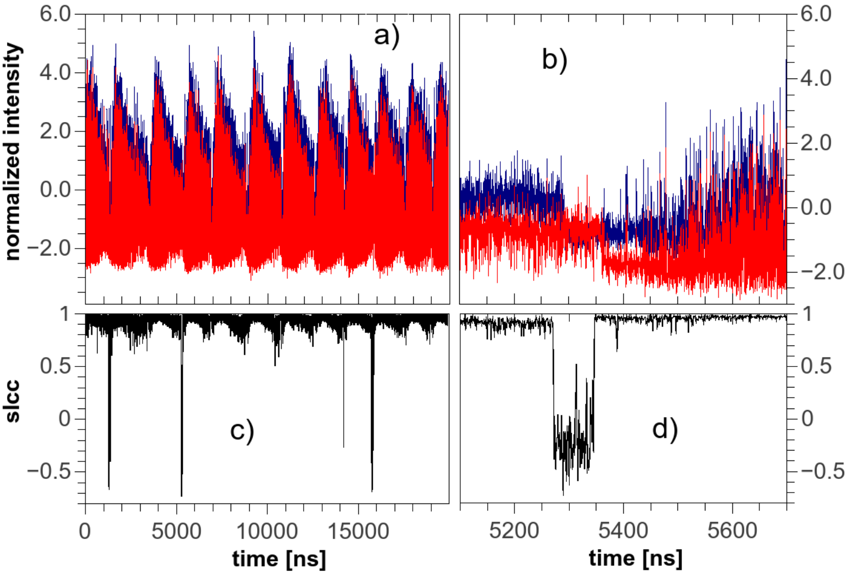

Figure 4.4: Zero-lag synchronization of experimentally-obtained LFF dynamics. Output intensity time series of the two lasers (a,b) and corresponding sliding cross-correlation (c,d) for a long time interval of 20 μs (a,c) and a magnification in time (b,d). The time series depicted in red was vertically shifted for better visibility. The applied pump current in this case corresponds to $p = 1.04$, being close to the solitary lasing thresholds. The intensities are normalized by shifting their mean values to zero and scaling them by their standard deviations.

The figure shows that the desynchronization events in the LFF regime coincide with intensity dropouts at the end of each LFF cycle, in agreement with previous numerical results [97, 161]. The desynchronization events begin when the trajectory approach a transversely unstable antimode. As mentioned above, the dropouts of both lasers usually occur with a relative time shift of τ, resulting in desynchronization (bubbling) events of that length (Fig. 4.4(d). Between the desynchronization events, the dynamics of both lasers are well-synchronized with slcc-values of 0.95 or higher in our experiments.

This experimentally-obtained desynchronization characteristic is evidence for the onset of bubbling in this configuration. The fact that desynchronization events are connected to the power dropouts implies that desynchronization is restricted to a certain region of the chaotic attractor of this system. This corresponds well to model predictions for bubbling [97, 98]. Flunkert [98] found, that desynchronization in the LFF regime occurs mainly for larger carrier numbers. This corresponds to dynamics around external cavity modes in the vicinity of the solitary laser mode, which have been transversely destabilized by the bubbling bifurcation. The lasers remain unsynchronized while their trajectory is close to these transversely unstable periodic orbits. The compliance of this localization of desynchronization events in the attractor with theoretical predictions [97, 98] serves as indication for the occurrence of bubbling instead of on-off-itermittency. In case of the latter, the entire synchronization manifold is transversely unstable, and intermittent desynchronization can take place over larger parts of the attractor.

In the case of fully-developed coherence collapse (CC), which arises for larger pump currents, the synchronization dynamics is very different. This is due to the fact that the overall dynamics differs substantially from the LFF behavior. In particular, there exists no slow time scale comparable to the one associated with the power dropouts in the LFF regime. Evidence for this is also the lack of significant low-frequency components in the rf-spectra of the CC-dynamics, in contrast to the LFF dynamics (not shown). Concurrently, the ejections of the trajectory due to unstable antimodes are more frequent and much shorter than in the LFF case. The duration of the desynchronization events is of the order of 1 ns. Fig. 4.5(a) shows synchronized intensity time traces in the CC exhibiting short desynchronization events with high frequency of occurrence emphasized by drops in the corresponding slcc time trace (Fig. 4.5(c)).

The desynchronization events are linked to the phase space ejections of the trajectory, and thus, have a comparable duration and the same frequency (Fig. 4.5(c,d)). After a critical event with a transversely unstable antimode, the dynamics rapidly intinerates through unstable modes until resynchronization occurs. For the case of CC, the restriction of desynchronization to a certain attractor region is not as clear as for the case of LFF dynamics. Nevertheless, the correspondence of the synchronization characteristics we found in our experiments with theoretical predictions make it plausible to assume that the measured desynchronization events in the CC regime are manifestations of bubbling and not on-off-intermittency too. It is, however, important to note, that increasing the pump current of a laser with feedback can result in the transition of the dynamics from weakly to strongly chaotic [207]. This corresponds to a transverse destabilization of the entire synchronization manifold.

The intervals of synchronized dynamics exhibit a high correlation with values of SLCC around 0.95, as is observed for the LFF regime. The high temporal resolution of the measurements and the comparably short window size for the slcc calculation allow us to resolve the fast synchronization dynamics

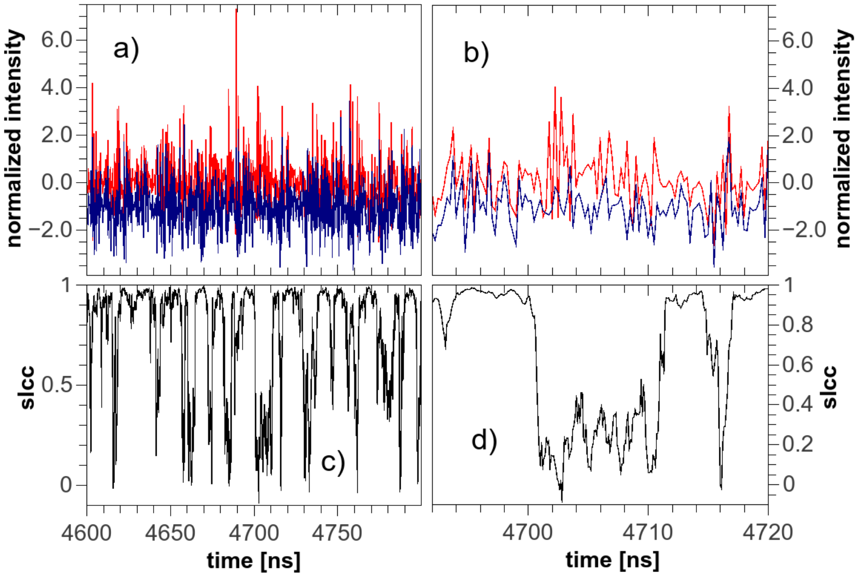

Figure 4.5: Synchronization of laser outputs in the CC regime. Normalized output intensity time series of the two lasers (a,b) and corresponding sliding cross-correlation (c,d) for a time interval of 200 ns (a,c) and a magnification in time (b,d). The blue intensity time series was vertically shifted for better visibility. The applied pump current in this case corresponds to $p = 1.39$. The normalization was done corresponding to Fig. 4.4.

with good accuracy (Fig. 4.5(b,d)).
The results shown in Figs. 4.4 and 4.5 allow us to infer that the overall deterioration of synchronization that is observed with increasing pump current (Fig. 4.3) is due to an increase in the frequency of occurrence of bubbling events. This deduction is seen as valid mainly due to the fact that the maximum value of the slcc, which measures the instantaneous correlation during synchronized time intervals, does not change much with increasing current.

We quantify the issue of the average slcc-value during intervals of synchronization in Fig. 4.6, which shows the normalized slcc distribution for six values of the normalized pump current. The normalization is done such that the integral over all 401 bins equals 1.

The histograms group into two qualitatively different sets. The distributions in the first group correspond to lower pump currents and the LFF regime ($p = 1.04$ and $p = 1.13$) and have bimodal characteristics. For the cases of higher currents and correspondingly the CC regime, the distributions are characterized by a single, broad and asymmetric peak.

The lower peaks in the slcc distributions for the two LFF-cases are dips

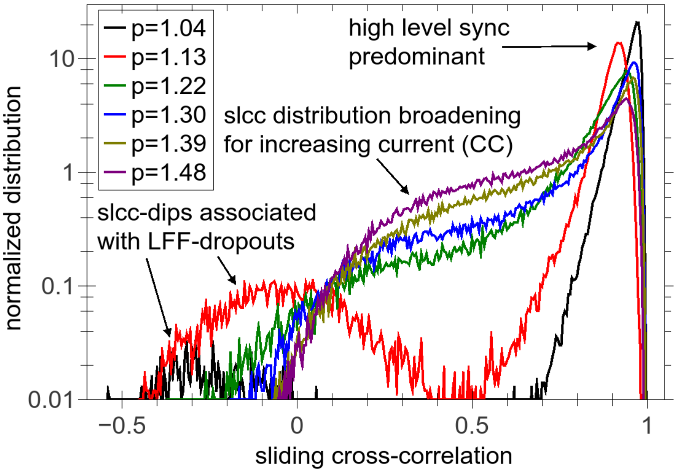

Figure 4.6: Normalized distributions of the sliding cross-correlation (slcc) for 6 different pump currents (see legend). The histograms have 401 bins. Note the log-scale.

to negative correlation that occur at the LFF-power dropouts. As for the coherence collapse regime, although the distributions broaden significantly with increasing current, they nevertheless clearly have their maximum peak at a correlation close to 1. Consequently, we conclude that intervals of high-level synchronization still occur even for large pump currents; a global decrease in synchronization would shift the distribution maxima in Fig. 4.6 toward lower correlation values. This conclusion is supported by calculating the fraction of time during which synchronized dynamics persists, as depicted by the red squares in Fig. 4.3. We choose $C_{\mathrm{thr}} = 0.5$ as synchronization threshold for the slcc, guided by the bimodal LFF distributions of Fig. 4.6. Even though this value is chosen arbitrarily, a different threshold changes the slope of the curve slightly, but the overall monotonic behavior persists. In view of the slcc-dips due to desynchronization in the CC regime as shown in Fig. 4.5(c), the choice of $C_{\mathrm{thr}} = 0.5$ can be considered appropriate for the coherence collapse as well.

4.4.2 Bubbling event statistics for different pump currents

Since the correlation level within the synchronized intervals does not diminish with the pump current, but the overall correlation does (see black circles in Fig. 4.3), the bubbling events must necessarily become either longer or more frequent as the dynamics transitions from the LFF to the coherence collapse. The increased desynchronization frequency can already be inferred from a comparison between Figs. 4.4(c) and 4.5(c). To gain more insight,

we follow a systematic approach.
To that end, we statistically quantify the duration of bubbling events and the inter-event intervals (IEI) between subsequent events by using the current slcc values. We consider the current dynamics of the coupled lasers to exhibit bubbling, if the current slcc value decreases below $C_{\mathrm{thr}} = 0.5$. We also introduce a threshold for a minimum duration for a bubbling event $\Delta T_{\mathrm{thr}} = 0.5$ ns, and a minimum inter-event interval $\mathrm{IEI}_{\mathrm{thr}} = 0.5$ ns below which two separate desychronization events are considered as part of a single, longer one.

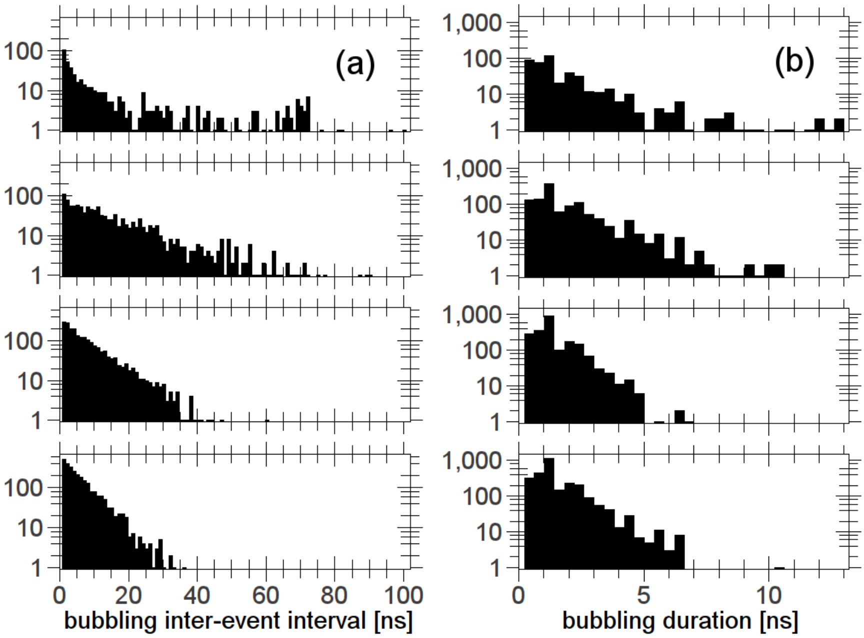

Figure 4.7: Histograms of the bubbling inter-event intervals (IEI) (a) and of the bubbling event duration (b) for pump currents $p = 1.22$, $p = 1.30$, $p = 1.39$ and $p = 1.48$ (from top to bottom). The IEI-histograms have 100 bins each, the histograms for the bubbling duration have 32 bins of width 0.4 ns. Note the log-scales.

Figure 4.7(a) shows the IEI-histograms for the cases corresponding to the coherence collapse, i.e., for the normalized pump currents $p = 1.22$, $p = 1.30$, $p = 1.39$, $p = 1.48$, Fig. 4.7(b) depicts the bubbling duration distributions for the same cases. Applying smaller pump currents with $p = 1.04$ and $p = 1.13$ results in LFF dynamics, and only 7 and 20 events are captured, respectively. These are mostly long events with a duration of the order of τ which are widely spaced, reflecting the underlying mechanism that induces them (see previous subsection).

The IEI are of the order of microseconds in these cases. Therefore, we present only histograms for the characteristic lengths of bubbling in the CC regime.

The IEI distributions shown in Fig. 4.7(a) reveal, that bubbling events become more closely spaced, i.e., become more frequent, (the distribution decays faster to 0) with increasing current. Isolated events (with a large value of the IEI) become continously scarcer with increasing p. The bubbling durations (Fig. 4.7(b)) are not much affected by a change in current. Nevertheless, for increasing pump current, fewer of the longer desynchronization events are captured. The enhancement of a bubbling duration of 1 ns can be considered a numerical artifact, caused by the choice of a window size of 1 ns for the computation of the slcc.

In this section, we have been able to explain the degradation of the overall correlation of dynamics in an experimental system of two bidirectionally relay-coupled lasers with increasing pump current with increasingly frequent occurring desynchronization events. We have found evidence that these events are bubbling events, by connecting their occurrence with the overall dynamics in the corresponding dynamical regimes.

4.5 Detuning-induced intermittent desynchronization

In this section, we study the effect of frequency detuning between two similar and symmetrically-coupled semiconductor lasers on their synchronization characteristics from an event-based perspective. We again consider a symmetric configuration where coupling and feedback are provided via a passive relay. Like in the previous section, we connect changes in the overall correlation levels with varying detuning with the occurrence of intermittent desynchronization events with varying frequency of occurrence. Following the approach in Section 3.6, the desynchronized episodes are interpreted in view of the concept of episodic synchronization, as introduced in [183].

The section is structured in two parts: in the first we analyze data obtained from experiments, and in the second one we consider numerical simulations. The latter allows us to access a case without laser-intrinsic noise and without any mismatches, which is not possible in the experiments.

4.5.1 Experimental work

For our experimental work, we use the same setup as depicted in Fig. 4.1. By varying the temperature of one of the lasers and leaving the other one fixed, we accomplish (asymmetric) spectral detuning of the two lasers. Because desynchronization events are more unique in the LFF regime, we pump both lasers close to threshold at $p = 1.04$ for our detuning investigation. We can then more easily observe alterations to the desynchronization characteristics with respect to the undetuned case, than if we considered fully-developed CC-dynamics.

Similar to Section 4.4, we calculate several overall measures to characterize the synchronization level in dependence on the detuning $\Delta\Omega$. These quantifyers are depicted in Fig. 4.8. They are the cross-correlation at zero-lag (black circles), the fraction of the slcc above a correlation threshold of $C_{\text{thr}} = 0.5$ (red squares) and the mean integrated synchronization error χ (blue diamonds), calculated according to Eq. (4.3). The slcc is calculated, like in the previous section, for a shifting window of length 1 ns with a step size of 0.1 ns.

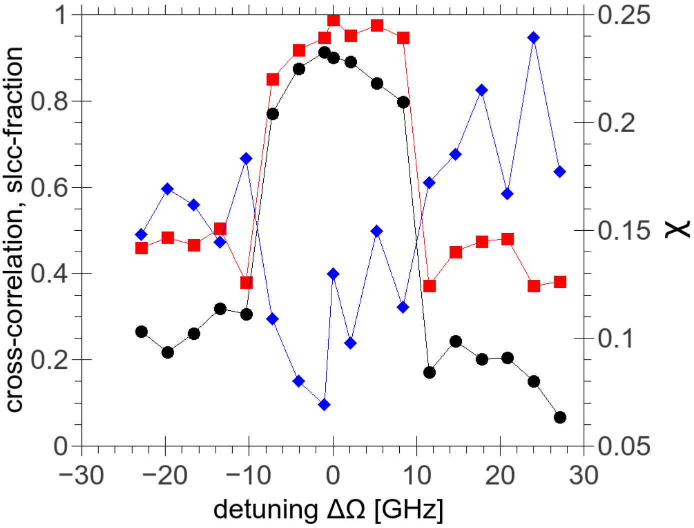

Figure 4.8: Crosscorrelation coefficient at zero lag (black circles), fraction of the sliding-window cross-correlation above the correlation threshold of $C_{\text{thr}} = 0.5$ (red squares) and mean integrated synchronization error χ (blue diamonds), respectively, versus the applied frequency detuning of both lasers $\Delta\Omega$.

One notices immediately the central (around $\Delta\Omega = 0$) detuning range, which is characterized by high correlation values and a rapid drop in correlation. This range also features a large fraction of the slcc above the synchronization threshold and comparably low mean integrated synchronization errors. Because of the dramatic decrease of the correlation measures at the edges of this detuning interval, we identify it with the locking range, although spectral properties are not recorded in these experiments. However, locking is a necessary condition for identical synchronization, so we attribute the sudden significant drop in correlation, and thus the loss of synchroniza-

tion to unlocking of both lasers. The features shown in Fig. 4.8 serve as indications that the detuning range with highly-correlated dynamics is approximately congruent with the locking range.
If we look at the slcc-dynamics for different detunings (see Fig. 4.9), we see that the low-frequency structure of the dropout-related correlation dips is retained for detuning-values inside the high-correlation range (Fig. 4.9(a-d)). This is due to the persistence of LFF dynamics for these detuning values (not shown). Fig. 4.10 shows a magnification of one slcc-trace around one of the power dropouts and the corresponding dynamics of both lasers. For increasing detuning, the correlation fluctuates towards the dropout but retains a high-valued maximum.

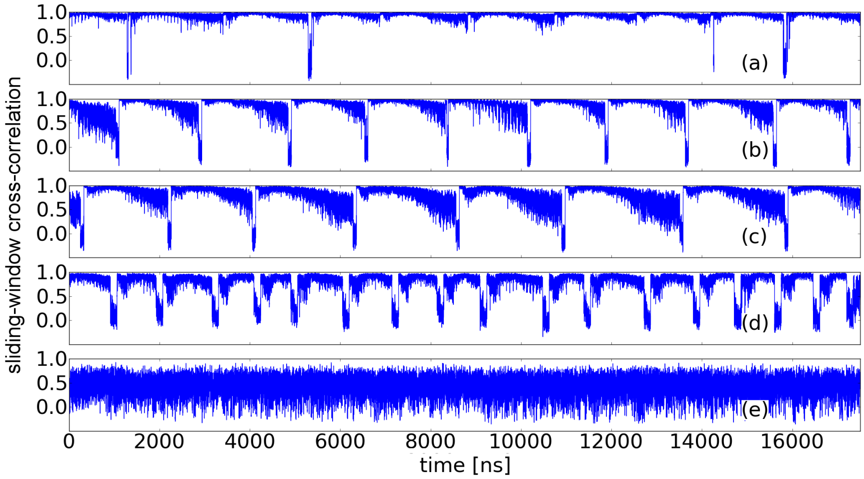

Figure 4.9: Exemplary time series of the sliding-window cross-correlation (slcc) for five experimentally-obtained pairs of intensity time series, corresponding to five different detuning values: (a) $\Delta\Omega = 0$ GHz, (b) $\Delta\Omega = -1.0$ GHz, (c) $\Delta\Omega = -4.1$ GHz, (d) $\Delta\Omega = -7.2$ GHz, (e) $\Delta\Omega = -10.4$ GHz.

Apart from synchronization dynamics, the detuning clearly has a significant effect on the dynamics of the lasers. The LFF-cycles tend to shorten with increasing absolute detuning, as is clear from the increased frequency of dropouts. This can be understood as follows: as the absolute detuning increases, the overlap of the broadened optical spectra of both lasers diminishes. The laser with the higher solitary lasing frequency - the (un)detuned one for negative (positive) detuning - exhibits the power dropout first, the lasers desynchronize. The dropout signal is fed into the other laser with a delay τ and induces a dropout in the second laser. The lasers then resynchronize (relock) close to the high-frequency limit of the spectral overlap of both lasers. Since the overlap is decreased by detuning, the dropouts are

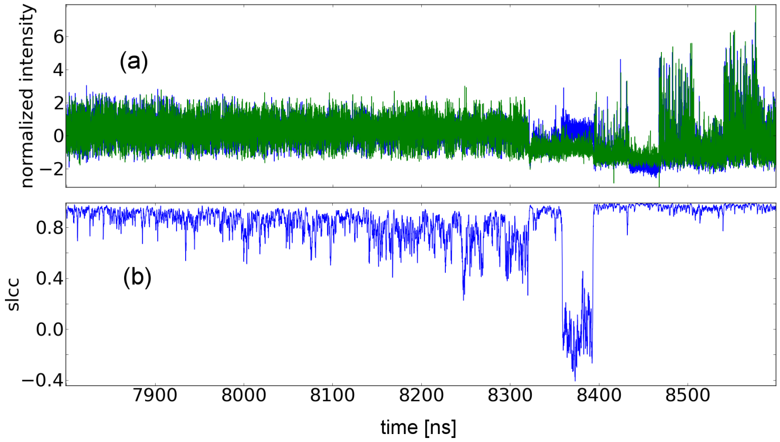

Figure 4.10: (a) Magnified view on experimental intensity timeseries of both lasers [corresponding to Fig. 4.9(b)] with detuning $\Delta\Omega = -1$ GHz. (b) depicts the corresponding sliding cross-correlation trace.

thus more closely spaced.

Reversing the sign of the frequency detuning results in the reversal of the order of which laser experiences a dropout first. The mechanism underlying the desynchronization and resynchronization of detuned identical lasers is explained in further detail in Section 3.6. There, we show numerically that the shared optical bandwidth is reduced by the detuning. In the LFF regime, this results in shorter dynamical cycles, i.e., more frequent dropouts. If the frequency detuning is too large, the overlap vanishes completely and even short episodes of synchronization, quantified by high instantaneous correlation values (slcc), no longer occur. This is exemplified by the intermediate correlation values centered around 0.5 shown in the slcc-timeseries in Fig. 4.9(e).

The loss of high-correlation synchronization is confirmed by an investigation of the slcc-distributions for various detunings, as is shown in Fig. 4.11. For detuning values of $\Delta\Omega \in [-7.2, +8.4]$ GHz, which correspond to regimes inside the range of high correlation, the maximum peak is close to one, signifying the predominance of high-level zero-lag synchronization. For an (absolute) increasing detuning, the peak broadens but the maximum remains close to 1.0. The broadening corresponds to fast correlation fluctuations as the dynamics approach the power dropout (see e.g. Fig. 4.9(b,c)). Once the lasers are detuned beyond the locking range, the slcc distributions completely lack a high correlation component. They are very broad single-peak distributions which center around the intermediate correlation value of slcc ≈ 0.5.

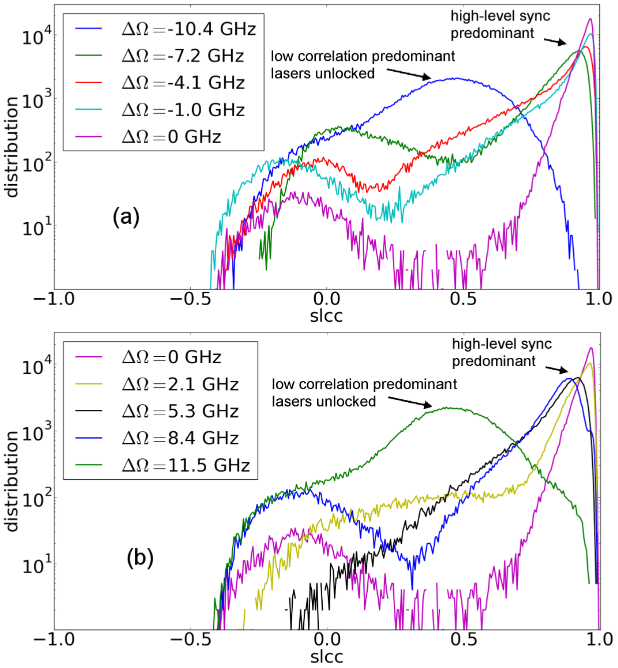

Figure 4.11: Normalized distributions of the sliding cross-correlation (slcc) for different negative values of the detuning (a) and for positive detuning (b). The distribution for zero detuning is depicted in purple in both diagrams. The histograms have 401 bins. Note the log-scale.

We now perform the same statistical analysis of the durations and inter-event intervals (IEI) of the detected desynchronization events, as in Section 4.5.1. Since we want to analyze intermittent unsynchronized episodes, we naturally limit our investigation to the range of high correlation. Beyond that range, synchronization is lost. For best comparability with the previous section, we employ the same threshold values to capture desynchronization events as before for the bubbling events: only events with a minimum duration of $\Delta T_{\text{thr}} = 0.5$ ns, a slcc-dip below the threshold $C_{\text{thr}} = 0.5$ and an inter-event interval greater than $\text{IEI}_{\text{thr}} = 0.5$ are considered.

The resulting distributions of IEI and desynchronization episode duration for the dynamics measured within the high correlation range are depicted in Fig. 4.12 for the desynchronization durations and in Fig. 4.13 for the inter-event intervals.

Figs. 4.12(e) and 4.13(e) correspond to the zero detuning case. In this case, only few desychronization events are captured. This corresponds to the regime with $p = 1.04$, which we investigated in terms of noise-induced bub-

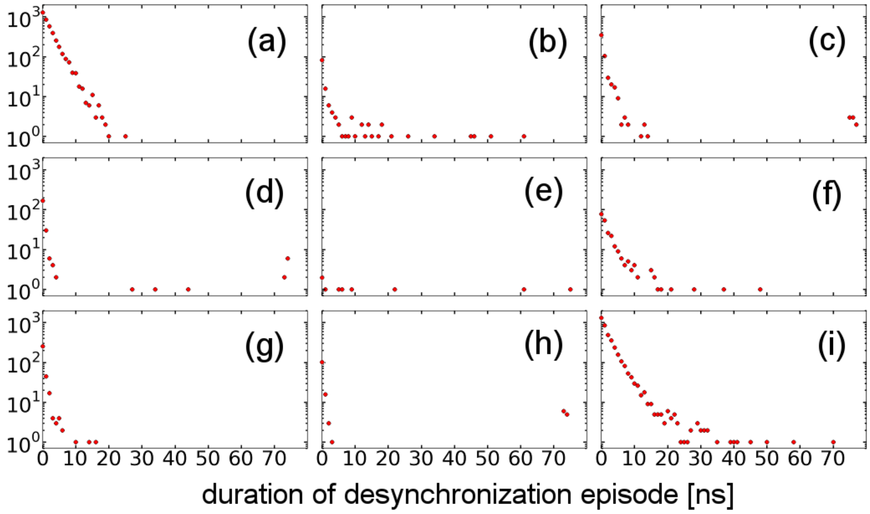

Figure 4.12: Distribution of duration of detected episodes of unsynchronized dynamics derived from experimental time traces for different detunings $\Delta\Omega$. (a) $\Delta\Omega = -10.4$ GHz, (b) $\Delta\Omega = -7.3$ GHz, (c) $\Delta\Omega = -4.1$ GHz, (d) $\Delta\Omega = -1.0$ GHz, (e) $\Delta\Omega = 0$ GHz, (f) $\Delta\Omega = 2.1$ GHz, (g) $\Delta\Omega = 5.3$ GHz, (h) $\Delta\Omega = 8.4$ GHz, (i) $\Delta\Omega = 11.5$ GHz. The detection thresholds for the events are $T_{\mathrm{thr}} = 0.5$ ns, $C_{\mathrm{thr}} = 0.5$, $\mathrm{IEI}_{\mathrm{thr}} = 0.5$ ns.

bling in the previous section. As the absolute detuning increases, more and more events are detected, with the IEI distributions showing long tails (Figs. 4.13(b,c,d,f,g,h)). The longer inter-event intervals roughly correspond to the time separation between dropouts. The majority of detected desynchronization intervals are short and closely spaced. These are measured because of the significant correlation fluctuations in the slcc when the dynamics approach a dropout in one of the lasers (see Fig. 4.9(b,c)).

The long events with a duration of ≈ 73 ns (Fig. 4.12(c,d,e,h)) correspond to desynchronization at the dropout of one of the lasers and subsequent resynchronization after the delay time $\tau = 73.1$ ns. That this characteristic desynchronization time is not prevalent for all dynamics time series measured within the locking range, stems from the fact that the slcc fluctuations mask the longer desynchronization. Statistical fluctuations of this instantaneous crosscorrelation traverse the chosen synchronization threshold of $C_{\mathrm{thr}} = 0.5$ from both directions and thus result in the detection of many short pseudo-separate events. The slcc exhibits these fast fluctuations because we choose a relatively short time interval of length 1 ns to calculate the slcc, which is necessary to capture fast-occurring real desynchronization episodes.

Beyond the limits of the detuning range exhibiting high correlation val-

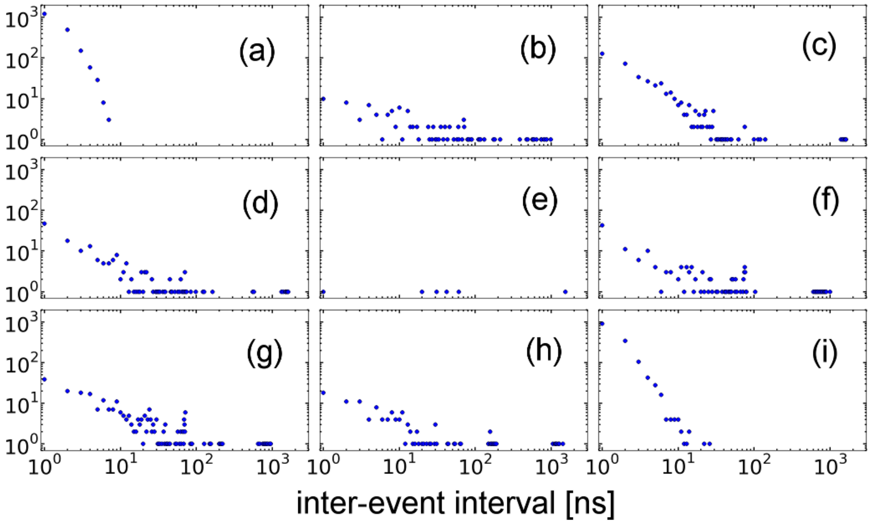

Figure 4.13: Distribution of inter-event intervals of desynchronization episodes determined from experimentally-obtained time series for different detunings $\Delta\Omega$. (a) $\Delta\Omega = -10.4$ GHz, (b) $\Delta\Omega = -7.3$ GHz, (c) $\Delta\Omega = -4.1$ GHz, (d) $\Delta\Omega = -1.0$ GHz, (e) $\Delta\Omega = 0$ GHz, (f) $\Delta\Omega = 2.1$ GHz, (g) $\Delta\Omega = 5.3$ GHz, (h) $\Delta\Omega = 8.4$ GHz, (i) $\Delta\Omega = 11.5$ GHz. The detection thresholds for the events are $T_{\text{thr}} = 0.5$ ns, $C_{\text{thr}} = 0.5$, $\text{IEI}_{\text{thr}} = 0.5$ ns.

ues, the dynamics of both lasers are largely desynchronized, leading to a broad distribution of desynchronization lengths (Fig. 4.12(a,i)) and many very short average inter-event intervals (Figs. 4.13(a,i). Again, this is due to the chosen detection thresholds for desynchronization events. As the slcc fluctuates around 0.5, many pseudo-events are detected, even though the dynamics are unsynchronized and only exhibit statistically-distributed short-time correlation peaks.

4.5.2 Numerical modeling of the noiseless system

In this subsection, we consider the same configuration as in the experiments, whose results are discussed in the previous subsection. We numerically simulate the described coupled laser system without spontaneous emission noise, making use of the rate equation model introduced in Chapter 2.

This way, we want to gain further insight into the characteristics of detuning-induced desynchronization without having to consider the effect of system-intrinsic noise. In experimental systems, noise is always prevalent; we discussed in Section 4.4 how noise leads to desynchronization due to bubbling. Here, we want to attain a refined perspective on the synchronization

Parameter	Value
α	3.0
γ	200 ns^{-1}
γ_e	1 ns^{-1}
β	0
κ_{fb}	20 ns^{-1}
κ_c	20 ns^{-1}
τ	10 ns
g	10^{-5} ns^{-1}
ϵ	0
n_T	$1.8 \cdot 10^8$
$I_{1,2}$	$1.01 I_{\text{thr}}$

Table 4.1: Laser parameter values used in the numerical simulations.

dynamics in the bidirectional coupling setup with frequency detuning, by excluding noise as a source for desynchronization and only considering the effect of detuning.

To describe our system we use the coupled rate equations model as introduced in Section 3.6. In order to limit our investigation to effects of detuning on synchronization characteristics and synchronized dynamics, we assume identical laser parameters and full symmetry of the delays and the coupling and feedback strengths. We neglect the Langevin noise terms ($\beta = 0$) and add a detuning term [193] for asymmetric frequency detuning:

$$\dot{\mathcal{E}}_1(t) = \frac{1}{2}(1+i\alpha)\left(\mathcal{G}_1 - \gamma\right)\mathcal{E}_1(t) + \kappa_{\text{fb}}\mathcal{E}_1(t-\tau) + \kappa_c\mathcal{E}_2(t-\tau) \tag{4.4}$$

$$\dot{\mathcal{E}}_2(t) = \frac{1}{2}(1+i\alpha)\left(\mathcal{G}_2 - \gamma\right)\mathcal{E}_2(t) + \kappa_{\text{fb}}\mathcal{E}_2(t-\tau) + \kappa_c\mathcal{E}_1(t-\tau) + i\Delta\mathcal{E}_2 \tag{4.5}$$

$$\dot{n}_1(t) = \frac{I_1}{e} - \gamma_e n_1(t) - \mathcal{G}_1\left|\mathcal{E}_1(t)\right|^2, \tag{4.6}$$

$$\dot{n}_2(t) = \frac{I_2}{e} - \gamma_e n_2(t) - \mathcal{G}_2\left|\mathcal{E}_2(t)\right|^2, \tag{4.7}$$

where $\Delta = 2\pi\Delta\Omega$ is the angular frequency detuning between the two lasers and $\mathcal{G}_{1,2} = g\frac{n_{1,2}-n_T}{1+\epsilon|\mathcal{E}_{1,2}(t)|^2}$ are the gain functions, following the definitions in Chapter 2. Because of the long delays, we neglect the coupling and feedback phase offsets. The parameter values are listed in Table 4.1. The equations are solved numerically using Milshtein's method [208, 209] with a stepsize corresponding to $0.1\gamma^{-1}$.

As for the experimental case, we calculate overall measures to characterize the synchronization level in dependence of the detuning. The crosscorrelation at zero-lag (black circles), the fraction of the slcc above a correlation

threshold of $C_{\mathrm{thr}} = 0.5$ (red squares) and the mean integrated synchronization error χ (blue diamonds) are depicted in Fig. 4.14.
The central detuning range exhibiting high correlation values is not as distinct as in the experiments, as the zero-lag cross-correlation decreases more gradually with increasing absolute detuning. There is no sudden dramatic decrease in correlation when the detuning exceeds a certain value. Nevertheless, larger zero-lag correlation values and larger slcc-fractions above $C_{\mathrm{thr}} = 0.5$ of $\gtrapprox 0.9$, respectively, are restricted to absolute detunings of $|\Delta\Omega| \lessapprox 5$ GHz. The mean integrated synchronizaion error χ exhibits a steep incline with increasing absolute detuning and a saturation for large detunings, i.e., for unlocked operation of the two lasers.

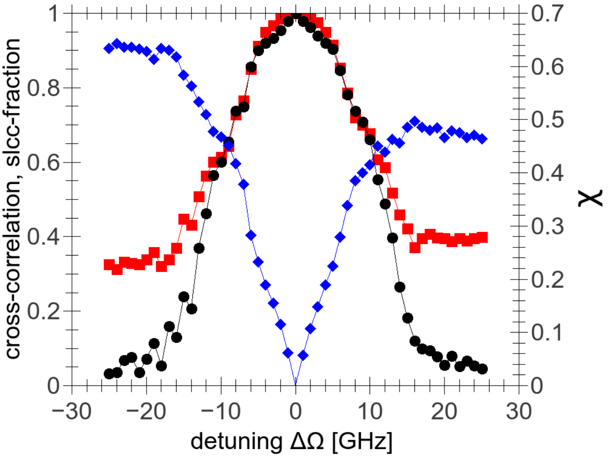

Figure 4.14: Cross-correlation coefficient at zero lag (black circles), fraction of the sliding-window cross-correlation above the correlation threshold of $C_{\mathrm{thr}} = 0.5$ (red squares) and mean integrated synchronization error χ (blue diamonds), respectively, versus the applied spectral detuning of both lasers. The simulation parameters are given in Table 4.1.

To observe the effects of the detuning on the dynamics and on the synchronization dynamics, we study the timetraces of the sliding-window cross-correlation for several increasing detuning values. Since the simulated system is noiseless and fully symmetric, the dynamics are completely identical for zero detuning. Therefore we present only traces with $|\Delta\Omega| > 0$. Four slcc-timetraces for positive detuning are shown in Fig. 4.15.

Similar to the experimental case, we notice an apparent overall shortening of the LFF dynamical cycles with increasing $\Delta\Omega$. The concurrent higher dropout-frequency leads to more desynchronization events that cluster around the time of the dropout in agreement with the experimental results presented in the previous section. Fig. 4.16 shows magnified views

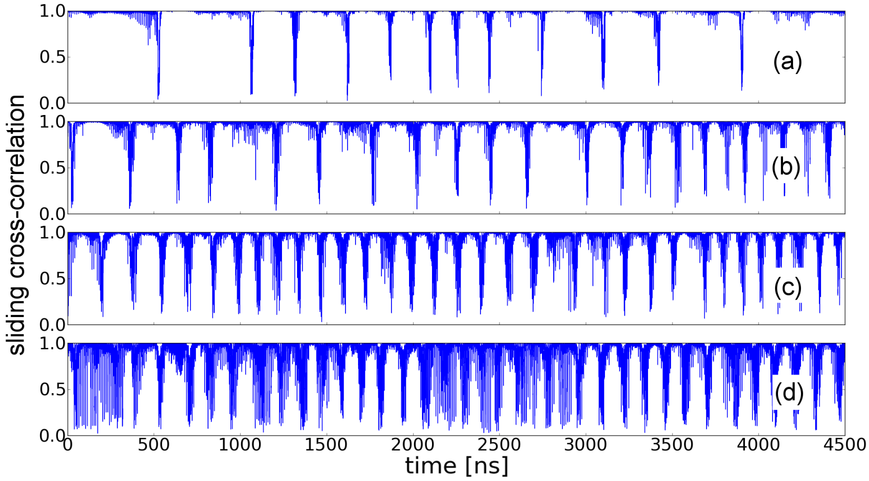

Figure 4.15: Exemplary time series of the sliding-window cross-correlation (slcc) for four numerically-obtained pairs of intensity time series, corresponding to four different detuning values: (a) $\Delta\Omega = 1$ GHz, (b) $\Delta\Omega = 2$ GHz, (c) $\Delta\Omega = 3$ GHz and (d) $\Delta\Omega = 4$ GHz. The other parameters are given in Table 4.1.

of individual desynchronization structures in the slcc-time series depicted in Fig. 4.15 and the corresponding intensity dynamics of both lasers.

We understand the intervals of strongly fluctuating instantaneous correlation around the power dropouts as episodes of unsynchronized dynamics. The duration of these episodes increases with increasing detuning, in agreement with the concept of episodic synchronization: The more the lasers are detuned, the longer are the intervals where each laser exhibits dynamics outside the spectral overlap of both lasers, and thus the longer are the times of unsynchronized behavior. The fluctuations of the slcc within these episodes can be understood as well. The slcc is computed for 1 ns windows, which in our numerical study corresponds to 200 points. Thus, coincidental higher correlation values are statistically bound to occur. These intermittent large instantaneous correlations do not imply resynchronization.
The slow gradual decrease in overall correlation and in synchronized fraction of the dynamics can be attributed to the increase in occurrence of unsynchronized episodes associated with the dropouts and to their increasing duration with increasing detuning.

A statistical investigation of the characteristics of the desychronization episodes reveals the expected results: for small detuning we observe few and short desynchronization episodes, with the duration usually limited by the delay time $\tau = 10$ ns. As the detuning increases, more events are captured

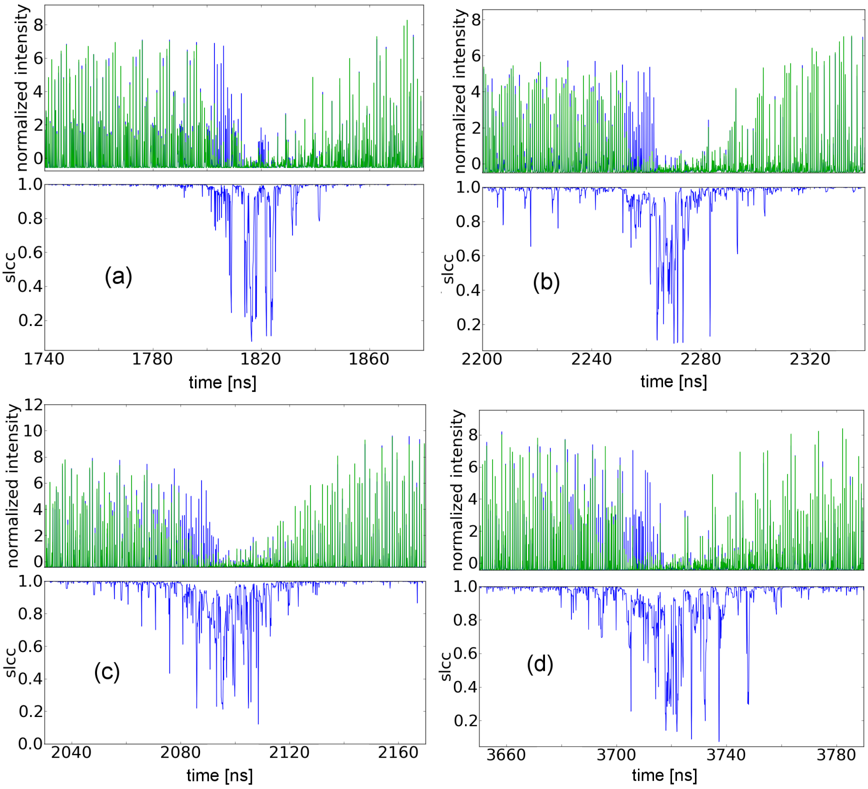

Figure 4.16: Magnified view of simulated intensity timeseries of both lasers (upper panels) [corresponding to Fig. 4.15] and the corresponding slcc (lower panels). (a) $\Delta\Omega = 1$ GHz, (b) $\Delta\Omega = 2$ GHz, (c) $\Delta\Omega = 3$ GHz and (d) $\Delta\Omega = 4$ GHz. The other parameters are given in Table 4.1.

and they become shorter on average. As the lasers are detuned, such that locking only occurs intermittently, long intervals of desynchronization are observed. For very large detunings, the distributions of the duration of the unsynchronized episodes are extremely broad and reflect complete loss of synchronization.

The desynchronization interval distributions for $\Delta\Omega = -20, -14, -11 - 6, -2, -1, 1, 2, 6, 11, 14, 20$ GHz are depicted in Fig. 4.17 (upper panel). The distributions for the inter-event interval lengths are shown in Fig. 4.17 (lower panel). They exhibit concurrent behavior: long distances between desynchronization events for smaller detuning, as expressed by the long tails in the IEI-distributions, and an increasing percentage of narrowly spaced bubbling events with increasing absolute detuning. For increasing but still interme-

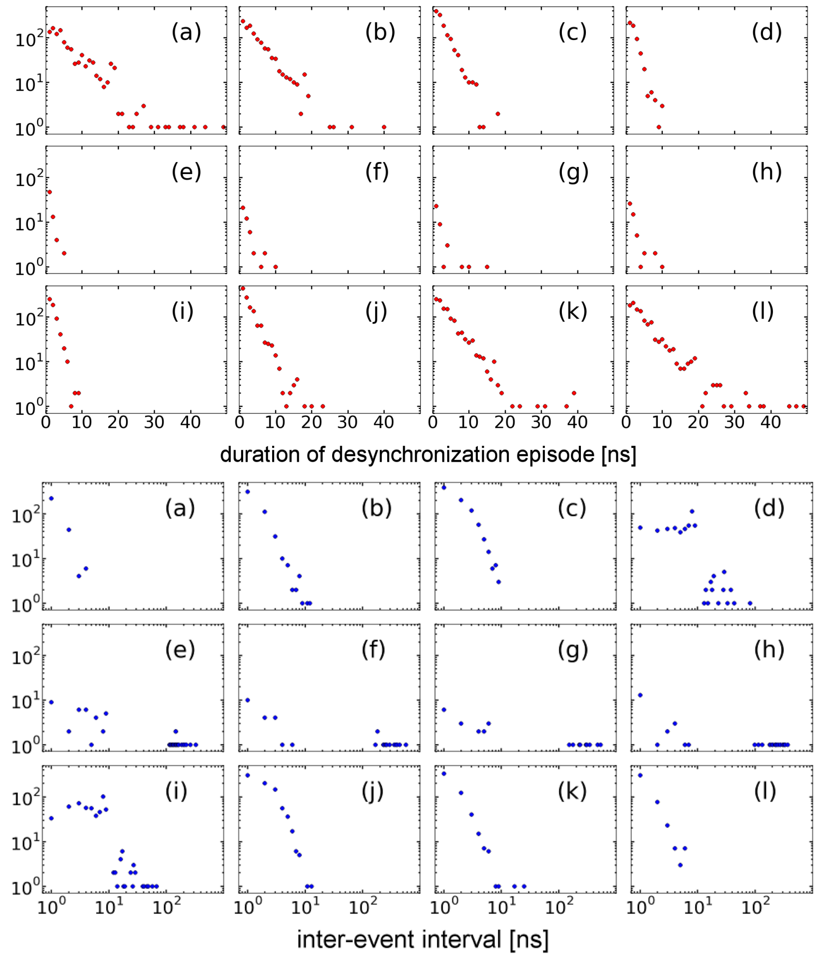

Figure 4.17: Distributions of duration of unsynchronized episodes (upper panel, red points) and of their inter-event intervals (IEI) (lower panel, blue points), respectively, for different detunings $\Delta\Omega$. (a) $\Delta\Omega = -20$ GHz, (b) $\Delta\Omega = -14$ GHz, (c) $\Delta\Omega = -11$ GHz, (d) $\Delta\Omega = -6$ GHz, (e) $\Delta\Omega = -2$ GHz, (f) $\Delta\Omega = -1$ GHz, (g) $\Delta\Omega = 1$ GHz, (h) $\Delta\Omega = 2$ GHz, (i) $\Delta\Omega = 6$ GHz, (j) $\Delta\Omega = 11$ GHz, (k) $\Delta\Omega = 14$ GHz and (l) $\Delta\Omega = 20$ GHz. The detection thresholds for the desynchronization events are $T_{\text{thr}} = 0.5$ ns, $C_{\text{thr}} = 0.5$, $\text{IEI}_{\text{thr}} = 0.5$ ns. The other simulation parameters correspond to those given in Table 4.1, except for $\kappa_c = \kappa_{\text{fb}} = 10$ ns^{-1}.

diate detuning, the long IEI-tails become shorter, reflecting the increase of the frequency of occurrence of power dropouts, which the desynchronization episodes are linked to. The distributions show only narrow-spaced desychronization events for large detuning, with desynchronization occurring, on average, every nanosecond. This implies, that synchronization no longer persists for such large detunings.

4.6 Bubbling and operating parameter mismatch

Intermittent desynchronization due to bubbling can also be induced by a small mismatch of parameters in the coupled lasers. Then, even in a noiseless and completely deterministic system, intermittent desynchronization can occur. Mismatches in operating parameters are common in experimental systems, their exact matching is challenging in real-life systems. In our bidirectional coupling scheme, the pump currents of both lasers need to be matched relative to the invidual laser's threshold to ensure the same dynamical regime and the same relaxation oscillation frequency (see Chapter 2).

Here, we investigate numerically the influence of a mismatch of the pump currents of both lasers on the synchronization, and we analyze the occurrence of bubbling events in dependence on the mismatch and the pump parameter [210], respectively. To exclude the influence of noise on the bubbling characteristics of this scheme, we simulate both lasers without intrinsic noise, i.e., $\beta = 0$.

Similar to the noise-induced bubbling case we covered in Section 4.4, we find indications for bubbling in the present scheme. With asymmetries present, an analytical treatment is complicated as the calculation of the maximal transverse Lyapunov exponent is hard to achieve. We thus can not prove bubbling. In this section, we link again the occurrence of desynchronization with certain dynamical states, in terms of a correlation analysis as we did before. In the present system, desynchronization does not occur without noise or mismatch, and varying the pump currents (or introducing a pump current mismatch Δp) does not result in the traversing of a blowout-bifurcation. Therefore, the desynchronization events, that are prevalent for small pump mismatches, can not be seen as manifestations of on-off-intermittency but rather as bubbling events.

We employ the set of equations (4.4)-(4.7) for our simulations, choosing the parameters as given in Table 4.1. For our numerical investigation, we vary the normalized pump currents of both lasers corresponding to $p_1 = 1.0 - 1.5$ and $p_2 = 1.0 - 1.5$.

The crosscorrelation coefficients at zero lag in dependence of both normalized pump currents are depicted in Fig. 4.18. On the diagonal, i.e., for matched pump currents, the crosscorrelation coefficients are 1.0. We notice that for only slight mismatches the correlation drops relatively suddenly toward values $C < 0.9$ for most of the studied pump current ranges (correlation around diagonal in Fig. 4.18). The exception is when both lasers are pumped

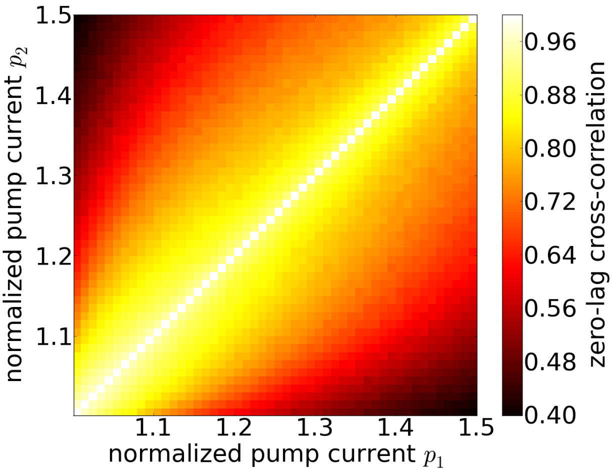

Figure 4.18: Cross-correlation at zero lag versus the normalized pump current values p_1 and p_2, respectively. The simulation parameters are to those given in Table 4.1, except for $\kappa_c = \kappa_{\text{fb}} = 10$ ns^{-1}.

close to threshold. The lower left region in Fig. 4.18 shows a broader region of high correlation coefficients. We attribute this behavior to LFF dynamics persisting for small mismatches and low pump currents. For this parameter region, desynchronization takes place around the power dropouts, with dynamics still being well-synchronized during the power buildup process. With such very small mismatches, mostly antimodes in the lower part of the mode ellipse, the high gain region, (see Chapter 2) are inducing the desynchronization events. If one increases the mismatch further, more and more modes that are involved in the LFF-power-buildup become transversely unstable. This leads to longer desychronization (bubbling) events and to a decrease in overall correlation.

If one laser is pumped close to threshold, giving rise to LFF dynamics, while the other is being pumped with a larger current, inducing fully-developed coherence collapse, the correlation decays more rapidly with increasing mismatch, probably because of their differing dynamical timescales. For large mismatches, the dynamics are still significantly correlated with $C > 0.4$ in the explored parameter ranges. However, identical zero-lag synchronization does not occur for too large mismatches. We note, nevertheless, that for larger mismatches the system shows a transition to a more generalized synchronization state with a significant correlation at a lag corresponding to the delay τ. The sign of the maximum peak position depends on which laser is pumped with a larger current. We exemplify this by calculating the crosscorrelation function (ccf) for the case $p_1 = 1.0$ and $p_2 = 1.5$.

The ccf is depicted in Fig. 4.19. Its maximum peak is at a lag $\Delta t = \tau$ and is significantly larger than the zero-lag peak $C_{\mathrm{corr}}(0)$. We note, that synchronization of leader-laggard kind with strongly asymmetric pump currents was also shown for face-to-face-coupled SLs without feedback in [210].

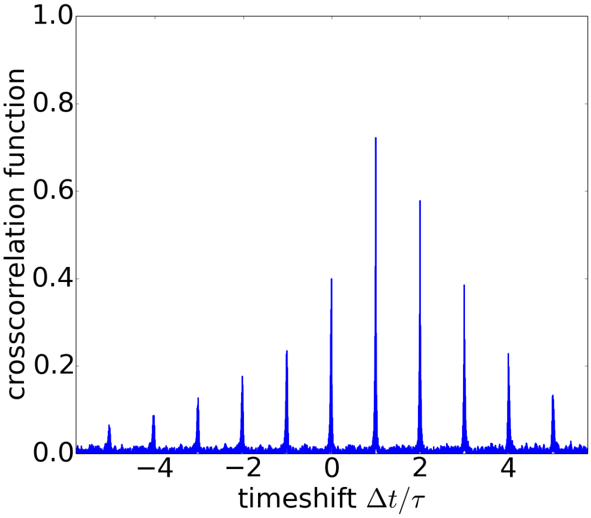

Figure 4.19: Crosscorrelation function for $p_1 = 1.0$ and $p_2 = 1.5$. The maximum peak is at shift $\Delta t = \tau$.

We now explore the dynamics timetraces of both lasers for three specific pump current mismatches. First, we focus on a relatively small mismatch when both lasers are pumped close to threshold and exhibit LFF dynamics: $p_1 = 1.01$, $p_2 = 1.02$. The very high zero-lag correlation implies only rare and limited desynchronization events. The second case we analyze involves a small mismatch as well. This time, however, the lasers are pumped with larger currents that induce fully-developed coherence collapse (CC) dynamics. In the second case, we employ the mismatch $p_1 = 1.2$ and $p_2 = 1.22$. Third, we explore a case with large pump mismatch, where the applied pump currents would lead to LFF and CC dynamics, respectively, if the lasers were not coupled but only subject to their respective feedback: $p_1 = 1.01$ and $p_2 = 1.2$.

In Fig. 4.20, we show the intensity dynamics (upper panels) and the corresponding slcc dynamics (lower panels) for each of the described pumping regimes. The panels on the right-hand side depict magnifications of desynchronization events in the intensity dynamics and the slcc, respectively.

As Fig. 4.20 shows, the desynchronization events are indeed associated with the dropout dynamics for small pump currents and small current mismatch, corresponding to the first mismatch case. When one laser exhibits

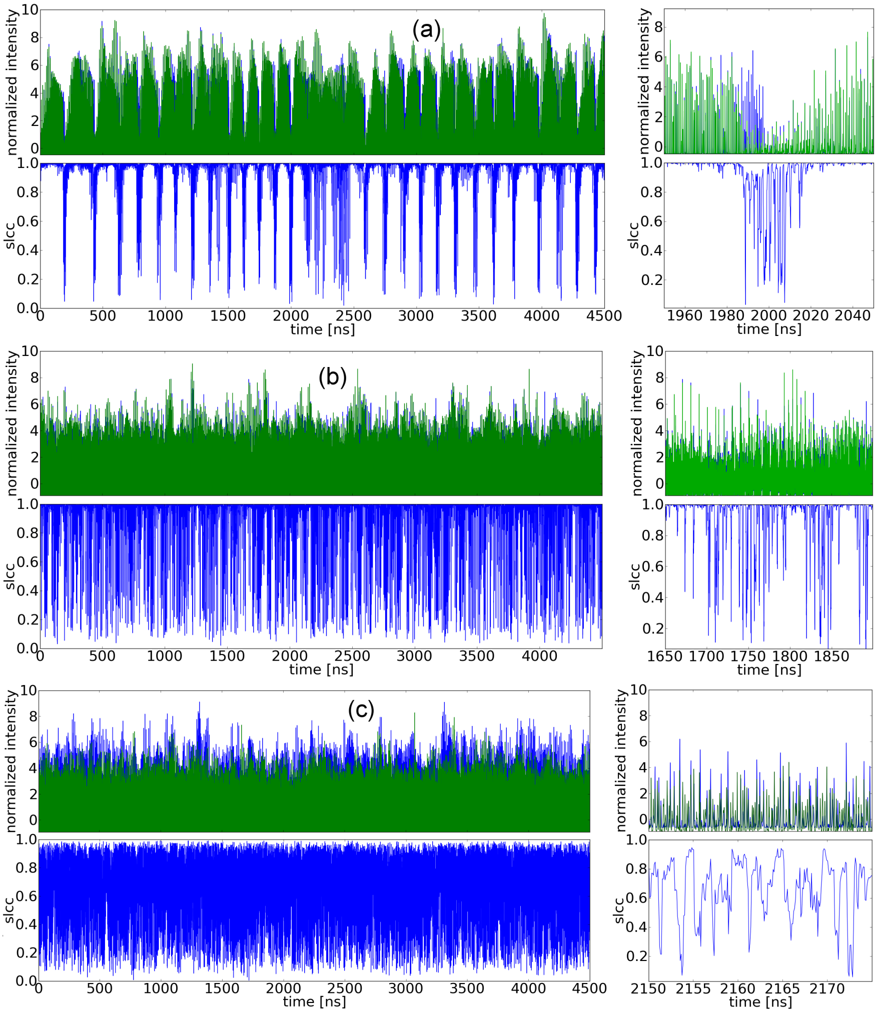

Figure 4.20: Normalized intensity dynamics of two coupled lasers with different pump current mismatches (upper panels) and the corresponding sliding-window cross-correlation time series (lower panels). The panels on the right hand side are zooms into both the dynamics and the slcc around certain desynchronization events. The set of mismatches are (a) $p_1 = 1.01$, $p_2 = 1.02$; (b) $p_1 = 1.2$, $p_2 = 1.22$ and (c) $p_1 = 1.01$, $p_2 = 1.2$. The simulation parameters are the same as for Figs. 4.18 and 4.17

a dropout, the lasers desynchronize and then resynchronize after the other laser experiences a dropout as well. However, due to the small window for the calculation of the slcc with size 1 ns (200 points in our simulations), the slcc timeseries exhibits fluctuations in a certain interval succeeding the first dropout. These correlation fluctuations persist after the second laser has experienced a power dropout, i.e., when both lasers emit with low intensity and at frequencies close to the solitary lasing frequency. This indicates, that several modes close to the SLM have become transversely unstable, and that the lasers remain unsynchronized while emitting on these modes.

The fast correlation fluctuations are reflected in the bubbling statistics as well. To characterize the bubbling events induced by pump current mismatches, we again employ the correlation threshold $C_{\mathrm{thr}} = 0.5$, the minimum duration threshold $\Delta T_{\mathrm{thr}} = 0.5$ ns and the minimum inter-event interval $\mathrm{IEI}_{\mathrm{thr}} = 0.5$ ns. The bubbling duration distribution and the IEI distribution for the first mismatch are depicted in Fig. 4.21(a) and (b), respectively.

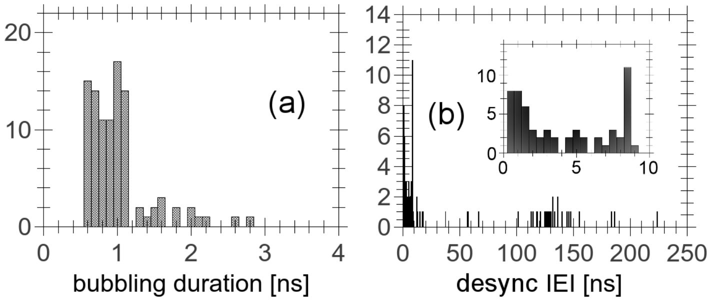

Figure 4.21: Distributions of bubbling event durations (a) and IEI (b) for the pump current mismatch $p_1 = 1.01$, $p_2 = 1.02$. The inset in (b) shows a magnification of the histogram for small IEI. The binsize corresponds to 0.1 ns for the duration distribution and 0.5 ns for the IEI distribution.

The detected desynchronization events are of short length (Fig. 4.21(a)), corresponding to the slcc fluctuations. The IEI distribution in Fig. 4.21(b) shows that most of the detected events are closely spaced with IEI ≤ 10 ns; these individual events collectively shape larger intervals of desynchronization. We identify these intervals as the actual bubbling events and the fast varying slcc as statistical fluctuations. The bubbling events are widely spaced in time, since they occur along the dropouts in both lasers. The long synchronized intervals between the bubbling episodes are represented by the long tail in the IEI distribution shown in Fig. 4.21(b).

The second case also involves a relatively small mismatch but with larger pump currents for both lasers. In this case, desynchronization occurs with a higher frequency (see Fig. 4.20(b)). Concurrently, their average separation is smaller than for the low pump current mismatch set. The corresponding statistics of desynchronization duration and IEI are depicted in Fig. 4.23. Longer intervals of synchronized dynamics are less prevalent, the maximum

IEI decreases with respect to the low pump current case. The more frequently occurring bubbling events can be linked to the underlying dynamics in the CC regime. To that effect, we plot exemplary timeseries of the carrier numbers of both lasers and the corresponding instantaneous correlation slcc in Fig. 4.22.

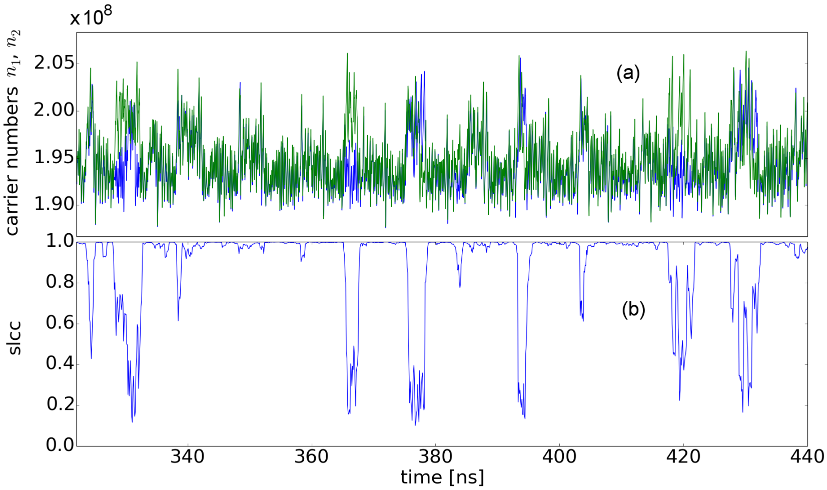

Figure 4.22: Numerically-obtained timeseries of the carrier numbers of two bidirectionally-coupled lasers with $p_1 = 1.2$ and $p_2 = 1.22$ (a) and the corresponding slcc timetrace (b).

It can be seen that desynchronization predominantly occurs at larger carrier numbers. This again is an indication that the observed desychronization is indeed bubbling. The limitation of the occurrence of bubbling to larger carrier numbers implies that desychronization occurs only in a specific region of the chaotic attractor. Bubbling at larger carrier numbers reflects the transverse instability of several modes which are located close to the solitary laser mode, where the transverse instability is induced by the mismatch. The onset of bubbling is induced when the trajectory approaches a transversely unstable antimode and bubbling persists while the trajectory is in the vicinity of the destabilized modes. Furthermore, there are significant intervals of synchronized dynamics as represented by the long tail in the IEI distribution as shown in Fig. 4.23(b). During these intervals the sliding cross-correlation returns to values of around 1.

For the third and last case we discuss, the lasers are pumped in different regimes. The intensity dynamics does not present real evidence of synchronized behavior, the slcc time series fluctuates rapidly between low and higher values (Fig. 4.20(c)). Larger instantaneous correlation coefficients in this case are seen as coincidental due to the short window for the

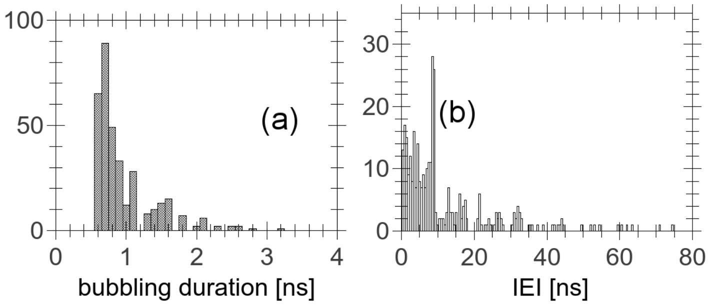

Figure 4.23: Distributions of bubbling event durations (a) and IEI (b) for the pump current mismatch $p_1 = 1.2$, $p_2 = 1.22$. The binsize corresponds to 0.1 ns for the duration distribution and 0.5 ns for the IEI distribution.

slcc calculation. The maximum of the slcc corresponds now only to values around slcc ≈ 0.8, which is significantly lower than for the previously discussed cases with small mismatch. Considering that we are investigating a symmetric coupling scheme with identical lasers and without noise, leads us to conclude that overall zero-lag synchronization is transversely unstable and is lost for such large pump current mismatches. Otherwise, at least short intervals of correlation coefficients close to 1 should prevail. We therefore find that we do not observe bubbling behavior in this case but only statistically occuring highly-correlated 1 ns intervals.

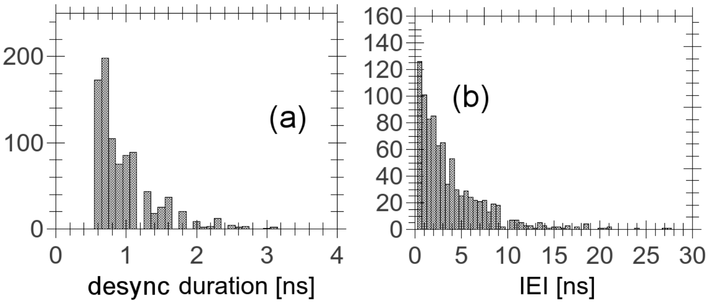

Figure 4.24: Distributions of desynchronization event durations (a) and IEI (b) for the pump current mismatch $p_1 = 1.01$, $p_2 = 1.2$. The inset in (b) shows a magnification of the histogram for small IEI. The binsize corresponds to 0.1 ns for the duration distribution and 0.5 ns for the IEI distribution.

The fast fluctuating correlation manifests itself in a narrow desynchronization duration distribution around very short events and an IEI distribution resembling an exponential decay (see Fig. 4.24). A bigger window size for the calculation of the slcc would result in low to intermediate values of the correlation coefficient.

Thus, we have found that small pump current mismatches lead to bubbling behavior on a timescale that is linked to the complex dynamics of both lasers in the respective operating (pump) regime. This means, that in the LFF regime, pump-mismatch-induced bubbling occurs with the frequency of the power dropouts. In the CC regime, bubbling takes place on a faster timescale. We have linked the occurrence of intermittent desynchronization to transversely unstable antimodes and its persistence to transversely unstable modes with larger carrier number, which have a frequency close to the solitary laser frequency. The larger bubbling frequency in the CC regime is then explained by the fact that the trajectory approaches the unstable antimodes more often in the CC than in the LFF regime due the CC characteristics (see Chapter 2).

4.7 Summary

In this chapter, we investigated the synchronization properties of two semiconductor lasers which are coupled bidirectionally and receive self-feedback via a passive relay. Implementing this configuration, we have experimentally achieved high-level zero-lag synchronization resulting in correlation coefficients larger than 0.95. Our investigations, making use of high-resolution measurements, have revealed general differences between the synchronization dynamics in the LFF regime and those in the CC regime. We have identified distinct desynchronization events which we interpret as manifestations of the bubbling phenomenon. We have found indications that these events are indeed bubbling events rather than on-off-intermittency, the latter implying transverse instability of the entire chaotic attractor embedded in the synchronization manifold. We see these events responsible for the decline of synchronization level (quantified by decreasing correlation coefficients) with increasing pump current. The desynchronization events become more frequent for an increasing current, especially with the transition from the LFF to the CC dynamical regime, and thus increasingly reduce the overall correlation. The episodes of unsynchronized dynamics are distinct from the rest of the dynamics, because the synchronized dynamics (in between the desynchronization events) maintain a high level of correlation, while the unsynchronized dynamics exhibit significantly lowered instantaneous correlation coefficients (quantified by the slcc).

We have also investigated experimentally and numerically the influence of frequency detuning of both lasers on the synchronization dynamics in the LFF regime. In accordance with the concept of episodic synchronization, which was introduced for unidirectional injection in a drive-response configuration, we have found in the previous chapter, that the lasers' dynamics show synchronization when emitting at frequencies within the mutual spectral overlap. This overlap is reduced with increasing detuning. Here, we have found, that such a reduction leads to longer and more frequent episodes of desynchronized behavior, as the lasers emit more often and for a longer time at frequencies outside the mutual locking range. This results in the degradation of correlation of the dynamics. For too large detuning, no distinct episodes of synchronization can be found anymore as the spectral overlap vanishes.

Furthermore, we have studied the effect of a mismatch of the pump currents of both lasers on the synchronization properties in a noiseless numerical framework. A pump mismatch leads to bubbling behavior as the dynamics are pushed towards transversely unstable periodic orbits. For small mismatches, desynchronization is only intermittent and high-level synchronization is maintained in between those intervals. The occurrence of the bubbling events can again be connected to the overall dynamics in the respective pumping regime. In the LFF regime, mismatch-induced bubbling occurs with power dropouts, while in the CC regime, the dynamics approach unstable antimodes more often, and bubbling thus takes place more frequently. Larger pump current mismatches result in the loss of zero-lag synchronization, though a certain correlation is retained. With increasing pump current mismatch, the system shows a transition toward a more generalized synchronization behavior with a dominant delay-lag correlation. The sign of the τ-lag of the maximum correlation peak is determined by which laser is pumped with a larger current.

Desynchronization due to bubbling, be it noise- or mismatch-induced, is seen to occur due to unstable antimodes and modes (periodic orbits) that have been transversely destabilized. The current dynamical characteristics of the lasers (which may be influenced by mismatches or asymmetries) affect the occurrence of desynchronization by determining the likelihood that the dynamics trajectories approach these transversely unstable sets and leave the synchronization manifold.

Dynamical excursions away from the synchronization manifold are adverse to all applications that rely on synchronization of the involved lasers. This is especially the case for chaotic optical communication. Noise- or mismatch/asymmetry-induced desynchronization events can strongly affect the efficiency of bidirectional communication schemes and must be considered during the evaluation of the efficiency of these schemes. Our results may therefore be helpful for future studies of concepts of chaotic communications or key-exchange.

5

Characterizing the deterministic nature of individual events in chaotic laser dynamics

5.1 Introduction

There has been a long ongoing debate in the complex systems community on how to qualify the dominant underlying mechanism of certain dynamical features or characteristic irregular events in noisy chaotic systems. An example that we are going to investigate here is the origin of the characteristic Low Frequency Fluctuations (LFF) dynamics, especially of the power dropouts in dynamics of semiconductor lasers subject to time-delayed feedback that are pumped close to threshold (as described in Chapter 2). These have led to controversial discussions in the past [39, 42, 55–62]. Some groups have argued that the power dropouts are mainly stochastically induced by spontaneous emission noise [39, 42]. Others have denoted the deterministic chaos induced by the delayed feedback as the principal drive [55, 211]. From a modeling point of view, it can be shown that the overall Low Frequency Fluctuations and the power dropouts are retained when applying the rate equation model introduced in Chapter 2 without the Langevin noise terms, i.e., $\beta = 0$ (see Fig. 5.1).

Therefore, noise is not required to evoke these dynamical characteristics. However, introducing noise to the system can have an effect on the duration of the LFF cycles. In general, increasing the noise strength can lead to shorter cycles, and the dynamics of a laser with feedback is affected by an intricate interplay between the deterministic mechanisms, i.e. the time-delayed feedback, and stochastic processes taking place due to spontaneous emission noise.

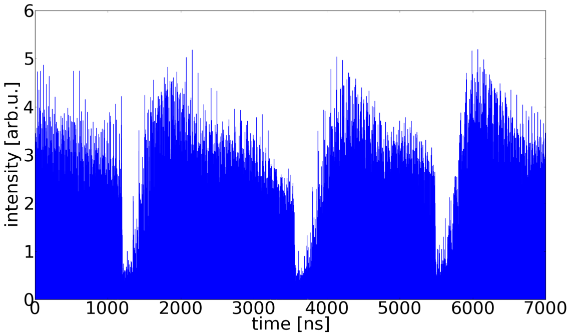

Figure 5.1: Numerically-obtained dynamics from the model in Chapter 2 with the the spontaneous emission factor set to zero. The LFF structure including the power dropouts are preserved in the noiseless situation. The simulation parameters were $\alpha = 3$, $K = 0.15$, $p = 0.1$, $T = 200$, $\mu = 0.01$, $\tau = 16000$.

Until now, investigations to identify whether deterministic mechanisms or stochastic processes dominate the dropout behavior have been based on statistical measures (see e.g. [56, 62]). In this chapter, we present an individual event-based approach allowing us to identify on an individual basis which power dropouts are deterministically-driven by the delayed feedback signal. Our method is based on the synchronization with a twin laser system. We have shown in Chapter 3, that the dynamics of a single chaotic system with delayed feedback equals the dynamics of two symmetrically-coupled identical systems that are synchronized. The chaotic attractor in the synchronization manifold of the coupled system is equal to the attractor of the single system with feedback.

We utilize synchronization as a test to determine whether a power dropout in one of the lasers has been the result of the deterministic chaotic dynamics fed back into the laser or of the intrinsic noise in the laser. We argue that if the outputs of the lasers exhibit synchronous power dropouts, the events were induced by a deterministic mechanism. Since each laser has its own independent noise characteristics, it is extremely improbable that both lasers experience a dropout in power at the same time due to the noise. This low probability can be estimated.

We conduct an experimental study to investigate the dependence of the ratio of synchronized-, and thus deterministically-induced, dropouts on the laser pump current, one of the laser's principal dynamical parameters. We find a very high fraction of the measured dropouts occur synchronously in both lasers close to the solitary lasing threshold. This fraction decreases significantly with increasing pump current. These results are verified by a numeri-

cal study using the rate equations introduced in Chapter 2. Furthermore, we use numerical modeling to investigate the dependence of the synchronized dropout fraction on the intrinsic noise strength in order to study the impact of stochastic processes on the laser dynamics.
Large parts of the results presented in this chapter have been published as "K. Hicke, X. Porte, and I. Fischer: *Characterizing the deterministic nature of individual power dropouts in semiconductor lasers subject to delayed feedback*, Physical Review E **88**, 052904 (2013)". The experiments were performed in collaboration with Xavier Porte.

5.2 Method

Our procedure to test for determinism is based on the zero-lag synchronization of the investigated single semiconductor laser (SL) with feedback with a twin laser, thus, the two laser subsystems have to be able to synchronize identically for our method to work. The synchronizability depends on their coupling and feedback topology (see Chapter 3) and their dynamical regime (see chapter 4). For this reason, we operate in the moderate feedback regime and use a setup that is as symmetric as possible. An asymmetry or parameter mismatch can affect the coupled systems' dynamics to leave the synchronization manifold or prevent isochronal synchronization alltogether. We employ a passive relay configuration to couple both lasers. We have shown that the implementation of a relay, which provides feedback and coupling for both lasers, allows for identical synchronization of the outputs of the laser systems. In case both arms of the configuration have the same optical length, zero-lag synchronization can be achieved (see Chapter 3 and e.g. [71]) and the synchronized dynamics is identical to the dynamics of a single laser system with corresponding feedback strength. If both lasers experience a drop in power at the same time, we consider the (pair of) dropout(s) as being dominantly driven by a deterministic mechanism induced by the delayed feedback.

In case both lasers exhibit dropouts but at different times, several reasons can be postulated. We show in Section 5.4, that non-synchronized dropouts do not necessarily mean that one or both dropouts are noise-driven. Nevertheless, a common situation is that noise induces a dropout event in one laser and, after the coupling delay, the other laser receives this dropout signal and experiences a dropout as well. Afterwards the lasers resynchronize fast.

5.3 Experiments

Our experimental setup is based on optical fibers, a schematic is depicted in Fig. 5.2. The coupling configuration consists of two single-mode quantum-well (QW) edge-emitting discrete mode semiconductor lasers (Eblana Photonics), operating at a nominal wavelength of $\lambda \approx 1540$ nm with a side-mode suppression ratio of >40 dB. The lasers have been particularly selected for their similar properties.

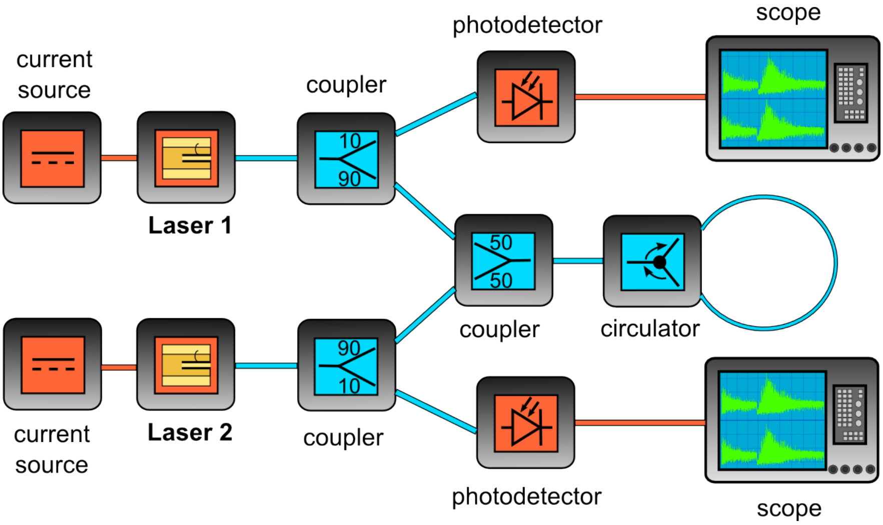

Figure 5.2: Schematic experimental setup. The lasers are symmetrically coupled via a feedback and coupling fiber loop consisting of a 50/50 optical coupler and a circulator. This loop serves as passive relay. The numbers featured on the symbols for the couplers correspond to their respective coupling ratios (in percent). The orange lines depict electrical connections, the blue ones represent polarization-maintaining (PM) optical fiber.

The lasers are coupled symmetrically via a relay fiber loop. This loop consists of a 50/50-optical coupler and an optical circulator. This corresponds to a semitransparent mirror, accounting for symmetric feedback and coupling, respectively, with equal coupling delays and equal coupling and feedback strengths. The two legs of the setup have been equalized in optical path length with an accuracy of the resulting feedback delays of $|\tau_{\mathrm{fb},1} - \tau_{\mathrm{fb},2}| \approx 25$ ps. We use polarization maintaining (PM) optical fiber. We can thus rule out effects related to polarization (mis-)alignment as the origin of desynchronization. The laser temperatures and pump currents are controlled by a Thorlabs PRO8000 laser controller with a temperature accuracy of $\Delta T = \pm 0.01$°C and a current accuracy of $\Delta I = \pm 0.01$ mA, respectively. We measure the laser outputs by using Miteq Dr-125G-A photodetectors with 13 GHz bandwidth, the output signals of which are recorded by a LeCroy WaveMaster 816Zi oscilloscope with an analog bandwidth of 16 GHz and a sampling rate of 40 GS/s. This corresponds to a sampling time of 25 ps.

Autocorrelation analysis yields the two feedback delays in our setup which are estimated to be $\tau_{\text{fb},1} = 89.75 \pm 0.025$ and $\tau_{\text{fb},2} = 89.73 \pm 0.025$ ns. Analyzing the autocorrelation peak positions to determine the delay time involves a systemic error which depends on the operating regime [206]. This may result in an offset to the determined delay times. However, determining the relative delay difference is unaffected. Thus, with the coupling delay $\tau_c = \frac{1}{2}\left(\tau_{\text{fb},1} + \tau_{\text{fb},2}\right)$, all delays in our setup can be considered equal within the uncertainty limits. We measured the feedback attenuation along both optical feedback paths as ≈ 11 dB, both values were determined to be equal within a margin of 1%. Due to this symmetry, the coupling between both lasers has the same attenuation and, thus, the same strength.

Considering the geometry and coupling topologies of the laser cavities, we estimate the total feedback rates (and thus the coupling rates) for each respective laser as $\kappa_1 = \kappa_2 = \kappa_c = 34\ \text{ns}^{-1}$. The feedback strengths correspond to a few percent of the output power coupled back into the respective cavity.

Both lasers are being operated in the low-frequency fluctuations (LFF) regime. This means that the pump current is relatively close to the solitary threshold. The lasing threshold pump currents are $I_{thr1} = 10.89$ and $I_{thr2} = 10.92$ mA, respectively. We define the normalized pump currents as $p_{1,2} = I_{1,2}/I_{thr1,2}$. For our experiments, p_1 and p_2 are varied simultaneously from $p_{1,2} = 1.01$ to $p_{1,2} = 1.12$ in steps corresponding to ≈ 0.15 mA. For each step, six output intensity time traces with a length of 100 μs of both lasers are recorded.

Because of its near-optimal symmetry in optical path length, our experimental setup exhibits an especially strong sensitivity to the optical phase. Even minor temperature gradients in the laboratory environment can affect the coupling phases in our configuration and alter the dynamical characteristics and coupling efficiency. We therefore identify and only record time series with appropriate phase conditions, exhibiting clear LFF dynamics. Nevertheless, the actual instantaneous phase conditions can not be determined.

The classification as synchronous or nonsynchronous dropouts is done manually for all measured power dropouts because this proved to be the most reliable method. If corresponding dropouts in both lasers occur within a 2 ns window they are considered synchronized. Figure 5.3 shows exemplary time traces of (a) an unsynchronized and (b) a synchronized pair of dropouts, respectively.

In order to evaluate our results, we define the total number of detected pairs of dropouts for a specific normalized pump current value as N_{total} and its subset of synchronized pairs of dropouts as N_{synced}. The extent of our data is shown in Fig. 5.4. As explained in Chapter 2, the frequency of dropouts increases with increasing pump current, the total number N_{total} therefore increases with pump current as well.

The main quantity we analyze is the synchronized dropout fraction ζ which is defined as

$$\zeta = N_{\text{synced}}/N_{\text{total}}.$$

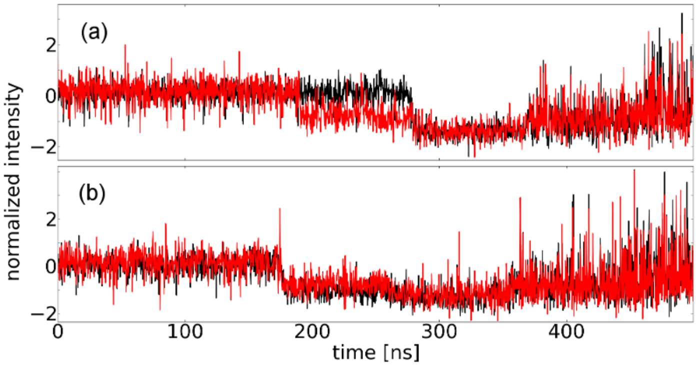

Figure 5.3: Experimental intensity time traces of both lasers. Panel (a) shows unsynchronized dropouts. The desynchronization lasts for approximately one delay $\tau_c \approx \tau_{\text{fb}}$. (b) depicts a pair of synchronized dropouts in both lasers.

We compute ζ to qualify the degree to which the dropout dynamics for a given pump current are dominated by deterministic mechanisms.

Our experimental results for ζ in dependence of the normalized applied pump currents p_1 and p_2 are depicted in Fig. 5.5. They exhibit a large maximum percentage of 83% of synchronous dropouts close to the solitary lasing threshold at $p_{1,2} = 1.009$ and a significant decrease with increasing bias current. The minimum of $\zeta = 13\%$ is reached for $p_{1,2} = 1.092$.

The first result is unanticipated: the fraction ζ has its maximum of $\zeta = 0.85$, only slightly above the solitary lasing threshold. A stronger effect of the intrinsic noise close to threshold could have been expected. This is due to the relatively large contribution of spontaneous emission to the output power at low pump currents. What we observe is contrary to that expectation. We assume that the noise is not sufficiently strong to induce more power dropouts with the pump current close to threshold as compared to cases with higher pump currents. This hypothesis is verified via our numerical studies presented in Section 5.5. With the ratio of synchronized dropouts ζ being this large, we can conclude that, close to threshold, a large majority of LFF power dropouts is induced by deterministic mechanisms rather than by noise. Moreover, we can identify which specific events are deterministic.

Since the noise due to spontaneous emission is independent for each laser, and correlated noise even for a single round trip is much smaller due to the feedback attenuation and coupling attenuation, we can dismiss stochastic effects as the principal drive of power dropouts in the low pump current regime. An analysis of the inter-dropout-interval (IDI) probability distributions with a 2 ns resolution reveals that the probability of dropouts in

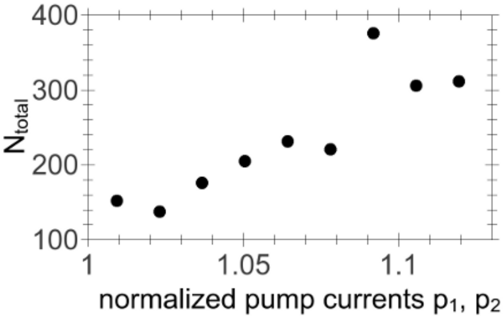

Figure 5.4: The total number N_{total} of measured pairs of power dropouts versus the applied normalized pump currents.

both lasers occurring within a 2 ns window is negligible ($\ll 10^{-4}$). Once we classify a pair of dropout events as synchronized, we can, therefore, name determinism as the dominant mechanism with high confidence.

For a larger pump current, the synchronized dropout fraction decreases. This can have multiple reasons. It might be due to an increased noise-sensitivity of the dynamics in a higher pump current regime. With a stronger pump current, the intensity fluctuations have a larger amplitude, and the dynamics get closer to unstable antimodes and smaller perturbations by the intrinsic noise are necessary to lead to a collision of the laser's trajectory with an antimode which is then followed by power dropout. As our numerical results suggest, this may be considered the main cause for the decline of the synchronized dropout ratio with increasing pump current p.

However, several other causes that are related to imperfections in the experiment can also lead to a decrease in ζ. Those are distorting the resulting fraction of synchronized power dropouts and, as ζ reflects not only the deterministic dynamics of a single laser with feedback and intrinsic noise, artificially amplify the fraction of unsynchronized pairs of dropouts. We will discuss these factors in the next section.

5.4 Limitations of method

Considering the lower synchronized dropout fraction for higher pump currents, we have to be aware of certain limitations our method has. On the individual event basis, we can only classify synchronized dropouts as deterministically driven, but we cannot determine the main cause of the unsynchronized ones. Attractor bubbling (see Chapter 4), mismatches in feedback strength and/or delay (see Chapter 3), mismatches in laser parameters

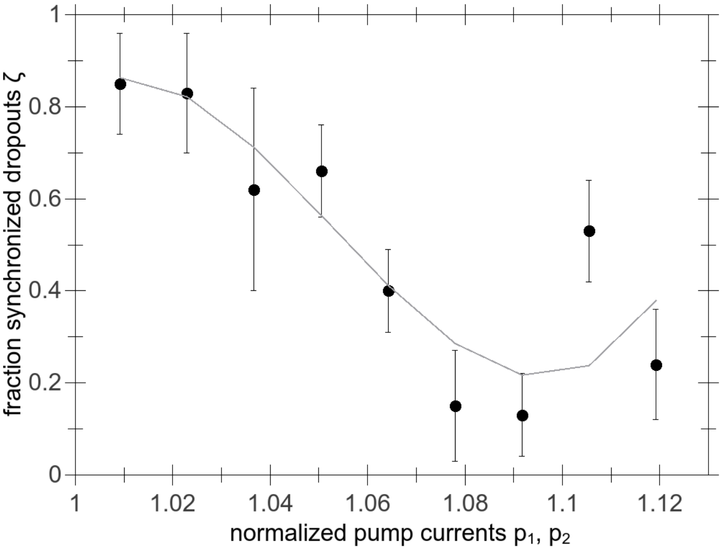

Figure 5.5: Experimental results for the fraction of synchronized power dropouts ζ versus the normalized pump currents p_1 and p_2 averaged among the corresponding measured time series. The error bars show the corresponding standard deviation. The gray curve results from a 3rd order polynomial fit and is only meant as a guide to the eyes.

and detection-related misclassifications reduce the fraction of synchronized dropouts without being related to the delayed feedback attractor. As described in Chapter 4, bubbling is an intermittent desynchronization phenomenon which makes the system's trajectory temporarily leave the synchronization manifold. In the LFF regime, occurrences of bubbling and of dropouts are strongly linked as we show in 4. If we assume complete symmetry in our configuration and identical lasers, the desynchronization events take place only due to transversely unstable saddle nodes, and not because of the drop in power. Because the frequency of occurrence of bubbling is connected to characteristic frequencies in the dynamics, increasing the pump current leads to more bubbling events. This would in part explain the strong decline in ζ with increasing pump current, as shown in Fig. 5.5. Pairs of dropouts that are unsynchronized due to bubbling will be (mis-)classified by our approach as not being deterministically driven. Since bubbling-induced desynchronization induces dynamics transverse to the synchronization manifold, our method loses applicability. We can thus make no statement about the actual principal mechanism underlying these dropouts.

With slight asymmetries in the experimental conditions and parameters, some of the laser's modes also become transversely unstable, and bubbling can occur at different parts of the attractor as well. In these cases, the phase space trajectories diverge, and the lasers might exhibit their dropouts at different times due to bubbling. Again, because the coupled lasers' dynamics can at these points no longer be identified with a single laser's dynamics, we can draw no conclusion about whether the corresponding dropouts are driven by determinism or not.

Furthermore, certain slight asymmetries or mismatches in the experimental setup, which in experiments are commonplace and unavoidable, will lead to more unsynchronized dropouts and therefore to additional misclassifications. This is, because they can result in dynamics partly outside the synchronization manifold as well and thus outside the single delay system's dynamics manifold. During the preparation of the experiment, all asymmetries are minimized as much as possible. Although these mismatches still might have an effect, the dynamics within the synchronization manifold is a good approximation for the dynamics of the single delayed feedback system.

There are two further possible sources for misclassification. One is detection noise which might blur the measured dynamics around the dropout event and contribute to the synchronization error. The second source is related to instances of LFF-dynamics where the precise time of occurrence is hard to determine. These uncertainties in the determination of the exact dropout time can arise because the shape of a dropout is not as clear. This particularly occurs toward higher pump currents, e.g. within the transitional range from the LFF regime to the fully-developed coherence collapse regime where the characteristic shape of the dropouts get lost. In a situation, where the coincidence of corresponding dropouts is less than clear, the pair is classified as non-synchronous and, thus, does not contribute to the share of deterministically-induced power-dropouts.

Considering these misclassification sources, our resulting fraction of synchronized dropouts ζ represents a lower limit to the fraction of actually deterministically-driven dropouts. We conclude that it is impossible to make clear statements about the overall dominant mechanism underlying the dropouts in the operating regimes where our results show only small to intermediate values for ζ. Since ζ is highest when the lasers are pumped close to their solitary thresholds, we can draw the strongest conclusions there.

5.5 Numerical corroboration

To corroborate our experimental results and also to gain further insight into the sensitivity of our system to spontaneous emission noise, we numerically study the problem making use of the single mode rate equation model introduced in Section 2.3 and extended rate equations for a coupled system in Chapter 4. Here, we assume the gain to be linear in the carriers ($\epsilon = 0$), thus the gain reads as $\mathcal{G}_{1,2} = g\frac{n_{1,2}(t)-n_T}{1+\epsilon|\mathcal{E}_{1,2}(t)|^2} = g\left(n_{1,2}(t) - n_T\right)$. The equations then read

$$\begin{aligned}
\dot{\mathcal{E}}_1(t) &= \frac{1}{2}(1+i\alpha_1)\left(g(n_1(t)-n_T)-\gamma\right)\mathcal{E}_1(t)+\kappa_{\mathrm{fb},1}\mathcal{E}_1(t-\tau_{\mathrm{fb},1}) \\
&\quad +\kappa_c\mathcal{E}_2(t-\tau_c)+F_{\mathcal{E}_1} \qquad (5.1)\\
\dot{\mathcal{E}}_2(t) &= \frac{1}{2}(1+i\alpha_2)\left(g(n_2(t)-n_T)-\gamma\right)\mathcal{E}_2(t)+\kappa_{\mathrm{fb},2}\mathcal{E}_2(t-\tau_{\mathrm{fb},2}) \\
&\quad +\kappa_c\mathcal{E}_1(t-\tau_c)+F_{\mathcal{E}_2} \qquad (5.2)\\
\dot{n}_1(t) &= p_1\frac{I_1}{eI_{\mathrm{thr1}}}-\gamma_e n_1(t)-g\left(n_1(t)-n_T\right)|\mathcal{E}_1(t)|^2 \qquad (5.3)\\
\dot{n}_2(t) &= p_2\frac{I_2}{eI_{\mathrm{thr2}}}-\gamma_e n_2(t)-g\left(n_2(t)-n_T\right)|\mathcal{E}_2(t)|^2 . \qquad (5.4)
\end{aligned}$$

$\mathcal{E}_{1,2}$ denote the slowly varying complex electric field amplitudes of lasers 1,2, and $n_{1,2}$ carrier numbers. $I_{1,2}$ denote the bias currents, $I_{\mathrm{thr}1,2}$ are the respective threshold currents, e is the elementary charge, and $p_{1,2}$ are the normalized pump current parameters. γ denotes the photon decay rate, γ_e is the carrier decay rate, g is the differential gain, and n_T represents the carrier number at transparency. $\tau_{\mathrm{fb},1,2}$ and $\kappa_{\mathrm{fb},1,2}$ describe the feedback delay times and feedback rates, respectively, while τ_c and κ_c are the coupling delay and coupling rate, respectively. The two coupled lasers are simulated as being identical in every parameter, and the coupling scheme is set to be completely symmetrical, neglecting any possible feedback delay or -strength mismatch. The parameter values of the simulation are given in Table 5.1. The noise is again modeled as Gaussian white noise with $\langle F_{\mathcal{E}_{1,2}}(t)\overline{F_{\mathcal{E}_{1,2}}(t')}\rangle = 2\beta_{1,2}\gamma_e n_{1,2}\delta(t-t')$ and $\langle F_{\mathcal{E}_{1,2}}(t)\rangle = 0$. The equations are numerically solved using Milshtein's method [208, 209] with a stepsize corresponding to $0.1\gamma^{-1}$. We solve the above equations to find the dependence of the fraction ζ on the normalized pump current p and on the strength of the spontaneous emission noise β. For this, we vary p from $p = 0.98$ to $p = 1.2$, and the spontaneous emission factor β from $\beta = 10^{-9}$ to $\beta = 10^{-3}$.

For each set of parameters, 20 timeseries with 10μs length are computed. The stepsize corresponds to 5 ps.

Classification of synchronized and non-synchronized dropouts is performed using an automated algorithm for the modeled time series. The dropouts are identified by the following algorithm:

The original time series are window-averaged with a window size of 2000 points corresponding to the delay time $\tau = 10$ ns and a step size of 5 ps. When the averaged intensity drops below the overall intensity average for at least 340 out of the consecutive 400 point interval (2 ns), the occurance of a power-dropout is identified. If a dropout is detected in both lasers within a 1 ns window, the drops are considered synchronized. Although this automated classification may be not as reliable as a manual one, it is sufficiently accurate. Due to the extent of the studied parameter dependencies, a manual classification can not be implemented. In Fig. 5.6, we show two

Parameter	Variable	Value
linewidth enhancement factor	α	3.0
differential gain	g	10^{-5} ns^{-1}
photon decay rate	γ	200 ns^{-1}
carrier decay rate	γ_e	1 ns^{-1}
feedback delay	τ_{fb}	10 ns
feedback rate	κ_{fb}	20.0 ns^{-1}
coupling delay	τ_c	10 ns
coupling strength	κ_c	20.0 ns^{-1}
carrier number at transparency	n_T	$1.8 \cdot 10^8$

Table 5.1: Laser and coupling parameters used for the numerical study. The laser-specific parameters are set as identical for both lasers.

exemplary pairs of simulated timeseries (black and red lines) which also illustrate the detection algorithm. Panel (a) shows an instance of detected synchronized dropouts, (b) displays two unsynchronized dropouts where the time difference between the occurrences approximately corresponds to the delay $\tau_{\mathrm{fb}} = \tau_c$. The black and red vertical dashed lines indicate the detected dropout time of timeseries 1 and 2, respectively, the grey and magenta horizontal dashed lines depict the overall mean intensity of timeseries 1 and 2, respectively, and the solid grey and magenta lines are the corresponding sliding window-averaged intensity timeseries. Whenever one of these lines listed above is not visible, it is overlain by the corresponding line for the other timeseries.

The main results for the numerically-obtained fraction ζ versus the normalized pump currents $p_{1,2}$ versus the spontaneous emission factors $\beta_{1,2}$ are shown in Fig. 5.7. A spontaneous emission factor of $\beta \approx 10^{-6} - 10^{-5}$ is considered realistic for quantum-well (QW) single-mode edge-emitting semiconductor lasers, which is the type of lasers used in our experiment.

Our numerical findings qualitatively reproduce the trends we find in the experimental data: the maximum of ζ for a given noise strength lies very close to the solitary threshold $p = 1.0$ for $\beta = 10^{-9}$ to $\beta \approx 5 \cdot 10^{-4}$, including the range of the spontaneous emission factor $\beta = 10^{-6} - 10^{-5}$ considered realistic for the lasers used in the experiments. Furthermore, the synchronized dropout fraction decreases with increasing pump current when applying noise with a magnitude from that range. This also corroborates the experimental results for ζ. In Fig. 5.8, we show horizontal (a) and vertical (b) cross sections of the data depicted in Fig. 5.7 to further underline the characteristics described in this paragraph.

The maximum values for a given noise factor shows a decrease from $\zeta = 1$ for $\beta \approx 10^{-9}$ to $\zeta \approx 0.1$ for $\beta \approx 10^{-3}$. For noise strengths $\beta < 10^{-4}$, the synchronized dropout fraction maximum is close to threshold and decreases

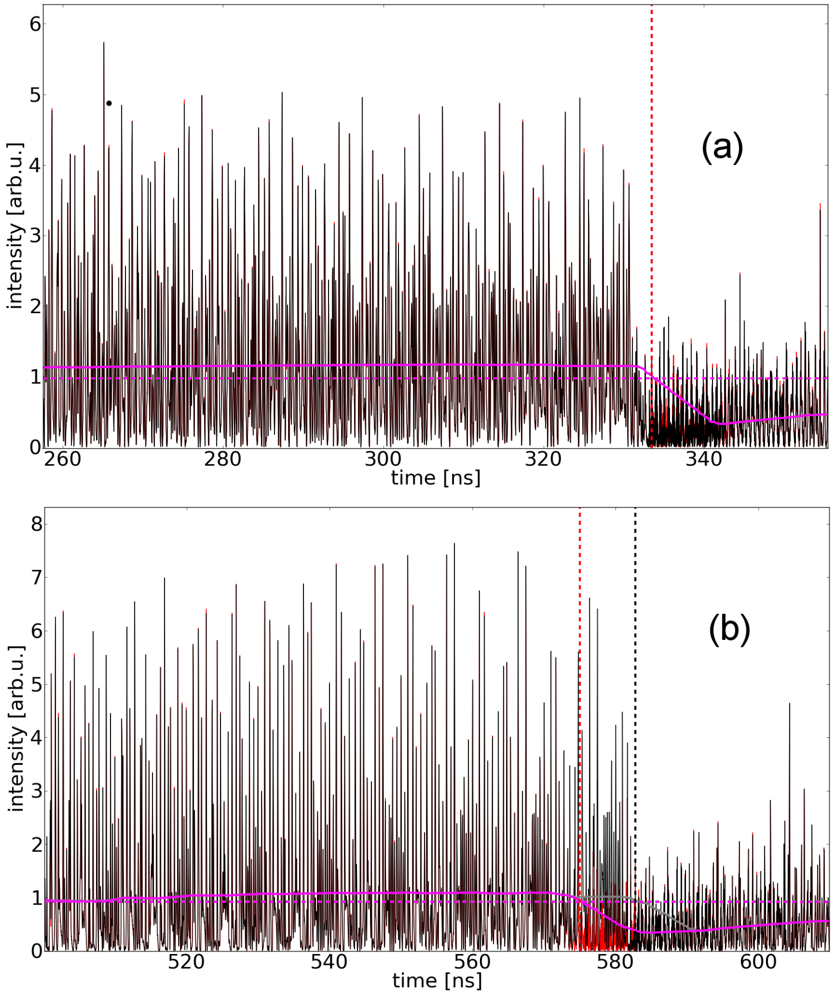

Figure 5.6: Examples of numerically-obtained timeseries for $p = 1.03$ and $\beta = 10^{-6}$ exhibiting synchronous (a) and asynchronous (b) dropouts. The dashed black and red lines indicate the time of occurence of a dropout as detected by the algorithm described above. The horizontal dashed grey and magenta lines represent the respective overall average intensity, and the solid grey and magenta lines depict the sliding window-averaged intensities. In panel (b), a time difference between both dropouts can be clearly seen, which corresponds approximately to the delay time.

with increasing current. From the numerics, we can see the effect of noise close to threshold: with a spontaneous emission factor $\beta > 10^{-4}$, which is

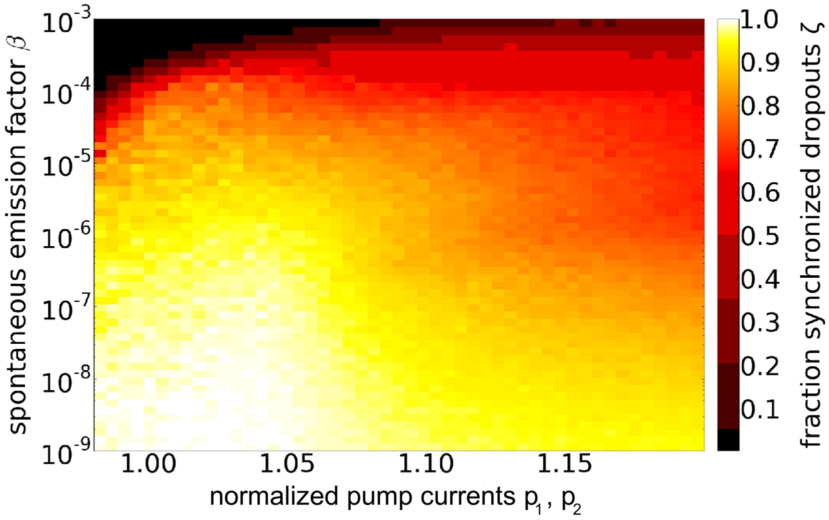

Figure 5.7: Numerical results for the fraction of synchronized power dropouts ζ versus the normalized pump currents p_1 and p_2 versus the spontaneous emission factor β for the case of a completely symmetric coupling configuration and identical lasers. The simulation parameters correspond to those listed in Table 5.1.

one to two orders of magnitude stronger than assumed for the experiment, the maximum of ζ is no longer close to threshold, but shifted to higher pump currents; ζ now exhibits a minimum around threshold. Stronger noise has a more pronounced effect and can be the dominant driving force close to threshold. With such strong noise, the originally expected behavior (see Section 5.3) can be found. This suggests that, for a large spontaneous emission factor, the majority of dropouts are actually mediated by stochastic processes.

Our result, that, close to threshold, the influence of noise on the occurance of dropouts is minimal, can be considered specific to the type of laser we use in the experiment - single mode QW edge-emitters. As the spontaneous emission factor β can be significantly higher for other laser types, e.g. photonic crystal lasers, ζ can have a minimum close to the lasing threshold with the effect of noise diminishing, and thus ζ increasing with increasing pump current.

One notices that the results exhibit relatively large values of $\zeta > 0.7$ for most of the scanned parameter ranges, which is large compared with the experimentally-obtained values. Especially for larger pump current values, the ratio ζ exhibits a much larger magnitude when compared to the experimental findings. This can be understood considering the complete symmetry

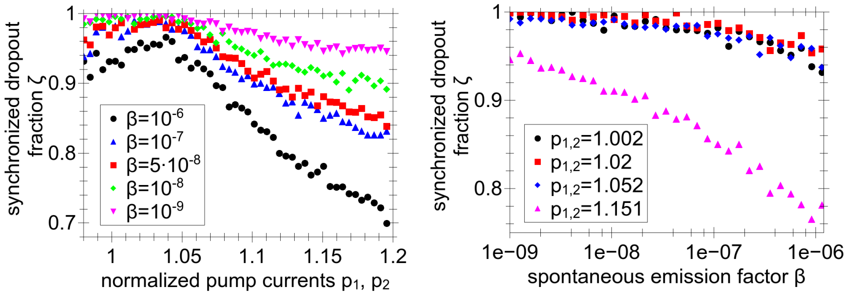

(a) (b)

Figure 5.8: Cross sections of the data presented in Fig. 5.7. (a) ζ versus the normalized pump currents for different noise strength values. (b) ζ versus the noise strength β for different values of the normalized pump currents.

of the simulated setup. Mismatch- and asymmetry-caused desynchronization is not present, and detection or measurement-related effects can also be dismissed.

For better comparability of the experimental and numerical results for ζ, we apply a set of mismatches to our model (5.1)-(5.4) to account for slight asymmetries in the experimental setups and minor mismatches in the laser parameters of the order of 1%.

The set of mismatches reads:

$$
\begin{aligned}
&\tau_{\mathrm{fb},1} = 2000,\ \tau_{\mathrm{fb},2} = 2040 \rightarrow \tau_c = 2020; \\
&K_{\mathrm{fb},1} = 0.1,\ K_{\mathrm{fb},2} = 0.103 \rightarrow K_c = 0.1015; \\
&\alpha_1 = 3.0,\ \alpha_2 = 3.02; \\
&p_2 = p_1 + 0.001.
\end{aligned}
\tag{5.5}
$$

The results for ζ with these mismatches included in the model and for the same parameter ranges as in Fig. 5.7 is depicted in Fig. 5.9.

Indeed, the resulting synchronized dropout fractions agree better with the experimental outcome for larger pump current values but they still reflect the main features from the symmetric case. The minimum value of ζ for small to moderate noise strengths $\beta = 10^{-9} - 10^{-6}$ has decreased from $\zeta = 0.7$ for the completely symmetric case to $\zeta = 0.4$ for the case with mismatches and asymmetries, as described by (5.5).

A horizontal cross section of Fig 5.9 at $\beta = 10^{-6}$ is shown in Fig. 5.10, together with the corresponding cross section from the symmetric case (Fig. 5.7) and the experimentally-obtained pump current dependence of ζ (Fig. 5.5). The improved correspondence of the numerical results for the asymmetric setup with the experimental results is clearly visible.

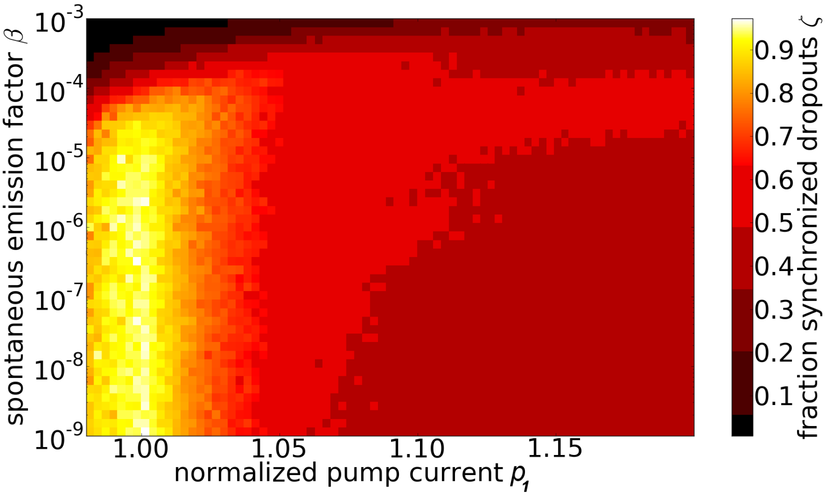

Figure 5.9: Numerical results for the fraction of synchronized power dropouts ζ versus the normalized pump current p_1 versus the spontaneous emission factor β in a setup with small asymmetries and slightly mismatched lasers. The simulation parameters correspond largely to those listed in Table 5.1 with the mismatches given by (5.5). $p_2 = p_1 + 0.001$

5.6 Discussion, Adaptability and Outlook

We have presented a method to characterize the deterministic nature of individual power dropouts in the LFF regime of a single semiconductor laser with feedback, utilizing zero-lag synchronization with a twin. From experimental data, we found 85% of dropouts to be synchronized when the laser was pumped close to its solitary threshold. We conclude that at least 85% of the power dropouts in that pump regime are deterministically driven. Within our approach, conclusions are strongest the larger the synchronized dropout fraction ζ is. For the regime with a smaller ζ, one can complement the presented method with statistical measures based on an information-theoretical analysis. Those measures are based on different approaches and therefore exhibit other opportunities and limitations. Aragoneses et al., for example, implemented ordinal pattern analysis by codyfying as symbols successive inter-drop-intervals (IDIs) in experimental intensity timeseries, and categorizing these patterns by statistically-obtained characteristic features related to a dynamical resting state. They use these features to distinguish signatures of determinism and stochasticity, and, thus, allow to statistically infer the prevalence of deterministically-driven or noise-driven power dropout for specific operating parameters [62]. Combining an individual event-based ap-

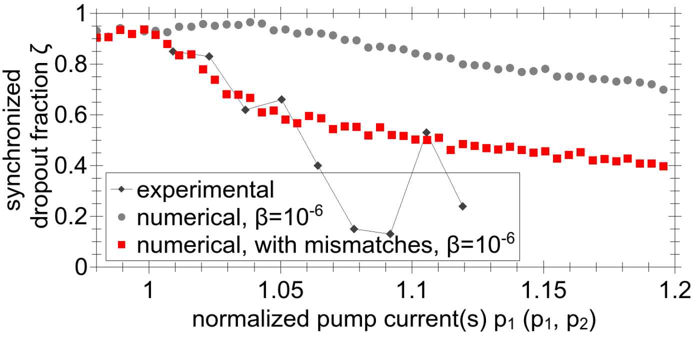

Figure 5.10: ζ versus normalized pump currents p_1, p_2 for the experimental and the symmetric numerical results (dark grey diamonds and light grey circles, respectively), and ζ versus normalized pump current p_1 for the numerical results with applied mismatches (see (5.5)), including $p_2 = p_1 + 0.001$ (red squares). For the numerical curves $\beta = 10^{-6}$.

proach with others based on statistical methods like the one described above could give a broader access to characterizing semiconductor laser dynamics over a wider range of parameters. This might enable further tailoring of dynamical features and their utilization in applications.
The presented approach can in general be applied to other chaotic systems with intrinsic noise that are synchronizable and exhibit irregular characteristic events (e.g. spikes, dips, patterns). As a necessary condition, the synchronized dynamics of two coupled twin subsystems have to be identical to the dynamics of a corresponding single system. If the required symmetry conditions apply, the presented method can even be applied to systems whose governing equations are unknown. Since bubbling is not present in all coupling schemes of noisy chaotic oscillators, the corresponding fraction ζ of synchronized characteristic events could have an even higher significance for those kinds of systems.

One example is the spiking dynamics of a cortical column. A few years ago, it was shown that two single neurons of Hodgkin-Huxley-type can synchronize identically their spiking behavior if coupled via a "relay-neuron". This also works for bidirectionally-coupled neuron populations (for both cases see e.g. [77]). In a forthcoming paper [212] the authors investigate the possibility to synchronize spikes of two neuron populations that are coupled bidirectionally via a third population. Each of the neuron populations are subject to independent noise which also drives the dynamics; still most spikes are synchronized. In comparison, in a motif where a pair of identical neuron masses are being unidirectionally stimulated by a third driver neuron mass (but not coupled to each other), the two neuron populations exhibit no correlation in their spiking behavior. The statistical distribution of the interspike-intervals (which corresponds to the spiking frequency) of the relay-coupled neuron populations corresponds to that of a single one. One could then investigate the deterministic nature of individual spikes or spike trains via synchronization and distinguish them from other spikes that are possibly dominantly induced by noise.

Future work could entail classification of dropout events as being deterministically-driven using statistical or pattern-recognition approaches utilizing machine learning concepts (see Chapter 6 and [99, 101, 104, 213]). This ansatz would work only if we assume the existence of common dynamical features as precursors of deterministically-induced power dropouts. The dynamics preceding known deterministic dropouts would be used to train the data processing reservoir. Yet unclassified dropout events would then be fed into the trained reservoir and be classified binarily - as deterministically-driven or not. Another potential implementation of reservoir computing concepts within this scheme could be the prediction of occurence of deterministic dropouts from precursors in the intensity timeseries utilizing the memory capabilities of a reservoir [104, 109, 213].

6

Data processing using transient laser dynamics

6.1 Reservoir computing

Our time exhibits a soaring amount of information and an ever-increasing number of information processing tasks due to new information technologies. At the same time, there is a higher demand for faster and more efficient data processing techniques that require novel computational concepts that surpass the capabilities of tradional computers [214, 215]. New concepts, some of which are neuro-inspired, are being considered and developed [101, 216]. One of the most promising is known as Reservoir Computing (RC). RC comprises Echo State Networks (ESN) [101] and Liquid State Machines (LSM) [103]. Traditional RC is based on utilizing the transient dynamics of complex recurrent networks for computational tasks. A schematic illustration of the RC concept is shown in Fig. 6.1. These complex networks form the reservoir and often consist of a large number of randomly-connected nonlinear nodes. The large number of nodes induces a high-dimensional state space of the reservoir.

Previously, artificial neurons have been chosen to serve as dynamical nodes. Recently, however, new approaches are being considered which include using other types of nonlinearities as nodes and employing different coupling topologies within the reservoir. Among these approaches, delayed feedback nonlinear systems [104], coupled semiconductor optical amplifiers (SOAs) [107, 217] or photonic crystal cavities [218] are being contemplated.

No matter which nonlinear nodes form the network, the reservoir always serves as the core element for information processing. The input signals, which are mostly low dimensional, are fed into the reservoir through certain input channels, as illustrated in Fig. 6.1. The connections from the input

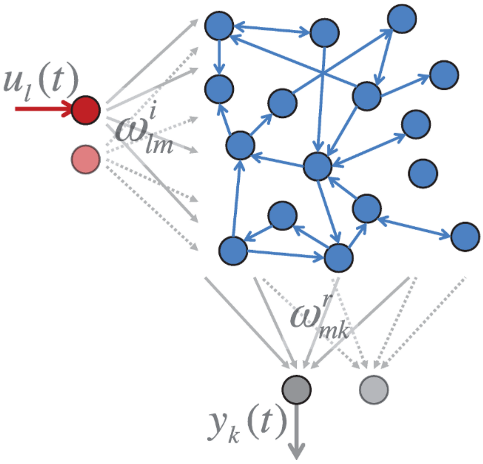

Figure 6.1: Schematic of the classic reservoir computing (RC) approach based on a complex network of coupled nonlinear nodes. $u_l(t)$ represents the input signal, w^i_{lm} are the input weights, w^r_{mk} are the readout weights and $y_k(t)$ corresponds to the output. Figure courtesy of D. Brunner.

layer to the nodes of the reservoir are usually assumed to have random weights w^i_{lm}. The signal dimension is expanded in proportion to the number of nodes via the dynamical response of the reservoir. The readout processing, i.e., the processing of the network's response to the injected information, is evaluated via a linear-weighted sum with coefficient w^r_{mk} of the states of all nodes in the reservoir. These weights connect each node with the output layer of the RC scheme. This evaluation of the processed data in the reservoir via a linear-weighted sum is possible because the input signal is nonlinearily projected onto the high-dimensional state space that is created by the many nodes in the reservoir. Because of the characteristics of the reservoir and its large number of dynamical degrees of freedom, complex classification tasks (like pattern recognition) and any nonlinear appproximation can be realized.

For the RC concept to work, the system needs to be trained for any task with known signals that correspond to that task. This training procedure determines the readout weights w^r_{mk}. After the training stage has finished, unknown signals that belong to the same group as the training signals can be analyzed and classified using the trained reservoir.

Reservoir computing requires the system to conform to certain properties to achieve good performance results, one of the most important ones being consistency [219]. Consistency means that the system's responses to identical or almost identical input signals have to be identical or sufficiently similar. Getting a similar response of the reservoir for different but similar inputs is called the approximation property, a crucial condition for RC to work.

Consistency in the networks response is typically attained by setting the reservoir to operate in an asymptotically stable quiescent state (fixed point) if no input is injected. When the reservoir is excited by an external stimulus (i.e., the to-be-processed information), it exhibits nonlinear transient dynamics. The transient states are essential for the information processing and have to exhibit some specific characteristics. First the approximation property is required, second, if two injected input signals belong to different classes, the corresponding transient states of the network must differ sufficiently (separation property). Moreover, these two properties should be complemented by a short-term (fading) memory of the system [213]. With such a memory, input information is processed in the context of information injected in the past, which enables meaningful processing of sequences of input information. If all these crucial requirents are met, the system can be used for Reservoir Computing.

In this chapter, we perform a thorough numerical study of the computational performance of a system consisting of a single semiconductor laser node which receives its own delayed feedback. We demonstrate how the rich dynamical properties of such a system can be employed to sucessfully process time-dependent input signals. The chapter is organized as follows. In Section 6.2, we introduce the concept of single-node RC, motivate the use of semiconductor lasers as dynamical node and describe some fundamental specifications of the approach. Following that, we describe the two computational tasks we have chosen to evaluate the computational capabilities of our system in Section 6.3. In Section 6.4, we characterize in detail the numerical model we use. Next, we present the results obtained from extensive numerics for the two data processing tasks in Section 6.5, after which we compare some of those results to recent experimental implementations of RC using a single laser with feedback in Section 6.6. The following Section 6.7 describes two simple methods to further improve upon the performance of our scheme. Finally, we summarize our findings and give an outlook for future work in Section 6.8.

Large parts of the results presented in this chapter have been published as "K. Hicke, M.A. Escalona-Moran, D. Brunner, M.C. Soriano, I. Fischer, C.R. Mirasso: *Information Processing Using Transient Dynamics of Semiconductor Lasers Subject to Delayed Feedback*, IEEE Journal of Selected Topics in Quantum Electronics **19**, 1501610 (2013)". The RC input training and the testing and evaluation procedures have been adapted to the laser system and implemented for the specific data processing tasks in close collaboration with Miguel-Angel Escalona. The program code framework for training and testing was adapted from the Oger toolbox [220]. The experiments described in Section 6.6 have been executed and their results have been analyzed by Daniel Brunner et al. from our laboratory. Their results have been published in [109].

6.2 Single dynamical node - semiconductor laser with delayed feedback

The experimental implementation of RC brings a key challenge with it. Large networks of randomly-connected nonlinear dynamical elements are required for traditional RC but hard to implement in hardware. Therefore, until recently, mostly software realizations were considered. To overcome this challenge, the use of delay-coupled systems has been recently proposed and proven to be as efficient as traditional RC in certain tasks, or even to outperform them [104–106].

One of the simplest possible delay systems consists of a single nonlinear node which receives time-delayed feedback from itself. Such a system is relatively easy to implement, since it comprises only two main elements, a nonlinear node and a delay loop. Recently, experimental evidence showed the capability of simple systems to perform computational tasks. In particular, the strengths of nonlinear systems, either electronic circuits [104], optoelectronic [105, 106, 221] or all-optical systems [108, 109], subject to delayed feedback have been demonstated. Such systems have been shown to perform similarly well as traditional reservoir computing techniques for certain computationally hard tasks.

Semiconductor lasers subject to delayed optical feedback from an external mirror [133] thus represent excellent candidates to implement all-optical RC. This system has been well-studied and exhibits a rich complex dynamical behavior under various conditions (see Chapter 2 and e.g. [30]). Moreover, semiconductor lasers are off-the-shelf, high-bandwidth components that are power efficient and already the main component in current actual fiber communication networks. Realizing information processing utilizing semiconductor lasers could lead to a paradigm shift in the field of photonic information processing, leaving behind traditional approaches and employing novel concepts of machine learning.

From a mathematical perspective, dynamical systems become infinite dimensional when delayed feedback is introduced. This is because their state at time t depends on the output of the nonlinear node during the continuous time interval $[t-\tau, t[$, with τ being the delay time. In practice, the dynamics of the delay system remains finite dimensional [222], but posesses the property of high dimensionality and a short-term memory, as is necessary for RC. Delay systems are very attractive from the implementation point of view, since only few components are required to build them. A schematic representation of single-node RC utilizing a semiconductor laser with delayed optical feedback is shown in Fig. 2.

Within one delay interval of length τ, we define N equidistant points separated in time by $\Theta = \tau/N$. These N equidistant points are called "virtual nodes", since they play a role analogous to the (physical) nodes of a

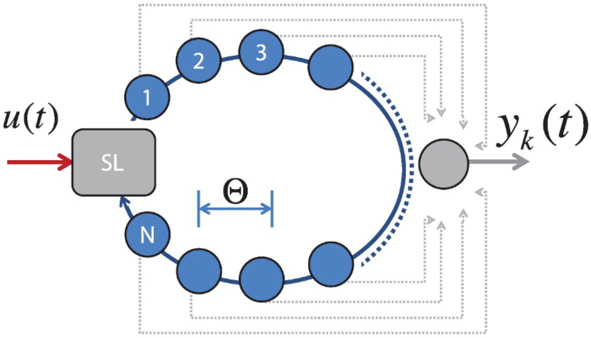

Figure 6.2: Schematic representation of RC based on a single semiconductor laser subject to time-delayed feedback via time multiplexing. SL stands for the semiconductor laser and the blue circles represent the N virtual nodes in the feedback delay loop. They are separated by time Θ. $y_k(t)$ represents the output signal. Figure courtesy of D. Brunner.

traditional reservoir. The values of the dynamical variable at each of the N points, in this case extracted from the light intensity at the output of the laser, define the states of the virtual nodes. These dynamical states of the nodes characterize the transient response of the laser to a certain input signal at a given time. The temporal separation Θ of the virtual nodes plays an important role and can be used to optimize the reservoir performance. We choose $\Theta < T$, where T is the characteristic time scale of the semiconductor laser dynamics. The time scale T is given by the inverse of the relaxation oscillation frequency. Due to this choice of Θ, the states of the virtual nodes become dependent on the states of neighboring nodes. Interconnected in this way, the virtual nodes emulate a network serving as reservoir [104].
The virtual nodes are subjected to a time-continuous input stream $u(t)$ or time-discrete input $u(k)$ which can be a time-varying scalar variable or a vector of any dimension Q. The injection of the respective information into the individual virtual nodes is realized by serializing the input using time multiplexing. Time multiplexing works as follows. The input stream $u(t)$ or $u(k)$ undergoes a sample and hold operation to define a stream $R(t)$ which is constant during one delay interval τ before it is updated. Our approach therefore always involves time-discretized inputs to the reservoir, irrespective of whether the input signals originate from time-continuous or time-discrete input streams. To define the coupling weights from the stream $R(t)$ to the virtual nodes, we introduce a random $(N \times Q)$ matrix M, called the con-

nectivity mask. Upon carrying out the multiplication $S(t_0) = M \times R(t_0)$ at a certain time t_0, we obtain a N dimensional vector $S(t_0)$ which represents the temporal input sequence within the interval $[t_0, t_0 + \tau[$. Each virtual node is updated using the corresponding component of $S(t_0)$. Alternatively one can view $S(t)$ as a continuous time scalar function which is constant over periods corresponding to the node separation Θ. After a period τ, the states of all virtual nodes are updated and the new reservoir state can be obtained. For this, $R(t_0)$ is updated in order to drive the reservoir during the next τ period. For each period, the reservoir state is read out for further processing.

A training algorithm assigns an output weight to each virtual node, such that the linear weighted sum of the node states approximates the desired target value as closely as possible (see [104] for details). The training of the readout follows the standard procedures for RC (see e.g. [99, 101]). Testing of the reservoir is executed using previously-unseen input data of the same kind as those used for the training procedure.

All-optical implementations of the Reservoir Computing paradigm can be built with off-the-shelf components, either based on semiconductor optical amplifiers [108] or semiconductor lasers [109]. These two approaches have been developed in parallel. The utilization of a semiconductor laser allows to benefit from injection locking of the laser to the injected optical information, thus increasing the signal to noise ratio considerably. This, in turn, enables to achieve better performance and to employ faster data injection. The capacity of a single semiconductor laser subject to optical feedback to process information will be the focus of this chapter.

For our numerical investigation, our reservoir is set to consist of $N = 400$ nodes with the delay being $\tau = 80$ ns. The resulting virtual node spacing $\Theta = \tau/N$ is therefore $\Theta = 200$ ps, which fulfills the condition $\Theta < T$ (see above).

6.3 Computational tasks

In this chapter, we consider two different tasks to evaluate the information processing capabilities of a single semiconductor laser subject to time-delayed optical feedback: a pattern recognition task where digital signals of spoken digits are classified, and the prediction of a chaotic time-series. These two tasks are well-recognized in the machine-learning community as benchmark tests for the data processing power of the system under investigation. However, different mathematical operations have also been implemented as computational tasks, using this scheme [102].

6.3.1 Isolated spoken digit recognition

We begin with the spoken digit recognition task. The spoken digit dataset consists of a total of 500 audio samples of five female speakers uttering numbers from zero to nine with a tenfold repetition for statistics [223]. Before we inject the information into the laser, the samples are preprocessed into cochleograms using the Lyon ear model [224]. In cochleograms, the acoustical information is split into 86 frequency channels, creating a two-dimensional sample matrix. Fig. 6.3 shows an example of such a cochleogram corresponding to the uttering of the number "nine".

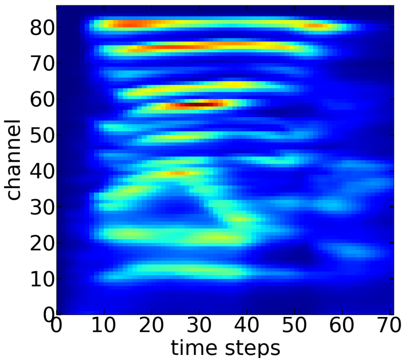

Figure 6.3: Sample cochleogram representing the acoustical signal of an uttering of the number "nine". The information is distributed over 86 frequency channels.

We subsequently perform matrix multiplication of the sample cochleograms with a random connectivity matrix (mask) M defining the coupling weights of the virtual nodes in our reservoir.

For this task, M is chosen to have sparse connectivity with only 10% of the elements of M being nonzero. The nonzero random weights take the values 0.59 and 0.41. The sparsity reduces the amount of redundant information that is coupled into the system. The input state matrices resulting from the multiplication are spatio-temporal representations of the input data stream that is injected into the system. Fig. 6.4 depicts the input state matrix corresponding to the sample cochleogram shown in Fig. 6.3.

To characterize the classification performance, we evaluate the word-error-rate (WER) as a function of several key parameters of our system: the pump current, the feedback strength and the noise intensity. This is done for different operating conditions.

For the WER evaluation, we choose 20 random partitions of 25 samples each from our 500 spoken digit dataset, and we use 19 of these partitions for training the readout weights and keep the remaining 25 samples for testing.

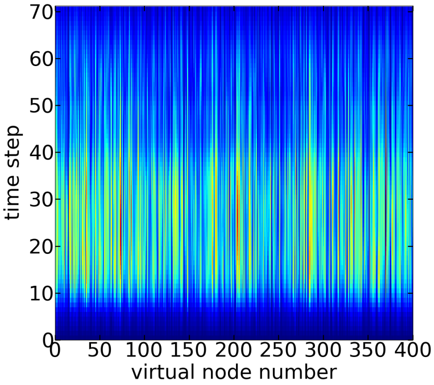

Figure 6.4: Spatio-temporal input state matrix corresponding to the acoustical signal represented by the cochleogram in Fig. 6.3. The horizontal axis represents one delay time τ with the virtual node number corresponding to the spatial position within the delay line.

The procedure is repeated such that each random partition and each sample are exactly used once for testing. This approach then describes a 20-fold cross-validation.

The measure we use as performance indicator is the average WER calculated from the error rates of each of the 20 folds.

6.3.2 Santa Fé timeseries prediction

The second computational task we tackle is time-series prediction. In this task, we evaluate the performance of our scheme in predicting the respective next point of a chaotic time series. Specifically, we employ data from the Santa Fé competition dataset A [225]. This time series was experimentally obtained by recording periodic and chaotic intensity pulsations of an unidirectional far-infrared NH_3 ring laser at a wavelength of 81.5 μm. A part of the used data is shown in Fig. 6.5. For a full description of the experimental scheme, see [226]. The time series data is normalized by substracting the overall mean value and scaling with the inverse of its standard deviation.

Of this dataset, we use 75% of the points for training of the readout weights and 25% for testing. Repeating the approach mentioned in the spoken digit recognition, we apply a 4-fold cross validation.

The information injected into the laser is given by the product of the samples in the Santa Fé time series competition dataset A and an one-dimensional input mask M. For this prediction task, the matrix M describes a fully connected reservoir made up of the virtual nodes in the delay line of our scheme. This means that M has only nonzero elements. They are chosen

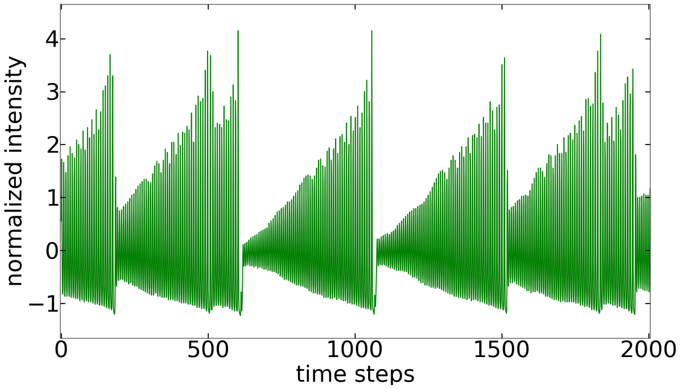

Figure 6.5: Part of a chaotic time series of laser intensity pulsations constituting the Santa Fé competition dataset A. The time series data has been normalized before preprocessing.

randomly from $\{-1.0, 1.0\}$. Memory-dependent prediction requires the full available information.

We characterize the prediction performance of our scheme by calculating the normalized mean square error (NMSE) of the prediction. It is defined as the normalized difference between the predicted value and the target value of the timetrace:

$$\mathrm{NMSE} = \frac{\left\langle (P_i - T_i)^2 \right\rangle}{\left\langle (T_i - \langle T_i \rangle)^2 \right\rangle} \tag{6.1}$$

where N is the number of values, P_i and T_i, $i = 1..N$ are the predicted values and target values, respectively, and $\langle \cdot \rangle$ denotes averaging.

Our investigation focuses on the dependence of the NMSE on the laser's pump current, the feedback rate and the injection strength, i.e., the input scaling. We also study the influence of spontaneous emission noise on the time series prediction performance. The performance is investigated for different feedback configurations and operating conditions.

6.4 Modeling

6.4.1 Model characteristics

To evaluate the computational capabilities of a single laser with delayed feedback within the reservoir computing scheme, we consider the extended two-mode model introduced in Chapter 2 and in [139]. The electric field is modeled as superposition of two orthogonal modes ($\|$ and $\perp$) which correspond to two orthogonal polarization axes. The model consists of three equations for the slowly varying complex electric field amplitude in two orthogonal polarization directions and the carrier number n. The parallel polarization direction of $\mathcal{E}_{\|}$ is defined by the axis of the laser cavity. We adapt the equations for two methods of signal injection (electrical and optical, respectively). The model reads

$$\begin{aligned}
\dot{\mathcal{E}}_{\|}(t) &= \frac{1}{2}(1+i\alpha)\left(\mathcal{G}_{\|}(\mathcal{E}_{\|},n)-\gamma_{\|}\right)\mathcal{E}_{\|}(t)+K_{\|\|}+K_{\perp\|} \\
&\quad +\sqrt{P_{\mathrm{inj}\|}(t)}e^{i\Delta\omega_{\|}t}+F_{\mathcal{E}_{\|}}, \qquad (6.2) \\
\dot{\mathcal{E}}_{\perp}(t) &= \frac{1}{2}(1+i\alpha)\left(\mathcal{G}_{\perp}(\mathcal{E}_{\perp},n)-\gamma_{\perp}\right)\mathcal{E}_{\perp}(t)+K_{\perp\perp}+K_{\|\perp} \\
&\quad +\sqrt{P_{\mathrm{inj}\perp}(t)}e^{i\Delta\omega_{\perp}t}-i\Delta\Omega\mathcal{E}_{\perp}(t)+F_{\mathcal{E}_{\perp}}, \qquad (6.3) \\
\dot{n}(t) &= \frac{I(t)}{e}-\gamma_e n(t)-\mathcal{G}_{\|}(\mathcal{E}_{\|},n)\left|\mathcal{E}_{\|}(t)\right|^2 \\
&- \mathcal{G}_{\perp}(\mathcal{E}_{\perp},n)\left|\mathcal{E}_{\perp}(t)\right|^2, \qquad (6.4)
\end{aligned}$$

The rate equations are normalized such that $\left|\mathcal{E}_{\|}(t)\right|^2$ and $\left|\mathcal{E}_{\perp}(t)\right|^2$ represent the number of photons in the parallel and perpendicular polarization direction, respectively. The output power is computed as

$$P = \left[hc^2\alpha_m/(2\mu_g\lambda)\right]\left|\mathcal{E}\right|^2 \qquad (6.5)$$

where h is the Planck constant, c the speed of light, λ the emission wavelength, α_m the facet losses and μ_g the group refractive index.
The quantity we use as readout measure to test the computational properties of this single laser system is the overall output intensity

$$P_{out} = \left|\mathcal{E}_{\|}\right|^2+\left|\mathcal{E}_{\perp}\right|^2. \qquad (6.6)$$

In the set of parameters, $K_{\|\|}$ denotes the delayed feedback from the parallel mode to itself, $K_{\|\perp}$ is the feedback term from the parallel mode to the perpendicular one and so forth. Optical signal injection into each mode is modeled by the injection term $\sqrt{P_{\mathrm{inj}\|,\perp}(t)}e^{i\Delta\omega_{\|,\perp}t}$ where $P_{\mathrm{inj}\|,\perp}(t)$ is the time-dependent power injected into the $\|$, $\perp$ mode and $\Delta\omega_{\|,\perp}$ is the frequency detuning between the optical injection and the respective mode. $I(t)$ is the time-dependent injection current which is used to model electrical signal injection. Details about the two injection methods will be given in subsection 6.4.4.

The gain functions are modeled as nonlinear to account for nonlinear gain saturation effects (see Chapter 2). The gain reads

$$\mathcal{G}_{\|}(\mathcal{E}_{\|}, n) = g_{\|} \frac{n(t) - n_T}{1 + \epsilon \left|\mathcal{E}_{\|}(t)\right|^2} , \tag{6.7}$$

$$\mathcal{G}_{\perp}(\mathcal{E}_{\perp}, n) = g_{\perp} \frac{n(t) - n_T}{1 + \epsilon \left|\mathcal{E}_{\perp}(t)\right|^2} . \tag{6.8}$$

Furthermore, α is the linewidth enhancement factor, $\gamma_{\|,\perp}$ are the photon decay rates, $\Delta\Omega$ is the detuning between $\mathcal{E}_{\|}(t)$ and $\mathcal{E}_{\perp}(t)$, $I(t)$ is the time-dependent injection current, e is the elementary charge, γ_e denotes the electron decay rate, $g_{\|,\perp}$ are the differential gains, n_T is the carrier number at transparency and ϵ is the gain saturation coefficient.

The spontaneous emission noise is implemented as complex Gaussian white noise terms $F_{\mathcal{E}_{\|,\perp}}$ in the field equations where the real and imaginary parts are independent random processes. The noise terms have zero mean

$$\left\langle F_{\mathcal{E}_{\|,\perp}}(t) \right\rangle = 0 \tag{6.9}$$

and a variance given by

$$\left\langle F_{\mathcal{E}_{\|,\perp}}(t) \overline{F_{\mathcal{E}_{\|,\perp}}(t')} \right\rangle = 2\beta_{\|,\perp}\gamma_e n(t)\delta(t - t') , \tag{6.10}$$

where $\beta_{\|,\perp}$ are the spontaneous emission factors, describing the fraction of spontaneously emitted photons coupled into the respective lasing modes.

In principle, carrier noise can be implemented in this model in a similar manner, i.e., by adding a Langevin term F_n to the carrier equation (6.4). Though some works have investigated the influence of carrier noise on the dynamics, it has been found that its effect can often be disregarded.

6.4.2 Relation of modes

Due to the characteristics of edge emitting lasers, the two orthogonal modes $\mathcal{E}_{\|}$ and $\mathcal{E}_{\perp}$ differ in sensitivity to perturbations. For simplicity, we assume that the dominant field component is $\mathcal{E}_{\|}(t)$, and, consequently, only the delay term of the parallel component appears in the equation for $\mathcal{E}_{\perp}(t)$ but not vice versa, i.e., $K_{\perp\|} = 0$. Because of its relative suppression, feedback from the orthogonal mode $\mathcal{E}_{\perp}$ to itself is here neglected for simplicity: $K_{\perp\perp} = 0$.

Furthermore, also because of the geometry of edge-emitting laser cavities, the differential gains for both modes is assumed to be different, with the gain for the parallel mode $g_{\|}$ being larger than the gain for the perpendicular mode $g_{\perp}$. The ratio of the differential gains are chosen according to [139]. They are considered adequate to describe single mode edge-emitting semiconductor lasers. The photon decay rates of both modes are assumed to be equal: $\gamma_{\|} = \gamma_{\perp} \equiv \gamma$.

In addition, we assume that both polarization components have the same frequency. Accordingly, the detuning is set to zero: $\Delta\Omega = 0$.

6.4.3 Feedback configurations

The delayed optical feedback is modeled for two different configurations: polarization-maintained optical feedback (PMOF) and polarization-rotated optical feedback (PROF). For the case of PMOF, as the polarization direction is yielding a higher optical gain, the optical feedback goes from the dominant mode ($\mathcal{E}_{||}$) back to itself. For PROF, the feedback goes from the dominant polarization mode ($\mathcal{E}_{||}$) to the weaker polarization mode ($\mathcal{E}_{\perp}$). The two remaining feedback terms are modeled as

$$
\begin{aligned}
K_{||||} &= \kappa_{||}\mathcal{E}_{||}(t-\tau) \qquad (6.11)\\
K_{||\perp} &= \kappa_{\perp}\mathcal{E}_{||}(t-\tau) \qquad (6.12)
\end{aligned}
$$

where $\kappa_{||,\perp}$ are the respective feedback rates, and τ is the external cavity roundtrip time, defining the feedback delay. In the case of PMOF the feedback rate $\kappa_{\perp} = 0$ and in case of PROF $\kappa_{||} = 0$.

6.4.4 Signal injection methods

Now we consider the injection of a time-dependent input signal $S(t)$ into the laser to study its data processing capabilities. We consider two different methods: electical injection and optical injection. The electrical signal injection scheme corresponds to a modulation of the laser injection current $I(t)$ around a pump (bias) current I_b, corresponding to

$$I(t) = I_b + \chi I_{thr} S(t) \qquad (6.13)$$

with the signal scaling χI_{thr}. Here, I_{thr} denotes the solitary laser threshold current. For electical injection, $S(t)$ is normalized and always positive; the modulation is therefore asymmetric. The modulation frequency is chosen to correspond to 5 GHz, thus the signal is injected with a rate of 5 Gigasamples per second (5 GS/s). Fig. 6.6 shows an example for the intensity response of our laser system (blue line) for the case of electrical signal injection. The input, which corresponds to the spoken digit "nine", modulates the injection current $I(t)$ (red line). The inset shows a zoomed view of both input current and output intensity time series, respectively. The feedback is PMOF with $\kappa_{||} = 10$ ns^{-1}.

In the case of optical injection, the signal $S(t)$ is injected optically via the time-dependent optical power P_{inj}. For the sake of comparison with experiments we assume that the injected light which is coming from a second (driver) laser is modulated externally via a Mach-Zehnder (MZ) electro-optic modulator device. The input is then modeled as the power P_{inj} modulated with a sine-squared nonlinearity around a mean value P^0_{inj}:

$$P_{inj}(t) = P^0_{inj} + P^s_{inj} \sin^2\left(a\frac{\pi}{4}S(t) + \Phi_0\right). \qquad (6.14)$$

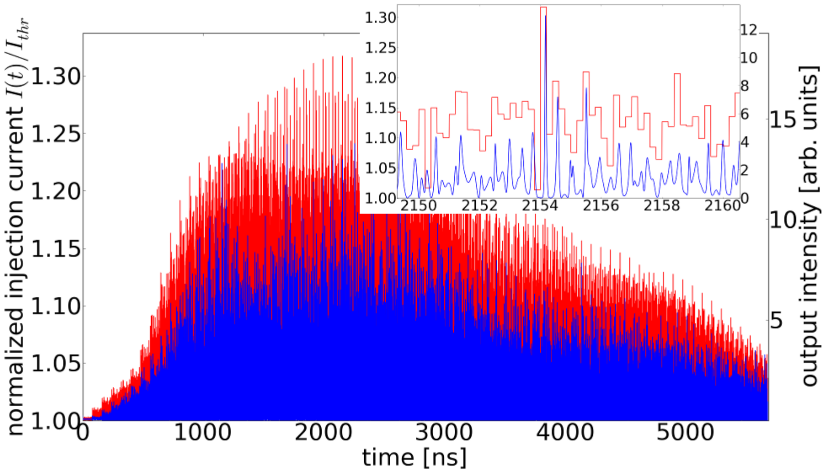

Figure 6.6: Laser response (blue curve) to an electrically-injected signal corresponding to the spoken digit "nine". The red curve corresponds to the time-varying injection current. The inset depicts a zoom of both traces. The modulation frequency corresponds to 5 GS/s. The applied feedback is PMOF with $\kappa_{\|} = 10$ ns^{-1}

We set $P^0_{inj} = \bar{P}_{inj}/4$ and $P^s_{inj} = 3/2\bar{P}_{inj}$ so that

$$P_{inj}(t) = \bar{P}_{inj}\left[1/4 + 3/2\sin^2\left(a\frac{\pi}{4}S(t) + \Phi_0\right)\right], \tag{6.15}$$

which means that the injected power is modulated between ±75% around the average injected power $\bar{P}_{\text{inj}}$.

For optical injection modulation, we distinguish between two different modulation methods. We consider symmetric modulation with $S(t)$ normalized between ± 1, $a = 1$ and $\Phi_0 = \frac{\pi}{4}$ and asymmetric modulation with $S(t)$ being normalized positive, $a = 2$ and $\Phi_0 = 0$. Fig. 6.7 shows an explanatory schematic of the MZ-nonlinearity to illustrate the modulation with two different bias values.

For further comparibility with experimentally obtained results, we model the optical signal injection only going into the dominant mode $\mathcal{E}_{\|}$ in our study. That means $P_{\text{inj}\perp}(t) = 0$.

Since we find that our scheme performs much better in the time series prediction task if the information is injected optically, we concentrate on this injection method. Due to the nature of the injected data in the Santa Fé time series, the prediction capability of our system will be tested by applying optical signal injection with symmetric modulation only. The spoken digit recognition task will be studied for electical injection and asymmetric optical injection.

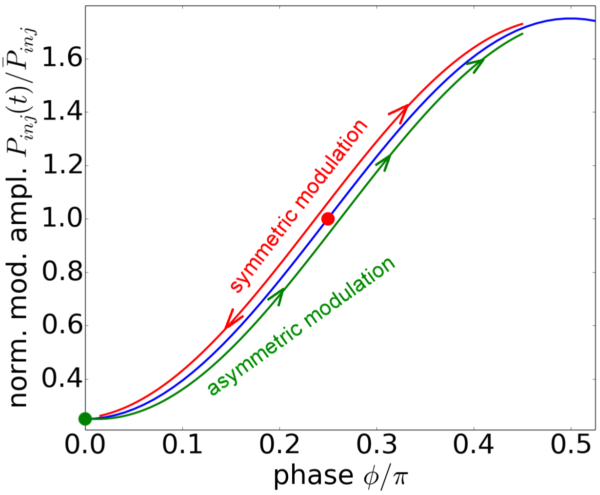

Figure 6.7: The sine-squared nonlinearity of the Mach-Zehnder electro-optic modulator (blue) corresponding to Eq. (6.15) vs the phase. The red dot illustrates the operating point for symmetric modulation while the green dot corresponds to the operating point for asymmetric modulation. The modulation ranges coincide.

To decrease the number of dependences of the computational performance on system parameters, we further assume that the injected signal has the same optical frequency as the laser, i.e., the detuning term is set to zero: $\Delta\omega = 0$. The input sample rate for optical injection, too, is set to 5 GS/s. Fig. 6.8 shows the response of the laser (blue line) to an optically-injected signal. The input power $P_{inj}(t)$ (red line) corresponds to the preprocessed spoken digit "nine" and originates from asymmetric modulation of the incident optical signal. The inset shows a zoomed view of both injected power and output intensity time series, respectively. One can nicely see the transient states with the dynamics exhibiting relaxation oscillations toward constant intensity. The modulation frequency corresponds to 5 GS/s, the laser is being pumped at threshold $I_b = I_{thr}$, the average injected power is $\bar{P}_{inj} = 436\mu$W and the feedback configuration is PMOF with $\kappa_{\|} = 10$ ns^{-1}.

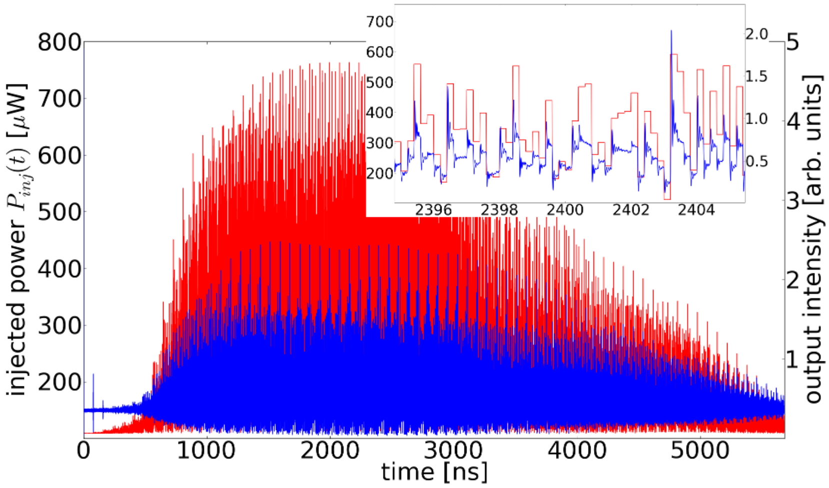

Figure 6.8: Laser response (blue curve) to an optically-injected signal corresponding to the spoken digit "nine". The red curve corresponds to the injected optical power. The inset depicts a zoom of both traces. The modulation frequency corresponds to 5 GS/s. The laser is pumped at threshold. The average injected power is $\bar{P}_{inj} = 436\mu$W. The applied feedback has a rate of $\kappa_{\parallel} = 10$ ns^{-1}.

6.4.5 Applied simplifications and parameters

When we apply the simplifications described above, the model reads

$$\dot{\mathcal{E}}_{\parallel}(t) = \frac{1}{2}(1+i\alpha)\left(\mathcal{G}_{\parallel}-\gamma\right)\mathcal{E}_{\parallel}(t) + \kappa_{\parallel}\mathcal{E}_{\parallel}(t-\tau) + \sqrt{P_{\text{inj}}(t)} + F_{\mathcal{E}_{\parallel}} \quad (6.16)$$

$$\dot{\mathcal{E}}_{\perp}(t) = \frac{1}{2}(1+i\alpha)\left(\mathcal{G}_{\perp}-\gamma\right)\mathcal{E}_{\perp}(t) + \kappa_{\perp}\mathcal{E}_{\parallel}(t-\tau) + F_{\mathcal{E}_{\perp}} \quad (6.17)$$

$$\dot{n}(t) = \frac{I(t)}{e} - \gamma_e n(t) - \mathcal{G}_{\parallel}\left|\mathcal{E}_{\parallel}(t)\right|^2 - \mathcal{G}_{\perp}\left|\mathcal{E}_{\perp}(t)\right|^2 . \quad (6.18)$$

We will use this model for our numerical investigations. The equations are numerically solved using Milshtein's method [208, 209] with a stepsize corresponding to $0.1\gamma^{-1}$. The chosen values for the parameters used in the numerical simulations are shown in Table 6.1. The given values are the default values for the numerics. Some of the feedback-related parameters only apply in certain cases, e.g. $\kappa_{\perp} = 10$ ns^{-1} applies only for the PROF case, otherwise $\kappa_{\perp} = 0$ (see subsection 6.4.3).

6.5 Numerical results

In this section, we present numerical results for the performance of our scheme in two different computational tasks: first we investigate spoken

Parameter	Value	Parameter	Value
α	3.0	$g_{\parallel}$	10^{-5} ns^{-1}
γ	200 ns^{-1}	$g_{\perp}$	$8.4{\cdot}10^{-6}$ ns^{-1}
$\beta_{\parallel}$	10^{-6}	ϵ	10^{-7}
$\beta_{\perp}$	10^{-6}	λ	1.5 μm
$\kappa_{\parallel}$	10 ns^{-1}	α_m	45 cm^{-1}
$\kappa_{\perp}$	10 ns^{-1}	μ_g	4
τ	80 ns	n_T	$1.8 \cdot 10^8$
$\Delta\omega$	0.0	χ	0.4
$\Delta\Omega$	0.0	P_{inj}	436μW
γ_e	1 ns^{-1}	I_{thr}	32.0 mA

Table 6.1: Laser parameter values used in the numerical simulations.

digit recognition as a classification task, then time series prediction is studied. The results are obtained from the simulations of a semiconductor laser subject to delayed optical feedback. While the former does not require much memory, and consequently the feedback is expected not to play an important role, the latter is memory-dependent, and feedback is expected to be essential. In our numerical analysis, the reservoir consists of $N = 400$ virtual nodes and the delay is $\tau = 80$ ns, resulting in a virtual node spacing of $\Theta = 200$ ps (τ/N). We begin with analyzing the performance in both tasks in dependence of laser pump current and feedback strength. The latter is evaluated both for PMOF and for PROF, respectively. Then, we investigate the robustness of our scheme against spontaneous emission noise for both different computational tasks.

6.5.1 Spoken digit recognition

We begin by evaluating the performance of the system for the spoken digit recognition task. Figure 6.9 depicts the word error rate (WER) as a function of the normalized laser pump current

$$p \equiv I_b/I_{\text{thr}}. \tag{6.19}$$

Here, I_b is the laser bias current and I_{thr} is the solitary threshold current. The exibited results are for the case of electrical input injection for three different feedback conditions. In particular, these are PMOF (black circles in Fig. 6.9), PROF (green diamonds in Fig. 6.9) and the case without any feedback (red squares in Fig. 6.9). We find that the best classification performance is found for pump currents around the solitary lasing threshold, independent of the feedback conditions. For all three feedback schemes, excellent performances with WER of 0.008, 0.008 and 0 for the PMOF, PROF and the laser without feedback, respectively, were obtained. We note that bias currents around threshold ensure that the laser starts its dynamics from a steady state, which is important for a consistent response. For larger pump currents the complex (chaotic) dynamics prevail, and injecting identical information leads to different transients. Thus, computations become less reproducible, and the system's performance decreases. Interestingly, the classification is best in the absence of optical feedback. This is due to the fact that, in this task with a small number of classes, the memory, and consequently the feedback, is not so crucial. We find no significant differences between the PMOF and PROF conditions in the case of electrical input injection if the laser is pumped below or close to its threshold. However, for larger currents $p > 1.02$ the PROF configuration performs significantly better than PMOF.

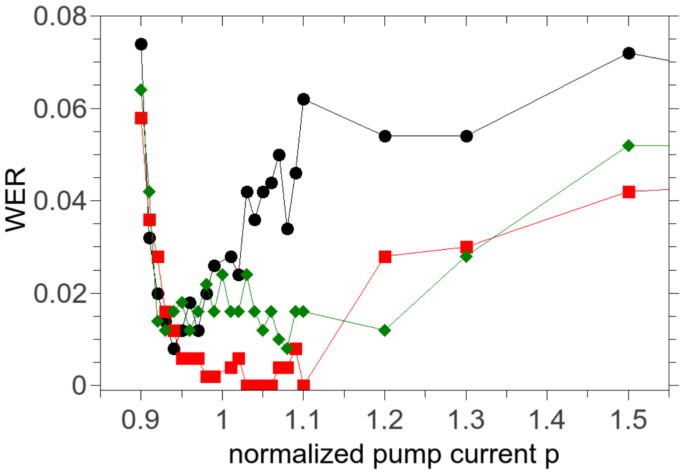

Figure 6.9: Word error rate (WER) for the spoken digit recognition task versus the normalized pump current $p = I_b/I_{thr}$ for electrical signal injection. Black circles denote the results for feedback with parallel polarization (PMOF) with a feedback rate of $\kappa_{\parallel} = 10\ \text{ns}^{-1}$. Green diamonds are the results PROF with the feedback rate $\kappa_{\perp} = 10\ \text{ns}^{-1}$. Red squares represent the resulting word error rates for the case without any feedback $\kappa_{\parallel} = \kappa_{\perp} = 0$. The other parameters are set as in Table 6.1. The lines are meant only as guide to the eyes.

The classification performance, as a function of the normalized pump current, for the case of optical input injection, is illustrated in Fig. 6.10. We again find that the WER depends on the laser bias current. We observe that the classification performance is qualitatively similar for PROF (red squares in Fig. 6.10), and, in the absence of feedback (green diamonds in Fig. 6.10), has an even better WER compared to the case of electrical input injection as shown in Fig. 6.9. In contrast, the classification error in the case of PMOF (black circles in Fig. 6.10) increases significantly above threshold. Like for the case of electrical signal injection, this is due to the increasing dominance of feedback-induced complex dynamics and the subsequent lack of consistency in the laser response. For optical injection, the classification error is minimum, reaching a 0 WER, for pump currents slightly below the solitary lasing threshold independent of the feedback conditions.

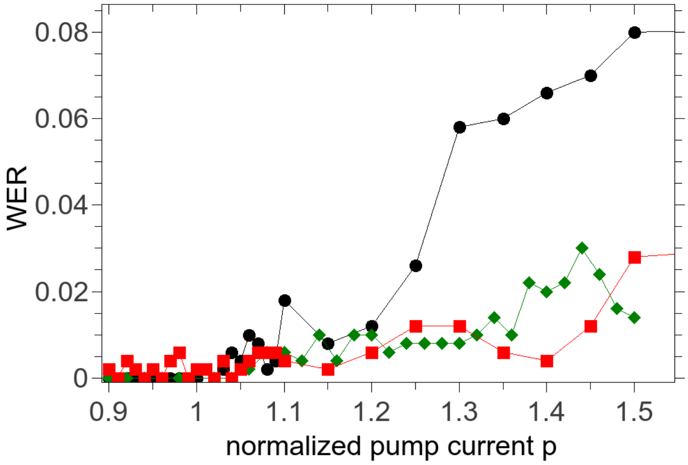

Figure 6.10: WER for the spoken digit recognition task versus the normalized pump current p for optical signal injection. Black circles denote the results for PMOF with a feedback rate of $\kappa_{\parallel} = 10\ \text{ns}^{-1}$. Red squares are the results for PROF with the same feedback rate $\kappa_{\perp} = 10\ \text{ns}^{-1}$. Green diamonds are the resulting word error rates for the case without feedback. The other parameters are chosen according to Table 6.1. Note that the lines are only a guide to the eyes.

These results suggest that the classification of spoken digits only requires the nonlinear transients created by the information injection, and that the memory introduced by the optical feedback is not important for this task. One can argue that a similar reason applies for the obviously better performance of the PROF configuration in this task when compared to PMOF. Since PROF excites the weaker mode with orthogonal polarization axis, the feedback has less impact (feedback-induced instabilities) on the transient dynamics than PMOF with the same feedback strength. Less feedback-induced irregular behavior means a more consistent response from the laser to inputs from the same class, thus exhibiting a better performance in this classification task.

6.5.2 Time series prediction

The second task that we tackle is time series prediction. We restrict ourselves to optical injection of the information and study the dependence of the normalized mean squared error (NMSE) on the normalized laser pump current $p = I_b/I_{\mathrm{thr}}$, the feedback rate and the injection strength, i.e., the average injected power $\bar{P}_{\mathrm{inj}}$. This prediction task requires the system to have memory, i.e., optical feedback is crucial for this task.
In Fig. 6.11, we show the NMSE as a function of p for two different values of the optical injection power. The first one corresponds to a large average power of the injected light, compared to the power of the laser subject to feedback, $\bar{P}_{inj} = 436\mu$W. In this case, the NMSE for the Sante Fe time series prediction task is below 0.2 both for polarization-maintained optical feedback (PMOF) (see blue squares in Fig. 6.11) and polarization-rotated optical feedback (PROF) (see green circles in Fig. 6.11) for laser bias currents above threshold, with a minimum NMSE for PMOF and $p = 1.25$ of 0.036 and 0.087 for PROF at $p = 1.5I$.

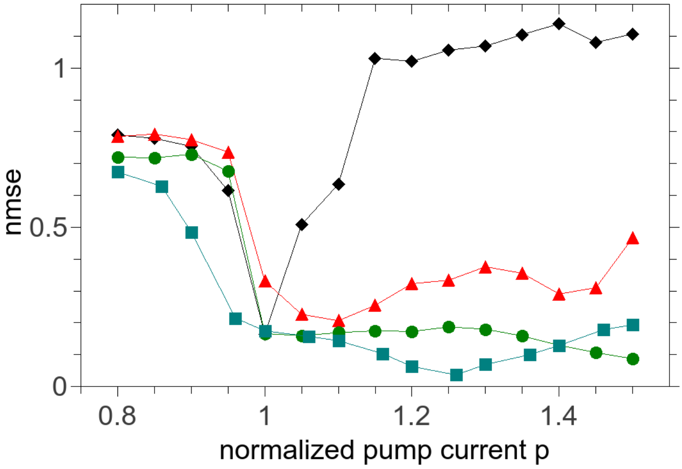

Figure 6.11: Normalized mean squared error (NMSE) for the Santa Fé time series prediction task versus the normalized pump current p for PROF with $\bar{P}_{inj} = 436\mu$W (green circles), PMOF with $\bar{P}_{inj} = 436\mu$W (blue squares), PMOF with $\bar{P}_{inj} = 11\mu W$ (black diamonds) and PROF with $\bar{P}_{inj} = 11\mu W$ (red triangles), respectively. The feedback rates were set to $\kappa_{\|} = 10$ ns^{-1} and $\kappa_{\perp} = 10$ ns^{-1}, respectively, while the respective other was set to zero. The other parameters are set as in Table 6.1. Note that the lines are only guide to the eyes.

We also present the results for a smaller average power of the optical input injection, $\bar{P}_{inj} = 11\mu W$. In this case we find that for PMOF low pre-

diction errors are restricted to laser pump currents close to the solitary lasing threshold (see black diamonds in Fig. 6.11), with a minimal NMSE value of 0.164 for $p = 1.0$. The prediction error increases significantly for higher pump currents due to the onset of delayed feedback instabilities. For PROF and low injection power, the pump current range for good performance is significantly broader (see red triangles in Fig. 6.11) with the minimal NMSE being 0.206 for $p = 1.1$. The error increases less with increasing bias current for PROF. In the case of high injection power, the prediction hardly changes with the pump current (above threshold) for both feedback configurations. On the contrary, prediction errors strongly increase for low current for both low and high injection powers. Nevertheless, in both cases, competitive prediction errors can be achieved. It is interesting to note, though, that a larger average optical injection power allows for a wider range of bias currents providing good performance. This can be interpreted such that because external optical injection can stabilize the dynamics to some degree, it counteracts some of the destabilizing effects of time-delayed feedback.
As the Santa Fé time series prediction requires the presence of memory in the system, we investigate in detail the influence of the feedback strength on the prediction performance.

Figures 6.12 and 6.13 show the NMSE, coded in color scale, versus the feedback rate and the average injected power for the case of PMOF. Results are shown for two different laser pump currents, namely a current close to threshold ($p = 1.01$, Fig. 6.12) and a current clearly above threshold ($p = 1.18$, Fig. 6.12), respectively.

The same parameter dependencies as for PMOF are studied for the case of PROF. The resulting NMSE for $p = 1.18$ is shown in Figure 6.14.

In the case of a bias current close to threshold ($p = 1.01$) shown in Fig. 6.12, we find that PMOF yields low NMSE values for feedback rates below $\kappa_{\|} = 20$ ns^{-1} independent of the average power of the injected signal $\bar{P}_{inj}$, reaching a minimum value of NMSE $= 0.099$. In addition, the time series prediction performance with PROF and a small bias current $p = 1.01$ shows almost no dependence on injection power or feedback strength, respectively. The minimum NMSE value in this situation is 0.161 while the overall average for the considered parameter ranges is NMSE $= 0.201$.
In the case of a current well above threshold ($p = 1.18$), as shown in Fig. 6.13 for PMOF, we find that PMOF yields low NMSE values for intermediate feedback rates and high average powers of the injected signal $\bar{P}_{inj}$, with a minimum value of 0.021. Interestingly, an increase in the laser pump current requires an increase in the average injection power and feedback rate to achieve a low prediction error in the case of PMOF. This result suggests that a balance between laser emission power, and the average injection power is needed. As shown in Fig. 6.14, PROF yields low NMSE values (minimum value 0.022) for high average powers of the injected signal and for large feedback rates.
Overall, the results obtained with the delayed feedback scheme are very com-

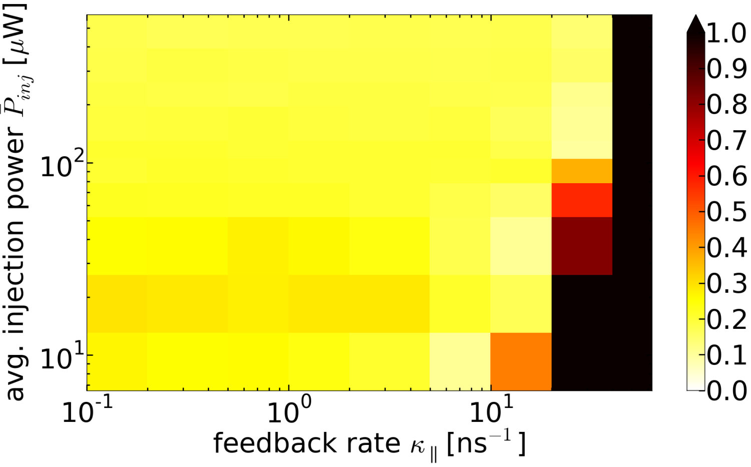

Figure 6.12: Normalized mean squared error (NMSE) for the Santa Fé time series prediction task as a function of the PMOF feedback rate $\kappa_{||}$ and of the average injected power $\bar{P}_{inj}$ (y-axis). The normalized pump current is set to $p = 1.01$. The other parameters are chosen as in Table 6.1.

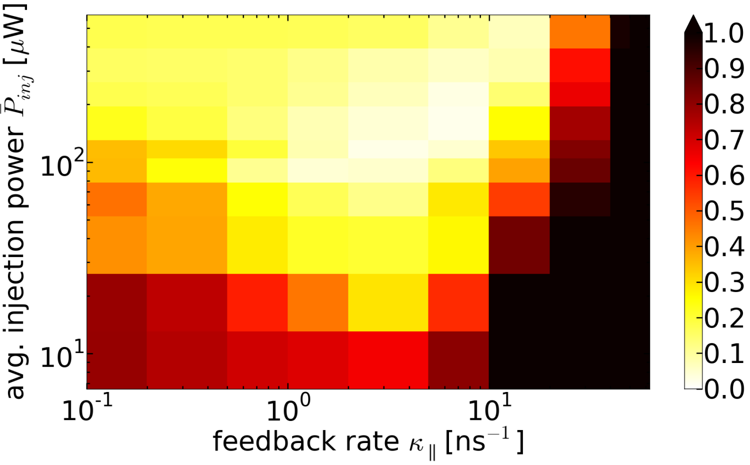

Figure 6.13: NMSE for the Santa Fé time series prediction task depending on the PMOF feedback rate $\kappa_{||}$ (x-axis) and on the average injected power $\bar{P}_{inj}$ (y-axis) for a stronger pump current of $p = 1.18$. The other parameters are chosen according to Table 6.1.

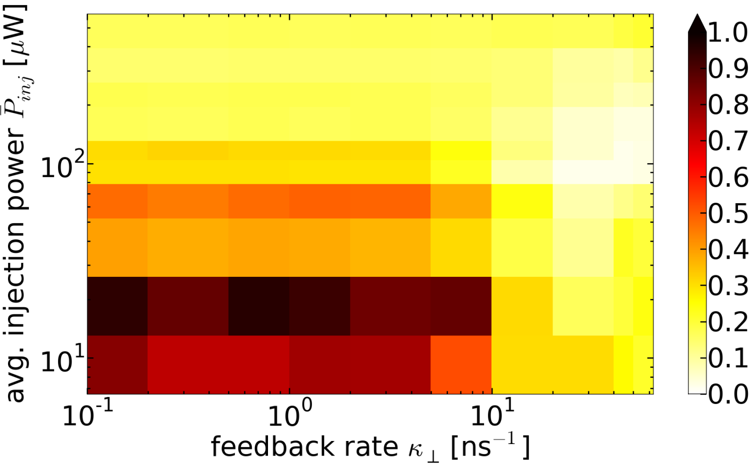

Figure 6.14: Normalized mean squared error (NMSE) for the Santa Fé time series prediction task as a function of the PROF feedback rate $\kappa_\perp$ and the average injected power $\bar{P}_{inj}$ (y-axis). The pump current corresponds to $p = 1.18$. The other parameters are chosen according to Table 6.1.

petitive compared to traditional reservoir computing techniques. All results presented so far have been obtained considering a spontaneous emission factor of 10^{-6}. In order to evaluate the influence of different noise levels in more detail, we discuss in the following the performance of our scheme for different spontaneous emission factors.

6.5.3 Influence of system-intrinsic noise

In this section, we evaluate the influence of spontaneous emission noise on the performance of the system for the two tasks described above. So far, we have used fixed values for the spontaneous emission factors for both polarization modes of $\beta_{||} = \beta_\perp = 10^{-6}$, which is thought to be realistic for a single-mode edge-emitting laser diode. Here, we study the change in performance for both tasks with a varying noise strength β. $\beta_{||} = \beta_\perp$ are always set to the same value β.

In the case of spoken digit recognition, we find that the task is extremely robust against spontaneous emission noise. As shown in Fig. 6.15(a), the classification error remains almost constant up to $\beta = 10^{-4}$, which is two orders of magnitude larger than a realistic value for the spontaneous emission, both for electrical (blue circles) and optical (red squares) input injection.
In contrast, in the case of the Santa Fé time series prediction, the NMSE degrades already for realistic values of the spontaneous emission. Figure 6.15(b)

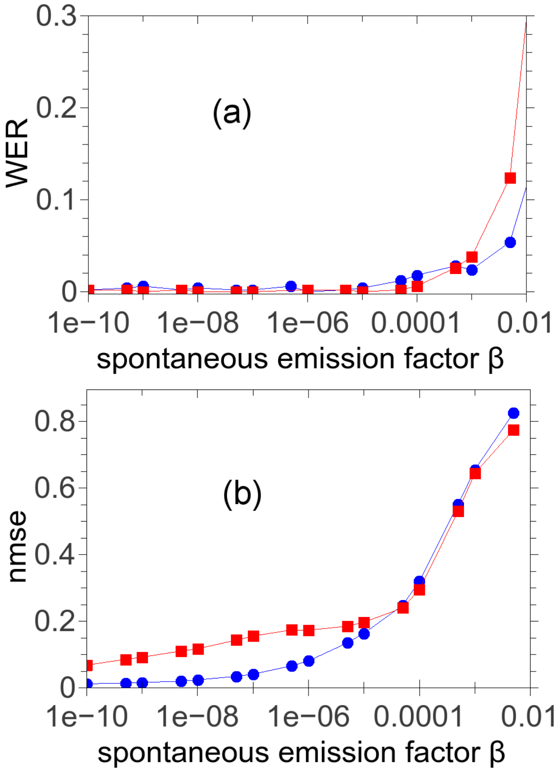

Figure 6.15: (a) WER for the spoken digit recognition task versus the spontaneous emission factor β. Shown are results for electrical (blue circles) and optical (red squares) signal injection. The feedback rate was set to zero: $\kappa_{\|} = \kappa_{\perp} = 0$. The laser was simulated as pumped at threshold $p = 1.0$. (b) NMSE for the Santa Fé time series prediction task versus β for PMOF (blue circles) and for PROF (red squares). The feedback rates are set to $\kappa_{\|} = 10$ ns^{-1} and $\kappa_{\perp} = 10$ ns^{-1}, respectively, while the respective other is set to zero. The pump parameter is $p = 1.18$. The values of the other parameters are given in Table 6.1. Note that the lines are only guides to the eye.

illustrates the degradation of the performance as a function of the spontaneous emission factor for PMOF (blue circles) and PROF (red squares). The prediction error increases when the noise term is included in the numerical simulations, with a gradual degradation at realistic values ($\beta = 10^{-6}$) and a sudden increase starting at $\beta = 10^{-4}$.
The difference in sensitivity originates from the different nature of the two tasks. While spoken digit recognition is a classification task which only demands a winner-takes-all decision, time series prediction actually requires

the precise approximation of a nonlinear transformation. Furthermore, time series prediction tasks are more sensitive to noise than classification tasks [175]. Soriano et al. [227] investigated the effect of quantization noise on the performance of a single nonlinear node for classification and prediction tasks, respectively. They also found, that classification tasks are generally more robust against noise than timeseries prediction, with quantization noise always having a crucial influence on the performance.

6.6 Comparison with experiments

Here we compare our numerically-obtained results for the computational performance of a single semiconductor laser with delayed feedback to the findings gained from corresponding experiments, and we show the robustness of the scheme. In our laboratory, Brunner et al. [109] investigated a system of a single semiconductor laser subject to its own delayed feedback with regards to its performance in the same two tasks we tackle as well with our numerical system. The input signals in their work were electrically- and optically-injected, respectively, as well. They were able to achieve competive performance results in both benchmark tasks when compared to traditional RC concepts.

The experimental configuration and operating conditions were very similar to the ones modeled in this work. The experiments involved a standard Z-mounted laser diode with an emission frequency of $\lambda = 1542$ nm. The feedback was provided by a fiber loop and a had a time-delay of $\tau_D = 77.6$ ns. The feedback conditions were controlled by employing a polarization controller and an optical attenuator in the optical path to achieve PMOF or PROF conditions, and to regulate the feedback strength, respectively. For the case of electrical information injection, the laser diode current was directly modulated. Optical signal injection was realized via the modulation of an externally-injected driver laser's output by a Mach-Zehnder electro-optic modulator, with the injected power being modulated between 15 nW $\leq u^o(t) \leq 15\mu$W. The polarization direction of the injected signal was parallel to the laser emission's. For electrical signal injection, the laser current was modulated between 0 mA $\leq u^e(t) \leq 12$mA, which corresponds to $0 \leq \chi S(t) \leq 1.62$ (see Eq. (6.13)). The polarization of the optical feedback was rotated for PROF.

The information was injected with a rate of 5 GSamples/s in both schemes. This configuration and the operating conditions are partly the same as or very similar to our own simulated conditions; it is, thus, legitimate to compare the performance results for the two tasks. The word-error-rate (WER) results for the spoken digit recognition task for both electrical and for optical information injection are shown in Fig. 6.16.

The achieved classification errors were very low for pump (bias) currents close to the solitary lasing threshold. The minimum WER were WER =

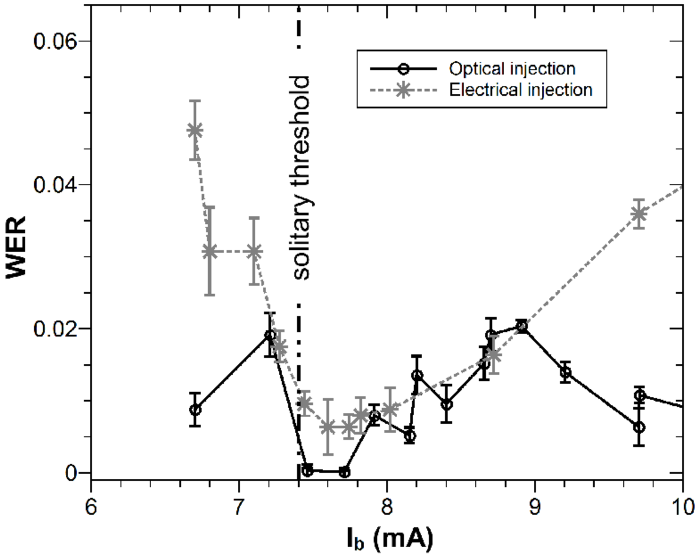

Figure 6.16: Experimentally-obtained WER results for the spoken digit recognition task considering electrical (asterisks) and optical (circles) signal injection, respectively, versus the laser bias current I_b. Courtesy of D. Brunner.

$(1.4(+5.1/-1.4)) \cdot 10^{-4}$ at a normalized pump current $p = 1.04$ for optical signal injection and WER $= (6.4 \pm 0.17) \cdot 10^{-3}$ at $p = 1.03$ for electrical signal injection. Further above threshold, the classification performance degrades for electrical injection, due to the prevalence of complex dynamics of the laser. The effect is such that the same injected input can lead to different transient states, and, therefore, to a lack of consistency. For the case of optical injection, the performance is best close to threshold, and the WER is higher farther from threshold, though the dependency is not monotonous. The results for the spoken digit recognition task compare well with our numerically-obtained ones. We also find that the system performs best close to threshold, and the WER increases with a larger pump current. The characteristics of the WER for optical injection resembles the numerically-attained one reasonably well (see Figs. 6.15 (green diamonds) and 6.10 (red quares)). The absolute WER values are very similar in both experiments and numerics.

The experimentally-attained prediction performance for the Santa Fé time series prediction task as a function of the laser bias current is shown in Fig. 6.17. The best performance with NMSE = 0.106 was again obtained for a bias current close to threshold. As for the spoken digit recognition, the performance significantly deteriorates for currents significantly above threshold.

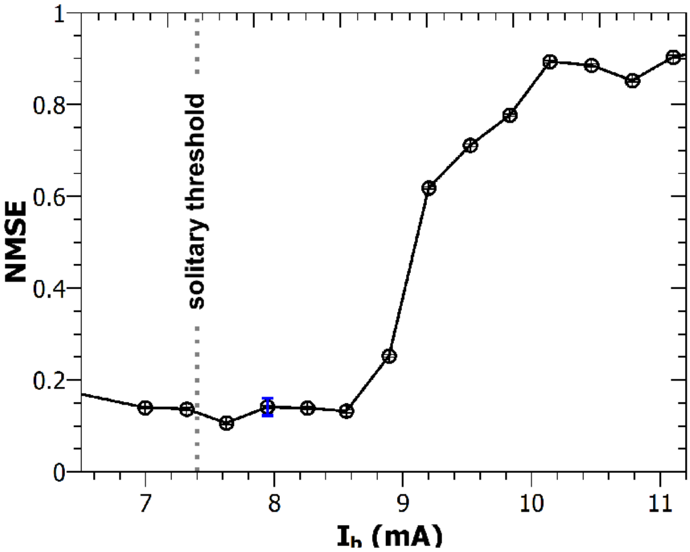

Figure 6.17: Experimentally-obtained NMSE results for the Santa Fé time series prediction task considering electrical (asterisks) and optical (circles) signal injection, respectively, versus the laser's bias current. The signal was injected optically. Figure courtesy of D. Brunner.

Qualitatively, this compares well with our numerically-gained results for the Santa Fé task (see red triangles in Fig. 6.11), although a relatively good performance with a NMSE around 0.2-0.3 is retained for larger pump currents. The error increases further only for much larger pump currents $p > 1.4$. This is due to the much higher average injected power in our numerical scheme ($\bar{P}_{\text{inj}} = 436\mu\text{W}$) as compared to the experimental value ($\bar{P}_{\text{inj}} \approx 10\mu\text{W}$). The strong injected optical signal stabilizes the dynamics of the laser for a broader pump current range, thus leading to a more consistent response and better prediction performance. We expect that simulating with a comparable injection power, a curve for the NMSE similar to the one in Fig. 6.17 could be obtained by numerical simulations.

When we take into account certain differences between the experimental and the numerical scheme, we see that the experimental results for spoken digit recognition and for time series prediction are quite well reproduced by our numerical work. We expect that our findings in other operating regimes and conditions not investigated in the experiments presented in [109] can be used as guidelines for future experiments.

6.7 Possible improvements

There are a few possible modifications to our single laser node reservoir computing scheme as described so far that are easy to implement and that can result in significantly-improved performance characteristics. We focus here on polarization-resolved intensity readout and optimization of the virtual node separation Θ.

6.7.1 Polarization-resolved intensity readout

So far, the readout of the laser output states has been modeled as an overall output intensity measurement where the intensity in each of the two orthogonal modes is collapsed into one (Eq. (6.6))

$$P_{\text{out}} = \left|\mathcal{E}_{\parallel}\right|^2 + \left|\mathcal{E}_{\perp}\right|^2 .$$

The information in P_{out} is used to create readout state vectors with dimension N which are then used for training and testing. However, if the intensity in both modes is measured independently, and the information is concatenated into a larger output state with dimension $2N$, the additional information can increase the system's computational performance. This approach corresponds to a mapping of the input information onto a higher-dimensional reservoir state when compared to a non-polarization-resolved readout. Experimentally, this modification can be implemented simply by introducing a polarization beam splitter in the readout line of the setup and measuring the laser output with two detectors instead of one.
To show the potential for performance improvements of this modification of our scheme, we focus on the results for the time series prediction error. Fig. 6.18 depicts the resulting NMSE values as a function of the pump current if the modal intensities are measured (read out) separately for a low average injection power $\bar{P}_{\text{inj}} = 11\mu\text{W}$ (black diamonds for the PMOF case, red triangles for PROF). We compare those errors with the ones obtained by simulating the corresponding case with an overall intensity readout (grey diamonds for PMOF, light red triangles for PROF) as already presented in Fig. 6.11.

One can see that the additional information provided by a polarization-resolved readout markedly improves the performance of our scheme for the PROF case. For PMOF, there is no change in the prediction error for pump currents below or around threshold but a deterioration for larger pump currents. This can be easily understood: in the case of PMOF, the weaker perpendicular polarization mode remains unexcited, and therefore, only exhibiting noise-like characteristics because of spontaneous emission. This noise does not depend on the input signal, the additional information is redundant and can not be used for the distinction of input signals in a meaningful way. The noise lessens the impact of the dynamics in the relevant parallel

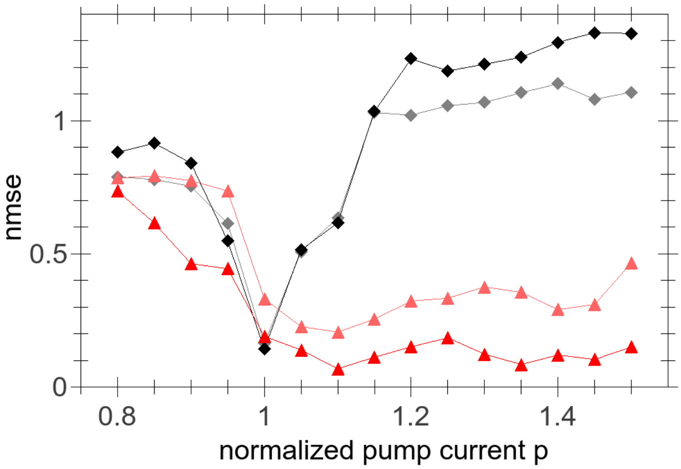

Figure 6.18: NMSE versus the normalized laser pump current for the case of PMOF (diamonds) and for PROF (triangles). The grey and light red colored symbols, respectively, correspond to the results shown in Fig. 6.11 with a non-polarization-resolved intensity readout. The black and dark red symbols depict the findings for separate modal intensity readouts. The feedback rates correspond to $\kappa_{\|} = 10$ ns^{-1} and $\kappa_{\perp} = 10$ ns^{-1} for PMOF and PROF, respectively. The average injection power is $\bar{P}_{\text{inj}} = 11\mu$W.

polarization mode and leads to an increased error. Therefore, for PMOF, a polarization-resolved readout is unnecessary and counterproductive.

In the case of PROF, on the other hand, both modes are excited significantly, and since the dynamics in both modes have different characteristics, their readout provides a truly increased amount of information. This leads to a better performance, especially for larger pump currents since the perpendicular mode $\mathcal{E}_{\perp}$ is stimulated more strongly.
To underline this conclusion, we present further results for the NMSE in the Santa Fé timeseries prediction task, corresponding to the ones specified for $p = 1.01$ and shown in Fig. 6.14 for $p = 1.18$, but with polarization-resolved readout. We see a negligible improvement of the error rates for a pump current close to threshold $p = 1.01$ (Fig. 6.19) when compared to the results for the case without polarization-resolution. This is because, with the laser pumped that close to threshold, the perpendicular mode excitation is still not very strong. In contrast, if the laser is pumped at $p = 1.18$ (Fig. 6.20), the parameter regions with low NMSE increase significantly in size when compared to the non-polarization-resolved readout case.

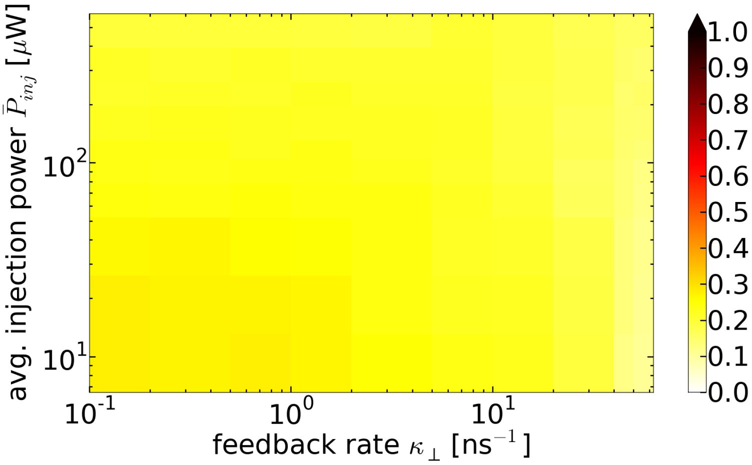

Figure 6.19: NMSE versus the PROF feedback rate $\kappa_\perp$ and the average injected power $\bar{P}_{\mathrm{inj}}$ for the case of polarization-resolved readouts. The laser was pumped with a normalized current of $p = 1.01$. The values of the other simulation parameters are given in Table 6.1..

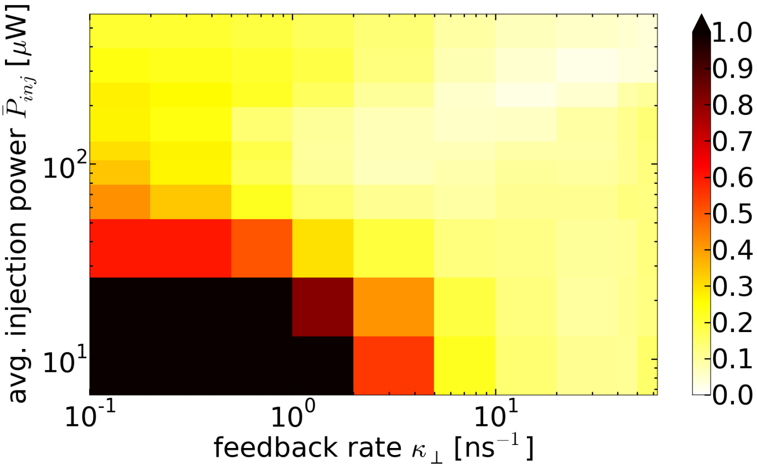

Figure 6.20: NMSE versus the PROF feedback rate $\kappa_\perp$ and the average injected power $\bar{P}_{\mathrm{inj}}$ for the case of polarization-resolved readouts. The laser was pumped with a normalized current of $p = 1.18$. The operating conditions correspond to the ones used to obtain the results in Fig. 6.14.

6.7.2 Virtual node separation optimization

Another way to further improve the performance of our single laser node RC scheme is to optimize the virtual node separation Θ. So far, we have rather arbitrily chosen $\Theta = 200$ ps as a fixed value, only applying the condition $\Theta < T$ where T is the characteristic time scale of the semiconductor laser (see Section 6.2). Changing Θ can be implemented in our scheme simply by changing the feedback delay τ or the number of virtual nodes N corresponding to

$$\Theta = \tau/N. \tag{6.20}$$

To test the possibility to improve the performance of our system by applying a different virtual node separation, we investigate the dependence of the Santa Fé prediction error on Θ for several different pump currents (Fig. 6.21) and for different feedback rates $\kappa_{\|}$ (Fig. 6.22). We choose this task to be able to see a significant change in performance.

We vary Θ by adjusting the feedback delay time τ of our system while keeping the number of virtual nodes fixed at $N = 400$.

Fig. 6.21 exhibits the NMSE results versus Θ for different pump currents $p = 1.0$ (black circles), $p = 1.05$ (red squares), $p = 1.1$ (green diamonds) and $p = 1.2$ (blue triangles) for the case of PMOF with $\kappa_{\|} = 10$ ns^{-1}. It is apparent that the optimal value for Θ is smaller than the previously-chosen one. The improvement in performance can be considerable, depending on the operating regime, i.e., the pump current. For $p = 1.0$, for example, the performance is enhanced from NMSE ≈ 0.132 for $\Theta = 200$ ps to NMSE ≈ 0.056 for $\Theta = 50$ ps. With increasing pump current, the minimum NMSE value is given for a decreasing Θ. Increasing the pump current means to decrease the characteristic time scale of the dynamics which is related to the laser's relaxation oscillations. The virtual node separation should be short enough to prevent the dynamics from getting close to a steady state so that all response dynamics are transient states. Since the dynamics become faster for an increasing pump current, the optimal Θ has to decrease.

Fig. 6.22 shows the prediction error versus Θ for different PMOF feedback rates $\kappa_{\|} = 10$ ns^{-1} (black circles), $\kappa_{\|} = 20$ ns^{-1} (red squares) and $\kappa_{\|} = 40$ ns^{-1} (green diamonds). The laser is pumped at threshold $p = 1.0$. Again, we see that the optimal value of $\Theta = 75$ ps is smaller than $\Theta = 200$ ps as previously chosen. The performance improves from NMSE ≈ 0.132 to NMSE ≈ 0.055. Also, the Θ with minimal prediction error decreases with increasing feedback rate. A similar argument can be applied as for the case of varying pump current. Faster dynamical fluctuations induced by an increasingly strong feedback can - in terms of the resulting NMSE - be partially compensated for by decreasing the virtual node separation Θ.

The above results indicate that there is no single optimal Θ for our considered system of a single laser with delayed feedback. The optimal value depends significantly on operating parameters like the pump current and

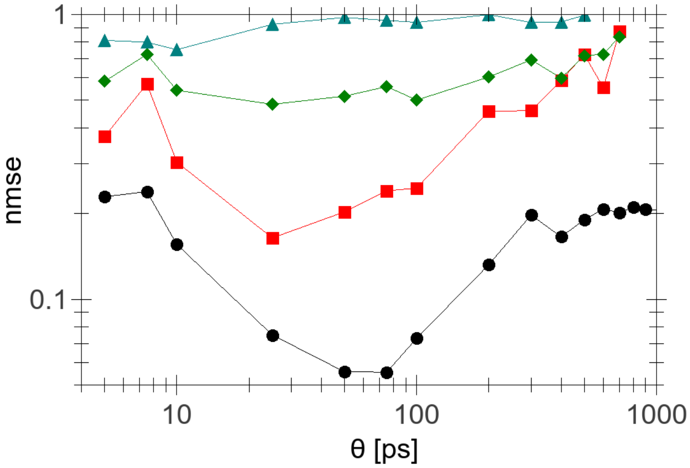

Figure 6.21: NMSE for the time series prediction task versus Θ for different normalized pump current values $p = 1.0$ (black circles), $p = 1.05$ (red squares), $p = 1.1$ (green diamonds) and $p = 1.2$ (blue triangles). The feedback is modeled as PMOF with rate $\kappa_{||} = 10\ \mathrm{ns}^{-1}$. The other parameters are set as in Table 6.1. Note the log-log scale.

the feedback strength. With carefully chosen Θ depending on operating conditions, the performance of our scheme can be substantially improved.

We note, that Nguimdo et al. [228] recently also investigated the Θ dependence of the scheme we consider here. However, the studied a case with $N = 200$ nodes, a differently constructed input mask and with a different injection strength, so our results can not be easily compared with theirs.

6.8 Summary and Outlook

In this chapter, we have studied the computational capabilities of a semiconductor laser subject to delayed optical feedback in a reservoir computing (RC) approach. Our numerical simulations highlight the potential and robustness of the proposed scheme. Moreover, the modeling provides guidelines for the experimental implementation of the scheme. We have achieved a qualitative agreement with first experimental results employing a corresponding setup.

We find that this configuration exhibits excellent computational performance for both investigated computational tasks, spoken digit recognition and time series prediction. Optical injection of the input signals result in general in a better performance of our scheme than electrical injection. Pumping the laser close to its threshold allows for the laser dynamics to stay in a tran-

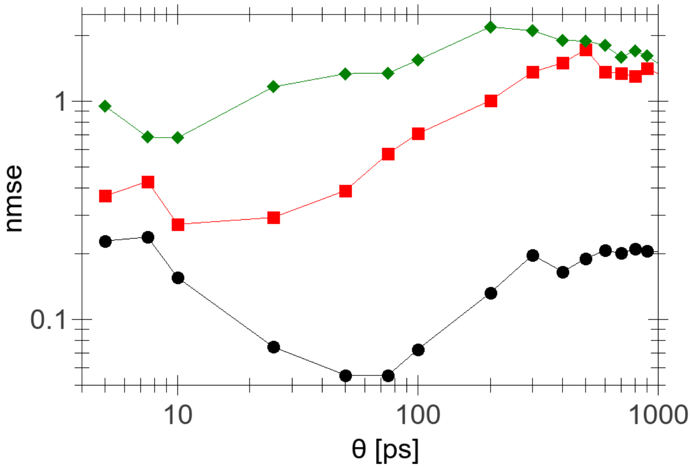

Figure 6.22: NMSE results versus Θ for different PMOF feedback rates $\kappa_{\|} = 10$ ns^{-1} (black circles), $\kappa_{\|} = 20$ ns^{-1} (red squares), and $\kappa_{\|} = 40$ ns^{-1} (green diamonds). The normalized pump current is $p = 1.0$, the other parameters are chosen according to Table 6.1. Note the log-log scale.

sient regime without too much interference from feedback-induced complex dynamics and therefore usually leads to the best performance. A stronger optical injection of the input signals can, to a degree, stabilize the dynamics, and, thus, compensate for a stronger optical feedback which might be needed for memory-intensive tasks.

The results obtained for the spoken digit recognition task (WER=0) are better than those obtained with other systems [229, 230]. For the case of time series prediction, our best numerical results of NMSE=0.02 are of the order of those obtained with more traditional techniques (<0.01 [231]), although, in the latter, additional memory is artificially added into the input data.

We further find potential to significantly improve the performance of the present scheme by implementing polarization-resolved intensity readouts, and by optimizing the virtual node separation depending on the operating regime. The polarization-resolved readouts promises a marked improvement in the time series prediction task if the feedback is configured as PROF. The peak performance for $p = 1.1$ and $\kappa_{\perp} = 10$ ns^{-1} then improves from NMSE $\approx$ 0.206 to NMSE $\approx$ 0.069, for $\Theta = 200$ ps and $\Theta = 75$ ps, respectively. With optimized Θ for different operating regimes, the NMSE can in our simulations be significantly reduced as compared to the case with $\Theta = 200$ ps. With $\kappa_{\|} = 10$ ns^{-1} and $p = 1.0$ the optimum node separation is $\Theta = 75$ ps and the NMSE reduced from 0.132 to 0.055. For $\kappa_{\|} = 10$ ns^{-1} and $p = 1.05$, the best performance is obtained for $\Theta = 25$ ps where the NMSE is

reduced from 0.458 to 0.164. In the situation with $\kappa_{\|} = 20\ \text{ns}^{-1}$ and $p = 1.0$ the error decreases from NMSE ≈ 1.009 for $\Theta = 200$ ps to NMSE ≈ 0.273 for $\Theta = 10$ ps.
Many parameter dependences and opportunities offered by this configuration remain unexplored so far. Also, other types of lasers than QW edge-emitters (e.g. quantum dot lasers or VCSELs) might offer an additional way to increase computational performance of a single laser system with feedback. They can exhibit different timescales than in the system investigated here, a more beneficial interplay between different laser modes (polarization mode detuning, multimode lasers, ...) or dynamical characteristics better suited for transient state excitation.

Another possible future work could be to study RC with multiple coupled laser nodes in a network with coupling and feedback topologies tailored to specific computational needs. Nonidentical coupled nodes could offer an even larger dimensional state space, with the node diversity resulting in a larger-dimensional state space.

The full potential of single laser systems or small laser networks for data processing is yet unknown.

Summary and Conclusions

The work in this thesis was focused on the complex dynamics of semiconductor laser (SL) devices which receive time-delayed feedback from an external cavity or are delay-coupled with a second semiconductor laser. These systems are of general interest as they serve as excellent testbeds for the study of delay systems and provide opportunities for photonic applications.

We investigated fundamental properties and dynamics induced by the time-delayed feedback and delayed coupling. Moreover, we explored the consequences for existing applications and we studied the utilization of transient complex dynamics of a single SL arising from delayed feedback and external signal injection for a neuro-inspired photonic data processing scheme. Based on experiments and numerical modelling, we investigated systems of two coupled SLs, gaining insights into the role of laser and coupling parameters for the synchronization characteristics of these systems. We could link certain features of the synchronization dynamics, like intermittent desynchronization events, to the underlying nonlinear dynamics in the coupled laser system.

This way, our research combined both fundamental insights into delay-coupled lasers as well as novel application perspectives.

To explore the capabilities of a single SL with delayed feedback, we followed the concept of reservoir computing based on delay systems. In particular, we studied two different computational tasks: time series prediction and classification of input patterns, representing computationally hard tasks for traditional computing concepts. We explored several feedback configurations, data injection methods and operating regimes of the laser and were able to identify the task-dependent optimal operating conditions. The best performance results we obtained are very competitive when compared to other, more traditional RC approaches. We also found that the performance of the single laser system with feedback exhibits a remarkable robustness against noise when it comes to classification, i.e., pattern recognition. Time series prediction utilizes more the inherent memory of the delay system, and the system performance is significantly affected by noise. Our work demonstrates the potential of simple photonic setups and the RC concept for future computational paradigms.

In one of the main lines of investigation in this thesis, we studied the synchronization properties in systems of two delay-coupled SLs with relay. We explored the consequences of asymmetries in the setup for the dynamics and synchronization properties. One key interest was, how synchronization decays or is lost, which is of significant importance for applications in chaotic communications schemes and key-exchange protocols that require synchronization. We followed an event-based approach and connected changes in the synchronization levels for varying operating parameters or varying mismatches to the onset and characteristics of desynchronization events. We studied these desynchronization events in experiments as well as in numerical simulations. We interpreted events induced by noise or by mismatches of the laser or operating parameters as bubbling, while desynchronization due to frequency detuning was interpreted following the concept of episodic synchronization. Our results regarding synchronization levels and synchronizability underline the significance of symmetry and matching parameters for the identical synchronization of delay-coupled oscillators. For chaos communication concepts based on synchronization, it is of crucial importance to keep asymmetries or mismatches small to suppress the occurrence of intermittent desynchronization events as much as possible.

We applied our findings regarding the possibility for identical synchronization to develop and implement an experimental method to identify determinism in the chaotic dynamics of a SL with delayed feedback. Our method is based on zero-lag synchronization of the laser in question with a twin system. We focused our investigation on power dropouts in the Low Frequency Fluctuations (LFF) regime of a SL since they represent distinct dynamical features whose origin had been controversially discussed in the past. The method identifies isochronously synchronized power dropouts with predominantly deterministic events. One central result was the surprisingly large fraction of 85% of LFF power dropouts being synchronized when the lasers were pumped close to their respective solitary threshold. This fraction being only a lower bound, we could thus identify the large majority of occurring power dropouts in the LFF regime as being deterministically driven and not primarily induced by the intrinsic noise. Our findings were confirmed by numerical simulations. Those resulted in an even larger fraction when the coupling setup was modeled as completely symmetric. Introducing a number of small scale asymmetries led to results comparable with the experimental results. Our method can be adapted in principle to other nonlinear delay systems which exhibit intrinsic noise to test for traces of determinism. The major necessary requirement for the adaptation is that the studied oscillator

must be able to identically synchronize with a twin oscillator.
Several of the results obtained in this thesis can be adapted or generalized to other systems of coupled nonlinear oscillators. They are, thus, of interest to other researchers and experimentalists beyond laser dynamics community. Our analytical findings regarding the effect of delay mismatches or coupling mismatches in a basic binary coupling configuration are of general validity. They hold for pairs of nonlinear oscillators that are delay-coupled in a relay configuration, irrespective of the nonlinear function describing their solitary dynamics. Moreover, the analytical and numerical results are relevant when studying the dynamics and synchronization properties of larger networks of delay-coupled semiconductor lasers. This might be helpful for the design of tailored network structures for specific applications. The insight we gained for the simple motif of two coupled semiconductor lasers is especially relevant since a coupled pair of elements forms the basic motif in more complex network structures.

From the perspective of applications in chaos communications and cryptography, our results on intermittent desynchronization due to bubbling or detuning will be helpful to determine optimal operating conditions and estimate performance limitations of bidirectional transmission schemes based on synchronization of coupled lasers. Our work underlines the necessity for high symmetry in those schemes. This refers specifically to the respective operating regimes of the communicating lasers and symmetric transmission over the communication channel.

Furthermore, we see our work on the application of complex laser dynamics in reservoir computing schemes as the foundation for prospective work in all-optical RC. Future research will explore more complex coupling topologies and larger networks of coupled lasers as reservoirs to increase the versatility of the systems and to provide more complex dynamical responses to input signals. An increasingly complex coupling topology of the reservoir network should also enable the capability to process more complex data. We see the extensive study of the single laser with feedback system as essential and a necessary first step before considering larger networks consisting of more than one hardware node.

Appendices

A

Nondimensionalization of Lang-Kobayashi rate equations

When studying dynamical systems it is convenient to bring the differential equations into a dimensionless form. This procedure is called nondimensionalization [98, 232].

Using dimensionless equations has significant advantages. First, it reduces the number of parameters by combining them into fewer independent constants, and second very large and very small numbers are avoided and the dimensionless equations are therefore better suited for numerical simulations.

Here we consider the two-mode Lang-Kobayashi (LK) model corresponding to Eqs. (2.26)-(2.30). The nondimensionalization of the one-mode model (Eq. (2.5)-(2.7)) works correspondingly. We convert the equations without the Langevin noise terms as we will convert the noise separately.

The noiseless two-mode LK rate equation model reads

$$\begin{aligned}
\dot{\mathcal{E}}_{\|}(t) &= \frac{1}{2}(1+i\alpha)\left(\mathcal{G}_{\|}(\mathcal{E}_{\|},N)-\gamma_{\|}\right)\mathcal{E}_{\|}(t)+\kappa_{\|}\mathcal{E}_{\|}(t-\tau_{ec}) && \text{(A.1)}\\
\dot{\mathcal{E}}_{\perp}(t) &= \frac{1}{2}(1+i\alpha)\left(\mathcal{G}_{\perp}(\mathcal{E}_{\|},N)-\gamma_{\perp}\right)\mathcal{E}_{\perp}(t)+\kappa_{\perp}\mathcal{E}_{\|}(t-\tau_{ec})\\
&\quad -i\Delta\Omega\mathcal{E}_{\perp}(t) && \text{(A.2)}\\
\dot{N}(t) &= \frac{I}{e}-\gamma_e N(t)-\mathcal{G}_{\|}(\mathcal{E}_{\|},N)\left|\mathcal{E}_{\|}(t)\right|^2-\mathcal{G}_{\perp}(\mathcal{E}_{\perp},N)\left|\mathcal{E}_{\perp}(t)\right|^2 && \text{(A.3)}
\end{aligned}$$

with the gain functions

$$\mathcal{G}_{\|}(\mathcal{E}_{\|}, N) = g_{\|}\frac{N(t)-N_T}{1+\epsilon\left|\mathcal{E}_{\|}(t)\right|^2} \tag{A.4}$$

$$\mathcal{G}_{\perp}(\mathcal{E}_{\perp}, N) = g_{\perp}\frac{N(t)-N_T}{1+\epsilon\left|\mathcal{E}_{\perp}(t)\right|^2}. \tag{A.5}$$

In order to convert the equations into dimensionless form, we introduce a dimensionless time s and dimensionless variables $E_{\|}$, $E_{\perp}$ and n. They are related to the original variables by a characteristic scaling factor, which carries the proper dimensions:

$$s = t/t_c \tag{A.6}$$

$$\mathcal{E}_{\|}(t) = \mathcal{E}_{c\|}E_{\|}(t/t_c) \tag{A.7}$$

$$\mathcal{E}_{\perp}(t) = \mathcal{E}_{c\perp}E_{\perp}(t/t_c) \tag{A.8}$$

$$N(t) = N_c n(t/t_c) + N_c^0. \tag{A.9}$$

We have to determine the values of the characteristic factors $\mathcal{E}_{c\|}$, $\mathcal{E}_{c\perp}$ and N_c. Note that we included a constant shift N_c^0 in the transformation of the carrier variable N. We will choose it such, that the new dimensionless carrier variable n is zero at the lasing threshold and thus describes the carriers in excess of the threshold.

Inserting ansatz (A.6)-(A.9) into Eqs. (A.1)-(A.5) yields

$$\dot{\mathcal{E}}_{\|}(t) = \frac{\mathcal{E}_{c\|}}{t_c}\dot{E}_{\|}(s) = \frac{1}{2}(1+i\alpha)\left(g_{\|}\frac{N_c n(s)+N_c^0-N_T}{1+\epsilon\mathcal{E}_{c\|}^2\left|E_{\|}(s)\right|^2}-\gamma_{\|}\right)\mathcal{E}_{c\|}E_{\|}(s) + \kappa_{\|}\mathcal{E}_{c\|}E_{\|}(s-\tau_{ec}/t_c) \tag{A.10}$$

$$\dot{\mathcal{E}}_{\perp}(t) = \frac{\mathcal{E}_{c\perp}}{t_c}\dot{E}_{\perp}(s) = \frac{1}{2}(1+i\alpha)\left(g_{\perp}\frac{N_c n(s)+N_c^0-N_T}{1+\epsilon\mathcal{E}_{c\perp}^2\left|E_{\perp}(s)\right|^2}-\gamma_{\perp}\right)\mathcal{E}_{c\perp}E_{\perp}(s) + \kappa_{\perp}\mathcal{E}_{c\|}E_{\|}(s-\tau_{ec}/t_c) - i\Delta\Omega\mathcal{E}_{c\perp}E_{\perp}(s) \tag{A.11}$$

$$\dot{N}(t) = \frac{N_c}{t_c}\dot{n}(s) = \frac{I}{e} - \gamma_e N_c n(s) - \gamma_e N_c^0 - g_{\|}\frac{N_c n(s)+N_c^0-N_T}{1+\epsilon\mathcal{E}_{c\|}^2\left|E_{\|}(s)\right|^2}\mathcal{E}_{c\|}^2\left|E_{\|}(s)\right|^2 - g_{\perp}\frac{N_c n(s)+N_c^0-N_T}{1+\epsilon\mathcal{E}_{c\perp}^2\left|E_{\perp}(s)\right|^2}\mathcal{E}_{c\perp}^2\left|E_{\perp}(s)\right|^2. \tag{A.12}$$

This then leads to

$$\begin{aligned}
\dot{E}_{\parallel}(s) &= \frac{1}{2}(1+i\alpha)\left(t_c N_c g_{\parallel}\frac{n(s)+(N_c^0-N_T)/N_c}{1+\epsilon\mathcal{E}_{c\parallel}^2\left|E_{\parallel}(s)\right|^2}-\gamma_{\parallel}t_c\right)E_{\parallel}(s) \\
&\quad +t_c\kappa_{\parallel}E_{\parallel}(s-\tau_{ec}/t_c) \qquad \text{(A.13)} \\
\dot{E}_{\perp}(s) &= \frac{1}{2}(1+i\alpha)\left(t_c N_c g_{\perp}\frac{n(s)+(N_c^0-N_T)/N_c}{1+\epsilon\mathcal{E}_{c\perp}^2\left|E_{\perp}(s)\right|^2}-\gamma_{\perp}t_c\right)E_{\perp}(s) \\
&\quad +t_c\kappa_{\perp}\frac{\mathcal{E}_{c\parallel}}{\mathcal{E}_{c\perp}}E_{\parallel}(s-\tau_{ec}/t_c)-i\Delta\Omega t_c E_{\perp}(s) \qquad \text{(A.14)} \\
\frac{1}{\gamma_e t_c}\dot{n}(s) &= \frac{I}{eN_c\gamma_e}-\frac{N_c^0}{N_c}-n(s) \\
&\quad -\frac{\mathcal{E}_{c\parallel}^2}{\gamma_e}g_{\parallel}\frac{n(s)+(N_c^0-N_T)/N_c}{1+\epsilon\mathcal{E}_{c\parallel}^2\left|E_{\parallel}(s)\right|^2}\left|E_{\parallel}(s)\right|^2 \\
&\quad -\frac{\mathcal{E}_{c\perp}^2}{\gamma_e}g_{\perp}\frac{n(s)+(N_c^0-N_T)/N_c}{1+\epsilon\mathcal{E}_{c\perp}^2\left|E_{\perp}(s)\right|^2}\left|E_{\perp}(s)\right|^2. \qquad \text{(A.15)}
\end{aligned}$$

By choosing the scaling factors t_c, $\mathcal{E}_{c\parallel}$, $\mathcal{E}_{c\perp}$ and N_c and shift N_c^0 appropriately, we can simplify the equations such:

$$\begin{aligned}
t_c &\to 1/\gamma_{\parallel} \qquad \text{(A.16)} \\
\mathcal{E}_{c\parallel} &\to \sqrt{\frac{\gamma_e}{g_{\parallel}}} \qquad \text{(A.17)} \\
\mathcal{E}_{c\perp} &\to \sqrt{\frac{\gamma_e}{g_{\perp}}} \qquad \text{(A.18)} \\
N_c &\to \frac{\gamma_{\parallel}}{g_{\parallel}} \qquad \text{(A.19)} \\
N_c^0 &\to \frac{\gamma_{\parallel}}{g_{\parallel}}+N_T. \qquad \text{(A.20)}
\end{aligned}$$

Eqs. (A.13)-(A.15) then become

$$
\begin{aligned}
\dot{E}_{\parallel}(s) &= \frac{1}{2}(1+i\alpha)\left(\frac{n(s)+1}{1+\mu\left|E_{\parallel}(s)\right|^{2}}-1\right)E_{\parallel}(s) \\
&\quad +K_{\parallel}E_{\parallel}(s-\tau) \qquad \text{(A.21)}\\
\dot{E}_{\perp}(s) &= -i\Delta E_{\perp}(s)+\frac{1}{2}(1+i\alpha)\left(\sigma\frac{n(s)+1}{1+\frac{\mu}{\sigma}\left|E_{\perp}(s)\right|^{2}}-\rho\right)E_{\perp}(s) \\
&\quad +K_{\perp}\sqrt{\sigma}E_{\parallel}(s-\tau) \qquad \text{(A.22)}\\
\dot{n}(s) &= \frac{1}{T}(p-n(s)-\frac{n(s)+1}{1+\mu\left|E_{\parallel}(s)\right|^{2}}\left|E_{\parallel}(s)\right|^{2} \\
&\quad -\frac{n(s)+1}{1+\frac{\mu}{\sigma}\left|E_{\perp}(s)\right|^{2}}\left|E_{\perp}(s)\right|^{2}). \qquad \text{(A.23)}
\end{aligned}
$$

with the dimensionless gain saturation coefficient $\mu = \epsilon\gamma_e/g_{\parallel}$, the ratio of photon lifetimes $\rho = \frac{\gamma_\perp}{\gamma_\parallel}$, the dimensionless feedback strengths $K_{\parallel,\perp} = \gamma_{\parallel}\kappa_{\parallel,\perp}$, the ratio of the modal gains $\sigma = \frac{g_\perp}{g_\parallel}$, the spectral detuning between the modes $\Delta = \frac{\Delta\Omega}{\gamma_\parallel}$, the time scale coefficient $T = \frac{\gamma_\parallel}{\gamma_e}$, and the dimensionless pump current $p(s) = \frac{g_\parallel}{\gamma_\parallel}\left(\frac{I/e}{\gamma_e}-N_T\right)-1$.

Noise conversion

The noise from spontaneous emission is implemented as complex Gaussian white noise terms $F_{\mathcal{E}_{\parallel,\perp}}$ in the field equations, which have zero mean

$$\left\langle F_{\mathcal{E}_{\parallel,\perp}}(t)\right\rangle = 0 \qquad \text{(A.24)}$$

and the following correlations

$$\left\langle F_{\mathcal{E}_{\parallel,\perp}}(t)\overline{F_{\mathcal{E}_{\parallel,\perp}}(t')}\right\rangle = \beta_{\parallel,\perp}\gamma_e N(t)\delta(t-t'). \qquad \text{(A.25)}$$

The noise in dimensionless variables is calculated by inserting (A.6)-(A.9) into Eq. (A.25):

$$\begin{aligned}
\left\langle F_{E_{\parallel,\perp}}(s)\overline{F_{E_{\parallel,\perp}}(s')}\right\rangle &= \frac{g_{\parallel,\perp}}{\gamma_e}\left\langle F_{\mathcal{E}_{\parallel,\perp}}(t)\overline{F_{\mathcal{E}_{\parallel,\perp}}(t')}\right\rangle \\
&= \frac{1}{\gamma_{\parallel,\perp}^2}\frac{g_{\parallel,\perp}}{\gamma_e}\left\langle F_{\mathcal{E}_{\parallel,\perp}}\left(\frac{s}{\gamma_{\parallel,\perp}}\right)\overline{F_{\mathcal{E}_{\parallel,\perp}}\left(\frac{s'}{\gamma_{\parallel,\perp}}\right)}\right\rangle \\
&= \frac{1}{\gamma_{\parallel,\perp}^2}\frac{g_{\parallel,\perp}}{\gamma_e}\beta_{\parallel,\perp}\gamma_e N\delta\left(\frac{1}{\gamma_{\parallel,\perp}}(s-s')\right) \\
&= \frac{g_{\parallel,\perp}}{\gamma_{\parallel,\perp}}\beta_{\parallel,\perp}N\delta(s-s') \qquad (A.26) \\
&= \frac{g_{\parallel,\perp}}{\gamma_{\parallel,\perp}}\beta_{\parallel,\perp}\left(\frac{\gamma_{\parallel,\perp}}{g_{\parallel,\perp}}n+\frac{\gamma_{\parallel,\perp}}{g_{\parallel,\perp}}+N_T\right)\delta(s-s') \\
&= \beta_{\parallel,\perp}\left(n+1+\frac{g_{\parallel,\perp}}{\gamma_{\parallel,\perp}}N_T\right)\delta(s-s') \qquad (A.27) \\
&=: \beta_{\parallel,\perp}\left(n+n_{0_{\parallel,\perp}}\right)\delta(s-s').
\end{aligned}$$

Here, $n_{0_{\parallel,\perp}}$ take the role of the carriers at threshold in dimensionless units for the respective mode.

B

Transverse stability of External Cavity Modes

For the case of potentially mismatched coupling strength K and feedback strength L, the transverse stability of a trajectory $S(t)$ is governed by the variational equation for a small transverse perturbation δA

$$\dot{\delta A}(t) = Df(S(t))\delta A(t) + (L-K)C\delta A(t-\tau) \tag{B.1}$$

where $Df(S(t))$ is the Jacobian of f, which describes the laser dynamics, evaluated along $S(t)$ and C is a coupling matrix describing the optical feedback and optical coupling.

An external cavity mode (ECM) of the Lang-Kobayashi equations is a rotating wave solution of the form $E = A_\star e^{i\omega_\star t}$ and $n = n_\star$. To calculate its (transverse) stability, we make the transformation $E \rightarrow Ee^{-i\omega_\star t}$, such that the ECM becomes a steady state and split the electric field into a real and an imaginary part $E = A = x + iy$.

We calculate the Jacobian Df to

$$Df = \begin{pmatrix} \frac{1}{2}\left(G-1-2x^2\frac{\partial G}{\partial I}\right) & \omega - \frac{\alpha}{2}\left(G-1-^2 y^2\frac{\partial G}{\partial I}\right) & \frac{1}{2}\frac{\partial G}{\partial n}(x-\alpha y) \\ -\omega + \frac{\alpha}{2}\left(G-1-^2 y^2\frac{\partial G}{\partial I}\right) & \frac{1}{2}\left(G-1-2x^2\frac{\partial G}{\partial I}\right) & \frac{1}{2}\frac{\partial G}{\partial n}(\alpha x + y) \\ -\frac{2x}{T}\left(G+I\frac{\partial G}{\partial I}\right) & -\frac{2y}{T}\left(G+I\frac{\partial G}{\partial I}\right) & -\frac{1}{T}\left(1+I\frac{\partial G}{\partial n}\right) \end{pmatrix}$$

where I represents the intensity of the laser, $I = |A|^2 = x^2 + y^2$. With this we calculate the Jacobian $Df(S)$ with trajectory S corresponding to the transformed ECM solution. We then determine the eigenvalues λ of the linearized right hand side of Eq. (B.1) according to

$$\det\left[Df + (L-K)Ce^{-\lambda\tau}\right] = 0 \tag{B.2}$$

If all the resulting eigenvalues have negative real parts, it indicates that the ECM is transversely stable: the magnitude of the small perturbation $\delta(t)$ in Eq. (B.1), decreases over time. On the other hand, if at least one eigenvalue has a positive real part, it means the ECM in question is transversely unstable.

List of Figures

2.1 Schematic of a semiconductor laser (SL) in an external cavity. The external cavity is characterized by the cavity length L_{EC}, the corresponding round trip delay τ, the feedback strength κ, and the feedback phase ϕ. 8

2.2 Experimentally obtained relaxation oscillations in a solitary laser's intensity output due to a pump current modulation pulse. The laser is pumped at $I = 1.05 I_{\mathrm{thr,sol}}$, the current modulation amplitude corresponds to $\delta I = 0.09 I_{\mathrm{thr,sol}}$. The plot was obtained after averaging 200 oscillations induced by modulation pulses of the same amplitude. Figure courtesy of Xavier Porte. 12

2.3 Measured relaxation oscillation frequencies of a SL in dependence of its normalized pump current. The black squares are the measured frequencies, the red line depicts a square-root fit. 13

2.4 Experimentally obtained rf-spectra of a single semiconductor laser for the cases of solitary operation and with feedback, respectively. The peak in the solitary laser spectrum corresponds to the relaxation oscillation frequency. The feedback leads to an undampening of a broad range frequencies. Figure courtesy of Xavier Porte. 14

2.5 Delay time signature in the low frequency part of the rf-spectrum of a single laser subject to moderate feedback for two different pump currents. The peak spacing corresponds to the inverse of the round-trip time through the external cavity (i.e., the delay time) τ. 15

2.6 Experimentally obtained power-bias current characteristics for a single mode QW edge-emitting laser. Shown are the P-I-curves of the solitary laser (blue) and of the laser receiving optical feedback (red). 16

2.7 Measured threshold pump currents (normalized with the solitary threshold) for different feedback strengths/feedback attenuations. The feedback strength increases exponentially with decreasing feedback attenuation (in dB). Zero attenuation means full strength feedback. In the experiments that corresponded to a few percent of emitted light coupled back into the cavity. 16

2.8 Optical spectra of a solitary edge-emitting SL (black) and of the same laser subject to optical feedback (red). The spectrum broadens to several GHz, the feedback accounted for $\approx 6-7\%$ of the emitted light. 17

2.9 ECM structure in (ω, n) phase space for different values of α. (a) $\alpha = 1.0$, (b) $\alpha = 2.0$, (c) $\alpha = 3.0$ and (d) $\alpha = 3.5$. The green circles are the modes, the red squares are the antimodes, the blue diamonds denote the stable modes, the yellow diamonds represent the maximum gain mode (MGM) and the black star is the solitary laser mode. For this calculation, the following parameters were chosen: $K = 0.1$, $\tau = 1000$, $p = 0.1$, $\mu = 0$, and $\psi = 0$. 22

2.10 Optical spectra numerically obtained from the model in Eqs. (2.5)-(2.7) for the solitary case with $K = 0$ (a) and the case with feedback (b). For (b) the feedback has strength $K = 0.1$. The other simulation parameters for both situations are $p = 2.0$, $\tau = 2000$, $\alpha = 3.0$, $\mu = 0.02$, $T = 200$ and $\beta = 10^{-6}$. 23

2.11 Numerically produced P-I-characteristics of a single SL subject to delayed optical with different strengths K. The growing reduction of the lasing threshold with increasing feedback level is reproduced. The simulation parameters correspond to those given for Fig. 2.10. 24

2.12 Experimentally obtained pump current-output power characteristics of an SL subject to polarization-rotated feedback (red) compared with the solitary case (blue). As can be seen, the lasing threshold and the slope of the P-I curve remain similar. 25

2.13 Experimentally obtained rf-spectra of a single SL with polarization-maintained feedback (PMOF, black) and with polarization-rotated feedback (PROF, red). The feedback attenuation along the optical path in the experimental setup is of comparable magnitude and in results in a low feedback level of a few percent of emitted light coupled back into the laser cavity after the external cavity round-trip. 26

2.14 Numerical P-I-curves for the solitary case ($K_{\parallel} = K_{\perp} = 0$) and for different PROF strengths $K_{\perp}$. The simulation parameters are $T = 200$, $\tau = 2000$, $\alpha = 3.0$, $\mu = 0.02$, $\sigma = 0.84$, $\rho = 1.0$, $\beta_{\parallel} = \beta_{\perp} = 10^{-6}$ and $\Delta = 0$. 30
2.15 Bifurcation diagram of single laser subject to polarization-maintained (a) and polarization-rotated (b) optical feedback, respectively. Depicted are (local) intensity extrema versus the nondimensional feedback strengths $K_{\parallel}$ and $K_{\perp}$, respectively. The perpendicular polarization mode requires much stronger feedback than the parallel polarization mode to induce instabilities. The defining parameter for this is the gain ratio $\sigma = 0.84$. The other system parameters are $T = 200$, $p = 1.0$, $\mu = 0.02$, $\tau = 2000$, $\alpha = 3.0$, $\rho = 1.0$, $\Delta = 0$. Noise due to spontaneous emission is neglected for these simulations $\beta_{\parallel} = \beta_{\perp} = 0$. 31
2.16 Numerically obtained LFF-dynamics in intensity (a) and frequency (b). The power buildup coincides with a drift toward lower frequencies. The simulation parameters are $p = 0.1$, $\tau = 2000$, $K_{\parallel} = 0.1$, $\alpha = 3.0$, $\mu = 0.02$, $T = 200$, $\beta_{\parallel} = \beta_{\perp} = 10^{-6}$. 32
2.17 Dynamical and spectral characteristics in the LFF regime: (a) depicts intensity (upper panel) and frequency (lower panel) dynamics within the interval between two subsequent power dropouts. (b) shows the corresponding phase space trajectory in (ω, n) space, where the green dots represent modes, red dots are antimodes, blue squares represent stable High Gain Modes and the yellow square depicts the Maximum Gain Mode (MGM). (c) shows a numerically computed optical spectrum for the corresponding parameters, the inset is a magnification depicting peaks corresponding to individual ECMs. The simulation parameters for all plots are $p = 0.1$, $\tau = 2000$, $K_{\parallel} = 0.1$, $\alpha = 3.0$, $\mu = 0.02$, $T = 200$, $\beta_{\parallel} = \beta_{\perp} = 10^{-6}$. . . . 34
2.18 Dynamics trajectory in (ω, n)-phase space for $\alpha = 3.5$ (a), $\alpha = 4.0$ (b), and $\alpha = 2.5$ (c). The lengths of the dynamics match as do their other simulation parameters. These correspond to the ones given in the caption of Fig. 2.17. Note the different scales in the frequency (x-) axis. Green symbols represent modes, red symbols are antimodes, the yellow squares corresponds to the Maximum Gain Mode (MGM) and the blue symbols are Stable High Gain Modes. 36
2.19 Coexistence between stable output and LFF in the dynamics of a single laser with feedback. The laser was pumped with $p = 1.1$, the feedback delay corresponded to $\tau = 75.2$ ns, and the feedback rate was $\kappa \approx 45$ ns^{-1}. Figure courtesy of Xavier Porte. 37

2.20 Numerically obtained dynamics showing the transition between LFF and stable emission. (a) depicts intensity dynamics and (b) shows the time evolution of the frequency ω. After three LFF cycles, the dynamics gets stuck within the basin of attraction of one high gain mode (HGM). The parameters are $p = 0.2$, $\tau = 2000$, $K_{\parallel} = 0.1$, $\alpha = 2.1$, $\mu = 0.02$, $T = 200$, $\beta_{\parallel} = \beta_{\perp} = 10^{-6}$ 38

2.21 Dynamical and spectral characteristics in the CC regime: (a) depicts intensity (upper panel) and frequency (lower panel) dynamics within a comparably short time interval. (b) shows the corresponding phase space trajectory in (ω, n) space, where the green dots represent modes, red dots are antimodes, blue squares represent stable High Gain Modes and the yellow square depicts the Maximum Gain Mode (MGM). (c) shows a numerically computed optical spectrum for the corresponding parameters. The simulation parameters for all plots are $p = 2.0$, $\tau = 2000$, $K_{\parallel} = 0.1$, $\alpha = 3.0$, $\mu = 0.02$, $T = 200$, $\beta_{\parallel} = \beta_{\perp} = 10^{-6}$. These parameters correspond to those of Fig. 2.17, except for the pump parameter. 40

2.22 PROF-induced intensity dynamics in the parallel polarization mode $|E_{\parallel}|^2$ (a), in the perpendicular polarization mode $|E_{\perp}|^2$(b) and in the overall intensity output $|E_{\parallel}|^2 + |E_{\perp}|^2$ (c). The parameters to obtain these dynamics are $\sigma = 0.84$, $\rho = 1.0$, $\Delta = 0$, $p = 1.0$, $\tau = 2000$, $K_{\perp} = 0.3$, $\alpha = 3.0$, $\mu = 0.02$, $T = 200$, $\beta_{\parallel} = \beta_{\perp} = 10^{-7}$. 41

2.23 PROF-induced instabilities in the overall intensity dynamics $|E_{\parallel}|^2 + |E_{\perp}|^2$ for low feedback strength $K_{\perp} = 0.1$ and for two different frequency detunings between the polarization modes. (a) shows stable emission for zero detuning $\Delta = 0$, (b) shows periodic relaxation oscillations for $\Delta = -0.2$. The other parameters to obtain these dynamics are $\sigma = 0.84$, $\rho = 1.0$, $p = 0.1$, $\tau = 2000$, $K_{\perp} = 0.1$, $\alpha = 3.0$, $\mu = 0.02$, $T = 200$, $\beta_{\parallel} = \beta_{\perp} = 0$. 42

2.24 Square wave switching in the intensity outputs of both modes $|E_{\parallel}|^2$ and $|E_{\perp}|^2$. The square waves exhibit antiphasic switching between both modes with a period of $\approx 2\tau = 4000$. The parameters to obtain these dynamics are $\sigma = 0.84$, $\rho = 1.0$, $\Delta = 0$, $p = 1.0$, $\tau = 2000$, $K_{\perp} = 0.3$, $\alpha = 3.0$, $\mu = 0.02$, $T = 200$, $\beta_{\parallel} = \beta_{\perp} = 10^{-7}$. 43

3.1 Symmetric setup of bidirectionally-coupled lasers with feedback. The distances are given in time for a one-way trip. L and K are the strength of the feedback and the coupling, respectively. 49

3.2 Zero-lag crosscorrelation $C(0)$ of the two coupled lasers' intensities in dependence of coupling strength K and feedback strength L. Coupling and feedback have the same delay τ. The parameters used for this simulation are $\mu = 0.26$, $p = 1.0$, $\alpha = 4.0$, $T = 200$, $\tau = 1000$ and $\beta = 10^{-5}$. 52

3.3 Dynamics of the symmetrized solution $S(t)$ (see Eq. (3.6)) of two lasers coupled according to Fig. 3.1 for different coupling mismatches. The dynamics are plotted in the (ω_S, n_S)-phase space. The frequency is calculated by $\omega_S = (\phi_S(t) - \phi_S(t - \tau))/\tau$, with $\phi_S = \frac{1}{2}(\phi_1 + \phi_2)$ describing the phase in the synchronization manifold. $n_S = \frac{1}{2}(n_1 + n_2)$ is the corresponding carrier number. The blue part of the trajectory is well synchronized, the grey part is not. Transversely stable modes are depicted as green triangles, unstable modes are shown as red circles. The insets depict the intensity difference corresponding to the shown phase space trajectory. The simulation parameters are $\tau = 500$, $T = 200$, $\alpha = 4$, $p = 0.1$, $\beta = 10^{-5}$. (a) shows the case without mismatch $K = L = 0.06$; for (b) the feedback-coupling mismatch corresponds to $K = 0.03$, $L = 0.09$. The computation was performed by O. D'Huys. . . 53

3.4 Peaks of the autocorrelation (a) and crosscorrelation function $C(\Delta t)$ (b), respectively, in dependence of the coupling mismatch $L - K$. Both correlations are calculated for the lasers' intensities. Black thick line: crosscorrelation at zero lag $C(0)$, blue circles): correlation peak at one delay time $C(\tau)$, red diamonds: $C(2\tau)$, green squares: $C(3\tau)$, magenta triangles: $C(4\tau)$. Simulation parameters are: $\tau = 1000$, $\mu = 0$, $p = 1.0$, $T = 200$, $\beta = 10^{-5}$. The computation to produce these plots were done by O. D'Huys. 54

3.5 Sketch of a closed loop setup as an example for a drive-response configuration. The feedback-delay is τ, the coupling delay is τ_c. 55

3.6 Scheme of a bidirectional coupling setup with a mismatch of the feedback delays of both lasers. This can be realized with a semitransparent mirror in the middle between the lasers, when the mirror is shifted from the exact center of the setup. The given delays correspond to the propagation times for a one-way trip. The orange lines represent the coupling signals from one laser to the other, being transmitted trought the mirror, the green lines are the respective feedbacks, reflected by the mirror. Both feedbacks have strength L, both coupling strengths equal K. 57

3.7 Numerically-obtained dynamics (a) and cross-correlation of two delay-coupled lasers with a feedback delay-mismatch of $\Delta\tau = 100$ operated in the coherence collapse regime. The simulation parameters are $\tau = 2000$, $\alpha = 4.0$, $p = 1.0$, $\mu = 0.26$, $T = 200$ and $L = K = 0.05$. For clarity, noise was disregarded for this simulation. 59

3.8 Cross-correlation $C(\delta t)$ peak at shift $\Delta t = \Delta\tau$ of the output intensities of two coupled lasers in a relay configuration as depicted in Fig. 3.6 (red line) and the peak at $\Delta t = 2\tau$ of the autocorrelation function of one laser's output (blue line) as a function of the delay mismatch parameter $\Delta\tau$. The peaks coincide: higher regularity of the dynamics (peak in the autocorrelation) implies crosscorrelation. The simulation parameters are $\tau = 1000$, $\alpha = 4.0$, $p = 1.0$, $\mu = 0.26$, $T = 200$ $\beta = 10^{-5}$. Coupling and feedback are equal in strength $L = K = 0.05$. . 60

3.9 Cross-correlation $C(\Delta t)$ peak at shift $\Delta t = \Delta\tau$ of the field intensities of two lasers coupled according to Fig. 3.6 versus the feedback strength L and the coupling strength K, respectively, for an applied delay-mismatch $\Delta\tau = 20$ (a) and for $\Delta\tau = 900$ (b). When compared to Fig. 3.2, one notes that the system's synchronization is more sensitive to a coupling mismatch $L - K$ if it also features a delay-mismatch. The other parameters for the numerics are $\tau = 1000$, $\mu = 0.26$, $p = 1.0$, $\alpha = 4.0$, $T = 200$ and $\beta = 10^{-5}$. 61

3.10 Dynamics of the symmetrized solution $S(t)$ (see Eq. (3.6)) in (ω_S, n_S)-phase space for different values of the delay mismatch parameter $\Delta\tau$ after $t = 5 \cdot 10^4$. For definition of ω_S and n_S, see Fig. 3.3. Green circles indicate transversely stable modes, red triangles are transversely unstable modes and antimodes. The dynamics trajectory (in blue) is marked with an arrow if stabilized. The mean delay time τ is fixed at $\tau = 1000$, the other parameters are $\alpha = 4.0$, $p = 1.0$ (except lower right), $\mu = 0.26$ and $L = K = 0.05$. Note that the lower right plot has a different y-scale than the others. 63

3.11 Cross-correlation $C(\delta t)$ at lag $\Delta t = \Delta\tau$ (red lines) and autocorrelation at $\Delta t = 2\tau$ (blue lines) vs the delay mismatch parameter $\Delta\tau$ for rational ratios of the feedback delays $r_\tau = \tau_1/\tau_2$. Magnification of Fig. 3.8 around (a) $r_\tau = 1$, (b) $r_\tau = 2/1$, (c) $r_\tau = 3/1$ and for (d) $\Delta\tau \approx \tau$. Simulation parameters are as for Fig. 3.8. 64

3.12 Intensity extrema of the two lasers versus the delay mismatch parameter $\Delta\tau$. Green points are maxima, red points are minima. Magnifications are shown for a small delay mismatch $\Delta\tau < 15$ (lower left), for a delay times ratio of $r_\tau \approx 2/1$ (lower center) and for one of the delays being very short $\tau_1 \gg \tau_2$ (lower right). The other simulation parameters are: $\tau = 1000$, $\alpha = 4.0$, $\mu = 0.26$, $p = 1.0$, $T = 200$, $\beta = 10^{-5}$, $K = L = 0.05$. 65

3.13 Dynamics of the coupled system without delay mismatch $\Delta\tau = 0$ (a) and the corresponding autocorrelation function (b). The other simulation parameters are $L = K = 0.05$, $\alpha = 4.0$, $p = 0.0$, $\mu = 0.0$, $T = 200$, $\beta = 10^{-6}$, $\tau = 997$. 67

3.14 Synchronized dynamics of the coupled system in (ω_S, n_S)-phase space (see Fig. 3.3) for the case of a delay mismatch $\Delta\tau = 17$ (a). The coupling delay is $\tau = 1014$, the other simulation parameters are $L = K = 0.05$, $\alpha = 4.0$, $p = 0.0$, $\mu = 0.0$, $T = 200$, $\beta = 10^{-6}$, $\tau = 997$. (b) shows a histogram of the corresponding phase differences of the delayed feedback and the delayed coupling $\phi_1(t + \tau + \Delta\tau) - \phi_2(t + \tau)$. 68

3.15 Effect of the nonlinear gain saturation on the position and transverse stability of the external cavity modes in (ω_S, n_S)-phase space. The pump current $p = 1.0$ results in coherence collapse dynamics. The larger the pump current value, the more pronounced the effect is. Red circles incicate transversely unstable modes and antimodes, green circles represent transversely stable modes. The dynamics is shown in blue. The other simulation parameters are: $\tau = 1000$, $\Delta\tau = 0$, $\alpha = 4.0$, $T = 200$, $L = K = 0.05$ and $\beta = 10^{-5}$. 69

3.16 Intensity extrema of the coupled system for varying μ. Green points represent intensity maxima, the red points are intensity minima. The numerical parameters are the same as for Fig. 3.15. 70

3.17 Cross-correlation of the field intensities versus the feedback strength L and the coupling strength K, respectively, with and without delay mismatch. (a) Symmetric delays $\Delta\tau = 0$ resulting in zero-lag synchronization; (b) with delay mismatch $\Delta\tau = 20$ - the crosscorrelation is computed for $\Delta t = \Delta\tau$. The nonlinear gain saturation is neglected for these simulations. Corresponding plots with $\mu > 0$ are shown in Figs. 3.2 and 3.9, respectively. The simulation parameters here correspond to $\mu = 0$, $p = 1.0$, $\alpha = 4.0$, $T = 200$, $\tau = 1000$ and $\beta = 10^{-5}$. 71

3.18 Zero-lag crosscorrelation (blue squares), crosscorrelation at $\Delta t = \tau$ (red pluses) and crosscorrelation at $\Delta t = -\tau$ (green crosses) versus the detuning Δ. Already for comparably small detuning lag-synchronization becomes predominant, even though the zero-lag synchronization exhibits high levels as well. The numerical parameters are: $\alpha = 3.0$, $\mu = 0.02$, $p = 0.0$, $T = 200$, $\tau = 2000$, $K = L = 0.15$ and $\beta = 10^{-6}$. 73

3.19 Spectral ranges computed from the average of several frequency extrema of two coupled lasers with feedback versus their relative symmetric detuning. The red shaded area describes the spectral range of laser 1, the green area is the spectral range of laser 2 and the brown region illustrates the spectral overlap. The frequencies are given relative to the mean solitary frequency $\omega_{\text{mean}} = (\omega_1 + \omega_2)/2 = 0$. The extrema are averaged from a five-fold sampling of one timetrace per detuning-value with a length of $8 \cdot 10^5$ points each. The frequencies are calculated according to Eqs. (3.29) and (3.30). The simulation parameters correspond to those given in Fig. 3.18. 75

3.20 Time series of the sliding cross-correlation (top panels), of both frequencies $\omega_{1,2}$ (middle panels) and of the corresponding output intensities $|E_{1,2}(t)|^2$ (lower panels) during one LFF cycle for different values of the detuning. The frequency dynamics and intensity dynamics, respecively, of laser 1 are depicted in blue, the corresponding dynamics of laser 2 are shown as green curves. The detuning values are $\Delta = 0.01$ (a), $\Delta = 0.025$ (b) and $\Delta = 0.04$ (c). The simulation parameters correspond to those given in Fig. 3.18. 77

3.21 Dynamical trajectories in (ω_S, n) phase space for different detuning values $\Delta = 0.01$ (a), $\Delta = 0.025$ (b) and $\Delta = 0.04$ (c). The light green and dark red trajectories are describe the dynamics of laser 1, the dark green and dark red parts describe laser 2. Both red shares of the trajectories describe dynamics which are unsynchronized according to a slcc-threshold value of $C_{\text{thr}} = 0.95$, the green curves are synchronized dynamics. The simulation parameters correspond to those given in Fig. 3.18. 79

3.22 Optical spectra generated by FFT from the dynamics shown in Fig. 3.20 and for larger detuning. Laser 1's spectra are shown in light red, the spectra of laser 2 are depicted as light blue and the overlap is the purple area. The detuning values are $\Delta = 0.01$ (a), $\Delta = 0.025$ (b), $\Delta = 0.04$ (c) and $\Delta = 0.075$ (d). Note that the y-axis is in log-scale. 80

4.1 Schematic experimental setup. The lasers are symmetrically coupled with a delay via a feedback and coupling fiber loop consisting of a 50/50 optical coupler and an optical isolator. The loop serves as passive relay. The numbers in the symbols for the couplers correspond to their respective coupling ratios (in percent). The orange lines depict electrical connections, the blue ones represent single-mode optical fiber (SMF). . . . 88

4.2 (a) Experimental time series of synchronized fast intensity dynamics in the coherence collapse regime. A short desychronization event is highlighted. The lasers are pumped with a pump current corresponding to $p = 1.25$. The intensities have been normalized by shifting the traces by their respective mean values and scaling with their standard deviations. (b) shows the corresponding synchronization error, i.e., the normalized intensity difference. 89

4.3 Cross-correlation coefficient at zero lag C_{corr} (black circles), fraction of the sliding-window cross-correlation above the correlation threshold of $C_{\mathrm{thr}} = 0.5$ (red squares) and mean averaged synchronization error χ (blue diamonds), respectively, versus the applied normalized pump current of both lasers. . 90

4.4 Zero-lag synchronization of experimentally-obtained LFF dynamics. Output intensity time series of the two lasers (a,b) and corresponding sliding cross-correlation (c,d) for a long time interval of 20 μs (a,c) and a magnification in time (b,d). The time series depicted in red was vertically shifted for better visibility. The applied pump current in this case corresponds to $p = 1.04$, being close to the solitary lasing thresholds. The intensities are normalized by shifting their mean values to zero and scaling them by their standard deviations. 92

4.5 Synchronization of laser outputs in the CC regime. Normalized output intensity time series of the two lasers (a,b) and corresponding sliding cross-correlation (c,d) for a time interval of 200 ns (a,c) and a magnification in time (b,d). The blue intensity time series was vertically shifted for better visibility. The applied pump current in this case corresponds to $p = 1.39$. The normalization was done corresponding to Fig. 4.4. 94

4.6 Normalized distributions of the sliding cross-correlation (slcc) for 6 different pump currents (see legend). The histograms have 401 bins. Note the log-scale. 95

4.7 Histograms of the bubbling inter-event intervals (IEI) (a) and of the bubbling event duration (b) for pump currents $p = 1.22$, $p = 1.30$, $p = 1.39$ and $p = 1.48$ (from top to bottom). The IEI-histograms have 100 bins each, the histograms for the bubbling duration have 32 bins of width 0.4 ns. Note the log-scales. 96
4.8 Crosscorrelation coefficient at zero lag (black circles), fraction of the sliding-window cross-correlation above the correlation threshold of $C_{\mathrm{thr}} = 0.5$ (red squares) and mean integrated synchronization error χ (blue diamonds), respectively, versus the applied frequency detuning of both lasers $\Delta\Omega$. 98
4.9 Exemplary time series of the sliding-window cross-correlation (slcc) for five experimentally-obtained pairs of intensity time series, corresponding to five different detuning values: (a) $\Delta\Omega = 0$ GHz, (b) $\Delta\Omega = -1.0$ GHz, (c) $\Delta\Omega = -4.1$ GHz, (d) $\Delta\Omega = -7.2$ GHz, (e) $\Delta\Omega = -10.4$ GHz. 99
4.10 (a) Magnified view on experimental intensity timeseries of both lasers [corresponding to Fig. 4.9(b)] with detuning $\Delta\Omega = -1$ GHz. (b) depicts the corresponding sliding cross-correlation trace. 100
4.11 Normalized distributions of the sliding cross-correlation (slcc) for different negative values of the detuning (a) and for positive detuning (b). The distribution for zero detuning is depicted in purple in both diagrams. The histograms have 401 bins. Note the log-scale. 101
4.12 Distribution of duration of detected episodes of unsynchronized dynamics derived from experimental time traces for different detunings $\Delta\Omega$. (a) $\Delta\Omega = -10.4$ GHz, (b) $\Delta\Omega = -7.3$ GHz, (c) $\Delta\Omega = -4.1$ GHz, (d) $\Delta\Omega = -1.0$ GHz, (e) $\Delta\Omega = 0$ GHz, (f) $\Delta\Omega = 2.1$ GHz, (g) $\Delta\Omega = 5.3$ GHz, (h) $\Delta\Omega = 8.4$ GHz, (i) $\Delta\Omega = 11.5$ GHz. The detection thresholds for the events are $T_{\mathrm{thr}} = 0.5$ ns, $C_{\mathrm{thr}} = 0.5$, $\mathrm{IEI}_{\mathrm{thr}} = 0.5$ ns. 102
4.13 Distribution of inter-event intervals of desynchronization episodes determined from experimentally-obtained time series for different detunings $\Delta\Omega$. (a) $\Delta\Omega = -10.4$ GHz, (b) $\Delta\Omega = -7.3$ GHz, (c) $\Delta\Omega = -4.1$ GHz, (d) $\Delta\Omega = -1.0$ GHz, (e) $\Delta\Omega = 0$ GHz, (f) $\Delta\Omega = 2.1$ GHz, (g) $\Delta\Omega = 5.3$ GHz, (h) $\Delta\Omega = 8.4$ GHz, (i) $\Delta\Omega = 11.5$ GHz. The detection thresholds for the events are $T_{\mathrm{thr}} = 0.5$ ns, $C_{\mathrm{thr}} = 0.5$, $\mathrm{IEI}_{\mathrm{thr}} = 0.5$ ns. 103
4.14 Cross-correlation coefficient at zero lag (black circles), fraction of the sliding-window cross-correlation above the correlation threshold of $C_{\mathrm{thr}} = 0.5$ (red squares) and mean integrated synchronization error χ (blue diamonds), respectively, versus the applied spectral detuning of both lasers. The simulation parameters are given in Table 4.1. 105

4.15 Exemplary time series of the sliding-window cross-correlation (slcc) for four numerically-obtained pairs of intensity time series, corresponding to four different detuning values: (a) $\Delta\Omega = 1$ GHz, (b) $\Delta\Omega = 2$ GHz, (c) $\Delta\Omega = 3$ GHz and (d) $\Delta\Omega = 4$ GHz. The other parameters are given in Table 4.1. . 106

4.16 Magnified view of simulated intensity timeseries of both lasers (upper panels) [corresponding to Fig. 4.15] and the corresponding slcc (lower panels). (a) $\Delta\Omega = 1$ GHz, (b) $\Delta\Omega = 2$ GHz, (c) $\Delta\Omega = 3$ GHz and (d) $\Delta\Omega = 4$ GHz. The other parameters are given in Table 4.1. 107

4.17 Distributions of duration of unsynchronized episodes (upper panel, red points) and of their inter-event intervals (IEI) (lower panel, blue points), respectively, for different detunings $\Delta\Omega$. (a) $\Delta\Omega = -20$ GHz, (b) $\Delta\Omega = -14$ GHz, (c) $\Delta\Omega = -11$ GHz, (d) $\Delta\Omega = -6$ GHz, (e) $\Delta\Omega = -2$ GHz, (f) $\Delta\Omega = -1$ GHz, (g) $\Delta\Omega = 1$ GHz, (h) $\Delta\Omega = 2$ GHz, (i) $\Delta\Omega = 6$ GHz, (j) $\Delta\Omega = 11$ GHz, (k) $\Delta\Omega = 14$ GHz and (l) $\Delta\Omega = 20$ GHz. The detection thresholds for the desynchronization events are $T_{\mathrm{thr}} = 0.5$ ns, $C_{\mathrm{thr}} = 0.5$, $\mathrm{IEI}_{\mathrm{thr}} = 0.5$ ns. The other simulation parameters correspond to those given in Table 4.1, except for $\kappa_c = \kappa_{\mathrm{fb}} = 10$ ns^{-1}. 108

4.18 Cross-correlation at zero lag versus the normalized pump current values p_1 and p_2, respectively. The simulation parameters are to those given in Table 4.1, except for $\kappa_c = \kappa_{\mathrm{fb}} = 10$ ns^{-1}. 110

4.19 Crosscorrelation function for $p_1 = 1.0$ and $p_2 = 1.5$. The maximum peak is at shift $\Delta t = \tau$. 111

4.20 Normalized intensity dynamics of two coupled lasers with different pump current mismatches (upper panels) and the corresponding sliding-window cross-correlation time series (lower panels). The panels on the right hand side are zooms into both the dynamics and the slcc around certain desynchronization events. The set of mismatches are (a) $p_1 = 1.01$, $p_2 = 1.02$; (b) $p_1 = 1.2$, $p_2 = 1.22$ and (c) $p_1 = 1.01$, $p_2 = 1.2$. The simulation parameters are the same as for Figs. 4.18 and 4.17 112

4.21 Distributions of bubbling event durations (a) and IEI (b) for the pump current mismatch $p_1 = 1.01$, $p_2 = 1.02$. The inset in (b) shows a magnification of the histogram for small IEI. The binsize corresponds to 0.1 ns for the duration distribution and 0.5 ns for the IEI distribution. 113

4.22 Numerically-obtained timeseries of the carrier numbers of two bidirectionally-coupled lasers with $p_1 = 1.2$ and $p_2 = 1.22$ (a) and the corresponding slcc timetrace (b). 114

4.23 Distributions of bubbling event durations (a) and IEI (b) for the pump current mismatch $p_1 = 1.2$, $p_2 = 1.22$. The binsize corresponds to 0.1 ns for the duration distribution and 0.5 ns for the IEI distribution. 115

4.24 Distributions of desynchronization event durations (a) and IEI (b) for the pump current mismatch $p_1 = 1.01$, $p_2 = 1.2$. The inset in (b) shows a magnification of the histogram for small IEI. The binsize corresponds to 0.1 ns for the duration distribution and 0.5 ns for the IEI distribution. 115

5.1 Numerically-obtained dynamics from the model in Chapter 2 with the the spontaneous emission factor set to zero. The LFF structure including the power dropouts are preserved in the noiseless situation. The simulation parameters were $\alpha = 3$, $K = 0.15$, $p = 0.1$, $T = 200$, $\mu = 0.01$, $\tau = 16000$. 120

5.2 Schematic experimental setup. The lasers are symmetrically coupled via a feedback and coupling fiber loop consisting of a 50/50 optical coupler and a circulator. This loop serves as passive relay. The numbers featured on the symbols for the couplers correspond to their respective coupling ratios (in percent). The orange lines depict electrical connections, the blue ones represent polarization-maintaining (PM) optical fiber.122

5.3 Experimental intensity time traces of both lasers. Panel (a) shows unsynchronized dropouts. The desynchronization lasts for approximately one delay $\tau_c \approx \tau_{\text{fb}}$. (b) depicts a pair of synchronized dropouts in both lasers. 124

5.4 The total number N_{total} of measured pairs of power dropouts versus the applied normalized pump currents. 125

5.5 Experimental results for the fraction of synchronized power dropouts ζ versus the normalized pump currents p_1 and p_2 averaged among the corresponding measured time series. The error bars show the corresponding standard deviation. The gray curve results from a 3rd order polynomial fit and is only meant as a guide to the eyes. 126

5.6 Examples of numerically-obtained timeseries for $p = 1.03$ and $\beta = 10^{-6}$ exhibiting synchronous (a) and asynchronous (b) dropouts. The dashed black and red lines indicate the time of occurence of a dropout as detected by the algorithm described above. The horizontal dashed grey and magenta lines represent the respective overall average intensity, and the solid grey and magenta lines depict the sliding window-averaged intensities. In panel (b), a time difference between both dropouts can be clearly seen, which corresponds approximately to the delay time. 130

5.7 Numerical results for the fraction of synchronized power dropouts ζ versus the normalized pump currents p_1 and p_2 versus the spontaneous emission factor β for the case of a completely symmetric coupling configuration and identical lasers. The simulation parameters correspond to those listed in Table 5.1. 131

5.8 Cross sections of the data presented in Fig. 5.7. (a) ζ versus the normalized pump currents for different noise strength values. (b) ζ versus the noise strength β for different values of the normalized pump currents. 132

5.9 Numerical results for the fraction of synchronized power dropouts ζ versus the normalized pump current p_1 versus the spontaneous emission factor β in a setup with small asymmetries and slightly mismatched lasers. The simulation parameters correspond largely to those listed in Table 5.1 with the mismatches given by (5.5). $p_2 = p_1 + 0.001$ 133

5.10 ζ versus normalized pump currents p_1, p_2 for the experimental and the symmetric numerical results (dark grey diamonds and light grey circles, respectively), and ζ versus normalized pump current p_1 for the numerical results with applied mismatches (see (5.5)), including $p_2 = p_1 + 0.001$ (red squares). For the numerical curves $\beta = 10^{-6}$. 134

6.1 Schematic of the classic reservoir computing (RC) approach based on a complex network of coupled nonlinear nodes. $u_l(t)$ represents the input signal, w^i_{lm} are the input weights, w^r_{mk} are the readout weights and $y_k(t)$ corresponds to the output. Figure courtesy of D. Brunner. 138

6.2 Schematic representation of RC based on a single semiconductor laser subject to time-delayed feedback via time multiplexing. SL stands for the semiconductor laser and the blue circles represent the N virtual nodes in the feedback delay loop. They are separated by time Θ. $y_k(t)$ represents the output signal. Figure courtesy of D. Brunner. 141

6.3 Sample cochleogram representing the acoustical signal of an uttering of the number "nine". The information is distributed over 86 frequency channels. 143

6.4 Spatio-temporal input state matrix corresponding to the acoustical signal represented by the cochleogram in Fig. 6.3. The horizontal axis represents one delay time τ with the virtual node number corresponding to the spatial position within the delay line. 144

6.5 Part of a chaotic time series of laser intensity pulsations constituting the Santa Fé competition dataset A. The time series data has been normalized before preprocessing. 145

6.6 Laser response (blue curve) to an electrically-injected signal corresponding to the spoken digit "nine". The red curve corresponds to the time-varying injection current. The inset depicts a zoom of both traces. The modulation frequency corresponds to 5 GS/s. The applied feedback is PMOF with $\kappa_{\|} = 10$ ns^{-1} 149

6.7 The sine-squared nonlinearity of the Mach-Zehnder electro-optic modulator (blue) corresponding to Eq. (6.15) vs the phase. The red dot illustrates the operating point for symmetric modulation while the green dot corresponds to the operating point for asymmetric modulation. The modulation ranges coincide. 150

6.8 Laser response (blue curve) to an optically-injected signal corresponding to the spoken digit "nine". The red curve corresponds to the injected optical power. The inset depicts a zoom of both traces. The modulation frequency corresponds to 5 GS/s. The laser is pumped at threshold. The average injected power is $\bar{P}_{inj} = 436\mu$W. The applied feedback has a rate of $\kappa_{\|} = 10$ ns^{-1}. 151

6.9 Word error rate (WER) for the spoken digit recognition task versus the normalized pump current $p = I_b/I_{thr}$ for electrical signal injection. Black circles denote the results for feedback with parallel polarization (PMOF) with a feedback rate of $\kappa_{\|} = 10$ ns^{-1}. Green diamonds are the results PROF with the feedback rate $\kappa_{\perp} = 10$ ns^{-1}. Red squares represent the resulting word error rates for the case without any feedback $\kappa_{\|} = \kappa_{\perp} = 0$. The other parameters are set as in Table 6.1. The lines are meant only as guide to the eyes. 153

6.10 WER for the spoken digit recognition task versus the normalized pump current p for optical signal injection. Black circles denote the results for PMOF with a feedback rate of $\kappa_{\|} = 10$ ns^{-1}. Red squares are the results for PROF with the same feedback rate $\kappa_{\perp} = 10$ ns^{-1}. Green diamonds are the resulting word error rates for the case without feedback. The other parameters are chosen according to Table 6.1. Note that the lines are only a guide to the eyes. 154

6.11 Normalized mean squared error (NMSE) for the Santa Fé time series prediction task versus the normalized pump current p for PROF with $\bar{P}_{inj} = 436\mu$W (green circles), PMOF with $\bar{P}_{inj} = 436\mu$W (blue squares), PMOF with $\bar{P}_{inj} = 11\mu W$ (black diamonds) and PROF with $\bar{P}_{inj} = 11\mu W$ (red triangles), respectively. The feedback rates were set to $\kappa_{\|} = 10$ ns^{-1} and $\kappa_{\perp} = 10$ ns^{-1}, respectively, while the respective other was set to zero. The other parameters are set as in Table 6.1. Note that the lines are only guide to the eyes. . . . 155

6.12 Normalized mean squared error (NMSE) for the Santa Fé time series prediction task as a function of the PMOF feedback rate $\kappa_{\|}$ and of the average injected power $\bar{P}_{inj}$ (y-axis). The normalized pump current is set to $p = 1.01$. The other parameters are chosen as in Table 6.1. 157

6.13 NMSE for the Santa Fé time series prediction task depending on the PMOF feedback rate $\kappa_{\|}$ (x-axis) and on the average injected power $\bar{P}_{inj}$ (y-axis) for a stronger pump current of $p = 1.18$. The other parameters are chosen according to Table 6.1. 157

6.14 Normalized mean squared error (NMSE) for the Santa Fé time series prediction task as a function of the PROF feedback rate $\kappa_{\perp}$ and the average injected power $\bar{P}_{inj}$ (y-axis). The pump current corresponds to $p = 1.18$. The other parameters are chosen according to Table 6.1. 158

6.15 (a) WER for the spoken digit recognition task versus the spontaneous emission factor β. Shown are results for electrical (blue circles) and optical (red squares) signal injection. The feedback rate was set to zero: $\kappa_{\|} = \kappa_{\perp} = 0$. The laser was simulated as pumped at threshold $p = 1.0$. (b) NMSE for the Santa Fé time series prediction task versus β for PMOF (blue circles) and for PROF (red squares). The feedback rates are set to $\kappa_{\|} = 10$ ns^{-1} and $\kappa_{\perp} = 10$ ns^{-1}, respectively, while the respective other is set to zero. The pump parameter is $p = 1.18$. The values of the other parameters are given in Table 6.1. Note that the lines are only guides to the eye. . . . 159

6.16 Experimentally-obtained WER results for the spoken digit recognition task considering electrical (asterisks) and optical (circles) signal injection, respectively, versus the laser bias current I_b. Courtesy of D. Brunner. 161

6.17 Experimentally-obtained NMSE results for the Santa Fé time series prediction task considering electrical (asterisks) and optical (circles) signal injection, respectively, versus the laser's bias current. The signal was injected optically. Figure courtesy of D. Brunner. 162

6.18 NMSE versus the normalized laser pump current for the case of PMOF (diamonds) and for PROF (triangles). The grey and light red colored symbols, respectively, correspond to the results shown in Fig. 6.11 with a non-polarization-resolved intensity readout. The black and dark red symbols depict the findings for separate modal intensity readouts. The feedback rates correspond to $\kappa_{\|} = 10$ ns^{-1} and $\kappa_{\perp} = 10$ ns^{-1} for PMOF and PROF, respectively. The average injection power is $\bar{P}_{\mathrm{inj}} = 11\mu$W. 164

6.19 NMSE versus the PROF feedback rate $\kappa_\perp$ and the average injected power $\bar{P}_{\mathrm{inj}}$ for the case of polarization-resolved readouts. The laser was pumped with a normalized current of $p = 1.01$. The values of the other simulation parameters are given in Table 6.1.. 165
6.20 NMSE versus the PROF feedback rate $\kappa_\perp$ and the average injected power $\bar{P}_{\mathrm{inj}}$ for the case of polarization-resolved readouts. The laser was pumped with a normalized current of $p = 1.18$. The operating conditions correspond to the ones used to obtain the results in Fig. 6.14. 165
6.21 NMSE for the time series prediction task versus Θ for different normalized pump current values $p = 1.0$ (black circles), $p = 1.05$ (red squares), $p = 1.1$ (green diamonds) and $p = 1.2$ (blue triangles). The feedback is modeled as PMOF with rate $\kappa_\parallel = 10$ ns^{-1}. The other parameters are set as in Table 6.1. Note the log-log scale. 167
6.22 NMSE results versus Θ for different PMOF feedback rates $\kappa_\parallel = 10$ ns^{-1} (black circles), $\kappa_\parallel = 20$ ns^{-1} (red squares), and $\kappa_\parallel = 40$ ns^{-1} (green diamonds). The normalized pump current is $p = 1.0$, the other parameters are chosen according to Table 6.1. Note the log-log scale. 168

Bibliography

[1] A. S. Pikovsky, M. G. Rosenblum, and J. Kurths, *Synchronization, A Universal Concept in Nonlinear Sciences.* Cambridge: Cambridge University Press, 2001.

[2] S. Boccaletti, J. Kurths, G. Osipov, D. L. Valladares, and C. S. Zhou, “The synchronization of chaotic systems,” *Phys. Rep.*, vol. 366, pp. 1–101, 2002.

[3] S. H. Strogatz, “From Kuramoto to Crawford: exploring the onset of synchronization in populations of coupled oscillators,” *Physica D*, vol. 143, pp. 1–20, 2000.

[4] S. H. Strogatz, *Sync: How order emerges from chaos in the universe, nature, and daily life.* Hyperion, 2004.

[5] L. Glass, “Synchronization and rhythmic processes in physiology,” *Nature*, vol. 410, no. 6825, pp. 277–284, 2001.

[6] C. Schäfer, M. G. Rosenblum, J. Kurths, and H.-H. Abel, “Heartbeat synchronized with ventilation,” *Nature*, vol. 392, pp. 239–240, 1998.

[7] C. Schäfer, M. G. Rosenblum, H.-H. Abel, and J. Kurths, “Synchronization in the human cardiorespiratory system,” *Physical Review E*, vol. 60, no. 1, p. 857, 1999.

[8] P. Roelfsema, A. Engel, P. Knig, and W. Singer, “Visuomotor integration is associated with zero time-lag synchronization among cortical areas,” *Nature*, vol. 385, pp. 157–161, 1997.

[9] M. Castelo-Branco, R. Goebel, S. Neuenschwander, and W. Singer, “Neural synchrony correlates with surface segregation rules,” *Nature*, vol. 405, no. 6787, pp. 685–689, 2000.

[10] K. Coffman, W. McCormick, and H. L. Swinney, “Multiplicity in a chemical reaction with one-dimensional dynamics,” *Physical review letters*, vol. 56, no. 10, p. 999, 1986.

[11] Z. Néda, E. Ravasz, Y. Brechet, T. Vicsek, and A.-L. Barabási, “Self-organizing processes: The sound of many hands clapping,” *Nature*, vol. 403, no. 6772, pp. 849–850, 2000.

[12] S. H. Strogatz, D. Abraham, A. D. McRobbie, B. Eckhardt, and E. Ott, “Crowd synchrony on the millennium bridge,” *Nature*, vol. 438, pp. 43–44, 2005.

[13] N. F. Rulkov, M. M. Sushchik, L. S. Tsimring, and H. D. I. Abarbanel, “Generalized synchronization of chaos in directionally coupled chaotic systems,” *Phys. Rev. E*, vol. 51, no. 2, pp. 980–994, 1995.

[14] L. Kocarev and U. Parlitz, “Generalized synchronization, predictability, and equivalence of unidirectionally coupled dynamical systems,” *Physical Review Letters*, vol. 76, no. 11, p. 1816, 1996.

[15] H. D. I. Abarbanel, N. F. Rulkov, and M. M. Sushchik, “Generalized synchronization of chaos: The auxiliary system approach,” *Phys. Rev. E*, vol. 53, no. 5, pp. 4528–4535, 1996.

[16] A. Uchida, R. McAllister, R. Meucci, and R. Roy, “Generalized synchronization of chaos in identical systems with hidden degrees of freedom,” *Phys. Rev. Lett.*, vol. 91, no. 17, p. 174101, 2003.

[17] M. C. Soriano, G. Van der Sande, I. Fischer, and C. R. Mirasso, “Synchronization in simple network motifs with negligible correlation and mutual information measures,” *Physical review letters*, vol. 108, no. 13, p. 134101, 2012.

[18] H. Kato, M. C. Soriano, E. Pereda, I. Fischer, and C. R. Mirasso, “Limits to detection of generalized synchronization in delay-coupled chaotic oscillators,” *Physical Review E*, vol. 88, no. 6, p. 062924, 2013.

[19] L. M. Pecora and T. L. Carroll, “Synchronization in chaotic systems,” *Phys. Rev. Lett.*, vol. 64, pp. 821–824, 1990.

[20] L. M. Pecora and T. L. Carroll, “Driving systems with chaotic signals,” *Phys. Rev. A*, vol. 44, pp. 2374–2383, 1991.

[21] L. M. Pecora, T. L. Carroll, G. A. Johnson, D. J. Mar, and J. F. Heagy, “Fundamentals of synchronization in chaotic systems, concepts, and applications,” *Chaos*, vol. 7, no. 4, pp. 520–543, 1997.

[22] M. Ding, E.-J. Ding, W. L. Ditto, B. Gluckman, V. In, J.-H. Peng, M. L. Spano, and W. Yang, "Control and synchronization of chaos in high dimensional systems: review of some recent results," *Chaos: An Interdisciplinary Journal of Nonlinear Science*, vol. 7, no. 4, pp. 644–652, 1997.

[23] T. Heil, I. Fischer, W. Elsäßer, J. Mulet, and C. R. Mirasso, "Chaos synchronization and spontaneous symmetry-breaking in symmetrically delay-coupled semiconductor lasers," *Phys. Rev. Lett.*, vol. 86, p. 795, 2001.

[24] K. M. Cuomo and A. V. Oppenheim, "Circuit implementation of synchronized chaos with applications to communications," *Phys. Rev. Lett.*, vol. 71, no. 1, pp. 65–68, 1993.

[25] A. Sanchez-Diaz, C. R. Mirasso, P. Colet, and P. Gracia-Fernandez, "Encoded Gbit/s digital communications with synchronized chaotic semiconductor lasers," *IEEE J. Quantum Electron.*, vol. 35, pp. 292–297, 1999.

[26] I. Fischer, Y. Liu, and P. Davis, "Synchronization of chaotic semiconductor laser dynamics on subnanosecond time scales and its potential for chaos communication," *Phys. Rev. A*, vol. 62, no. 1, p. 011801, 2000.

[27] C. R. Mirasso, P. Colet, and P. GarciaFernandez, "Synchronization of chaotic semiconductor lasers: Application to encoded communications," *IEEE Photon. Technol. Lett.*, vol. 8, pp. 299–301, 1996.

[28] Q. Y. Wang, Q. S. Lu, G. R. Chen, and D. H. Guo, "Chaos synchronization of coupled neurons with gap junctions," *Physics Letters A*, vol. 356, no. 1, pp. 17–25, 2006.

[29] V. Z. Tronciu, C. Mirasso, P. Colet, M. Hamacher, M. Benedetti, V. Vercesi, and V. Annovazzi-Lodi, "Chaos generation and synchronization using an integrated source with an air gap," *IEEE J. Quantum Electron.*, 2010.

[30] M. C. Soriano, J. García-Ojalvo, C. R. Mirasso, and I. Fischer, "Complex photonics: Dynamics and applications of delay-coupled semiconductors lasers," *Rev. Mod. Phys.*, vol. 85, pp. 421–470, 2013.

[31] G. Orosz, R. E. Wilson, R. Szalai, and G. Stépán, "Exciting traffic jams: Nonlinear phenomena behind traffic jam formation on highways," *Physical Review E*, vol. 80, no. 4, p. 046205, 2009.

[32] K. Pyragas, "Continuous control of chaos by self-controlling feedback," *Phys. Lett. A*, vol. 170, p. 421, 1992.

[33] E. Schöll, "Delayed feedback control of chaotic spatio-temporal patterns in semiconductor nanostructures," in *Handbook of Chaos Control* (E. Schöll and H. G. Schuster, eds.), ch. 24, pp. 533–558, Weinheim: Wiley-VCH, 2008. Second completely revised and enlarged edition.

[34] R. N. Hall, G. E. Fenner, J. D. Kingsley, T. J. Soltys, and R. O. Carlson, "Coherent light emission from Ga-As junctions," *Phys. Rev. Lett*, vol. 9, p. 366, 1962.

[35] M. I. Nathan, W. P. Dumke, G. Burns, F. H. Dill, and G. Lasher, "Stimulated emission of radiation from gaas p-n junctions," *Applied Physics Letters*, vol. 1, no. 3, pp. 62–64, 1962.

[36] T. M. Quist, R. H. Rediker, R. J. Keyes, W. E. Krag, B. Lax, A. L. McWhorter, and H. J. Zeigler, "Semiconductor maser of GaAs," *Applied Physics Letters*, vol. 1, no. 4, pp. 91–92, 1962.

[37] C. Risch and C. Voumard, "Selfpulsation in the output intensity and spectrum of GaAsAlGaAs cw diode lasers coupled to a frequencyselective external optical cavity," *Journal of Applied Physics*, vol. 48, no. 5, pp. 2083–2085, 1977.

[38] D. Lenstra, B. Verbeek, and A. Den Boef, "Coherence collapse in single-mode semiconductor lasers due to optical feedback," *IEEE J. Quantum Electron.*, vol. 21, no. 6, pp. 674–679, 1985.

[39] C. H. Henry and R. F. Kazarinov, "Instability of semiconductor lasers due to optical feedback from distant reflectors," *IEEE J. Quantum Electron.*, vol. 22, pp. 294–301, 1986.

[40] A. Chomette, B. Deveaud, A. Regreny, and G. Bastard, "Observation of carrier localization in intentionally disordered GaAs/GaAlAs superlattices," *Phys. Rev. Lett.*, vol. 57, p. 1464, 1986.

[41] G. C. Dente, P. S. Durkin, K. A. Wilson, and C. E. Moeller, "Chaos in the coherence collapse of semiconductor lasers," *IEEE J. Quantum Electron.*, vol. 24, no. 12, pp. 2441–2447, 1988.

[42] J. Mørk, B. Tromborg, and P. L. Christiansen, "Bistability and low-frequency fluctuations in semiconductor lasers with optical feedback: a theoretical analysis," *IEEE J. Quantum Electron.*, vol. 24, no. 2, pp. 123–133, 1988.

[43] J. Mørk, J. Mark, and B. Tromborg, "Route to chaos and competition between relaxation oscillations for a semiconductor laser with optical feedback," *Phys. Rev. Lett.*, vol. 65, no. 16, pp. 1999–2002, 1990.

[44] J. Mørk, B. Tromborg, and J. Mark, "Chaos in semiconductor lasers with optical feedback-Theory and experiment," *IEEE J. Quantum Electron.*, vol. 28, p. 93, 1992.

[45] E. Ott, *Chaos in dynamical systems.* Cambridge: Cambridge University Press, 1993.

[46] J. Ye, H. Li, and J. G. McInerney, "Period-doubling route to chaos in a semiconductor laser with weak optical feedback," *Physical Review A*, vol. 47, no. 3, pp. 2249–2252, 1993.

[47] E. Ott, T. Sauer, and J. A. Yorke, "Coping with chaos. analysis of chaotic data and the exploitation of chaotic systems," *Wiley Series in Nonlinear Science, New York: John Wiley,| c1994, edited by Ott, Edward; Sauer, Tim; Yorke, James A.*, vol. 1, 1994.

[48] G. H. M. van Tartwijk, A. M. Levine, and D. Lenstra, "Sisyphus effect in semiconductor lasers with optical feedback," *IEEE J. Sel. Top. Quantum Electron.*, vol. 1, no. 2, pp. 466–472, 1995.

[49] G. H. M. van Tartwijk and D. Lenstra, "Semiconductor laser with optical injection and feedback," *Quantum Semiclass. Opt.*, vol. 7, p. 84, 1995.

[50] I. Fischer, G. H. M. van Tartwijk, A. M. Levine, W. Elsäßer, E. O. Göbel, and D. Lenstra, "Fast pulsing and chaotic itinerancy with a drift in the coherence collapse of semiconductor lasers," *Phys. Rev. Lett.*, vol. 76, p. 220, 1996.

[51] B. Krauskopf and D. Lenstra, eds., *Fundamental Issues of Nonlinear Laser Dynamics*, AIP Conference Proceedings 548, (Melville (New York)), American Institute of Physics, 2000.

[52] R. Vicente, J. Dauden, P. Colet, and R. Toral, "Analysis and Characterization of the Hyperchaos Generated by a Semiconductor Laser Subject to a Delayed Feedback Loop," *IEEE J. Quantum Electron.*, vol. 41, no. 4, pp. 541–548, 2005.

[53] J. Sacher, W. Elsäßer, and E. O. Göbel, "Intermittency in the coherence collapse of a semiconductor laser with external feedback," *Phys. Rev. Lett.*, vol. 63, no. 20, pp. 2224–2227, 1989.

[54] T. Erneux, F. Rogister, A. Gavrielides, and V. Kovanis, "Bifurcation to mixed external cavity mode solutions for semiconductor lasers subject to optical feedback," *Opt. Commun.*, vol. 183, no. 5-6, pp. 467–477, 2000.

[55] T. Sano, "Antimode dynamics and chaotic itinerancy in the coherence collapse of semiconductor lasers with optical feedback," *Phys. Rev. A*, vol. 50, no. 3, pp. 2719–2726, 1994.

[56] A. Hohl, H. J. C. van der Linden, and R. Roy, "Determinism and stochasticity of power-dropout events in semiconductor lasers with optical feedback," *Opt. Lett.*, vol. 20, no. 23, pp. 2396–2398, 1995.

[57] T. Heil, I. Fischer, and W. Elsäßer, "Coexistence of low-frequency fluctuations and stable emission on a single high-gain mode in semiconductor lasers with external optical feedback," *Phys. Rev. A*, vol. 58, p. 2672, 1998.

[58] T. Heil, I. Fischer, W. Elsäßer, J. Mulet, and C. R. Mirasso, "Statistical properties of low-frequency fluctuations during single-mode operation in distributed-feedback lasers: experiments and modeling," *Opt. Lett.*, vol. 24, no. 18, pp. 1275–1277, 1999.

[59] T. Heil, I. Fischer, and W. Elsäßer, "Stabilization of feedback-induced instabilities in semiconductor lasers," *J. Opt. B: Quantum Semiclass. Opt.*, vol. 2, pp. 413–420, 2000.

[60] Y. Hong and K. A. Shore, "Statistical measures of the power dropout ratio in semiconductor lasers subject to optical feedback," *Opt. Lett.*, vol. 30, no. 24, pp. 3332–3334, 2005.

[61] J. Tiana-Alsina, J. M. Buldú, M. C. Torrent, and J. García-Ojalvo, "Quantifying stochasticity in the dynamics of delay-coupled semiconductor lasers via forbidden patterns," *Phil. Trans. R. Soc. A*, vol. 368, no. 1911, pp. 367–377, 2010.

[62] A. Aragoneses, N. Rubido, J. Tiana-Alsina, M. C. Torrent, and C. Masoller, "Distinguishing signatures of determinism and stochasticity in spiking complex systems," *Sci. Rep.*, vol. 3, no. 1778, 2013.

[63] J. K. White, M. Matus, and J. V. Moloney, "Achronal generalized synchronization in mutually coupled semiconductor lasers," *Phys. Rev. E*, vol. 65, no. 3, p. 036229, 2002.

[64] A. Locquet, C. Masoller, and C. R. Mirasso, "Synchronization regimes of optical-feedback-induced chaos in unidirectionally coupled semiconductor lasers," *Phys. Rev. E*, vol. 65, p. 56205, 2002.

[65] J. Mulet, C. R. Mirasso, T. Heil, and I. Fischer, "Synchronization scenario of two distant mutually coupled semiconductor lasers," *J. Opt. B*, vol. 6, no. 1, pp. 97–105, 2004.

[66] E. A. Rogers-Dakin, J. García-Ojalvo, D. J. DeShazer, and R. Roy, "Synchronization and symmetry breaking in mutually coupled fiber lasers," *Phys. Rev. E*, vol. 73, p. 045201, 2006.

[67] L. B. Shaw, I. B. Schwartz, E. A. Rogers, and R. Roy, "Synchronization and time shifts of dynamical patterns for mutually delay-coupled fiber ring lasers," *Chaos*, vol. 16, no. 1, pp. 015111–015111–9, 2006.

[68] O. D'Huys, R. Vicente, J. Danckaert, and I. Fischer, "Amplitude and phase effects on the synchronization of delay-coupled oscillators," *Chaos*, vol. 20, p. 043127, 2010.

[69] V. Flunkert, S. Yanchuk, T. Dahms, and E. Schöll, "Synchronizing distant nodes: A universal classification of networks," *Phys. Rev. Lett.*, vol. 105, p. 254101, 2010.

[70] Just, W. and Pelster, A. and Schanz, M. and Schöll, E. (eds.), "Delayed complex systems: an overview," *Phil. Trans. R. Soc. A*, vol. 368, no. 1911, pp. 303–304, 2010. Theme Issue on Delayed Complex Systems.

[71] I. Fischer, R. Vicente, J. M. Buldú, M. Peil, C. R. Mirasso, M. C. Torrent, and J. García-Ojalvo, "Zero-lag long-range synchronization via dynamical relaying," *Phys. Rev. Lett.*, vol. 97, no. 12, p. 123902, 2006.

[72] R. Vicente, I. Fischer, and C. R. Mirasso, "Synchronization properties of three delay-coupled semiconductor lasers," *Physical Review E*, vol. 78, no. 6, p. 066202, 2008.

[73] S. Tang, R. Vicente, M. C. Chiang, C. R. Mirasso, and J. M. Liu, "Nonlinear dynamics of semiconductor lasers with mutual optoelectronic coupling," *IEEE J. Sel. Top. Quantum Electron.*, vol. 10, no. 5, pp. 936–943, 2004.

[74] E. A. Viktorov, P. Mandel, I. O'Driscoll, O. Carroll, G. Huyet, J. Houlihan, and Y. Tanguy, "Low-frequency fluctutations in two-state quantum dot lasers," *Opt. Lett.*, vol. 31, no. 15, 2006.

[75] A. S. Landsman, L. B. Shaw, and I. B. Schwartz, "Zero Lag Synchronization of mutually coupled lasers in the presence of delays," in *Recent Advances in Laser Dynamics: Control and Synchronization* (A. N. Pisarchik, ed.), p. 359, Research Signpost, 2007.

[76] R. Vicente, G. Pipa, I. Fischer, and C. R. Mirasso, "Zero-lag long range synchronization of neurons is enhanced by dynamical relaying," in *Artificial Neural Networks ICANN 2007*, vol. 4668 of *Lecture Notes in Computer Science*, pp. 904–913, Berlin / Heidelberg: Springer, 2007.

[77] R. Vicente, L. L. Gollo, C. R. Mirasso, I. Fischer, and G. Pipa, "Dynamical relaying can yield zero time lag neuronal synchrony despite long conduction delays," *Proc. Natl. Acad. Sci.*, vol. 105, no. 44, p. 17157, 2008.

[78] M. Peil, L. Larger, and I. Fischer, "Versatile and robust chaos synchronization phenomena imposed by delayed shared feedback coupling," *Phys. Rev. E*, vol. 76, no. 4, p. 045201 (R), 2007.

[79] A. Wagemakers, J. M. Buldú, and M. A. F. Sanjuán, "Isochronous synchronization in mutually coupled chaotic circuits," *Chaos: An Interdisciplinary Journal of Nonlinear Science*, vol. 17, no. 2, p. 023128, 2007.

[80] E. Klein, N. Gross, M. Rosenbluh, W. Kinzel, L. Khaykovich, and I. Kanter, “Stable isochronal synchronization of mutually coupled chaotic lasers,” *Phys. Rev. E*, vol. 73, no. 6, p. 066214, 2006.

[81] P. Colet and R. Roy, “Digital communication with synchronized chaotic lasers,” *Opt. Lett.*, vol. 19, pp. 2056–2058, Dec 1994.

[82] J. P. Goedgebuer, L. Larger, and H. Porte, “Optical cryptosystem based on synchronization of hyperchaos generated by a delayed feedback tunable laser diode,” *Phys. Rev. Lett.*, vol. 80, no. 10, pp. 2249–2252, 1998.

[83] G. D. VanWiggeren and R. Roy, “Optical communication with chaotic waveforms,” *Phys. Rev. Lett.*, vol. 81, no. 16, pp. 3547–3550, 1998.

[84] G. D. VanWiggeren and R. Roy, “Communication with chaotic lasers,” *Science*, vol. 279, pp. 1198–1200, 1998.

[85] G. D. VanWiggeren and R. Roy, “Chaotic communication using time-delayed optical systems,” *Int. J. Bifurcation Chaos*, vol. 9, pp. 2129–2156, 1999.

[86] A. Argyris, D. Syvridis, L. Larger, V. Annovazzi-Lodi, P. Colet, I. Fischer, J. García-Ojalvo, C. R. Mirasso, L. Pesquera, and K. A. Shore, “Chaos-based communications at high bit rates using commercial fibre-optic links,” *Nature*, vol. 438, pp. 343–346, 2005.

[87] V. Z. Tronciu, C. R. Mirasso, and P. Colet, “Chaos-based communications using semiconductor lasers subject to feedback from an integrated double cavity,” *J. Phys. B: At. Mol. Opt. Phys.*, vol. 41, p. 155401, 2008.

[88] I. Kanter, E. Kopelowitz, J. Kestler, and W. Kinzel, “Chaos synchronization with dynamic filters: Two-way is better than one-way,” *Europhys. Lett.*, vol. 83, no. 5, p. 50005, 2008.

[89] W. Kinzel and I. Kanter, “Secure communication with chaos synchronization,” in *Handbook of Chaos Control* (E. Schöll and H. G. Schuster, eds.), Weinheim: Wiley-VCH, 2008. Second completely revised and enlarged edition.

[90] M. C. Soriano, P. Colet, and C. R. Mirasso, “Security implications of open- and closed-loop receivers in all-optical chaos-based communications,” *IEEE Photon. Technol. Lett.*, vol. 21, pp. 426–428, 2009.

[91] A. Uchida, *Optical communication with chaotic lasers: applications of nonlinear dynamics and synchronization*. Weinheim, Germany: John Wiley & Sons, 2012.

[92] P. Ashwin, J. Buescu, and I. Stewart, "Bubbling of attractors and synchronisation of chaotic oscillators," *Phys. Lett. A*, vol. 193, no. 2, pp. 126–139, 1994.

[93] E. Ott and J. C. Sommerer, "Blowout bufurcations: the occurrence of riddled basins and on-off intermittency," *Phys. Lett. A*, vol. 188, no. 1, pp. 39–47, 1994.

[94] D. J. Gauthier and J. C. Bienfang, "Intermittent loss of synchronization in coupled chaotic oscillators: Toward a new criterion for high-quality synchronization," *Phys. Rev. Lett.*, vol. 77, no. 9, pp. 1751–1754, 1996.

[95] M. Sauer and F. Kaiser, "On-off intermittency and bubbling in the synchronization break-down of coupled lasers," *Phys. Lett. A*, vol. 243, no. 1-2, pp. 38–46, 1998.

[96] J. R. Terry, K. S. Thornburg, D. J. DeShazer, G. D. VanWiggeren, S. Zhu, P. Ashwin, and R. Roy, "Synchronization of chaos in an array of three lasers," *Phys. Rev. E*, vol. 59, no. 4, pp. 4036–4043, 1999.

[97] V. Flunkert, O. D'Huys, J. Danckaert, I. Fischer, and E. Schöll, "Bubbling in delay-coupled lasers," *Phys. Rev. E*, vol. 79, p. 065201 (R), 2009.

[98] V. Flunkert, *Delayed complex systems and applications to lasers.* PhD thesis, TU Berlin, 2010.

[99] M. Lukoševičius and H. Jaeger, "Reservoir computing approaches to recurrent neural network training," *Computer Science Review*, vol. 3, no. 3, pp. 127–149, 2009.

[100] M. D. Skowronski and J. G. Harris, "Automatic speech recognition using a predictive echo state network classifier," *Neural networks*, vol. 20, no. 3, pp. 414–423, 2007.

[101] H. Jaeger and H. Haas, "Harnessing Nonlinearity: Predicting Chaotic Systems and Saving Energy in Wireless Communication," *Science*, vol. 304, no. 5667, pp. 78–80, 2004.

[102] D. Brunner, M. C. Soriano, and I. Fischer, "High-speed optical vector and matrix operations using a semiconductor laser," *IEEE Photonics Technology Letters*, vol. 25, pp. 1680–1683, 2013.

[103] W. Maass, T. Natschläger, and H. Markram, "Real-time computing without stable states: A new framework for neural computation based on perturbations," *Neural computation*, vol. 14, no. 11, pp. 2531–2560, 2002.

[104] L. Appeltant, M. C. Soriano, G. Van der Sande, J. Danckaert, S. Massar, J. Dambre, B. Schrauwen, C. R. Mirasso, and I. Fischer, "Information processing using a single dynamical node as complex system," *Nature Comm.*, vol. 2, no. 468, 2011.

[105] L. Larger, M. Soriano, D. Brunner, L. Appeltant, J. M. Gutiérrez, L. Pesquera, C. R. Mirasso, and I. Fischer, "Photonic information processing beyond turing: an optoelectronic implementation of reservoir computing," *Optics express*, vol. 20, no. 3, pp. 3241–3249, 2012.

[106] Y. Paquot, F. Duport, A. Smerieri, J. Dambre, B. Schrauwen, M. Haelterman, and S. Massar, "Optoelectronic reservoir computing," *Scientific reports*, vol. 2, 2012.

[107] K. Vandoorne, J. Dambre, D. Verstraeten, B. Schrauwen, and P. Bienstman, "Parallel reservoir computing using optical amplifiers," *Neural Networks, IEEE Transactions on*, vol. 22, no. 9, pp. 1469–1481, 2011.

[108] F. Duport, B. Schneider, A. Smerieri, M. Haelterman, and S. Massar, "All-optical reservoir computing," *Optics express*, vol. 20, no. 20, pp. 22783–22795, 2012.

[109] D. Brunner, M. C. Soriano, C. R. Mirasso, and I. Fischer, "Parallel photonic information processing at gigabyte per second data rates using transient states," *Nature Comm.*, vol. 4, no. 1364, 2013.

[110] M. Peil, *Dynamics and Synchronization Phenomena of Semiconductor Lasers with Delayed Optical Feedback: Utilizing Nonlinear Dynamics for Novel Applications*. PhD thesis, Technische Universität Darmstadt, 2006.

[111] Y. Cho and M. Umeda, "Chaos in laser oscillations with delayed feedback; numerical analysis and observation using semiconductor laser," *J. Opt.Soc.Am. B*, vol. 1, pp. 497–498, 1984.

[112] G. Lasher and F. Stern, "Spontaneous and stimulated recombination radiation in semiconductors," *Phys. Rev.*, vol. 133, no. 2A, p. A553, 1964.

[113] C. H. Henry, R. A. Logan, and K. A. Bertness, "Spectral dependence of the change in refractive index due to carrier injection in gaas lasers," *Journal of Applied Physics*, vol. 52, no. 7, pp. 4457–4461, 1981.

[114] H. A. Kramers, "La Diffusion de la lumière par les atomes," *Atti. Congr. Int. Fis. Como*, vol. 2, pp. 545–557, 1927.

[115] R. d. Kronig, "On the theory of dispersion of X-rays," *JOSA*, vol. 12, no. 6, pp. 547–556, 1926.

[116] H. Haug and H. Haken, “Theory of noise in semiconductor laser emission,” *Zeitschrift für Physik*, vol. 204, no. 3, pp. 262–275, 1967.

[117] C. H. Henry, “Theory of the linewidth of semiconductor lasers,” *IEEE J. Quantum Electron.*, vol. 18, no. 2, pp. 259–264, 1982.

[118] A. Yariv, *Quantum Electronics, 3rd ed.* New York: Wiley, 1975.

[119] M. Osinski and J. Buus, “Linewidth broadening factor in semiconductor lasers – an overview,” *IEEE J. Quantum Electron.*, vol. 23, no. 1, pp. 9–29, 1987.

[120] B. W. Hakki and T. L. Paoli, “Gain spectra in GaAs doubleheterostructure injection lasers,” *Journal of Applied Physics*, vol. 46, no. 3, pp. 1299–1306, 1975.

[121] I. D. Henning and J. V. Collins, “Measurements of the semiconductor laser linewidth broadening factor,” *Electronics Letters*, vol. 19, no. 22, pp. 927–929, 1983.

[122] M. P. Van Exter, W. A. Hamel, J. P. Woerdman, and B. R. P. Zeijlmans, “Spectral signature of relaxation oscillations in semiconductor lasers,” *IEEE Journal of Quantum Electronics*, vol. 28, no. 6, pp. 1470–1478, 1992.

[123] Y. Yu, G. Giuliani, and S. Donati, “Measurement of the linewidth enhancement factor of semiconductor lasers based on the optical feedback self-mixing effect,” *Photonics Technology Letters*, vol. 16, no. 4, pp. 990–992, 2004.

[124] T. Keating, X. Jin, S. L. Chuang, and K. Hess, “Temperature dependence of electrical and optical modulation responses of quantum-well lasers,” *IEEE J. Quantum Electron.*, vol. 35, no. 10, pp. 1526–1534, 1999.

[125] K. Vahala, S. N. Chiu, S. Margalit, and A. Yariv, “On the linewidth enhancement factor alpha in semiconductor injection lasers,” *Appl. Phys. Lett.*, vol. 42, no. 8, pp. 631–633, 1983.

[126] A. L. Schawlow and C. H. Townes, “Infrared and optical masers,” *Physical Review*, vol. 112, no. 6, p. 1940, 1958.

[127] G. A. Acket, D. Lenstra, A. Den Boef, and B. Verbeek, “The influence of feedback intensity on longitudinal mode properties and optical noise in index-guided semiconductor lasers,” *IEEE Journal of Quantum Electronics*, vol. 20, no. 10, pp. 1163–1169, 1984.

[128] J. S. Cohen, R. R. Drenten, and B. H. Verbeeck, “The effect of optical feedback on the relaxation oscillation in semiconductor lasers,” *IEEE Journal of Quantum Electronics*, vol. 24, no. 10, pp. 1989–1995, 1988.

[129] J. Sigg, "Effects of optical feedback on the light-current characteristics of semiconductor lasers," *Journal of Quantum Electronics*, vol. 29, no. 5, pp. 1262–1270, 1993.

[130] I. Fischer, T. Heil, and W. Elsäßer, "Emission dynamics of semiconductor lasers subject to delayed optical feedback: An experimentalist's perspective," in *Fundamental Issues of Nonlinear Laser Dynamics* (B. Krauskopf and D. Lenstra, eds.), AIP Conference Proceedings 548, (Melville, New York), p. 218, American Institute of Physics, 2000.

[131] J. Osmundsen and N. Gade, "Influence of optical feedback on laser frequency spectrum and threshold conditions," *Journal of Quantum Electronics*, vol. 19, no. 3, pp. 465–469, 1983.

[132] V. Annovazzi-Lodi, S. Merlo, and S. Moroni, "Power efficiency of a semiconductor laser with an external cavity," *Optical and Quantum Electronics*, vol. 32, no. 12, pp. 1343–1350, 2000.

[133] R. Lang and K. Kobayashi, "External optical feedback effects on semiconductor injection laser properties," *IEEE J. Quantum Electron.*, vol. 16, p. 347, 1980.

[134] M. Yousefi, D. Lenstra, and G. Vemuri, "Carrier inversion noise has important influence on the dynamics of a semiconductor laser," *IEEE J. Sel. Top. Quantum Electron.*, vol. 10, pp. 955–960, 2004.

[135] M. C. Soriano, T. Berkvens, G. Van der Sande, G. Verschaffelt, J. Danckaert, and I. Fischer, "Interplay of current noise and delayed optical feedback on the dynamics of semiconductor lasers," *IEEE Journal of Quantum Electronics*, vol. 47, no. 3, pp. 368–374, 2011.

[136] V. Rottschäfer and B. Krauskopf, "The ECM-backbone of the Lang-Kobayashi equations: A geometric picture," *Int. J. Bif. Chaos*, vol. 17, no. 5, pp. 1575–1588, 2007.

[137] A. M. Levine, G. H. M. van Tartwijk, D. Lenstra, and T. Erneux, "Diode lasers with optical feedback: Stability of the maximum gain mode," *Phys. Rev. A*, vol. 52, no. 5, pp. R3436–R3439, 1995.

[138] T. Heil, *Delay Dynamics in Semiconductor Lasers: Feedback and Coupling Induced Instabilities, Stabilization, and Synchronization.* PhD thesis, Technische Universität Darmstadt, 2001.

[139] T. Heil, A. Uchida, P. Davis, and T. Aida, "TE-TM dynamics in a semiconductor laser subject to polarization-rotated optical feedback," *Phys. Rev. A*, vol. 68, p. 033811, 2003.

[140] D. Lenstra, "Fundamental nonlinear dynamics of semiconductor lasers," *Quantum Semiclass. Opt.*, vol. 9, no. 5, pp. U3–U5, 1997.

[141] D. W. Sukow, A. Gavrielides, T. Erneux, M. J. Baracco, Z. A. Parmenter, and K. L. Blackburn, "Polarization dynamics in semiconductor lasers with incoherent optical feedback," in *Integrated Optoelectronic Devices 2005*, pp. 256–266, International Society for Optics and Photonics, 2005.

[142] D. W. Sukow, A. Gavrielides, T. Erneux, M. J. Baracco, Z. A. Parmenter, and K. L. Blackburn, "Two-field description of chaos synchronization in diode lasers with incoherent optical feedback and injection," *Phys. Rev. A*, vol. 72, p. 043818, 2005.

[143] N. Oliver, M. C. Soriano, D. W. Sukow, and I. Fischer, "Dynamics of a semiconductor laser with polarization-rotated feedback and its utilization for random bit generation," *Optics Letters*, vol. 36, no. 23, pp. 4632–4634, 2011.

[144] H. D. Mittelmann and H. Weber, *Bifurcation Problems & Their Numerical Solution.* Birkhauser, 1980.

[145] A. Gavrielides, T. Erneux, D. W. Sukow, G. Burner, T. McLachlan, J. Miller, and J. Amonette, "Square-wave self-modulation in diode lasers with polarization-rotated optical feedback," *Opt. Lett.*, vol. 31, pp. 2006–2008, 2006.

[146] A. Gavrielides, T. Erneux, D. W. Sukow, G. Burner, T. McLachlan, J. Miller, and J. Amonette, "Square-wave oscillations in edge-emitting diode lasers with polarization-rotated optical feedback," *Proc. SPIE*, vol. 6184, pp. 255–261, 2006.

[147] A. Gavrielides, D. W. Sukow, G. Burner, T. McLachlan, J. Miller, and J. Amonette, "Simple and complex square waves in an edge-emitting diode laser with polarization-rotated optical feedback," *Physical Review E*, vol. 81, no. 5, p. 056209, 2010.

[148] D. W. Sukow, A. Gavrielides, T. Erneux, B. Mooneyham, K. Lee, J. McKay, and J. Davis, "Asymmetric square waves in mutually coupled semiconductor lasers with orthogonal optical injection," *Physical Review E*, vol. 81, no. 2, p. 025206, 2010.

[149] D. W. Sukow, T. Gilfillan, B. Pope, M. S. Torre, A. Gavrielides, and C. Masoller, "Square-wave switching in vertical-cavity surface-emitting lasers with polarization-rotated optical feedback: Experiments and simulations," *Physical Review A*, vol. 86, no. 3, p. 033818, 2012.

[150] N. Shibasaki, A. Uchida, S. Yoshimori, and P. Davis, "Characteristics of chaos synchronization in semiconductor lasers subject to polarization-rotated optical feedback," *IEEE Journal of Quantum Electronics*, vol. 42, no. 3, pp. 342–350, 2006.

[151] Y. Takeuchi, R. Shogenji, and J. Ohtsubo, “Chaotic dynamics in semiconductor lasers subjected to polarization-rotated optical feedback,” *Applied Physics Letters*, vol. 93, no. 18, p. 181105, 2008.

[152] N. Oliver, M. C. Soriano, D. W. Sukow, and I. Fischer, “Fast random bit generation using a chaotic laser: approaching the information theoretic limit,” *IEEE J. Quant. Electron.*, vol. 49, no. 11, pp. 910–918, 2013.

[153] J. Mulet, M. Giudici, J. Javaloyes, and S. Balle, “Square-wave switching by crossed-polarization gain modulation in vertical-cavity semiconductor lasers,” *Physical Review A*, vol. 76, no. 4, p. 043801, 2007.

[154] C. Masoller, T. Sorrentino, M. Chevrollier, and M. Oria, “Bistability in semiconductor lasers with polarization-rotated frequency-dependent optical feedback,” *IEEE J. Quantum Electron.*, vol. 43, no. 3, p. 261, 2007.

[155] T. Sorrentino, O. Di Lorenzo, L. C. de Oliveira, M. Chevrollier, and M. Oria, “All-optical frequency-controlled frequency switch,” *J. Opt. Soc. Am. B*, vol. 27, no. 7, p. 1458, 2010.

[156] K. Otsuka and J. L. Chern, “High-speed picosecond pulse generation in semiconductor lasers with incoherent optical feedback,” *Opt. Lett.*, vol. 16, no. 22, pp. 1759–1761, 1991.

[157] J. Houlihan, G. Huyet, and J. McInerney, “Dynamics of a semiconductor laser with incoherent optical feedback,” *Opt. Commun.*, vol. 199, no. 1-4, pp. 175–179, 2001.

[158] D. W. Sukow, K. L. Blackburn, A. R. Spain, K. J. Babcock, J. V. Bennett, and A. Gavrielides, “Experimental synchronization of chaos in diode lasers with polarization-rotated feedback and injection,” *Optics Letters*, vol. 29, no. 20, pp. 2393–2395, 2004.

[159] C. Masoller, D. Sukow, A. Gavrielides, and M. Sciamanna, “Bifurcation to square-wave switching in orthogonally delay-coupled semiconductor lasers: Theory and experiment,” *Physical Review A*, vol. 84, no. 2, p. 023838, 2011.

[160] G. Friart, L. Weicker, J. Danckaert, and T. Erneux, “Relaxation and square-wave oscillations in a semiconductor laser with polarization rotated optical feedback,” *Optics Express*, vol. 22, no. 6, pp. 6905–6918, 2014.

[161] V. Ahlers, U. Parlitz, and W. Lauterborn, “Hyperchaotic dynamics and synchronization of external-cavity semiconductor lasers,” *Phys. Rev. E*, vol. 58, no. 6, pp. 7208–7213, 1998.

[162] R. L. Davidchack, Y.-C. Lai, A. Gavrielides, and V. Kovanis, "Dynamical origin of low frequency fluctuations in external cavity semiconductor lasers," *Phys. Lett. A*, vol. 267, no. 5-6, pp. 350–356, 2000.

[163] D. Yu, I. Wallace, R. G. Harrison, and A. Gavrielides, "Low frequency fluctuations and locked states in a multi-mode semiconductor laser with external cavity," *Optics Communications*, vol. 195, no. 1, pp. 249–258, 2001.

[164] F. Rogister, D. Pieroux, M. Sciamanna, P. Mégret, and M. Blondel, "Anticipating synchronization of two chaotic laser diodes by incoherent optical coupling and its application to secure communications," *Optics communications*, vol. 207, no. 1, pp. 295–306, 2002.

[165] A. Aragoneses Aguado, T. Sorrentino Amaral, S. Perrone, D. Gauthier, M. d. C. Torrent Serra, and C. Masoller Alonso, "Experimental and numerical study of the symbolic dynamics of a modulated external-cavity semiconductor laser," *Optics Express*, vol. 22, no. 4, pp. 4705–4713, 2014.

[166] J. Zamora-Munt, C. Masoller, and J. García-Ojalvo, "Transient low-frequency fluctuations in semiconductor lasers with optical feedback," *Physical Review A*, vol. 81, no. 3, p. 033820, 2010.

[167] J. Mulet and C. R. Mirasso, "Numerical statistics of power dropouts based on the lang-kobayashi model," *Phys. Rev. E*, vol. 59, no. 5, pp. 5400–5405, 1999.

[168] E. Schöll and H. G. Schuster, eds., *Handbook of Chaos Control.* Weinheim: Wiley-VCH, 2008. Second completely revised and enlarged edition.

[169] W. Singer, "Neuronal synchrony: A versatile code review for the definition of relations?," *Neuron*, vol. 24, pp. 49–65, 1999.

[170] W. Singer, "Neurobiology: Striving for coherence," *Nature*, vol. 397, pp. 391–393, 1999.

[171] I. Fischer, O. Hess, W. Elsäßer, and E. O. Göbel, "High-dimensional chaotic dynamics of an external-cavity semiconductor-laser," *Phys. Rev. Lett.*, vol. 73, no. 16, pp. 2188–2191, 1994.

[172] C.-U. Choe, T. Dahms, P. Hövel, and E. Schöll, "Controlling synchrony by delay coupling in networks: from in-phase to splay and cluster states," *Phys. Rev. E*, vol. 81, no. 2, p. 025205(R), 2010.

[173] W. Kinzel, A. Englert, G. Reents, M. Zigzag, and I. Kanter, "Synchronization of networks of chaotic units with time-delayed couplings," *Phys. Rev. E*, vol. 79, no. 5, p. 056207, 2009.

[174] A. Englert, W. Kinzel, Y. Aviad, M. Butkovski, I. Reidler, M. Zigzag, I. Kanter, and M. Rosenbluh, "Zero lag synchronization of chaotic systems with time delayed couplings," *Phys. Rev. Lett.*, vol. 104, no. 11, p. 114102, 2010.

[175] M. C. Soriano, S. Ortín, D. Brunner, L. Larger, C. R. Mirasso, I. Fischer, and L. Pesquera, "Optoelectronic reservoir computing: tackling noise-induced performance degradation," *Optics express*, vol. 21, no. 1, pp. 12–20, 2013.

[176] R. Vicente, C. R. Mirasso, and I. Fischer, "Simultaneous bidirectional message transmission in a chaos-bases communication scheme," *Opt. Lett.*, vol. 32, no. 4, pp. 403–405, 2007.

[177] I. B. Schwartz and L. B. Shaw, "Isochronal synchronization of delay-coupled systems," *Phys. Rev. E*, vol. 75, no. 4, p. 046207, 2007.

[178] R. Vicente, L. L. Gollo, C. R. Mirasso, I. Fischer, and G. Pipa, "Far in space and yet in synchrony: neuronal mechanisms for zero-lag long-range synchronization," in *Coherent Behavior in Neuronal Networks* (K. Josic, J. Rubin, M. A. Matias, R. Romo, ed.), vol. 3 of *Computational Neuroscience*, pp. 143–167, Berlin / Heidelberg: Springer, 2009.

[179] J. Ohtsubo, "Feedback induced instability and chaos in semiconductor lasers and their applications," *Opt. Rev.*, vol. 6, pp. 1–15, 1999.

[180] A. Murakami and J. Ohtsubo, "Synchronization of feedback-induced chaos in semiconductor lasers by optical injection," *Phys. Rev. A*, vol. 65, p. 033826, 2002.

[181] Y. Nagai and Y. C. Lai, "Periodic-orbit theory of the blowout bifurcation," *Phys. Rev. E*, vol. 56, pp. 4031–4041, 1997.

[182] H. Erzgräber, B. Krauskopf, and D. Lenstra, "Compound laser modes of mutually delay-coupled lasers," *SIAM J. Appl. Dyn. Syst.*, vol. 5, no. 1, pp. 30–65, 2006.

[183] J. M. Buldú, T. Heil, I. Fischer, M. C. Torrent, and J. García-Ojalvo, "Episodic synchronization via dynamic injection," *Phys. Rev. Lett.*, vol. 96, p. 024102, 2006.

[184] H. Erzgräber, D. Lenstra, B. Krauskopf, E. Wille, M. Peil, I. Fischer, and W. Elsäßer, "Mutually delay-coupled semiconductor lasers: Mode bifurcation scenarios," *Opt. Commun.*, vol. 255, no. 4-6, pp. 286–296, 2005.

[185] L. M. Pecora and T. L. Carroll, "Master stability functions for synchronized coupled systems," *Phys. Rev. Lett.*, vol. 80, no. 10, pp. 2109–2112, 1998.

[186] V. Rottschäfer and B. Krauskopf, "The ECM-backbone of the Lang-Kobayashi equations: a geometric picture," *Applied Nonlinear Mathematics Research Report, University of Bristol*, 2005. preprint.

[187] S. Yanchuk and M. Wolfrum, "Synchronous and asynchronous instabilities of two lasers with a long delayed coupling," in *Proc. 5th EUROMECH Nonlinear Dynamics Conference ENOC-2005, Eindhoven* (D. H. van Campen, M. D. Lazurko, and W. P. J. M. van den Oever, eds.), (Eindhoven, Netherlands), pp. 2069–2073, Eindhoven University of Technology, 2005. ENOC Eindhoven (CD ROM), ISBN 90 386 2667 3.

[188] R. Vicente, T. Pérez, and C. R. Mirasso, "Open-versus closed-loop performance of synchronized chaotic external-cavity semiconductor lasers," *IEEE J. Quantum Electron.*, vol. 38, no. 9, pp. 1197–1204, 2002.

[189] T. Heil, J. Mulet, I. Fischer, C. R. Mirasso, M. Peil, P. Colet, and W. Elsäßer, "On/off phase shift keying for chaos-encrypted communication using external-cavity semiconductor lasers," *IEEE J. Quantum Electron.*, vol. 38, no. 9, pp. 1162–1170, 2002.

[190] S. E. Würtenberger, "Unterdrückung und Kontrolle chaotischer Instabilitäten von Halbleiterlasern unter externer optischer Rückkopplung," Master's thesis, Technische Universität Darmstadt, 2000.

[191] Y. Liu and J. Ohtsubo, "Dynamics and chaos stabilization of semiconductor lasers with optical feedback from an interferometer," *IEEE J. Quantum Electron.*, vol. 33, no. 7, pp. 1163–1169, 1997.

[192] F. Rogister, P. Mégret, O. Deparis, M. Blondel, and T. Erneux, "Suppression of low-frequency fluctuations and stabilization of a semiconductor laser subjected to optical feedback from a double cavity: theoretical results," *Opt. Lett.*, vol. 24, no. 17, pp. 1218–1220, 1999.

[193] J. Mulet, C. Masoller, and C. R. Mirasso, "Modeling bidirectionally coupled single-mode semiconductor lasers," *Phys. Rev. A*, vol. 65, no. 6, p. 63815, 2002.

[194] A. S. Landsman and I. B. Schwartz, "Complete chaotic synchronization in mutually coupled time-delay systems," *Phys. Rev. E*, vol. 75, no. 2, p. 026201, 2007.

[195] S. C. Venkataramani, B. R. Hunt, and E. Ott, "Bubbling transition," *Phys. Rev. E*, vol. 54, no. 2, pp. 1346–1360, 1996.

[196] S. C. Venkataramani, B. R. Hunt, E. Ott, D. J. Gauthier, and J. C. Bienfang, "Transitions to bubbling of chaotic systems," *Phys. Rev. Lett.*, vol. 77, no. 27, pp. 5361–5364, 1996.

[197] A. Gonzalez-Buelga, D. Wagg, and S. Neild, "Parametric variation of a coupled pendulum-oscillator system using real-time dynamic substructuring," *Structural Control and Health Monitoring*, vol. 14, no. 7, pp. 991–1012, 2007.

[198] J. F. Heagy, L. M. Pecora, and T. L. Carroll, "Short wavelength bifurcations and size instabilities in coupled oscillator systems," *Phys. Rev. Lett.*, vol. 74, no. 21, pp. 4185–4188, 1995.

[199] S.-Y. Kim and W. Lim, "Mechanisms for the hard bubbling transition in symmetrically coupled chaotic systems," *Journal of Physics A: Mathematical and General*, vol. 36, no. 25, p. 6951, 2003.

[200] N. Platt, E. A. Spiegel, and C. Tresser, "On-off intermittency: A mechanism for bursting," *Phys. Rev. Lett.*, vol. 70, no. 3, pp. 279–282, 1993.

[201] J. F. Heagy, N. Platt, and S. Hammel, "Characterization of on-off intermittency," *Phys. Rev. E*, vol. 49, no. 2, pp. 1140–1150, 1994.

[202] S. H. Ashworth, M. Joschko, M. Woerner, E. Riedle, and W. Elsäßer, "Generation of 16 fs pulses at 425 nm by extracavity frequency doubling of a mode-locked Ti:sapphire laser," *Opt. Lett.*, vol. 20, p. 2120, 1996.

[203] A. N. Pisarchik, R. Jaimes-Rategui, and J. H. Garcia, "Synchronization of coupled bistable chaotic systems: experimental study," *Phil. Trans. R. Soc. A*, vol. 366, pp. 459–473, 2008.

[204] B. Lading, E. Mosekilde, S. Yanchuk, and Y. Maistrenko, "Chaotic synchronization between coupled pancreatic -cells," *Prog. Theor. Phys. Suppl.*, vol. 139, pp. 164–177, 2000.

[205] N. Jiang, W. Pan, B. Luo, L. Yan, S. Xiang, L. Yang, D. Zheng, and N. Li, "Properties of leader-laggard chaos synchronization in mutually coupled external-cavity semiconductor lasers," *Phys. Rev. E*, vol. 81, p. 066217, 2010.

[206] X. Porte, M. C. Soriano, and I. Fischer, "Similarity properties in the dynamics of delayed-feedback semiconductor lasers," *Phys. Rev. A*, vol. 89, p. 023822, Feb 2014.

[207] S. Heiligenthal, T. Jüngling, O. D'Huys, D. A. Arroyo-Almanza, M. C. Soriano, I. Fischer, I. Kanter, and W. Kinzel, "Strong and weak chaos in networks of semiconductor lasers with time-delayed couplings," *Phys. Rev. E*, vol. 88, p. 012902, 2013.

[208] G. N. Milshtein, "Approximate integration of stochastic differential equations," *Theory. Prob. Appl.*, vol. 19(3), pp. 557–562, 1974.

[209] M. San Miguel and R. Toral, "Stochastic effects in physical systems," in *Instabilities and Nonequilibrium Structures VI* (E. Tirapegui, J. Martinez, and R. Tiemann, eds.), vol. 5 of *Nonlinear Phenomena and Complex Systems*, pp. 35–127, Springer Netherlands, 2000.

[210] T. Deng, G.-Q. Xia, Z.-M. Wu, X.-D. Lin, and J.-G. Wu, "Chaos synchronization in mutually coupled semiconductor lasers with asymmetrical bias currents," *Optics express*, vol. 19, no. 9, pp. 8762–8773, 2011.

[211] F. Heinrichsdorff, *MOCVD growth and laser applications of In(Ga)As/GaAs Quantum Dots.* PhD thesis, Technische Universität Berlin, 1998.

[212] L. Gollo, C. Mirasso, O. Sporns, and M. Breakspear, "Mechanisms of Zero-Lag Synchronization in Cortical Motifs," *J. Comp. Neurosc.*, 2014. to appear presently, arXiv:1304.5008.

[213] J. Dambre, D. Verstraeten, B. Schrauwen, and S. Massar, "Information processing capacity of dynamical systems," *Scientific reports*, vol. 2, 2012.

[214] J. P. Crutchfield, W. L. Ditto, and S. Sinha, "Introduction to focus issue: intrinsic and designed computation: information processing in dynamical systemsbeyond the digital hegemony," *Chaos: An Interdisciplinary Journal of Nonlinear Science*, vol. 20, no. 3, p. 037101, 2010.

[215] D. Woods and T. J. Naughton, "Optical computing: Photonic neural networks," *Nature Physics*, vol. 8, no. 4, pp. 257–259, 2012.

[216] "Online:." http://www.research.ibm.com/cognitive-computing/. Accessed: 09-05-2014.

[217] G. Van der Sande, M. C. Soriano, I. Fischer, and C. R. Mirasso, "Dynamics, correlation scaling, and synchronization behavior in rings of delay-coupled oscillators," *Phys. Rev. E*, vol. 77, no. 5, p. 055202, 2008.

[218] M. Fiers, K. Vandoorne, T. Van Vaerenbergh, J. Dambre, B. Schrauwen, and P. Bienstman, "Optical information processing: Advances in nanophotonic reservoir computing," in *Transparent Optical Networks (ICTON), 2012 14th International Conference on*, pp. 1–4, IEEE, 2012.

[219] A. Uchida, R. McAllister, and R. Roy, "Consistency of nonlinear system response to complex drive signals," *Phys. Rev. Lett.*, vol. 93, no. 24, p. 244102, 2004.

[220] D. Verstraeten, B. Schrauwen, S. Dieleman, P. Brakel, P. Buteneers, and D. Pecevski, "Oger: modular learning architectures for large-scale sequential processing," *The Journal of Machine Learning Research*, vol. 13, no. 1, pp. 2995–2998, 2012.

[221] R. Martinenghi, S. Rybalko, M. Jacquot, Y. K. Chembo, and L. Larger, "Photonic nonlinear transient computing with multiple-delay wavelength dynamics," *Physical review letters*, vol. 108, no. 24, p. 244101, 2012.

[222] M. Le Berre, E. Ressayre, A. Tallet, H. M. Gibbs, D. L. Kaplan, and M. H. Rose, "Conjecture on the dimensions of chaotic attractors of delayed-feedback dynamical systems," *Physical Review A*, vol. 35, no. 9, p. 4020, 1987.

[223] "Texas instruments-developed 46-word speaker-dependent isolated word corpus (TI46), September 1991," *NIST Speech Disc 7-1.1 (1 disc)*.

[224] R. F. Lyon, "A computational model of filtering, detection, and compression in the cochlea," in *Acoustics, Speech, and Signal Processing, IEEE International Conference on ICASSP'82.*, vol. 7, pp. 1282–1285, IEEE, 1982.

[225] A. S. Weigend and N. A. Gershenfeld, "Time series prediction: Forecasting the future and understanding the past," 1993. Available: http://www-psych.stanford.edu/ andreas/Time-Series/SantaFe.html.

[226] U. Huebner, N. B. Abraham, and C. O. Weiss, "Dimensions and entropies of chaotic intensity pulsations in a single-mode far-infrared nh3 laser," *Physical Review A*, vol. 40, no. 11, p. 6354, 1989.

[227] M. C. Soriano, S. Ortín, L. Keuninckx, L. Appeltant, J. Danckaert, L. Pesquera, and G. Van der Sande, "elay-based reservoir computing: noise effects in a combined analog and digital implementation,"

[228] R. M. Nguimdo, G. Verschaffelt, J. Danckaert, and G. Van der Sande, "Fast photonic information processing using semiconductor lasers with delayed optical feedback: Role of phase dynamics," *Optics express*, vol. 22, no. 7, pp. 8672–8686, 2014.

[229] W. Walker, P. Lamere, P. Kwok, B. Raj, R. Singh, E. Gouvea, P. Wolf, and J. Woelfel, "Sphinx-4: A flexible open source framework for speech recognition," *TR-2004-139*, 2004.

[230] D. Verstraeten, B. Schrauwen, D. Stroobandt, and J. Van Campenhout, "Isolated word recognition with the liquid state machine: A case study," *Information Processing Letters*, vol. 95, no. 6, pp. 521–528, 2005.

[231] A. Rodan and P. Tino, "Minimum complexity echo state network," *Neural Networks, IEEE Transactions on*, vol. 22, no. 1, pp. 131–144, 2011.

[232] S. H. Strogatz, *Nonlinear Dynamics and Chaos.* Cambridge, MA: Westview Press, 1994.